

ABSOLUTE QUANTIFICATION OF OXYGEN METABOLISM IN THE HUMAN  
BRAIN USING FMRI

ABSOLUTE QUANTIFICATION OF OXYGEN METABOLISM IN THE HUMAN  
BRAIN USING FMRI

By

ALAN J. STONE, M.Sc.

A Thesis

Submitted to the School of Graduate Studies

in Partial Fulfilment of the Requirements

for the Degree

Doctor of Philosophy

Cardiff University

©Copyright by Alan Stone, December 2014

DOCTOR OF PHILOSOPHY (2014)  
(Psychology)

Cardiff University  
Cardiff, Wales

TITLE: Absolute Quantification of Oxygen Metabolism in the Human Brain  
using FMRI

AUTHOR: Alan Stone, M.Sc.

SUPERVISORS: Prof. Richard G. Wise, Dr. Kevin Murphy

NUMBER OF PAGES: xix, 257

# Declaration Form

The following declaration is required when submitting your PhD thesis under the University's regulations.

## Declaration

This work has not previously been accepted in substance for any degree and is not concurrently submitted in candidature for any degree.

.....

.....

Candidate

Date

## Statement 1

This thesis is being submitted in partial fulfillment of the requirements for the degree of PhD.

.....

.....

Candidate

Date

## Statement 2

This thesis is the result of my own independent work/investigation, except where otherwise stated. Other sources are acknowledged by explicit references.

.....

Candidate

Date

**Statement 3**

I hereby give consent for my thesis, if accepted, to be available for photocopying and for inter-library loan, and for the title and summary to be made available to outside organisations.

.....

Candidate

Date

**Statement 4: Previously approved bar on access**

I hereby give consent for my thesis, if accepted, to be available for photocopying and for inter-library loans after expiry of a bar on access previously approved by the Graduate Development Committee.

.....

Candidate

Date

# Acknowledgements

Firstly I would like to thank everyone at CUBRIC, both past and present, who have made it a great place to work. I would like to thank my supervisors, Professor Richard Wise and Dr. Kevin Murphy whose encouragement, guidance and support throughout every aspect of this project was invaluable. I am grateful for all the time and knowledge they invested in me and this project. I would also like to thank Dr. Ashley Harris, Dr. John Evans and everybody working as part of the FMRI group for all the useful discussions and guidance throughout my studies. Finally I would like to say a huge thank you to Sinéad, my family and friends, for providing all the support possible and particularly for putting up with me!

# List of Abbreviations

Abbreviation	Description
AAT	Arterial Arrival Time
ASE	Asymmetric Spin Echo
ASL	Arterial Spin Labelling
ATP	Adenosine TriPhosphate
BOLD	Blood Oxygen Level Dependent
$C_aO_2$	Arterial Oxygen Content
CASL	Continuous Arterial Spin Labelling
CBF	Cerebral Blood Flow
CBV	Cerebral Blood Volume
CMRO <sub>2</sub>	Cerebral Metabolic Rate of Oxygen
$C_vO_2$	Venous Oxygen Content
dcfMRI	dual calibrated Functional Magnetic Resonance Imaging
dHb	deoxyHaemoglobin
EPI	Echo Planar Imaging
EPISTAR	Echo Planar Imaging and Signal Targeting with Alternating Radio-frequency
ET	End Tidal
FAIR	Flow-sensitive Alternating Inversion Recovery
fMRI	Functional Magnetic Resonance Imaging
GKM	General Kinetic Model
GM	Grey Matter
GRE	Gradient Echo
Hb	Haemoglobin
MRI	Magnetic Resonance Imaging

NIRS	Near InfraRed Spectroscopy
NMR	Nuclear Magnetic Resonance
$^{15}\text{O}$	Oxygen 15 isotope
OEF	Oxygen Extraction Fraction
OL	Occipital Lobe
PASL	Pulsed Arterial Spin Labelling
PCASL	Pseudo Continuous Arterial Spin Labelling
PET	Positron Emission Tomography
PG	Precentral Gyrus
PICORE	Proximal Inversion with Control for Off-Resonance Effects
PLD	Post Labelling Delay
PROM	Phase-based Regional Oxygen Metabolism
$\text{PCO}_2$	Partial pressure of carbon dioxide
$\text{PO}_2$	Partial pressure of oxygen
qBOLD	quantitative Blood Oxygen Level Dependent
QUIPSS	QUantitative Imaging of Perfusion using a Single Subtraction
QUIXOTIC	QUantitative Imaging of eXtraction of Oxygen and TIssue Consumption
RF	RadioFrequency
ROI	Region Of Interest
SE	Spin Echo
SNR	Signal to Noise Ratio
$\text{S}_v\text{O}_2$	Venous oxygen saturation
TE	Echo Time
TI	Inversion Time
TR	Repetition Time



TRUST	T <sub>2</sub> Relaxation Under Spin Tagging
VSEAN	Velocity-Selective Excitation with Arterial Nulling

# Summary

To produce energy and maintain healthy function the brain requires a steady supply of oxygen which if interrupted results in impaired function and tissue damage. Oxygen metabolism is therefore presented as a desirable physiological function to measure as it is closely linked with brain tissue function and health. Recently an MRI method was introduced capable of measuring absolute oxygen metabolism in the brain [1–3]. The technique is based on using both hypercapnic and hyperoxic respiratory challenges to calibrate the blood oxygen level dependent (BOLD) functional MRI (fMRI) signal. The aim of this thesis is to further develop this promising technique, referred to here as dual calibrated fMRI (dcfMRI), proving its suitability for application in further studies of oxygen metabolism in the brain.

Initially, in this thesis, the role of oxygen metabolism in energy production, brain function and disease is discussed. To motivate the development of dcfMRI a review of current measurement techniques is presented followed by an introduction to the basic MRI concepts underpinning the dcfMRI approach. The dcfMRI technique is then described in detail.

The optimal ASL acquisition available in our centre for application in the dcfMRI measurement was experimentally investigated, allowing a dcfMRI protocol to be implemented. A comparison of dcfMRI respiratory designs, for detecting regional changes in oxygen metabolism, was made and the within and between session repeatability of these measurements were assessed. In order to make the technique more clinically feasible, reductions in acquisition time were assessed using a retrospective analytical approach. The ability of dcfMRI to detect global flow related changes in oxygen metabolism was demonstrated and a novel dcfMRI approach was implemented. This availed of an  $R_2'$  based measure to replace the hypercapnic respiratory challenge in the dcfMRI protocol. Potential areas for future work and further application of the dcfMRI technique are then considered.

# Table of Contents

<b>Declaration Form</b>	iii
<b>Acknowledgements</b>	v
<b>List of Abbreviations</b>	vi
<b>Summary</b>	ix
 <b>Chapter 1 Energy Metabolism and the Brain</b>	 <b>1</b>
1.1 The Brain on a Cellular Level . . . . .	1
1.1.1 The Neuron . . . . .	2
1.1.2 Neural Signalling . . . . .	2
1.1.3 Restoring the Resting Potential . . . . .	4
1.2 Oxygen Metabolism in the Brain . . . . .	5
1.2.1 Adenosine Triphosphate . . . . .	5
1.2.2 Arterial Blood Gases . . . . .	6
Oxygen Transport . . . . .	6
Carbon Dioxide Transport . . . . .	7
Measurement of Blood Gases . . . . .	8
Effect of CO <sub>2</sub> on Blood Flow . . . . .	9
1.2.3 Oxygen Extraction Fraction and Cerebral Blood Flow . . . . .	9
OEF and CBF in Disease . . . . .	11
1.2.4 Cerebral Metabolic Rate of Oxygen Consumption . . . . .	11
CMRO <sub>2</sub> , Neural Activity and Disease . . . . .	12
1.3 Measurement of Cerebral Oxygen Metabolism . . . . .	13
1.3.1 Kety-Schmidt Approach . . . . .	13
1.3.2 PET . . . . .	14

1.3.3	Near Infrared Spectroscopy . . . . .	15
1.3.4	Magnetic Resonance Imaging . . . . .	16
<b>Chapter 2</b>	<b>Magnetic Resonance Imaging</b>	<b>17</b>
2.1	Basic MRI Concepts . . . . .	17
2.1.1	Main Magnetic Field . . . . .	19
2.1.2	RF Excitation . . . . .	20
2.1.3	RF Receive . . . . .	20
2.1.4	Gradient System . . . . .	21
2.1.5	Image Localisation . . . . .	22
	Slice Selection . . . . .	22
	Signal Encoding . . . . .	22
2.1.6	Relaxation . . . . .	23
	Longitudinal Relaxation . . . . .	23
	Transverse Relaxation . . . . .	24
2.1.7	Refocusing and Echo Creation . . . . .	24
	Spin Echo . . . . .	25
	Gradient Echo . . . . .	25
	K-space . . . . .	26
	Filling K-space . . . . .	27
2.2	Functional MRI . . . . .	29
2.2.1	Echo Planar Imaging . . . . .	29
	K-space Trajectory, Spiral EPI . . . . .	30
	GRE-EPI and T2* . . . . .	31
2.2.2	Blood Oxygen Level Dependent Signal . . . . .	31

2.2.3	Arterial Spin Labelling and CBF . . . . .	33
	PASL . . . . .	35
	QUIPSS II . . . . .	36
	CASL . . . . .	36
	PCASL . . . . .	37
2.2.4	CBF Quantification . . . . .	38
	The GKM . . . . .	38
	Equilibrium Magnetisation Estimation . . . . .	42
	Coil Sensitivity Correction . . . . .	43
2.2.5	ASL Acquisitions to Detect Simultaneous CBF and BOLD	
	Signals . . . . .	43
	Dual-Echo Acquisition . . . . .	44
2.2.6	Calibrated BOLD . . . . .	44
	Hypercapnia . . . . .	45
	Hyperoxia . . . . .	45
	BOLD Signal Model . . . . .	45
	Limitations of Calibrated BOLD . . . . .	48
2.3	MRI for Measuring OEF and Absolute CMRO <sub>2</sub> . . . . .	50
2.3.1	Phase Based Methods . . . . .	50
	Extravascular R' <sub>2</sub> Based Methods . . . . .	51
	Intravascular T <sub>2</sub> Based Methods . . . . .	52
2.4	Dual Calibrated fMRI . . . . .	53
2.4.1	Expanded BOLD-Signal Model . . . . .	54
2.5	Thesis Outline . . . . .	55

### **Chapter 3 Comparison of Acquisition Techniques for Detecting Task-Related Changes in CBF and BOLD** **58**

3.1	Introduction . . . . .	58
3.1.1	Arterial Spin Labelling . . . . .	59
	Comparison of ASL Techniques . . . . .	59
3.2	Methods . . . . .	63
3.2.1	Participants . . . . .	63
3.2.2	Scanning Protocol . . . . .	63
	Dual-Echo PASL with Spiral EPI Readout . . . . .	64
	Single-Echo PCASL with Cartesian EPI Readout . . . . .	65
3.2.3	Analysis . . . . .	67
	CBF and BOLD Time-Series . . . . .	67
	General Linear Model . . . . .	67
3.3	Results . . . . .	69
3.4	Discussion . . . . .	72
3.5	Conclusion . . . . .	76

### **Chapter 4 Comparison of Dual Calibrated fMRI Respiratory Designs for the Detection of Regional Alterations in Absolute CMRO<sub>2</sub>** **77**

4.1	Introduction . . . . .	77
4.1.1	PET . . . . .	78
4.1.2	MRI . . . . .	79
	Relative CMRO <sub>2</sub> and Calibrated BOLD . . . . .	79
	Absolute CMRO <sub>2</sub> . . . . .	80
4.1.3	Dual Calibrated fMRI . . . . .	80

4.2	Methods . . . . .	85
4.2.1	Participants . . . . .	85
4.2.2	MRI . . . . .	85
	CBF and BOLD Acquisition . . . . .	87
4.2.3	Stimulus Design . . . . .	87
	Functional Localiser . . . . .	88
	Baseline and Elevated Baseline CMRO <sub>2</sub> Conditions . . . . .	88
4.2.4	Respiratory Manipulations . . . . .	89
	Interleaved and Simultaneous Hypercapnic-Hyperoxic Res- piratory Designs . . . . .	90
4.2.5	Analysis . . . . .	90
	Preprocessing . . . . .	90
	Anatomical ROI Timeseries . . . . .	91
	Functionally Localised ROI Timeseries . . . . .	92
	Block Averaging . . . . .	92
	Absolute CMRO <sub>2</sub> Quantification . . . . .	93
	Statistical Testing . . . . .	94
4.3	Results . . . . .	95
4.4	Discussion . . . . .	100
4.5	Conclusion . . . . .	110

**Chapter 5 Test-Retest Repeatability of Dual Calibrated fMRI Measures of Oxygen Metabolism in the Brain. 111**

5.1	Introduction . . . . .	111
5.2	Methods . . . . .	113

5.2.1	Participants . . . . .	113
5.2.2	MRI . . . . .	115
5.2.3	Acquisition Overview . . . . .	115
5.2.4	Data Preprocessing . . . . .	116
5.2.5	Regions of Interest (ROI's) . . . . .	117
	Quantification of Physiological Parameters . . . . .	118
5.2.6	Statistical Analysis . . . . .	119
	Coefficients of variation . . . . .	119
	Intraclass Correlation . . . . .	121
5.3	Results . . . . .	122
5.3.1	Coefficients of Variation . . . . .	122
5.3.2	Intraclass Correlation . . . . .	122
5.4	Discussion . . . . .	126
5.4.1	CV's . . . . .	127
5.4.2	ICC's . . . . .	129
5.5	Conclusion . . . . .	133

## **Chapter 6 Optimisation of Acquisition Time for a Dual Calibrated fMRI**

<b>Protocol</b>	<b>134</b>
6.1	Introduction . . . . .
6.1.1	Reducing Acquisition Time . . . . .
6.1.2	Interleaved Hypercapnic-Hyperoxic Respiratory Design . . .
6.1.3	Simultaneous Hypercapnic-Hyperoxic Respiratory Design . .
6.1.4	Block Averaging Time-Points . . . . .
6.1.5	Analytical Approach . . . . .



	Timecourse Splitting . . . . .	139
	Varying Block Average Window Sizes . . . . .	139
	Block Averaged Time-Point Resampling . . . . .	140
6.2	Methods . . . . .	144
6.2.1	Participants . . . . .	144
6.2.2	MRI . . . . .	144
6.2.3	Respiratory Manipulation . . . . .	145
6.2.4	Preprocessing . . . . .	146
6.2.5	ROI's . . . . .	147
6.2.6	Block Averaging . . . . .	148
6.2.7	Split Design Analysis . . . . .	148
6.2.8	Block Averaging using Varying Window Duration . . . . .	149
6.2.9	Block Averaged Time-Point Resampling . . . . .	149
6.2.10	Calculating Absolute CMRO <sub>2</sub> . . . . .	152
6.3	Results . . . . .	153
6.3.1	Split Design Analysis . . . . .	153
6.3.2	Varying Window Duration Analysis . . . . .	153
6.3.3	Block Averaged Time-Point Resampling . . . . .	157
6.4	Discussion . . . . .	160
6.4.1	Split Design Comparison . . . . .	160
6.4.2	Varying Window Size for Block Averaging . . . . .	163
6.4.3	Block Averaged Time-Point Resampling . . . . .	166
6.5	Conclusion . . . . .	167

**Chapter 7 Investigation of Changes in OEF due to Hypocapnia Induced  
by Voluntary Hyperventilation Measured using Dual Calibrated FMRI 169**

7.1	Introduction . . . . .	169
7.1.1	Dual Calibrated FMRI . . . . .	170
7.1.2	Hyperventilation and Hypocapnia . . . . .	170
7.2	Methods . . . . .	172
7.2.1	Participants . . . . .	172
7.2.2	MRI . . . . .	172
7.2.3	Respiratory Manipulations . . . . .	174
7.2.4	Analysis . . . . .	177
	Preprocessing . . . . .	177
	Grey Matter Analysis . . . . .	177
	Whole Brain Analysis . . . . .	179
	Statistical Analysis . . . . .	179
7.3	Results . . . . .	180
7.3.1	Hypocapnic $P_{Et}CO_2$ . . . . .	180
7.3.2	Global Grey Matter Analysis . . . . .	180
7.3.3	Whole Brain Parameter Maps . . . . .	183
7.4	Discussion . . . . .	183
7.5	Conclusion . . . . .	190

**Chapter 8 Comparison of Asymmetric Spin Echo with Dual Calibrated  
FMRI using Hypercapnic-Hyperoxic Respiratory Challenges 191**

8.1	Introduction . . . . .	191
8.1.1	Hypercapnia . . . . .	192

8.1.2	Relaxometry and Quantitative BOLD . . . . .	193
8.2	Background and Theory . . . . .	195
8.2.1	Calibrated BOLD . . . . .	195
8.2.2	Dual Calibrated FMRI . . . . .	198
8.2.3	$R'_2$ . . . . .	199
	Asymmetric Spin Echo (ASE) for Measuring $R'_2$ . . . . .	201
8.3	Methods . . . . .	203
8.3.1	Participants . . . . .	203
8.3.2	MRI . . . . .	204
	Dual Calibrated FMRI . . . . .	204
	Asymmetric Spin Echo . . . . .	205
8.3.3	Analysis . . . . .	206
	$M_{R'_2}$ , ASE . . . . .	206
	Respiratory Manipulated FMRI . . . . .	207
	$M$ , Calibrated BOLD . . . . .	208
	Dual Calibrated FMRI . . . . .	209
8.3.4	ASE- $R'_2$ and Hyperoxic Calibrated BOLD . . . . .	210
8.4	Results . . . . .	210
8.4.1	ASE Signal Attenuation Correction, $F(\tau)$ . . . . .	210
8.4.2	Characterisation of $M_{R'_2}$ with $\tau$ . . . . .	211
8.4.3	Comparison of Haemodynamic Variables Measured using Cal- ibrated BOLD, dcFMRI and $ASE_{R'_2}$ . . . . .	211
	Maximum BOLD Signal Change, $M$ . . . . .	212
	Comparison of $S_vO_2$ and $CMRO_2$ Measured using dcFMRI and $ASE_{R'_2}$ with hyperoxic calibrated BOLD . . . .	213

8.5	Discussion . . . . .	216
8.5.1	ASE Signal Attenuation Correction, $F(\tau)$ . . . . .	217
8.5.2	Characterisation of $M_{R'_2}$ with $\tau$ . . . . .	218
8.5.3	Comparison of Haemodynamic Variables Measured using Cal- ibrated BOLD, dcfMRI and $ASE_{R'_2}$ . . . . .	218
	Maximum BOLD Signal Change, $M$ . . . . .	218
	Comparison of $S_vO_2$ and $CMRO_2$ Measured using dcfMRI and $ASE_{R'_2}$ with Hyperoxic Calibrated BOLD . . .	219
	Limitations and Further Work . . . . .	221
8.6	Conclusion . . . . .	222
<b>Chapter 9</b>	<b>Discussion and Conclusions</b>	<b>223</b>
<b>Appendix A</b>		<b>229</b>
<b>Bibliography</b>		<b>235</b>

# Chapter 1

## Energy Metabolism and the Brain

The brain serves as the centre of the nervous system providing centralised control over the other organs in the body. As with all organs, energy metabolism is vital to fuel basic cellular processes and maintain proper working function of the brain and therefore the body. In this chapter motivation will be provided for the measurement of physiological processes related to energy metabolism.

### 1.1 The Brain on a Cellular Level

The brain is composed mainly of glial cells and neurons. Glial cells are responsible for the structural support, metabolism, insulation and guidance of development whereas neurons are responsible for relaying information throughout the brain and body. Neurons are electrically excitable cells that process and transmit information through electrochemical signals. They form the basis of the vastly complicated signalling system which allows the brain centralised control over the body. In order to achieve this billions of interconnected neurons form the nervous system and relay signals to and from the brain.

### 1.1.1 The Neuron

A single neuron is composed of a number of different parts, each with a specific function. The soma or cell body, contains the cell nucleus and serves to maintain the cell and keep the neuron functional. Dendrites branch outward from the soma and act as receivers for neural signals communicated by connected neurons. Neural signals are transported through the neuron via the axon, an elongated fibre that extends from the cell body to terminal endings. The terminal endings form connections with dendrites of other cells, which may be neurons, through the synapse. The synapse allows the transmission of the electrochemical signals from the terminal endings (pre-synaptic) to the dendrites (post-synaptic) using a neurotransmitter. When an electrochemical signal has travelled the length of the axon it stimulates the release of neurotransmitters into the synapse. The neurotransmitter crosses the synapse and attaches to receptors on the neighbouring cell. These receptors can change the properties of the receiving cell and if the receiving cell is also a neuron, the signal can continue the transmission to the next cell.

### 1.1.2 Neural Signalling

The signals transported by neurons are in the form of electrochemical pulses referred to as action potentials. These electrochemical signals are formed due to the distribution of ions inside and outside the cell. Ions are atoms with a net positive or negative electrical charge. The cell membrane is the division which divides the interior and exterior of the cell and the membrane potential describes the electrical potential or voltage across the cell membrane due to the presence of ions. As a

result, the membrane potential depends on the intra / extra - cellular distribution of ions across the cell membrane and the permeability of the membrane to those ions. The membrane potential is the medium for neuronal signalling as it is the property in the neuron which is altered when a signal is received from another neuron.

The principle ions involved in neuronal signalling are sodium ( $\text{Na}^+$ ), potassium ( $\text{K}^+$ ), calcium ( $\text{Ca}^{2+}$ ) and chloride ( $\text{Cl}^-$ ) with higher concentrations of  $\text{K}^+$  inside the cell and  $\text{Na}^+$ ,  $\text{Ca}^{2+}$  and  $\text{Cl}^-$  outside the cell. This leads to a net negative resting potential. These ions cannot freely diffuse through the cell membrane but instead their passage is controlled by ion channels. Importantly these ion channels can be modulated to allow the passage of different ions through the membrane.

To form an initial action potential, a signal is sent, from the cell body to the neural membrane, to open ion channels allowing positively charged ions inside the cell and negatively charged ions out. This process causes a rapid increase in the positive charge of the nerve fibre. When the charge reaches a threshold level the impulse is propagated down the nerve fibre. This electrical impulse is carried down the nerve through a series of action potentials. An action potential which arrives at a synapse with another neuron initiates a process, releasing neurotransmitters from vesicles in the pre-synaptic terminal which cause ion channels on the post-synaptic neuron to open or close. Depending on the type of ion channels which are opened or closed the membrane potential may depolarise again producing a propagation of the action potential.

A given neuron may receive signals from many other neurons at any given time, creating fluctuations in the membrane potential on the dendritic tree. If a sufficient cumulative current reaches the cell body, the membrane potential will be depolarised, generating an action potential and sending a new signal to other neurons. However it is important to note that there is likely to be a lot of synaptic activity that does not lead to spiking or action potentials.

### 1.1.3 Restoring the Resting Potential

After the neuron has fired, there is a refractory period in which another action potential is not possible and the cell must return to its original high energy resting state. This allows the neuron to produce further action potentials. It is at this stage where an energy source is required to perform work. The resting potential of the neuron must be restored and the neurotransmitter returned to the vesicles in a process which requires movement of atoms and molecules against their concentration gradients. As such, neuronal signalling can be considered a spontaneous but controlled process. The neuron is stored in a high energy state where it is waiting for a trigger to release this energy.

From this it can be seen that neurons require energy in order to maintain proper function. Energy is required for basic cellular maintenance, the generation and propagation of the action potential, pre-synaptic recovery involving the clearance of ions and repackaging of neurotransmitter to the vesicles and post-synaptic recovery involving restoration of the intra / extra - cellular ion distribution. How much energy is required depends on the spiking rate and average number of synapses



reached by each action potential. However, the most energy intensive process involves the restoration of post-synaptic resting potential [4].

## 1.2 Oxygen Metabolism in the Brain

### 1.2.1 Adenosine Triphosphate

Adenosine triphosphate (ATP) is the main source of energy used by cells in the body and is therefore the main source of energy used to fuel the cellular processes associated with neural signalling and activity. It is estimated that at least half of the ATP used in the brain is consumed in the restoration of post-synaptic resting potential [5].

ATP can be produced in the brain through aerobic respiration, a process which requires oxygen, and anaerobic respiration, in a process which does not require oxygen. Aerobic respiration occurs when oxygen and hydrogen atoms bond together to break down glucose, and facilitate an exchange of energy, producing by-products of carbon dioxide and water. Anaerobic glycolysis, occurs when glucose is broken down without the presence of oxygen and has lactic acid as a by-product.

Another distinguishing feature between the two processes is that aerobic respiration produces considerably more ATP molecules, 38 per glucose molecule, compared to anaerobic respiration, 2 ATP molecules per glucose molecule. The importance of oxygen to the brain is therefore highlighted by the fact that virtually all of the ATP used to fuel cellular work is derived from the metabolism of glu-

cose and oxygen. If the brain is deprived of oxygen, energy production through purely anaerobic means cannot meet the brain's energy demands, leading to unconsciousness and irreversible cellular death. Following on from this, as the brain has no reserve supplies of oxygen and glucose it must be continuously supplied with these raw materials in order to maintain sufficient production of ATP and maintain proper cellular function.

### 1.2.2 Arterial Blood Gases

#### Oxygen Transport

Human blood is primarily comprised of plasma and red blood cells (RBC's) which carry haemoglobin. Since oxygen is only soluble in water in small quantities, the main constituent of blood, an oxygen transport protein is required to carry sufficient amounts of oxygen in the blood. In humans this oxygen transport protein is haemoglobin. Haemoglobin is composed of four chains of proteins (globins), with a haem group attached to each chain, each of which contains one iron ion. The iron ion is the site of oxygen binding and as such each haemoglobin molecule is capable of binding a total of four oxygen molecules.

The partial pressure of oxygen ( $pO_2$ ) determines how much oxygen is bound to haemoglobin. The vast majority of oxygen present in blood is bound to haemoglobin, with only a very small amount dissolved in plasma. The maximum amount of oxygen that can be carried in the blood is therefore determined by the amount

of haemoglobin present. When every oxygen binding site is occupied the blood is said to be 100% saturated.

The oxygen-haemoglobin dissociation curve plots the proportion of haemoglobin in its saturated form on the vertical axis against  $pO_2$  on the horizontal axis. The curve typically follows a sigmoidal shape with higher  $pO_2$  values demonstrating higher oxygen saturation. The oxygen-haemoglobin dissociation curve is essential in understanding how blood carries and releases oxygen. Values of  $pO_2$  in the lungs are typically 100 mmHg whereas  $pO_2$  in tissue capillaries are typically lower,  $\sim 40$  mmHg. Highly saturated arterial blood which has travelled from the lungs to the tissue capillaries therefore releases oxygen to the tissue due to the gradient in  $pO_2$  between lung and tissue capillaries. Tissue which is more active uses more oxygen, dropping tissue  $pO_2$  and leading to a greater gradient causing larger oxygen delivery to the active tissue.

### Carbon Dioxide Transport

Carbon dioxide is produced in the tissue, and diffuses down its concentration gradient into the extracellular fluid and then into the blood. Carbon dioxide is not easily stored and transported in its original form, but reacts with water to form bicarbonate ions that are dissolved in the plasma for removal.

The formation of bicarbonate is normally slow in blood plasma, however in RBC's the presence of enzymes dramatically accelerate this process through the transformation of diffusing carbon dioxide into bicarbonate and hydrogen ions. These end products can greatly alter the local pH, and several proteins (including haemoglobin)

help buffer the additional hydrogen ions to maintain stable pH. Haemoglobin acts as a better buffer when deoxygenated thus the unloading of oxygen from haemoglobin enables better absorption and removal of carbon dioxide from the tissue.

Changes in respiration can affect the concentration gradient of gases in the lungs, which in turn can affect the loading and unloading of both oxygen and carbon dioxide throughout the circulatory system. Insufficient ventilation decreases the concentration gradient of carbon dioxide in the lungs and reduces the amount of carbon dioxide transferred from blood to air in the lungs. This causes a rise in vascular carbon dioxide concentrations. Hyperventilation can increase the concentration gradient of carbon dioxide in the lungs causing more carbon dioxide to diffuse out of the blood and into the lungs, reducing the concentrations of carbon dioxide throughout the vasculature.

### Measurement of Blood Gases

The most direct way to measure arterial gas tensions is to sample the blood via arterial puncture, however this method is highly invasive. Pulse oximetry enables non-invasive measurement of oxygen saturation through spectrophotometry while simultaneously monitoring the pulse amplitude and heart rate. Limitations with this technique are associated with the oxygen dissociation curve that correlates  $P_aO_2$  with oxygen saturation and suggests that this method would not be very sensitive to changes in  $P_aO_2$  within the upper flat section of the sigmoid.

Another non-invasive method for estimation of  $P_aO_2$  and  $P_aCO_2$  is to analyse the gas content of expired air. Because these gases diffuse rapidly across biological membranes, arterial partial pressures equilibrate rapidly with alveolar partial pressures (becoming effectively identical). The measured end-tidal values represent the averaging of alveolar gas levels, and are used as an approximation of  $P_aO_2$  and  $P_aCO_2$ . Several studies have supported this relationship [6, 7], and end-tidal values are commonly used in place of actual arterial values that require more invasive sampling methods.

### Effect of $CO_2$ on Blood Flow

Changes in  $P_aCO_2$  are known to cause changes in local CBF. Local concentrations of carbon dioxide determine the local pH level and it is the altered levels of hydrogen ions that initiate a network of signalling resulting in changes in vascular resistance. Changes in pH cause a range of pathways to be initiated, resulting in an increase or decrease of CBF due to smooth muscle relaxation or constriction, respectively.

#### 1.2.3 Oxygen Extraction Fraction and Cerebral Blood Flow

By design glucose and oxygen are delivered to the brain in arterial blood. Glucose is absorbed through the small intestine into the bloodstream through capillaries and is transported to the brain in arterial blood. Once it has reached the capillary beds in the brain, glucose diffuses from the high glucose concentration in the arterial blood to the low glucose concentration in the capillary beds. It must then

diffuse across the interstitial space separating blood vessels and cells and enter the intracellular environment.

Similarly blood becomes oxygenated in the capillary rich, alveoli present in the lungs. As previously described, oxygen does not dissolve in blood so readily and instead becomes bound to haemoglobin in RBC's with a small fraction dissolved in blood plasma. The heart then pumps the oxygen rich blood to the brain via the arteries. Oxygen diffuses into the tissue down a concentration gradient between dissolved gas in capillary plasma and dissolved gas in brain tissue. The proportion of oxygen extracted from arterial blood is referred to as the oxygen extraction fraction (OEF) and is approximately 40% in a healthy human brain at rest. OEF can be calculated if the arterial oxygen content ( $C_aO_2$ ) and venous oxygen content ( $C_vO_2$ ) are known.

$$OEF = \frac{C_aO_2 - C_vO_2}{C_aO_2} \quad (1.1)$$

Cerebral blood flow (CBF) refers to the amount of blood delivered to the brain or a specific region of the brain in a given unit of time and is measured in millilitres of blood delivered per 100g of tissue per minute (ml/100g/min). CBF is therefore a vital physiological parameter that is tightly regulated to meet the brain's metabolic demands. Typical values of CBF in the resting human brain are approximately 50 ml/100g/min for grey matter with CBF in white matter being lower [8].

Once glucose and oxygen has been delivered to the capillary beds by CBF, carbon dioxide, water and heat, the by products of ATP production, produced by oxygen

and glucose metabolism, diffuse out of the cells into the blood and are carried off to the lungs via venous blood.

### OEF and CBF in Disease

Local OEF measures can be used to assess compensatory responses made by the brain due to alterations in CBF. In healthy brain tissue, energy production and consumption is closely matched to CBF with little regional variation in OEF. In order to maintain acceptable oxygen levels within brain tissue, reductions in CBF can lead to progressive increases in OEF. Severe reductions in CBF can be implicated in chronic disease, brain trauma and particularly stroke [9] where mismatches in OEF may mean that sufficient levels of oxygen are not maintained leading to cell dysfunction and ischaemia. In conditions such as stroke, OEF provides an important marker of tissue at risk from impaired blood supply, but which is not yet ischemic.

#### 1.2.4 Cerebral Metabolic Rate of Oxygen Consumption

The cerebral metabolic rate of oxygen consumption ( $CMRO_2$ ) refers to the amount of oxygen consumed, in  $\mu\text{mols}$ , per 100g of tissue, per minute ( $\mu\text{mols}/100\text{g}/\text{min}$ ). Assuming all oxygen extracted from arterial blood is used to form ATP in brain cells,  $CMRO_2$  can be related to OEF and CBF through Fick's first law:

$$CMRO_2 = OEF \cdot CBF \cdot C_aO_2 \quad (1.2)$$

Where  $C_aO_2$  is the oxygen content of arterial blood and is typically  $8 \mu\text{mol}/\text{ml}$  of blood. Typical values of CBF and OEF in grey matter, previously discussed, would therefore suggest a typical  $\text{CMRO}_2$  of  $160 \mu\text{mol}/100\text{g}/\text{min}$  in grey matter.

### **$\text{CMRO}_2$ , Neural Activity and Disease**

The brain is known to have a relatively high, constant rate of metabolism with baseline brain activity having a large energy budget [10]. As previously discussed the brain does not have a reserve supply of oxygen or glucose and due to this high maintenance level of energy required, the brain must be continuously supplied with oxygen and glucose rich blood, through CBF, in order to fuel general basal activity in the brain. OEF is thought to be relatively uniform across the brain despite a larger regional variation of the resting  $\text{CMRO}_2$  [11]. Considering Fick's principle, Equation 1.2, and a constant  $C_aO_2$ , changes in  $\text{CMRO}_2$  can be driven by either changes in OEF, CBF or both. It follows from this that regional increases in metabolism due to increased brain activity and neural signalling lead to an increased ATP demand and therefore an increase in  $\text{CMRO}_2$ .

$\text{CMRO}_2$  is also an important indicator of brain tissue integrity, reflecting the metabolic function of the underlying cells [12]. Perturbations in cerebral oxygen metabolism are associated with neurodegenerative disorders such as Alzheimer's disease, Parkinson's disease and multiple sclerosis [13–15] whilst directly measuring  $\text{CMRO}_2$  can assist in assessing the extent of brain damage after stroke [16] and aid in tumour management and outcome [17].



## 1.3 Measurement of Cerebral Oxygen Metabolism

As  $\text{CMRO}_2$  is closely related to brain function and health and will change regionally with disease or functional activation, a quantifiable measure of oxygen metabolism in the brain will provide a valuable insight into the underlying metabolic changes that accompany normal brain development, ageing and brain disease in which tissue damage or dysfunction alters metabolic activity. Oxygen metabolism presents a functional biomarker which could aid in the diagnosis and development of new treatment pathways of such diseases.

### 1.3.1 Kety-Schmidt Approach

Among the first attempts to quantify oxygen metabolism in the human brain involved the introduction of the Kety-Schmidt method [18]. The approach relies on Fick's principle, measuring CBF alongside arterio-venous differences of oxygen content. The subject breathes nitrous oxide ( $\text{N}_2\text{O}$ ) continuously for several minutes. During this time the arterial and venous concentrations of  $\text{N}_2\text{O}$  are sampled frequently from the carotid artery and the jugular vein. This is done until the arterial, venous and tissue  $\text{N}_2\text{O}$  concentrations come into equilibrium. Information regarding CBF can be calculated by the time it takes to reach this equilibrium state and OEF can be calculated by measuring the arterial-venous difference in oxygen content allowing global  $\text{CMRO}_2$  to be given using Fick's principle (Equation 1.2). However, this technique is highly invasive, requiring substantial surgical

set-up and the measure provided is of global  $\text{CMRO}_2$  and may be insensitive to regional changes in metabolism.

This practical implementation of Fick's principle paved the way for a number of tracer based techniques. The most notable of these being Positron Emission Tomography.

### 1.3.2 PET

Positron emission tomography (PET) is a nuclear imaging technique capable of producing three-dimensional (3D) images of functional processes in the body. A PET system detects pairs of gamma rays emitted indirectly by a positron-emitting radionuclide that is introduced into the body on a biologically active molecule allowing tissue concentrations of that molecule to be measured. By using the isotope,  $^{15}\text{O}$ , imaging of CBF, cerebral blood volume (CBV), OEF and  $\text{CMRO}_2$  can be conducted using PET.

Triple oxygen Positron Emission Tomography (PET) is the current gold standard for performing oxygen metabolism measurements in the brain [19]. This approach involves three separate PET measurements [20–22]. Oxygen gas enriched with  $^{15}\text{O}$  is inhaled into the human body and the spatial distribution and accumulation rate of the labelled water ( $\text{H}_2^{15}\text{O}_2$ ) metabolised from the inhaled  $^{15}\text{O}_2$  can be measured to produce a three dimensional map of  $\text{CMRO}_2$  consumption in the brain providing regional metabolic information. However  $^{15}\text{O}$  PET is unable to distinguish between radioactive signals from  $^{15}\text{O}$  bound to haemoglobin and  $\text{H}_2^{15}\text{O}_2$ . To overcome

this CBV is measured using the inhalation of  $C^{15}O$  gas in addition to a CBF measurement based on the intravenous injection of  $H_2^{15}O_2$  allowing  $CMRO_2$  to be measured accurately [21].

There are however a number of disadvantages to this technique which result from the use of radionuclides and its overall expense. As  $^{15}O$  has a half-life of approximately two minutes it requires an on sight cyclotron. The technique does not lend itself to repeat or longitudinal studies due to the radiation dose acquired by the patient. It also requires an intravenous injection and the scan time is relatively long as sufficient time between scans is necessary to ensure specificity taking  $\sim 45$  minutes to run.

### 1.3.3 Near Infrared Spectroscopy

Near Infrared Spectroscopy (NIRS) takes advantage of the optical window in which skin, tissue, and bone are mostly transparent to NIR light in the spectrum of 700-900 nm, while haemoglobin and deoxygenated haemoglobin absorb this light. Differences in the absorption spectra of oxygenated and deoxygenated haemoglobin allow the measurement of relative changes in haemoglobin concentration through the use of light attenuation at multiple wavelengths. Typically a light emitter and detector are placed ipsilaterally on the subjects skull so recorded measurements are due to reflected light. NIRS is cost effective and portable but cannot be used to measure cortical activity more than 4 cm deep due to limitations in light emitter power. The technique also has very limited spatial resolution, requires a

separate measure of CBF and can only measure relative changes in  $\text{CMRO}_2$  from an unknown baseline [23].

#### 1.3.4 Magnetic Resonance Imaging

Magnetic Resonance Imaging (MRI) is a medical imaging technique that is widely available in research and clinical settings and is capable of providing detailed anatomical and functional images of the body in both health and disease. MRI is a versatile technique with many intrinsic contrast mechanisms and as such MR methods have begun to emerge for estimating absolute  $\text{CMRO}_2$ . The measurement of  $\text{CMRO}_2$  using MRI is not trivial, but this imaging modality offers excellent image resolution, is non-invasive and avoids complications associated with radioisotopes. As such an MRI technique capable of producing whole-brain parameter maps providing regional detail of oxygen metabolism is desirable and has applications in the longitudinal monitoring of ageing and development, disease diagnosis and treatment as well as drug development and functional neuroimaging.

In **Chapter 2** the basic concepts behind MRI are introduced alongside how MRI can be applied to provide further information on the underlying physiological functions of the brain. The pros and cons of the current MR techniques capable of measuring absolute  $\text{CMRO}_2$  are discussed and a recently introduced, non-invasive MR method will be described.

# Chapter 2

## Magnetic Resonance Imaging

In this chapter, the principles of nuclear magnetic resonance (NMR) and MRI are introduced. The MRI methods which are utilised throughout this thesis are also discussed alongside a review of MR techniques capable of measuring oxygen metabolism in the brain. For the purposes of this chapter and introducing the concepts of NMR and MRI, classical mechanics provides a sufficient description of the behaviour of the net magnetisation vector. However a more thorough derivation of the concepts of spin and its behaviour can be found by using a quantum formalism.

### 2.1 Basic MRI Concepts

The human body is composed of approximately 80% water with each water molecule consisting of two hydrogen and one oxygen atom. As a result hydrogen is the most abundant element in the body and forms the basis for MRI. Each hydrogen atom has a proton and an electron. The hydrogen proton has an electrical charge and in the classical model 'spins' around its own axis creating a magnetic field referred to as a nuclear magnetic dipole. The gyromagnetic ratio refers to the ratio of the magnetic dipole moment to angular momentum. For a hydrogen proton or

'spin' the gyromagnetic ratio is 42.56 MHz/Tesla. The spinning hydrogen protons are analogous to tiny bar magnets which are randomly orientated throughout the body. As a result the small magnetic component contributed by the spins cancel each other out resulting in the body having no net magnetisation.

In the presence of an applied magnetic field, proton spins will align parallel or anti-parallel to the direction of the field, representing a low and high energy state, respectively. Slightly more protons align with the applied magnetic field, as this is a lower energy state, leading to a net magnetisation of the body pointing in the direction of the applied magnetic field. This effect is known as spin excess and the ratio of protons in the high energy state ( $N_+$ ) compared to those in a low energy state ( $N_-$ ) is described by a Boltzmann distribution ( $\frac{N_+}{N_-} = \exp\left(\frac{-\Delta E}{kT}\right)$ ) where  $\Delta E$  is the energy difference between states,  $k$  is the Boltzmann constant and  $T$  is temperature.

The net magnetisation vector  $\vec{M}$  precesses as described by the equation:

$$\frac{d\vec{M}(t)}{dt} = \gamma(\vec{M} \times \vec{B}) \quad (2.1)$$

The frequency of this precession is dependent on the magnetic field strength  $|\vec{B}|$  and the gyromagnetic ratio of the proton  $\gamma$ . For a hydrogen proton experiencing a 3 Tesla (3T) magnetic field the Larmor frequency is 127.6 MHz.

$$\omega = \gamma \cdot |\vec{B}| \quad (2.2)$$

The magnetic moment of each of these precessing spins, present in the applied magnetic field, can be split into longitudinal and transverse components.

The longitudinal component is static, pointing with or against the direction of the applied field and is referred to as  $M_z$ . The transverse component, where present, is perpendicular to the applied magnetic field and precesses in the laboratory frame at the Larmor frequency. The transverse component is referred to as  $M_{xy}$ . The net magnetisation magnitude,  $M_0$ , of the ensemble of spins placed in the applied magnetic field, is proportional to the excess of spins in the parallel state, the spin density and the spin magnetic moment. Due to spin excess,  $M_0$  is in the direction of the applied field,  $M_z$ . The protons, which  $M_0$  is composed of, will precess out of phase and therefore  $M_0$  has no net transverse component.

When placed in an MRI scanner the magnetic field experienced by the protons in the body are a combination of the local chemical environment, the main magnetic field ( $B_0$ ) created by a superconducting magnet, inhomogeneities in this magnetic field due to uniformity or susceptibility differences in the object and magnetic fields produced by gradient coils (G) or radio frequency (RF) pulses.

### 2.1.1 Main Magnetic Field

The main magnetic field in an MRI scanner creates a bulk magnetisation in the participant from head to foot along the z-axis. This static magnetic field is usually supplied by a superconducting magnet allowing high field strengths to be achieved. The ideal static field is strong, stable and homogenous. In reality the

static magnetic field has some non-uniformities and shimming can be performed to improve uniformity.

### 2.1.2 RF Excitation

RF pulses act to give  $M_0$  a transverse component ( $M_{xy}$ ), perpendicular to the z-axis, which rotates at the Larmor frequency and is detectable.  $M$  returns to its original low energy, pre-RF pulse orientation at rates referred to as  $T_1$  and  $T_2$  relaxation. The difference in energy between the low and high energy spins, created by the application of an external magnetic field, is given by  $\Delta E = hf_{\text{larmor}}$  where  $h$  is Planck's constant. As RF energy is delivered by photons, photons with exactly the right energy,  $\Delta E$ , can be used to excite protons from low to high energy. The effect of RF energy on  $M$  is described in terms of flip angle (FA). As spins are promoted from low energy states to high energy states the net magnetisation,  $M_0$ , changes direction in relation to the original spin excess state. An RF pulse with a  $90^\circ$  FA results in  $M_z = 0$  and  $M_{xy} = M_0$ . An RF with a  $180^\circ$  FA results in  $M_z = -M_0$  and  $M_{xy} = 0$ .

### 2.1.3 RF Receive

Detectable MR signal is derived from the time varying, transverse component of the magnetisation vector,  $M_{xy}$  and can be detected by an RF coil. The time varying magnetic field induces a current in the coil proportional to the rate of change of the magnetic flux. The amplitude of the detected signal is proportional to the



amplitude of  $M_{xy}$ . The signal detected after an RF excitation decays exponentially as  $M_z$  returns back to  $M_0$  and this is referred to as a free induction decay (FID). As  $M_{xy}$  is a time varying magnetic field, FID results in an exponentially decaying sinusoid.

### 2.1.4 Gradient System

Following the definition of the longitudinal and transverse axis it is beneficial to define a coordinate system in terms of  $B_0$ . In an MRI scanner set-up the patient is usually positioned head to foot in the direction of the static magnetic field ( $B_0$ ) lying on their back. The z-axis is therefore in the inferior-superior direction, the x-axis refers to left-right and the y-axis in the anterior-posterior direction.

Gradients are designed to introduce small, transient, linear variations in the static magnetic field in the x, y and z direction. These magnetic fields are generated by resistive electromagnetic coils inside the body of the scanner with a separate set of coils used for the three gradient directions. The net field in the bore is equivalent to the sum of the main field and the gradient fields. The gradient strength determines how much the gradient field varies the static field with distance from the isocentre ( $x=0$ ,  $y=0$ ,  $z=0$ ). As the Larmor frequency is dependent on field strength the application of a gradient causes a positional variation in Larmor frequency.

### 2.1.5 Image Localisation

The gradient system allows a controlled, spatially varying Larmor frequency to be introduced across the imaging volume during a sequence. This aids with slice selection, signal localisation (phase and frequency encode) and echo formation.

#### Slice Selection

To select a transverse slice (an xy-plane perpendicular to the z-axis) a slice select gradient is used. This is a gradient which causes a spatial variation in the magnetic field along the z-axis, resulting in protons which precess at a frequency dependent on their position in the magnet. An RF pulse can selectively excite all spins in an xy-plane at a particular z-axis location. The position of the slice along the z-axis is determined by the frequency of the RF pulse and this process is referred to as slice selective excitation. The thickness of the excited plane, in the z-direction, is controlled by the bandwidth of the RF pulse (range of frequencies) and the gradient strength.

#### Signal Encoding

Once the appropriate spins in a given slice have been selectively excited the RF receiver simultaneously detects signal from all spins in that slice. In order to spatially differentiate where the signals come from signal encoding is used. Each excited spin has an amplitude, phase and frequency. The amplitude of the excited spin provides contrast in the final image and therefore signal encoding is done via frequency and phase encoding. A frequency encode gradient can be applied

orthogonal to the slice select gradient. If the slice select gradient is considered to be applied along the z-axis the frequency encode gradient is applied along the x-axis. The frequency encode gradient causes a positional variation in frequency dependent on the location of protons along the x-axis. A phase encode gradient can also be applied orthogonal to both the slice select and frequency encode gradients, in the y-direction. This causes protons to acquire a phase difference which is dependent on their position along the y-axis. After signal encoding, the protons present, in a given x-y position, in a given slice, have a unique phase and frequency indicating their location. In a simple encoding implementation phase encoding is performed first, then as the echo is forming frequency encoding is performed. Signal localisation is discussed in more detail in Section 2.1.7

### 2.1.6 Relaxation

When an RF excitation pulse is applied some spins are flipped into a high energy state, pointing anti-parallel to the static field and spins begin to rotate in phase in the transverse plane. Once the RF is no longer applied two processes occur,  $M_0$  recovers back to its low energy state and spins begin to dephase.

#### Longitudinal Relaxation

$T_1$  or longitudinal relaxation is the term used to describe the time it takes for spins to return back to their original low energy state, aligned with the static magnetic field.  $T_1$  is the time it takes for  $M_0$  to recover to 63% of its original

pre RF value. Different tissues have different  $T_1$  values based on their molecular environments.

## Transverse Relaxation

RF forces spins into phase creating a transverse magnetisation component. Spins quickly lose this transverse magnetisation through spin-spin relaxation and the transverse magnetisation component soon returns back to zero when the RF is no longer applied. This is referred to as transverse relaxation and is due to local variations in the magnetic field. Local variations cause spins to precess at different speeds and can be due to the thermal motion of molecules and imperfections in the magnetic field.  $T_2$  relaxation describes dephasing as a result of thermal motion whereas  $T_2^*$  describes the combined effect of thermal motion and imperfections in magnetic field. As a result  $T_2^*$  dephasing is faster than  $T_2$ .

### 2.1.7 Refocusing and Echo Creation

When an RF pulse has been applied there is an inevitable delay before the signal from the excited spins can be acquired. Due to FID that occurs during the enforced delay, this decayed signal is not ideal for making measurements. However the effects of some dephasing can be reversed using an echo created by additional RF pulses or the application of gradient pairs. Spin-echo creation can reverse the effects of some dephasing, causing spins to return to nearly identical phase and net transverse magnetisation to grow back to measurable values.

## Spin Echo

In the case of a spin echo (SE) an initial  $90^\circ$  RF pulse is followed by a  $180^\circ$  RF pulse, called a refocusing pulse. The initial  $90^\circ$  pulse gives  $M_0$  a detectable transverse component. As soon as the RF is switched off this transverse component decays due to dephasing at a rate of  $T_2^*$ . By applying a  $180^\circ$  refocusing pulse the transverse component is rotated around its own axis by  $180^\circ$ . This has the effect of reversing the process of dephasing, rephasing the dephased spins and eventually resulting in the net transverse magnetisation being refocused. The refocussed transverse magnetisation vector is referred to as an echo. Once the echo has formed the spins will continue to dephase. Effects of spin-spin relaxation are not reversed with SE and therefore the amplitude of the rephased transverse magnetisation will be affected by  $T_2$ -relaxation. In terms of timings the echo is formed at an echo time (TE) from the original  $90^\circ$  pulse. To form the echo at TE the  $180^\circ$  pulse must be applied at  $\frac{TE}{2}$ . To summarise the process of spin echo creation, after a  $90^\circ$  pulse FID decay occurs where transverse magnetisation is dephasing. A  $180^\circ$  pulse is applied and spins rephase reaching the max echo amplitude at TE. Max echo amplitude is not equal to the initial net transverse magnetisation as spin-spin dephasing cannot be refocused by the  $180^\circ$  refocusing pulse. After TE the spins continue to dephase with  $T_2^*$ .

## Gradient Echo

A gradient echo (GRE) employs bipolar gradients instead of a  $180^\circ$  RF pulse to refocus transverse magnetisation. GRE acquisitions are typically faster than SE acquisitions. As gradient rephasing cannot reverse dephasing due to magnetic field

inhomogeneities, unlike a  $180^\circ$  refocusing pulse, gradient echoes show a sensitivity to  $T_2^*$  rather than  $T_2$ . After the initial  $90^\circ$  excitation a negative transverse gradient is applied to speed up dephasing. After this an equivalent positive transverse gradient is applied to refocus this dephasing. The area under the positive gradient is twice that of the negative gradient and TE occurs half way through this positive gradient. These gradients are referred to as dephasing and rephasing gradients. As discussed later in this chapter, the sensitivity of GRE to detect changes in  $T_2^*$  provide the basis for Blood Oxygen Level Dependent (BOLD), functional MRI (fMRI).

## K-space

K-space represents spatial frequency information and is related to MR image space via a Fourier transform. K-space is a vital concept in MR image acquisition which will be described here in detail.

A Fourier transform is a mathematical transformation used to transform signals between the time (or spatial domain) and the frequency domain. Using a Fourier transform any image may be decomposed into a spectrum of 2D spatial frequencies. This spectrum of 2D spatial frequencies is known as k-space. A 2D spatial frequency is essentially a sinusoidal grating which can be defined by two parameters,  $k_x$  and  $k_y$ , that describe the spatial frequencies in the x and y direction respectively.

K-space is a 2D plane with axes  $k_x$  and  $k_y$  where each point in k-space ( $k_x, k_y$ ) is a spatial frequency component. The amplitude at a given point in k-space represents

the amplitude of that spatial frequency in the image. Each point in k-space holds data on the entire image with the centre of k-space responsible for low spatial frequencies and the outer areas of k-space responsible for high spatial frequencies. For an image with M-by-N pixels, k-space will have M rows and N columns. The image frequency content is therefore approximated by M-by-N spatial frequency components as described by k-space.

### Filling K-space

MR signal localisation uses gradients to manipulate the MR signal allowing the spatial frequencies necessary to form an image to be measured. In a 2D acquisition, an RF excitation is performed during the application of a slice selection gradient in order to excite the spins in a 2D plane that is the imaging slice.

A phase encoding gradient is applied orthogonally to the slice select gradient. During the application of the phase encode gradient, spins will accumulate a phase difference dependent on their position along the phase encode direction. When the phase encode gradient is switched off this phase difference remains and spins are said to be phase encoded. The amplitude of the MR detected signal, after phase encoding, is dependent on the number of in-phase spins, which is in turn dependent on the spatial frequency of protons in the phase encode direction. Each value of phase encoding provides a probe of one spatial frequency (spatial distribution of spins). To acquire enough information for a whole image the entire range of spatial frequencies must be sampled. This involves multiple repetitions of the excitation process followed by a different phase-encoding gradient until all spatial frequencies are interrogated.

However, phase encoding only allows us to probe the spatial frequency of MR signals along the phase encode direction. In order to produce a 2D image, or slice through an object, the spatial frequency of MR signals needs to be probed orthogonal to the slice select and phase encode directions.

Frequency encoding acquires all the spatial frequency information needed from one MR signal following one RF excitation. During the continuous application of the frequency encode gradient the MR signal is continuously measured at discrete time-points. At each time-point the MR signal is affected by a different amount of gradient moment and therefore has a different amount of phase change. Each data point reflects a different amount of 'phase encoding' and corresponds to a different spatial frequency. All spatial frequencies can be investigated in the frequency encode direction in real time following a single RF excitation. To summarise, frequency encoding and phase encoding are performed so that data is spatially encoded by differences in frequency and phase, amenable to analysis by Fourier transform.

The application of phase and frequency encode gradients allow us to traverse through k-space, acquiring signal amplitudes from in-phase spins corresponding to the spatial frequency imposed by these gradients. The phase encode gradient allows movement to a new row in the  $k_y$  direction and the frequency encode gradient allows movement along a new row in the  $k_x$  direction. As previously mentioned, to acquire enough information for a whole image the entire range of spatial frequencies must be sampled. This involves choosing a point on the  $k_y$  axis using phase encoding and acquiring signal amplitudes for all relevant spatial frequencies along the  $k_x$  axis using a frequency encode readout. However taking



this approach leads to lengthy acquisition times proportional to  $N_{PE} \times TR$ , where  $N_{PE}$  is the size of the phase-encoding matrix and  $TR$  is time between RF excites, also referred to as repetition time. Methods such as echo planar imaging (EPI) attempt to speed up this process by acquiring multiple lines of k-space from a single RF excitation.

## 2.2 Functional MRI

MRI not only provides detailed structural images of the brain but also important information about the physiological processes which contribute to the function of the brain. fMRI is a class of MR techniques capable of providing information on the physiological processes in the brain. A cornerstone of this technique is an imaging method which allows fast image acquisition and high temporal resolution.

### 2.2.1 Echo Planar Imaging

EPI is an MR imaging technique that allows very rapid data acquisition [24]. Rather than acquiring a single line of k-space after each RF excitation, all of k-space is acquired in one  $TR$ , in the case of single shot-EPI (SS-EPI). This is achieved by using a series of bipolar readout gradients to generate a train of gradient echoes. The positive and negative frequency encode gradients are equivalent to scanning back and forth through k-space along the  $k_x$  axis. With an accompanying blipped phase encoding gradient, the acquisition is moved onto the next

line in k-space on the  $k_y$  axis and k-space is effectively filled in a single TR by rastering through the  $k_x$  and  $k_y$  axes. Each GRE is distinctively spatially encoded so that multiple k-space lines can be sampled under the envelope of an RF-spin echo (in the case of Spin Echo-EPI,  $T_2$ -weighting) or FID (in the case of Gradient Echo-EPI,  $T_2^*$  weighting).

### K-space Trajectory, Spiral EPI

The k-space trajectory described previously refers to a blipped-EPI acquisition and results in a Cartesian k-space trajectory. In an attempt to speed up image acquisition and sample k-space more efficiently, spiral k-space trajectories have been introduced [25]. The trajectory starts at the origin of k-space and spirals to the edge of k-space. It is accomplished by applying an oscillatory gradient, which increases in amplitude as a function of time with both frequency and phase gradients oscillating simultaneously. Spiral acquisitions offer faster image acquisition as both frequency and phase encode gradients are used to simultaneously track through k-space. This is in contrast to the Cartesian trajectory which uses the frequency encode gradient to do most of the work. The shorter readout reduces off-resonance-induced geometric distortion (in EPI) and blurring (in spiral) as well as signal dropout due to susceptibility differences [26, 27]. Spiral acquisitions are however highly demanding on the gradient system and require complicated reconstruction. Although these hardware limitations have mostly been overcome, the availability of spiral acquisition sequences are still limited [28].

## GRE-EPI and $T_2^*$

By pairing GRE signal refocusing with an EPI readout, a rapid MRI imaging technique with sensitivity to  $T_2^*$  weighting is possible.

### 2.2.2 Blood Oxygen Level Dependent Signal

BOLD FMRI is a functional neuroimaging procedure that takes advantage of the high temporal resolution of GRE-EPI as well as its sensitivity to changes in  $T_2^*$  to map brain activity. It relies on an intrinsic contrast mechanism that is derived from blood.

In its fully deoxygenated state haemoglobin is paramagnetic and disrupts the local magnetic field homogeneity. As oxygen molecules begin to occupy the binding sites in haemoglobin the paramagnetic nature of the molecule is reduced. As oxygen is mainly transported in blood by haemoglobin the magnetic susceptibility of the haemoglobin molecule is directly indicative of the blood oxygenation. The presence of deoxyhaemoglobin induces magnetic field gradients that surround RBC's and affect the proximal extravascular tissue. The measurable result of these localised field inhomogeneities is to shorten the  $T_2^*$  of the nearby tissue.

Although the intravascular compartment is a small fraction of total tissue volume ( $\sim 4\%$ ) the intravascular and extravascular spins have been shown to contribute a comparable amount to BOLD signal change at 1.5T [29]. This is as a result of the intrinsic signal change in blood being of an order of magnitude larger than the extravascular signal change. Large magnetic field gradients are present around the

RBC's carrying deoxyhaemoglobin and as a result the venous blood signal may be reduced by as much as 50% when compared to fully oxygenated blood. This provides a much wider dynamic range for intravascular signal when compared to extravascular signal.

The fact that changes in the amount of de-oxygenated blood present has a measurable effect on MR signal was discovered by *Ogawa et al.* [30]. The magnitude of the signal change depends upon the change in  $T_2^*$  induced by neural activation and the echo time, TE. The contrast to noise ratio is maximised when  $TE = T_2^*$  [31]. If TE is very short, the signal is insensitive to  $T_2^*$ , and so the signal change with activation is minimal. If TE is very long, most of the signal decays away before it is measured, so again the sensitivity is low because the signal is lost in the noise.

BOLD fMRI is used to identify regional areas of neural activation in the brain. However the BOLD signal does not directly measure neural activity and is instead reliant on metabolic and blood flow changes that accompany such activity and modulate local concentrations of deoxyhaemoglobin. A schematic outlining the relationship between neural activation, haemodynamic response, deoxyhaemoglobin concentration and BOLD signal change is shown in Figure 2.1. With increased neural activity, additional oxygen is extracted from the blood to support the additional energy requirements associated with such increases. Typically, a large increase in CBF and moderate increase in CBV accompany  $CMRO_2$  increases in an active, local brain region. However the OEF drops with the increase in oxygen rich blood brought to the local region, due to the magnitude of the CBF response [32]. It is the dilution of venous deoxyhaemoglobin that gives us the

BOLD contrast in an active region of the brain and it is the relative changes in these distortions in the brain over time, imaged using GRE-EPI, that we exploit. As a result the BOLD signal provides a non-quantitative, mapping tool for brain activity. However a direct measure of these underlying physiological quantities that contribute to the BOLD signal, would be considerably more useful in clinical research and application across a wide range of diseases.

### 2.2.3 Arterial Spin Labelling and CBF

CBF delivers glucose and oxygen to the brain and is linked with neural activation. Arterial spin labelling (ASL) is a non-invasive fMRI technique allowing quantitative measures of CBF to be made. Many variations on the ASL technique exist but are all based around a simple experimental design. This involves perfusion-weighting the MR signal and converting it to units of CBF using an appropriate model. Protons travelling in the blood vessels outside the imaging plane are labelled using a  $180^\circ$  RF inversion pulse to flip the protons in arterial blood. Following a delay to allow the labelled blood reach the brain tissue, images are obtained of the tissue in a labelled state. This is then repeated without labelling to acquire a control image. The goal of the control image is to create an image where the arterial blood is not inverted but the signal from static spins in the slice are precisely the same as in the tagged image. The difference signal directly reflects quantitative local perfusion. CBF maps can then be obtained by scaling this tag-control difference image appropriately using techniques such as the General Kinetic Model (GKM) [33].

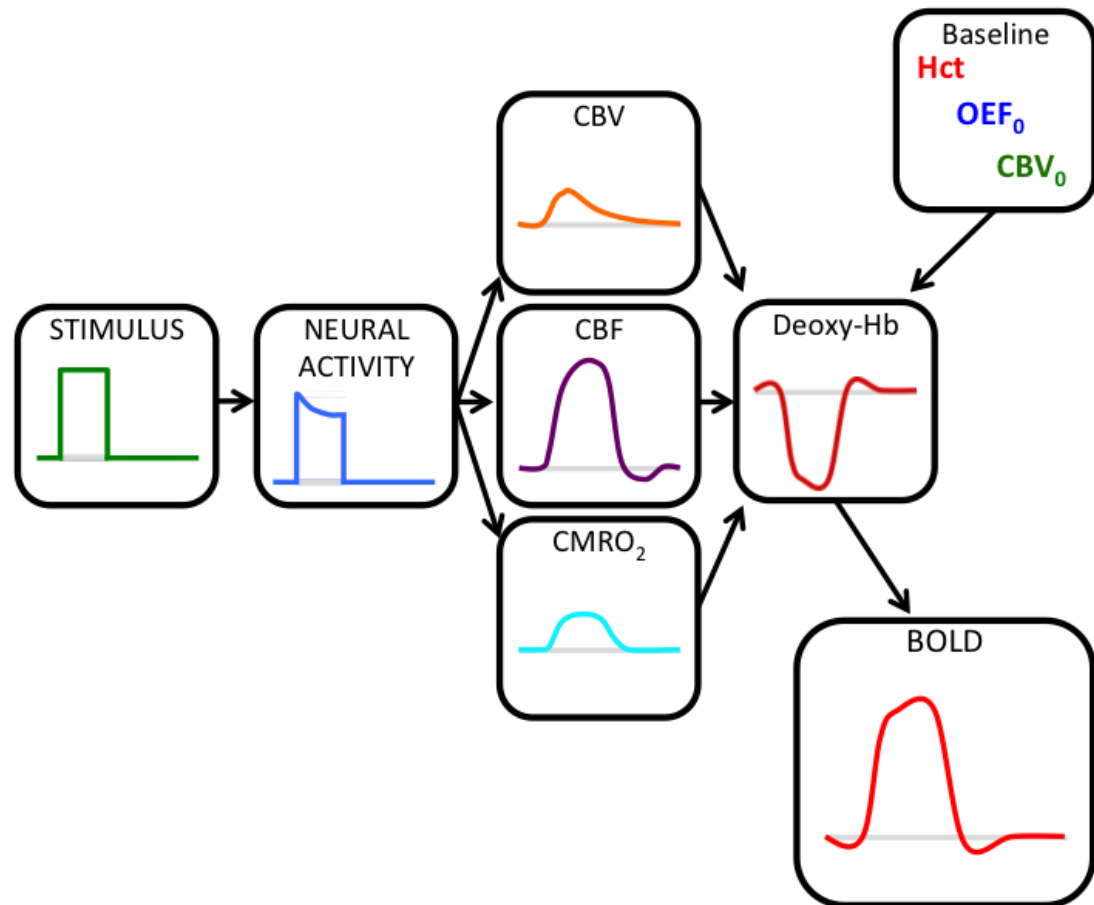


Figure 2.1: Schematic detailing the relationship between neural stimulation and BOLD signal change. A stimulus evokes neuronal activity which in turn provokes a haemodynamic response. This haemodynamic response is comprised of changes in CBV, CBF and CMRO<sub>2</sub> that are modulated by baseline haematocrit, OEF and CBV. This in turn leads to a change in venous deoxyhaemoglobin concentration which manifests as a BOLD signal change

Two major classifications of ASL techniques are pulsed ASL (PASL) and continuous ASL (CASL). The variations between these techniques lie within the method used for spin preparation. The spin preparation or tagging in PASL is spatially selective whereas CASL tags protons travelling through a plane for a given amount of time and is therefore a temporally dependent tag.

## PASL

PASL techniques are characterised by a single  $180^\circ$  RF pulse which is applied as a spatially selective pulse that tips over all spins in a thick band proximal to the image slice of interest. After a delay to allow the tagged blood to flow into the slice and the labelled water to exchange into the tissue, the tag image is acquired. There are a number of different PASL techniques including EPISTAR (echo planar imaging and signal targeting with alternating radio frequency) [34], FAIR (flow sensitive alternating inversion recovery) [35] and PICORE (proximal inversion with control for off resonance effects) [36]. These techniques differ in how the tag-control images are acquired. PICORE works by applying a control pulse in the absence of field gradients but shifted in frequency so that the image plane experiences the same off resonance RF pulse in both control and tag images. In this way, any asymmetry of magnetisation transfer effects is automatically balanced between tag and control images. This technique has the advantage that venous blood entering from the superior side of the image plane is not tagged, whereas with EPISTAR, such blood appears as a negative signal, and with FAIR, it appears with a positive signal.

## QUIPSS II

Due to the spatial nature of the PASL tag the temporal duration of the label is not well defined. QUantitative Imaging of Perfusion using a Single Subtraction II (QUIPSS II) [37] is a method designed to create a well-defined bolus duration which aids in CBF quantification. The QUIPSS II modification to PASL is to add a  $90^\circ$  saturation pulse, after the inversion pulse and before the imaging excitation pulse, that saturates the same tagging band as the inversion pulse. During labelling, the initial tag is spatially applied below the imaging plane as previously described at time = 0. A saturation band is then applied to the same tagging region at time =  $TI_1$ . This is referred to as the tag cut-off. During this time the spatially tagged blood is travelling through the arteries towards the imaging plane. The tag cut-off saturates any tagged arterial blood remaining in the tagging plane effectively creating an arterial bolus with a well defined trailing edge which has a temporal duration equal to  $TI_1$ . The time between tagging and saturation becomes the temporal bolus of the tag. This temporal component aids in accurate modelling and quantification of the perfusion weighted images. At time =  $TI_2$  after the initial tag was applied image acquisition happens.  $TI_2$  allows sufficient time for the tagged blood to travel to the capillary beds in the imaging plane.

## CASL

While many routine examinations use PASL techniques due to their easier implementation, CASL has been shown to obtain perfusion images of the human brain with a higher signal to noise ratio (SNR) [38, 39]. CASL uses long RF irradiations in the presence of a slice select gradient to adiabatically label the inflowing



blood before it reaches the imaging slice. The labelling duration and post labelling delay (PLD) are key timing parameters in a CASL acquisition. The PLD refers to the amount of time that has elapsed between labelling and image acquisition. The primary drawback of CASL is the requirement of continuous RF transmitting hardware that is not commonly available on most MRI scanners.

## PCASL

Pseudo continuous ASL (PCASL) [40] is a sub category of the CASL techniques and was introduced to overcome hardware limitations associated with CASL without compromising labelling efficiency. To circumvent these problems PCASL breaks the RF and gradient pulses into a series of short pulses  $\sim 500 \mu\text{s}$  in duration with a spacing of  $\sim 1500 \mu\text{s}$  between pulses. This has the same effect of producing an adiabatic inversion of the magnetisation of blood as it flows through the zero plane of the gradient. However, the gradient used during each pulse is stronger than the constant gradient used in traditional CASL, and this means that the slice to be imaged is farther off resonance, with reduced magnetisation transfer effects. Because the RF is pulsed, it is highly compatible with the majority of MR scanner hardware. Moreover, it does not require any additional hardware and provides high labelling efficiency, as in standard CASL, whilst possessing the same high SNR advantage over PASL. The control tagging procedure is performed by alternating the sign of the RF from pulse to pulse and ensuring that there is zero average gradient between each pair of pulses. In the acquired control image, the average field strength of the RF pulses is zero, but the averaged RF power, and

hence the magnetisation transfer effects, will be matched between the control and label sequences.

### 2.2.4 CBF Quantification

In order to convert the perfusion weighted subtraction images to absolute units of CBF they must be appropriately scaled. The GKM was introduced by *Buxton et al.* [40] to model the kinetics of the tagged blood throughout the vasculature and brain tissue. It offers a method to quantify CBF using slightly modified models for PASL and CASL.

#### The GKM

$\Delta M$  is considered the perfusion weighted signal (tag minus control) in a given voxel that is described by three components in the GKM. The delivery function,  $c(t)$ , describes the amount of tagged blood arriving in the voxel at time  $t$ , the residue function,  $r(t)$ , describes the amount of tagged blood left in the voxel at time  $t$  and the magnetisation relaxation function,  $m(t)$ , describes the amount of remaining longitudinal magnetisation of the tagged blood after relaxing over time  $t$ .  $M_{0B}$  is the equilibrium magnetisation of arterial blood.

$\Delta M$  is now described as  $\Delta M(t)$ , an integral of the history of tag delivery weighted by the fraction of those tagged spins that remain in the voxel.

$$\Delta M(t) = 2M_{0B} \cdot CBF \int_0^t c(t') \cdot r(t - t') \cdot m(t - t') \cdot dt' \quad (2.3)$$

$A_{eff}$ , is a term used to summarise the effect of these functions and can be used to translate local perfusion values into magnetisation signal that is observed.

$$\Delta M(t) = CBF \cdot A_{eff}; \quad A_{eff} = 2M_{0B} \int_0^t c(t') \cdot r(t - t') \cdot m(t - t') \cdot dt' \quad (2.4)$$

The amount of time it takes for the tagged blood to reach the voxel of interest is called the arterial arrival time (AAT). AAT describes the delay in the arrival of tagged blood in the voxel and during this time the tagged spins experience longitudinal relaxation. The tag also has a finite duration, which is better defined by the QUIPSS II cut-off in the case of PASL, and as such the delivery function can be described as Equation 2.5 where  $\alpha$  is the tagging efficiency,  $\tau$  is the tag duration and  $T_{1B}$  is the longitudinal relaxation of tagged blood. Separate terms are included in the partition function to describe the different characteristics of PASL and CASL tags. This is due to the continuous nature of the CASL tag as it reaches a steady state in the voxel, unlike the PASL tag.

$$c(t) = \begin{cases} 0 & [0 < t < AAT] \\ \alpha e^{-t/T_{1B}} & (PASL) \quad [AAT < t < AAT + \tau] \\ \alpha e^{-AAT/T_{1B}} & (CASL) \quad [AAT < t < AAT + \tau] \\ 0 & [AAT + \tau < t] \end{cases} \quad (2.5)$$

The residue function  $r(t)$  is described using single compartment kinetics as a decaying exponential, where  $\lambda$  is the partition coefficient for water.

$$r(t) = e^{(-CBF \cdot t)/\lambda} \quad (2.6)$$

Once labelled spins have reached the capillary bed in the voxel of interest, spins will exchange with the tissue and relax with the tissue relaxation rate  $T_{1T}$ .

$$m(t) = e^{t/T_{1T}} \quad (2.7)$$

Combining Equations 2.3, 2.5, 2.6 and 2.7 leads to Equations which can be used to describe pulsed or continuous ASL. For **Pulsed ASL** the difference signal can be described as:

$$\begin{aligned}
\Delta M(t) &= 0 & [0 < t < AAT] \\
&= 2M_{0B} \cdot CBF(t - AAT) \cdot \alpha \cdot e^{-t/T_{1B}} \cdot q_p(t) & [AAT < t < AAT + \tau] \\
&= 2M_{0B} \cdot CBF \cdot \tau \cdot \alpha \cdot e^{-t/T_{1B}} \cdot q_p(t) & [AAT + \tau < t]
\end{aligned}$$

$$\begin{aligned}
q_p(t) &= \frac{e^{kt}(e^{-k \cdot AAT} - e^{-kt})}{k(t - AAT)} & [AAT < t < AAT + \tau] \\
&= \frac{e^{kt}(e^{-k \cdot AAT} - e^{-k(\tau + AAT)})}{k\tau} & [AAT + \tau < t]
\end{aligned}$$

$$\begin{aligned}
k &= \frac{1}{T_{1B}} - \frac{1}{T'_1} \\
\frac{1}{T'_1} &= \frac{1}{T_{1T}} + \frac{f}{\lambda}
\end{aligned}$$

For **Continuous ASL** the difference signal can be described as:

$$\begin{aligned}
\Delta M(t) &= 0 & [0 < t < AAT] \\
&= 2M_{0B} \cdot CBF \cdot T_1' \cdot \alpha \cdot e^{-AAT/T_{1B}} \cdot q_{ss}(t) & [AAT < t < AAT + \tau] \\
&= 2M_{0B} \cdot CBF \cdot T_1' \cdot \alpha \cdot e^{-AAT/T_{1B}} \cdot e^{-(t-\tau-AAT)/T_1'} \cdot q_{ss}(t) & [AAT + \tau < t]
\end{aligned}$$

$$\begin{aligned}
q_{ss}(t) &= 1 - e^{-(t-AAT)/T_1'} & [AAT < t < AAT + \tau] \\
&= 1 - e^{-\tau/T_1'} & [AAT + \tau < t]
\end{aligned}$$

## Equilibrium Magnetisation Estimation

$M_0$  is the equilibrium magnetisation of brain tissue and can be estimated using an EPI, equivalent to the ASL control acquisition, with an infinite TR.

$$M_{0B} = R \cdot M_{CSF} \cdot e^{(\frac{1}{T_{2,CSF}^*} - \frac{1}{T_{2,Blood}^*}) \cdot TE} \quad (2.8)$$

$M_{CSF}$  is the mean signal intensity measured from this image from a region of interest in the lateral ventricles.  $R$  is the ratio of the proton density of blood in the sagittal sinus to CSF and is taken as 0.87 [41],  $T_{2,CSF}^*$  is the  $T_2^*$  of CSF and  $T_{2,Blood}^*$  is  $T_2^*$  of blood which are 43.6 ms and 74.9 ms respectively at 3T.

## Coil Sensitivity Correction

Coil sensitivity correction can be performed to correct for nonuniform receiver coil sensitivity. Such background modulation, if not properly accounted for, can confound flow quantification [42]. A low resolution, minimal contrast image is acquired which provides a map of signal non-uniformity with low-spatial frequency. This is directly related to non-uniformity caused by coil sensitivity and the minimum contrast image can be divided into the perfusion map to remove these non-uniformities.

### 2.2.5 ASL Acquisitions to Detect Simultaneous CBF and BOLD Signals

ASL can be used to collect multiple tag-control volumes in an appropriate scan time,  $\sim 5$  minutes. The tag-control subtractions are usually averaged together, to improve SNR, and a CBF parameter map produced from the perfusion weighted image through kinetic modelling. However ASL tag-control runs can also be processed to produce CBF and BOLD weighted time-series. In an ASL fMRI experiment, a series of tag-control images are acquired in an interleaved manner. The time course of signal differences (control – tag) is flow weighted and can be used to calculate a CBF time-series. However, as these images are typically acquired with GRE-EPI readout sequence they will have sensitivity to  $T_2^*$  changes and therefore contain some BOLD signal contrast. This influence of BOLD contrast on the acquired time-series can be optimised by acquiring at a TE  $\sim 30$  ms and the influence of the ASL tag can be minimised by averaging the tag-control

time course ( $\frac{control+tag}{2}$ ) [43]. Conversely the influence of BOLD weighting on the CBF measure can be reduced by minimising the TE and acquisition time of the readout sequence.

### Dual-Echo Acquisition

Dual-echo GRE acquisitions allow image acquisition at different echo times,  $TE_1$  and  $TE_2$ . Two successive GRE readouts are used to acquire echoes under the  $T_2^*$  decay envelope. Dual-echo acquisition can be optimised for simultaneous CBF and BOLD sensitivity by acquiring  $TE_1$  at a short echo time to increase perfusion SNR [44] and  $TE_2$  can be acquired at  $\sim 30$  ms to optimise BOLD weighting [31]. As spiral readouts provide accelerated acquisition they are ideal for implementation in a dual-echo pulse sequence in particular as they can provide a very short  $TE_1$  maximising CBF signal and minimising BOLD weighting.

#### 2.2.6 Calibrated BOLD

The calibrated BOLD methodology was introduced to improve interpretability of task related changes in BOLD. This is achieved by estimating the maximum BOLD signal change,  $M$ , for the current physiological baseline state allowing estimates of relative change in  $CMRO_2$  to be inferred from task related changes in BOLD and CBF. To measure  $M$  a calibration scan is performed where BOLD signal changes are induced by manipulating venous deoxyhaemoglobin concentrations. This can be done by inducing mild hypercapnia [45] or hyperoxia [46] in the participant.



## Hypercapnia

Hypercapnia is an increase in the concentration of carbon dioxide in arterial blood. This can be achieved by increasing the amount of inspired carbon dioxide. Hypercapnia causes an assumed isometabolic increase in CBF [47, 48] which reduces the deoxyhaemoglobin concentration on the venous side of the vasculature.

## Hyperoxia

Similarly hyperoxia is an increase in the concentration of oxygen oxygen in arterial blood above normal levels. The concentration of oxygen in arterial blood can be referred to as the arterial oxygen content ( $C_aO_2$ ). Hyperoxia can be achieved by increasing the amount of inspired oxygen and causes a reduction in the amount of deoxyhaemoglobin on the venous side of the vasculature.

## BOLD Signal Model

The BOLD signal changes induced by hypercapnia and hyperoxia can be interpreted using a simple BOLD signal model derived by *Davis et al.* [45] and *Hoge et al.* [49].

BOLD signal changes depend on changes in the amount of deoxyhaemoglobin present. Due to its paramagnetic nature and presence in blood vessels, deoxyhaemoglobin (dHb) creates a susceptibility difference with surrounding brain tissue resulting in local signal decreases due to the enhanced relaxation rate. This is dependent on the volume of blood present, described as CBV [29], and the concentration of deoxyhaemoglobin ( $[dHb]$ ) in the blood which can be related to  $R_2^*$ ,

the transverse relaxation rate ( $R_2^* = \frac{1}{T_2^*}$ ).  $R_2^*$  is also dependent on the volume of blood present. Considering a voxel with a normal resting  $R_2^*$ , removing all dHb from that voxel causes a change in  $R_2^*$  that can be described by  $\delta R_2^*$ , Equation 2.9, where constants  $\kappa$  and  $\beta$  are both field dependent constants and  $\beta$  is dependent on vessel size and geometry.

$$\delta R_2^* = \kappa \cdot CBV_0 \cdot [dHb]_0^\beta \quad (2.9)$$

Maximum BOLD signal change,  $M$ , can then be calculated.

$$M = TE \cdot \kappa \cdot CBV_0 \cdot [dHb]_0^\beta = TE \cdot \delta R_2^* \quad (2.10)$$

Changes in BOLD signal can be described as  $\Delta R_2^*$ .

$$\Delta R_2^* = \kappa \cdot CBV \cdot [dHb]^\beta - \kappa \cdot CBV_0 \cdot [dHb]_0^\beta \quad (2.11)$$

Small changes in  $\Delta R_2^*$ , such as those that are experienced during an FMRI experiment can be approximated by Equation 2.12 where  $\frac{\Delta S}{S_0}$  is the fractional increase in BOLD signal which takes the echo time (TE) of the acquisition sequence into account.

$$\frac{\Delta S}{S_0} = e^{-TE \cdot \Delta R_2^*} - 1 \approx -TE \cdot \Delta R_2^* \quad (2.12)$$

Substituting Equation 2.11 for  $\Delta R_2^*$  in Equation 2.12 gives:

$$\frac{\Delta S}{S_0} = TE \cdot \kappa \cdot CBV_0 \cdot [dHb]_0^\beta \left( 1 - \left( \frac{CBV}{CBV_0} \right) \left( \frac{[dHb]}{[dHb]_0} \right)^\beta \right) \quad (2.13)$$

Substituting Equation 2.10 into Equation 2.13, the term for maximum BOLD signal change can be incorporated into the model.

$$\frac{\Delta S}{S_0} = M \left( 1 - \left( \frac{CBV}{CBV_0} \right) \left( \frac{[dHb]}{[dHb]_0} \right)^\beta \right) \quad (2.14)$$

In the case of hypercapnia, Equation 2.14 reduces to Equation 2.15 where increases in inspired  $\text{CO}_2$  are assumed to cause isometabolic CBF changes.  $\alpha$  is the Grubb constant [50], a value taken from literature that relates changes in CBF to changes in CBV as  $[\frac{CBF}{CBF_0}]^\alpha = [\frac{CBV}{CBV_0}]$ .

$$\frac{\Delta S}{S_0} = M \left( 1 - \left( \frac{CBF}{CBF_0} \right)^{\alpha-\beta} \right) \quad (2.15)$$

In the case of hyperoxia an isometabolic increase in  $\text{C}_a\text{O}_2$  is assumed to have no effect on CBF and Equation 2.14 is simplified to:

$$\frac{\Delta S}{S_0} = M \left( 1 - \left( 1 + \frac{\Delta[dHb]}{[dHb]_0} \right)^\beta \right) \quad (2.16)$$

$[dHb]_0$  is calculated by assuming haemoglobin concentration  $[Hb]$  and venous oxygen saturation,  $S_v\text{O}_2$ .

$$[dHb]_0 = [Hb](1 - S_v\text{O}_2) \quad (2.17)$$

$\Delta[dHb]$  is inferred from increases in  $\text{C}_a\text{O}_2$ .  $\text{C}_a\text{O}_2$  is estimated from arterial partial pressure of oxygen ( $\text{P}_a\text{O}_2$ ), which in subjects with normal pulmonary function can reasonably be represented with only a small systematic error by measuring the partial pressure of end-tidal oxygen ( $\text{P}_{ET}\text{O}_2$ ) [51].  $\text{C}_a\text{O}_2$  is calculated using

a variation of Fick's principle, Equation 2.19, after calculating arterial oxygen saturation ( $S_aO_2$ ) from  $P_aO_2$  as described by the Severinghaus equation:

$$S_aO_2 = \left( \frac{1}{\frac{23400}{(P_aO_2)^3 + 150(P_aO_2)} + 1} \right) \quad (2.18)$$

$$C_aO_2 = \phi[Hb]S_aO_2 + P_aO_2 \cdot \epsilon \quad (2.19)$$

where  $\epsilon$  is the coefficient of solubility of oxygen in blood (0.0031 ml  $O_2$ /(dl blood mmHg)) and  $\phi$  is the  $O_2$  carrying capacity of haemoglobin (1.34 ml  $O_2$ /gHb).

Both equations can then be solved for M with all other parameters being measured or assumed. However it is important to note that hyperoxic calibration requires a value for  $S_vO_2$  to be assumed. It is also important to note that assuming fully saturated arterial blood,  $OEf = 1 - S_vO_2$ .

With the experiment calibrated by determination of M, the normalised time courses of perfusion,  $\frac{CBF}{CBF_0}$ , and BOLD,  $\frac{S}{S_0}$ , can be used to compute dynamic oxidative metabolism maps ( $rCMRO_2(t)$ ) relative to baseline.

$$rCMRO_2(t) = \left( \frac{CBF}{CBF_0} \right)^{1-\alpha/\beta} \left( 1 - \frac{\frac{S}{S_0} - 1}{M} \right)^{1/\beta} \quad (2.20)$$

### Limitations of Calibrated BOLD

As previously mentioned, calibrated BOLD relies on the assumption that hypercapnia and hyperoxia do not modulate baseline  $CMRO_2$ . Currently there are

contrasting results in the literature due to the limited availability and sensitivity of suitable techniques to measure  $\text{CMRO}_2$  changes in vivo. Hyperoxia has been observed to cause increases [52], decreases [53, 54] and no change [55] in oxygen metabolism. Similarly hypercapnia has been observed to cause increases [47, 48, 56], decreases [57–60] and no change [18, 61, 62] in oxygen metabolism. These studies were conducted over a range of species, techniques, states and pathologies which may explain the wide range of results. The most relevant MR studies [53, 57] suggest a decrease in oxygen metabolism with hyperoxia and hypercapnia. However as a result of the global nature of the measurements applied in these studies it is difficult to interpret the effect of hyperoxia or hypercapnia on brain metabolism particularly in grey matter, the region of focus in calibrated FMRI techniques. Changes in CBF with hyperoxia have also been observed in some cases [51, 59]. Further investigation is required, but if indeed hypercapnia and hyperoxia were found to modulate baseline  $\text{CMRO}_2$  (and CBF in the case of hyperoxia), and these changes were correctly characterised, terms could be introduced into the BOLD signal model to account for this.

Other limitations associated with this technique are related to the relative nature of the measurement. As these methods are based on calibrating the BOLD signal and result in estimates of relative changes in  $\text{CMRO}_2$  from an unquantified baseline, the interpretation of these relative changes prove problematic where the baseline may be altered in disease or drug studies [63]. As such MRI methods capable of measuring absolute  $\text{CMRO}_2$  would be more effective for the longitudinal study of metabolism changes in brain.

## 2.3 MRI for Measuring OEF and Absolute CMRO<sub>2</sub>

MRI methods capable of measuring absolute CMRO<sub>2</sub> have been developed in order to offer an MR alternative capable of measuring metabolism in the brain non-invasively. These methods fall into two broad categories. Techniques which provide global or bulk measures of CMRO<sub>2</sub> for the whole brain and those capable of producing parameter maps capable of regionally distinguishing areas of varying metabolism. Techniques capable of producing regional measurements are preferable and offer a true alternative to the 'gold standard' PET techniques.

### 2.3.1 Phase Based Methods

Phase based susceptibility methods, such as PROM (Phased-based Regional Oxygen Metabolism) [64], are based on measuring the susceptibility differences between veins and surrounding tissue using phase based images. Phase based images can be acquired using a GRE with a fixed TE. These approaches require mean region of interest (ROI) measures from an appropriate vein and surrounding tissue to calculate the average phase difference ( $\Delta\phi$ ) between these ROI's. Under the assumption that the selected vein segment is an infinite cylinder (length is much greater than diameter), the phase difference estimate is combined with an estimate of the angle between the vein and the direction of the static magnetic field and an estimate of susceptibility difference ( $\Delta\chi$ ) is calculated between the vein and tissue.  $\Delta\chi$  can be related to OEF allowing absolute CMRO<sub>2</sub> to be calculated using an additional CBF measure such as ASL. However this class of techniques has a

number of disadvantages related to the lack of spatial sensitivity (global measure) and the manual identification of a suitable vein. Vein size may heavily influence the results achieved as small veins may be susceptible to partial voluming effects and larger veins will reflect oxygenation in many capillary beds. This means the territory that is drained may not be well identified making it hard to calculate local OEF changes.

### Extravascular $R'_2$ Based Methods

Quantitative BOLD style techniques [65–67] relate the reversible relaxation rate ( $R'_2 = \frac{1}{T'_2} = \frac{1}{T_2^*} - \frac{1}{T_2}$ ) to deoxyhaemoglobin induced signal loss. This class of techniques can employ a number of different acquisitions to acquire the MR signal required to calculate  $R'_2$ , using a combination of GRE and SE MR sequences with  $T_2^*$  and  $T_2$  sensitivity respectively, as well as hybrid SE-GRE sequences providing sensitivity to both types of dephasing or asymmetric spin echoes (ASE), directly sensitive to  $R'_2$ . These techniques assume no diffusion effects are present in the capillaries. This allows deoxyhaemoglobin concentration to be related to  $R'_2$  and through signal modelling whole brain maps of CBV and  $S_vO_2$  can be measured. However the distinction between CBV and  $S_vO_2$  is quite challenging under normal experimental conditions and multi-parametric qBOLD approaches have been introduced [68] in an attempt to increase the spatial resolution of the acquisitions and improve the accuracy of the oxygenation estimates by using independent measurements of model parameters. It is also important to note that  $R'_2$  is sensitive to [dHb] and CBV. It has recently been proposed [69] that  $R'_2$  could therefore be related to maximum BOLD signal change,  $M$ . As  $M$  is dependent on both CBV

and  $S_vO_2$ , issues related to separating these two terms can be sidestepped and over fitting can be avoided.

### Intravascular $T_2$ Based Methods

Intravascular  $T_2$  measurements attempt to directly measure the effect of deoxy-haemoglobin induced signal loss in intravascular blood. This relates the  $T_2$  of blood directly to its oxygenation using a  $T_2$ -oxygenation calibration curve. However in order to measure  $S_vO_2$ , the  $T_2$  signal must be localised to venous blood.

Initial studies focused on measuring  $T_2$  in large veins similar to the approach described in Section 2.3.1. TRUST ( $T_2$  relaxation under spin tagging) provides a measure of  $T_2$  in a large draining vein, such as the sagittal sinus, by using an ASL style tagging scheme to tag venous blood as opposed to inflowing arterial blood. A tag-control subtraction is then used to better isolate the signal in the vein of interest and the signal is acquired at multiple TE's to characterise the  $T_2$  of venous blood. Combining this with a global CBF measure acquired using phase contrast MR, global absolute  $CMRO_2$  can be calculated.

QUIXOTIC (QUantitative Imaging of eXtraction of Oxygen and TIssue Consumption) [70] and VSEAN (Velocity Selective Excitation with Arterial Nulling) [71] are extensions of the TRUST methodology using the same venous tagging approach as TRUST. Velocity-selective spin labelling is then applied to isolate the signal to venous blood and the oxygenation of the signal can be estimated using a  $T_2$ -oxygenation calibration curve. These techniques are currently limited to single



slice acquisitions but have the scope for larger brain coverage with the addition of a 3D acquisition.

The main difficulty with this class of technique is related to confidently localising the signal to the venous vasculature requiring intricate tagging and vessel selective pulses. The VSEAN approach in particular is promising but is still a new technique in the development stage and the ease of implementation and application still remains to be seen. Mapping techniques based on venous  $T_2$  also inherently suffer from low SNR due to the small compartment under investigation.

## 2.4 Dual Calibrated fMRI

Recently the approach of *Davis et al.* [45] and *Hoge et al.* [49] has been extended to use both hypercapnia and hyperoxia induced CBF and BOLD signal changes to estimate venous deoxyhaemoglobin concentration and thus regional OEF and absolute  $CMRO_2$  [1–3].

Dual calibrated fMRI (dcfMRI) effectively uses a two point calibration, inducing BOLD and CBF changes, by hypercapnic and hyperoxic respiratory manipulations performed in the same session. In its simplest form, as described by *Bulte et al.* [1],  $M$  can be calculated using the hypercapnic calibrated BOLD approach, meaning  $S_vO_2$  no longer needs to be assumed in the hyperoxic calibration. Instead the equation can now be solved for  $S_vO_2$ . Assuming arterial blood is fully saturated the oxygen extraction fraction can be calculated using Fick's equation.

The approach of *Gauthier et al.* [2] and *Wise et al.* [3] to dcfMRI differ only in the application of the BOLD signal model. Instead of estimating  $M$  independently using hypercapnic calibration and determining  $S_vO_2$  using hyperoxic calibration, the *Davis/Hoge* model (Equation 2.14) is expanded to accommodate simultaneous modulations of CBF and  $C_aO_2$ . The model reduces to the hypercapnic (Equation 2.15) and hyperoxic (Equation 2.16) based models when arterial oxygen levels and CBF are held constant respectively. However  $M$  and  $S_vO_2$  are estimated by simultaneously optimising these parameters to the data through the expanded model.

### 2.4.1 Expanded BOLD-Signal Model

An expanded BOLD signal model was presented by *Wise et al.* [3]. The full derivations, from this paper, leading to Equation 2.21 are presented in the Appendix A. The assumptions for hypercapnia and hyperoxia are that with physiologically moderate modulation of CBF through hypercapnia and  $C_aO_2$ , brain tissue oxygen consumption remains unaltered. With hyperoxia additional oxygen is largely dissolved in arterial blood plasma and therefore manifests as increased venous oxygen saturation ( $S_vO_2$ ). The conservation of oxygen allows us to derive an expression for the venous deoxyhaemoglobin concentration with respect to baseline conditions denoted by subscript zero ( $_0$ ):

$$\frac{[dHb]}{[dHb]_0} = \frac{CBF_0}{CBF} - \frac{1}{[dHb]_0} \left( \frac{1}{\phi} \left( C_a O_2 - \left( \frac{CBF_0}{CBF} \right) C_a O_{2|0} \right) + [Hb] \left( \frac{CBF_0}{CBF} - 1 \right) \right) \quad (2.21)$$

By combining the Grubb equation to relate CBF to CBV and Equations 2.14 and 2.21 estimates of M and  $S_v O_2$  can be produced.

By simultaneously varying arterial concentrations of carbon dioxide and oxygen the relationship between the Grubb equation, Equation 2.14 and Equation 2.21 can be exploited to concurrently produce estimates of  $\alpha$  and  $\beta$  as well as M and  $[dHb]_0$ . Essentially BOLD signal changes resulting from modulation of arterial oxygen content are simultaneously modulated by hypercapnia induced changes in CBF. Considering two different levels of CBF,  $CBF_1$  and  $CBF_2$ , produced as a result of two different arterial carbon dioxide levels, the ratio of the superimposed arterial oxygen induced changes in BOLD signal can be approximated by:

$$\frac{\Delta S_{1,O_2}}{\Delta S_{2,O_2}} = \left( \frac{CBF_1}{CBF_2} \right)^{1+\alpha-\beta} \quad \text{where} \quad \Delta S_{i,O_2} = \frac{\Delta S_i}{\Delta C_a O_{2|i}} \quad (2.22)$$

## 2.5 Thesis Outline

The aim of this thesis is to further develop and optimise dcfMRI for the measurement of oxygen metabolism, proving its suitability for application in further clinical and research studies of oxygen metabolism in the brain.

In **Chapter 1** an introduction to energy metabolism in the brain is provided. The role of oxygen metabolism in energy production, brain function and disease is discussed. To motivate the development of dcfMRI, a review of current measurement techniques is also presented.

**Chapter 2** introduces a background to basic MRI concepts followed by a description of the fMRI techniques which underpin the dcfMRI approach. Current MRI methods capable of producing absolute oxygen consumption measures are discussed and the background and theory involved in measuring oxygen metabolism using dcfMRI is described.

**Chapter 3** aims to choose the optimal ASL acquisition available in our centre for application in the dcfMRI measurement.

**Chapter 4** compares hypercapnic-hyperoxic respiratory designs for detecting regional changes in oxygen metabolism. This allows the sensitivity of dcfMRI for detecting regional changes in oxygen metabolism to be assessed, where regional changes in metabolism are induced using continuous visual and motor stimulation throughout the dcfMRI measurement.

**Chapter 5** investigates the within and between session repeatability of resting oxygen metabolism measurements made using dcfMRI.

**Chapter 6** uses a retrospective analytical approach to optimise the acquisition time of dcfMRI with an aim to provide a more time efficient measure.

**Chapter 7** demonstrates the ability of dcfMRI to detect CBF related changes in OEF suggesting that the technique is appropriate for clinical application in areas such as stroke or vascular dysfunction in which flow is impaired.

**Chapter 8** introduces a novel dcfMRI approach for the measurement of absolute oxygen metabolism. This is achieved by replacing the hypercapnic challenge in the dcfMRI protocol with an  $R'_2$  based measure of maximum BOLD signal change,  $M$ . The concept and techniques used have the potential for a fast and effective method of producing whole brain, absolute CMRO<sub>2</sub> maps in a short scan time without hypercapnia.

**Chapter 9** discusses the experimental work presented, considers potential areas of application and future work required to further progress this technique.

Throughout the main experimental work (**Chapter 4 to 8**) there is some repetition of theory and methods to improve readability and subsets of data from a given experiment are presented in more than one chapter.

## Chapter 3

# Comparison of Acquisition Techniques for Detecting Task-Related Changes in CBF and BOLD

### 3.1 Introduction

FMRI experiments typically use blood oxygen level dependent (BOLD) signal contrast to probe the regional and spatial extent of task-related neural activity. However BOLD signal changes are measured from an unknown baseline and are a function of underlying haemodynamic processes such as cerebral blood flow (CBF) and oxygen metabolism. Techniques such as calibrated BOLD [45, 46] attempt to measure these underlying physiological processes to better interpret BOLD signal changes and provide a clearer understanding of brain physiology. This is achieved by inducing isometabolic CBF and BOLD signal changes using hypercapnic [45] or hyperoxic [46] respiratory manipulations and relating them to the cerebral rate of oxygen metabolism ( $\text{CMRO}_2$ ) through a BOLD signal model.

### 3.1.1 Arterial Spin Labelling

In order for this technique to be feasible, it is beneficial to use a scanning protocol capable of detecting changes in CBF and BOLD simultaneously. Consequently the application of ASL to task based fMRI experiments and the ability to process the acquisition in such a way as to provide simultaneous, non-invasive measures of CBF and BOLD has made it a cornerstone of the calibrated BOLD methodology. In an ASL fMRI experiment, a series of control and tag images are acquired in an interleaved manner. Control images are acquired in which arterial blood is fully relaxed. Tag images are then made, in which arterial blood is magnetically inverted and the tag image acquired after waiting an appropriate amount of time for the tagged blood to perfuse into the tissue. The time course of signal differences (control - tag) is flow weighted and can be used to calculate CBF. These images are typically acquired with a rapid imaging sequence such as an echo-planar imaging (EPI) readout sequence. The sensitivity of the rapid imaging sequence to changes in  $T_2^*$  means that the ASL acquisition also contains some influences from BOLD signal contrast. This influence of BOLD contrast on the acquired time-series can be optimised by acquiring at a  $TE \approx 30$  ms and the influence of the ASL tag can be minimised by averaging the tag-control time course ( $\frac{control+tag}{2}$ ) [43]. Conversely the influence of BOLD weighting on the CBF measure can be reduced by minimising the TE and acquisition time of the readout sequence.

### Comparison of ASL Techniques

Although most ASL techniques are capable of being processed in such a way as to provide both CBF and BOLD signal time-series, techniques are often optimised

for either BOLD or CBF acquisition, not both. Moreover, different variations of ASL (i.e. pulsed, continuous or pseudo-continuous) each offer specific benefits and disadvantages.

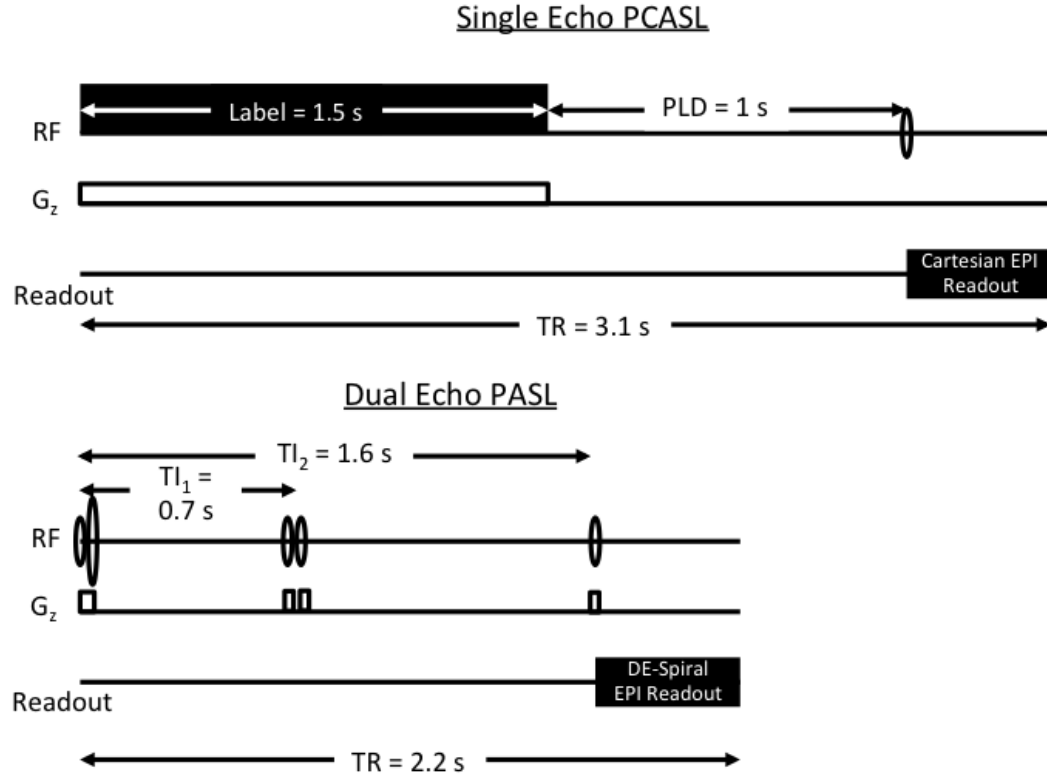


Figure 3.1: Schematic showing the timings of the single echo PCASL with Cartesian EPI readout and dual-echo PASL spiral EPI readout ASL acquisitions.

In this study we aim to compare two ASL acquisition schemes available in our centre, shown in Figure 3.1, that are capable of detecting task related changes in CBF and BOLD. The two ASL acquisition schemes used for comparison were a dual-echo pulsed ASL (PASL) acquisition with a spiral EPI readout (supplied by University of California at San Diego (UCSD) [44]) and a single-echo pseudo-continuous ASL (PCASL) with Cartesian EPI readout (supplied by the National



Institutes of Health (NIH), Bethesda, Maryland, USA). The benefits and disadvantages of the different elements of each acquisition are discussed below.

As previously mentioned, ASL is based on the difference between a tag and control image, the subtraction of which can be directly related to CBF. The tagging preparation module used can directly affect the signal-to-noise ratio (SNR) of the perfusion signal [37]. The spin preparation or tagging of arterial blood performed by PASL is spatially selective whereas continuous ASL (CASL) tags protons travelling through a plane for a well defined period of time and is therefore temporally dependent. In general, temporal tagging schemes lead to a higher amount of tagged arterial blood and therefore CASL techniques usually afford a higher SNR perfusion signal compared to PASL. However the primary drawback of CASL is the requirement of continuous radio frequency (RF) transmitting hardware that is not commonly available on most MRI scanners. PCASL is a subcategory of CASL developed to circumvent the hardware limitations that are encountered. This is achieved by breaking the RF and gradient pulses into a series of rapid pulses.

Dual-echo protocols allow data to be acquired at two different TE's and therefore can be optimised for the acquisition of CBF and BOLD data. CBF measurements are preferably made with a TE as short possible, improving the SNR of the ASL measurement and minimising  $T_2^*$  influences. Conversely, BOLD signal contrast can be optimised by imaging at a more optimal, longer TE ( $\approx 30$  ms). With a spiral trajectory through k-space, the effective TE (i.e. the time at which the centre of k-space is acquired) can be very short (a few ms), improving the SNR of the ASL measurement. The second echo is optimised for the BOLD signal, generally at  $\sim 30$  ms [44]. By way of contrast, single echo techniques require a compromise on

TE usually at  $\sim 20$  ms. This leads to a reduction in the SNR of the CBF signal and a loss of BOLD signal contrast due to the reduced echo time [31].

Ideally a comparison of techniques for detecting task-related changes in CBF and BOLD would be performed in a systematic manner comparing each feature of the pulse sequence including pulsed and pseudo-continuous tagging modules, single-echo and dual-echo acquisitions and Cartesian EPI with spiral EPI readouts for detecting task-related changes in CBF and BOLD. However, the comparison presented in this chapter was limited to ASL techniques available in our centre. The multi-echo pulse sequence is limited to a PASL tagging module with a spiral EPI readout allowing short readout times. The other available technique used a PCASL tagging module, offering improved perfusion-related SNR compared to PASL, but limited to a single echo acquisition with Cartesian EPI readout.

The aim of this study is to choose the pulse sequence most sensitive to simultaneous detection of stimulus induced changes in both CBF and BOLD signal. The chosen pulse sequence will be applied in a calibrated BOLD style protocol where the measurement of hypercapnic and hyperoxic induced changes in CBF and BOLD signals are essential. In order to assess the sensitivity of the two techniques for detecting stimulus induced changes in CBF and BOLD, both ASL acquisition schemes were used to acquire CBF and BOLD time-series during an on/off visual stimulus paradigm. CBF and BOLD time-series were calculated from both acquisitions and analysed to identify the statistical significance of visually induced changes in CBF and BOLD signals using a linear modelling approach. The number of task correlated 'active' voxels and mean z-score of these voxels was assessed in the visual cortex at a number of significance levels for CBF and BOLD time-series that

were acquired using both techniques. Correlation between CBF and BOLD time-series was also assessed at the same thresholding levels using different functionally localised ROI's to assess the correspondence between task related changes in the CBF and BOLD time-series. As positive BOLD signal change is intrinsically linked with increases in CBF a high correlation is expected between these two physiological measures. Comparing correlations in this manner has the added benefit of making the comparison independent of the task model and provides a useful measure even if the activity time-course is not what would be expected.

## 3.2 Methods

### 3.2.1 Participants

Five normal healthy participants (aged 27-39; mean age  $34.2 \pm 4.4$ ; 1 female) were recruited and scanned having given written consent. Experimental procedures were approved by the local institutional ethical review committee.

### 3.2.2 Scanning Protocol

Scanning was performed on a 3T GE HDx MRI (GE Healthcare, Milwaukee WI) with a body transmit coil and 8-channel head receive only coil. All participants had previous whole brain  $T_1$ -weighted structural scans available (fast spoiled gradient recalled echo, 1x1x1 mm voxels, TI/TR/TE = 450/7.8/3 ms).

PASL and PCASL techniques were limited to 10 minute acquisition runs during which the participant viewed a 90 second on/off visual stimulus consisting of a reversing checkerboard pattern (8 Hz). Comparing dual-echo PASL and single-echo PCASL acquisitions, the repetition time (TR) or time taken to acquire a single volume was longer for PCASL (TR = 3.1 s) than PASL (TR = 2.2 s). Due to this difference in TR the total acquisition time was used as the limiting factor. This was considered a fair comparison as the intended application of the acquisition was to a calibrated BOLD protocol containing hypercapnic and hyperoxic challenges with a predetermined acquisition time already decided upon. The imaging prescriptions, including orientation and coverage of slices were consistent between the two techniques (Flip angle  $90^\circ$ , FOV 22 cm, matrix 64x64, 12 slices of 7 mm thickness with an inter-slice gap of 1 mm acquired in ascending order). The sequence in which ASL scans were acquired was randomised to control for order effects. A separate single shot,  $M_0$  scan (TR =  $\infty$ ) with the same parameters as each functional run was used to measure the equilibrium brain tissue magnetisation for purposes of quantifying CBF.

Perfusion and BOLD imaging time-series were acquired during the on/off visual paradigm using the following acquisitions:

### **Dual-Echo PASL with Spiral EPI Readout**

PASL, proximal inversion and control for off-resonance effects (PICORE), quantitative imaging of perfusion using a single subtraction (QUIPSS II) [37] imaging sequence was used with a dual-echo, single-shot, gradient echo (GRE) readout and spiral k-space acquisition [72] ( $TE_1 = 3$  ms,  $TE_2 = 29$  ms, TR = 2.2 s, flip

angle  $90^\circ$ ,  $TI_1 = 700$  ms,  $TI_2 = 1600$  ms for the most proximal slice and was incremented by 54.6 ms for subsequent slices, tag thickness = 20 cm, adiabatic hyperbolic secant inversion pulse, 10 mm gap between labelling slab and bottom slice, 10 cm QUIPSS II saturation band thickness with an EPI acquisition time of 600 ms). During the 10 minute task, 272 volumes (136 tag-control pairs) were acquired.

### Single-Echo PCASL with Cartesian EPI Readout

PCASL labelling [40] was used with GRE echo-planar imaging, full k-space, Cartesian EPI readout ( $TR = 3.1$  s,  $TE = 22$  ms, EPI readout flip angle  $90^\circ$ , no acceleration factor). A TE of 22 ms was chosen as it was considered short while still maintaining a good proportion of maximum possible BOLD weighting [31]. A labelling duration of 1.5 seconds was accompanied by a post-labelling delay of 1 second for the most proximal slice and incremented for the subsequent slices by 54.6 ms and leading to an EPI acquisition time of 600 ms. During the 10 minute task 192 volumes (96 tag-control pairs) were acquired.

As the positioning of the labelling plane for PCASL affects the labelling efficiency [73], a 3D time-of-flight angiogram was acquired in order to choose the position of the PCASL labelling plane. This enables optimal placement of the labelling plane in the straight portion of the carotid arteries avoiding twists and kinks in the arteries that may affect the labelling efficiency Figure 3.2.

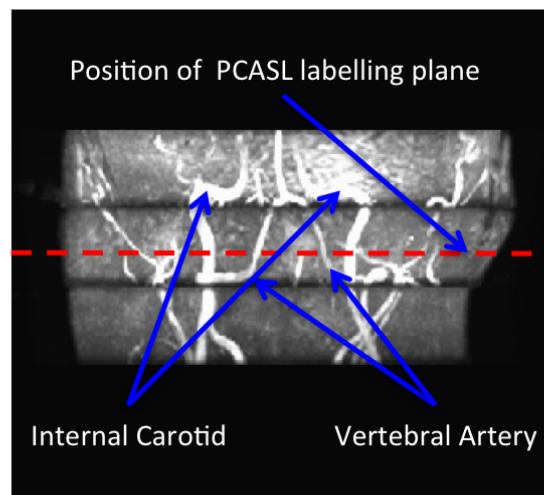


Figure 3.2: A 3D time-of-flight angiogram showing the position of the PCASL labelling plane in relation to the internal carotids and vertebral arteries.

### 3.2.3 Analysis

The AFNI (Analysis of Functional NeuroImages) [74] and FSL (FMRIB Software Library) [75] libraries of analysis tools are used extensively throughout this thesis for image manipulation.

Image time-series were motion corrected using *3dvolreg* and brain extracted using *3dAutomask* [74].

### CBF and BOLD Time-Series

Interpolated surround subtraction was performed on the PASL (first-echo) and PCASL tag-control image time-series to yield a perfusion-weighted time-series [43]. From the  $M_0$  calibration image an ROI in the ventricles was produced to calculate the mean  $M_0$  of CSF and related to the  $M_0$  of blood. This value was used to calculate CBF image time-series from the perfusion-weighted PASL and PCASL data using the PASL and CASL general kinetic model (GKM) [33] respectively whilst correcting for slice timing delays. Interpolated surround averaging of the tag-control images was performed to yield a BOLD weighted time-series. In the case of dual-echo PASL, the second echo was used for the calculation of the BOLD time-series.

### General Linear Model

The CBF and BOLD time-series for both ASL techniques were analysed to identify significant visual task induced changes in CBF and BOLD signals using a linear modelling approach. A boxcar regressor with on/off periods of 90 seconds each was

convolved with a single haemodynamic response function and fitted to the CBF and BOLD image time-series, for both methods, in each subject, using *3dDeconvolve* [74]. Parameter estimates were converted to z-scores and thresholded at varying levels of significance ( $p = 5 \times 10^{-2}$ ,  $p = 1 \times 10^{-2}$ ,  $p = 1 \times 10^{-3}$ ,  $p = 1 \times 10^{-4}$ ). No clustering was performed as it could potentially introduce a degree of nonlinearity and complexity to the comparison and instead the measures were restricted to the occipital lobe (OL). An OL mask, as defined by the MNI152 (Montreal Neurlogical Institute) atlas [76], was registered back to the native space of each of the CBF and BOLD time-series through the high-resolution structural image using FLIRT [77]. This was used to constrain the following calculations to OL as no clustering was used. The number of voxels and mean z-score below each of the probability thresholding levels, in OL, was then calculated for CBF and BOLD using both ASL acquisitions. The OL anatomical ROI and the CBF and BOLD functional ROI's at each thresholding level were used to investigate how well CBF and BOLD signal time-series correlated during the paradigm for both ASL techniques. This was performed by extracting CBF and BOLD signal time-series using three pairs of functionally localised ROI's. The BOLD functional localiser was used to extract CBF and BOLD time-series allowing a comparison of BOLD localised CBF and BOLD. In a similar manner, the CBF functional localiser was used to extract CBF and BOLD time-series allowing a comparison of CBF localised CBF and BOLD. A third comparison was performed from the previously extracted time-series using CBF extracted using the CBF functional localiser and BOLD extracted using the BOLD functional localiser.



### 3.3 Results

The number of significantly active voxels in the occipital lobe at each thresholding level for CBF and BOLD using both PASL and PCASL techniques are shown in Figure 3.3. The group mean ( $\pm$  standard deviation) number of active voxels are displayed for differing levels of significance allowing the spatial extent of the activation in each technique to be demonstrated.

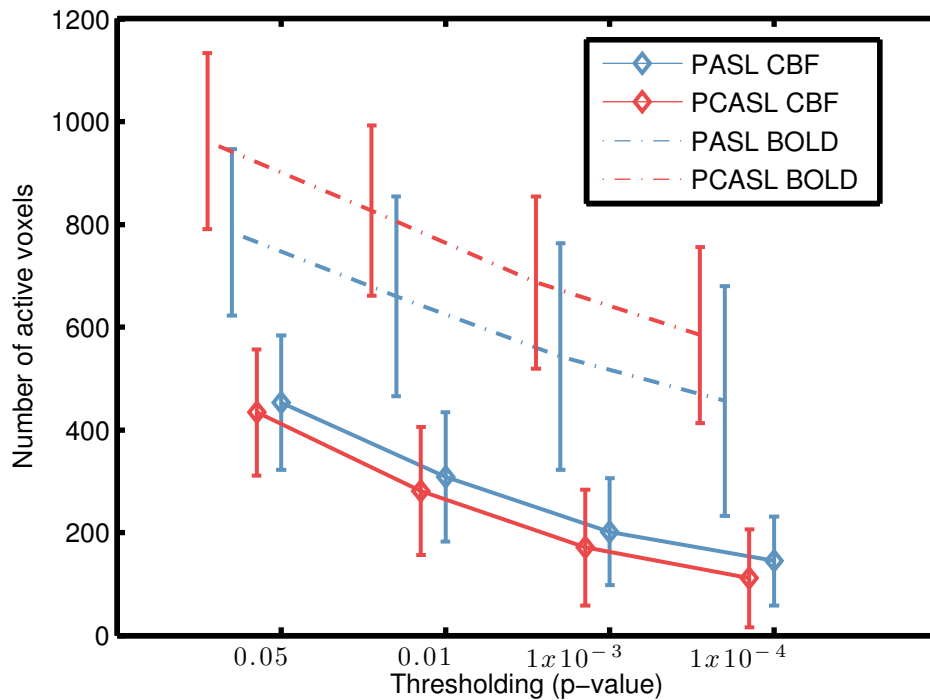


Figure 3.3: PASL (Blue) and PCASL (Red) were used to investigate the spatial extent of CBF (solid line) and BOLD (dashed line) changes with a visual stimulus paradigm. The mean number of active voxels ( $\pm$  standard deviation) across the five subjects are displayed for differing levels of significance (x-axis labels) allowing the spatial extent of the activation in each technique to be demonstrated.

The mean z-score at each thresholding level for CBF and BOLD using both techniques are shown in Figure 3.4. This allows the sensitivity of the response to the visual paradigm to be assessed. A higher z-score suggests better correlation with

the signal model and therefore better sensitivity to task related changes in CBF and BOLD.

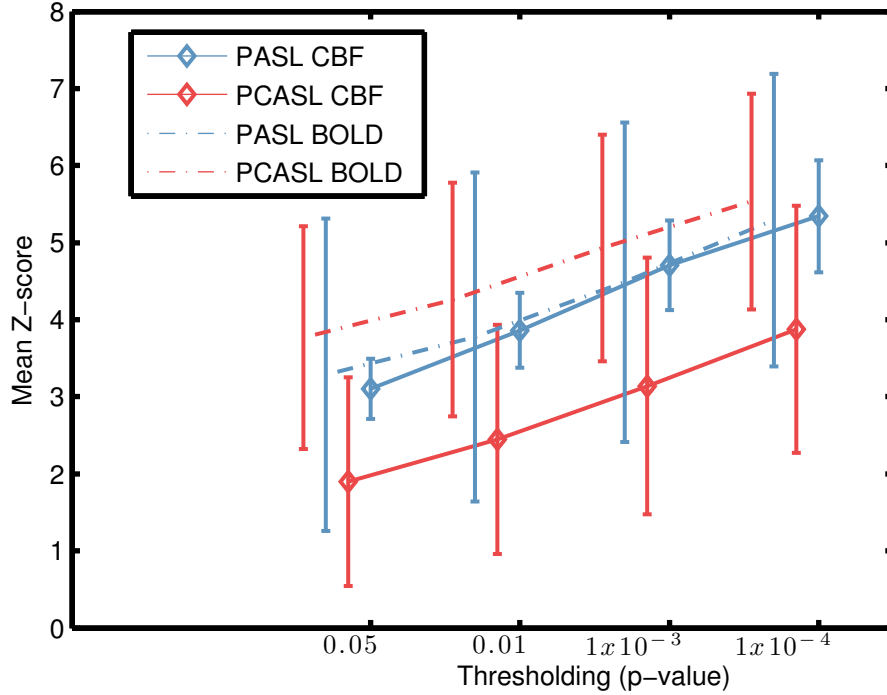


Figure 3.4: PASL (Blue) and PCASL (Red) were used to investigate the sensitivity of CBF (solid line) and BOLD (dashed line) changes with a visual stimulus paradigm. The mean z-score ( $\pm$  standard deviation) across the five subjects are displayed for differing levels of significance (x-axis labels) allowing the sensitivity of the response to the visual paradigm to be assessed. A higher z-score suggests better correlation with the signal model and therefore better sensitivity to task related changes in CBF and BOLD.

Figure 3.5 shows the correlation coefficient,  $R$ , between the BOLD and CBF signal time-series extracted using an anatomical ROI (OL) and three different combinations of the functional localisers for both techniques.  $R$  values in each ROI are compared between PASL and PCASL.

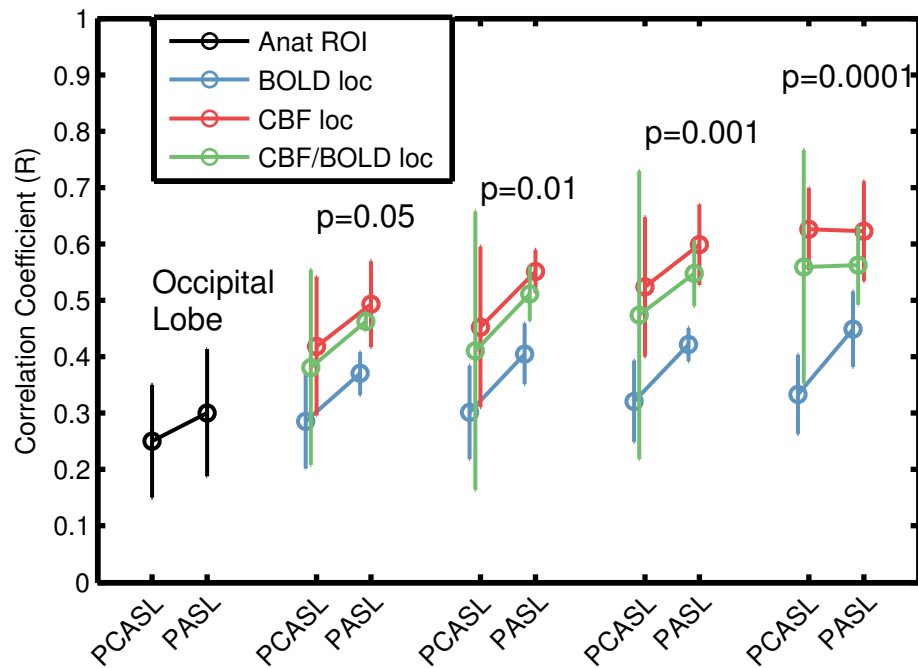


Figure 3.5: Correlation coefficients,  $R$ , representing the similarity between CBF and BOLD signal time-series during the on/off visual paradigm. Mean  $R$  ( $\pm$  standard deviation) across the five subjects were calculated for the OL anatomical ROI (Black) and three different functionally localised ROI's. These were used to extract the time-series as follows: BOLD localised CBF and BOLD time-series (Blue), CBF localised CBF and BOLD time-series (Red) and CBF localised CBF time-series and BOLD localised BOLD time-series (Green). The functional localisers were thresholded at four different levels and the mean group correlation coefficients compared for PASL and PCASL techniques.

## 3.4 Discussion

Two characteristically different ASL acquisition schemes, a dual-echo PASL with spiral EPI readout and single-echo PCASL with Cartesian EPI readout, were assessed for their sensitivity to detecting task related changes to an on/off visual paradigm lasting ten minutes in five participants.

By determining the correlation between the expected response to a visual paradigm and the CBF and BOLD time-series on a voxel-wise basis, the number of task correlated "active" voxels and mean z-score of these voxels were assessed in OL at a number of significance levels. By investigating the number of voxels at each thresholding level it can be inferred which technique provides a larger number of significantly correlated voxels. A larger spatial activation suggests greater sensitivity to detect changes, however the mean z-score of the remaining voxels at each thresholding level was also calculated to assess the sensitivity of the technique to detecting significant correlation with the task. Correlation between CBF and BOLD time-series was also assessed, using both techniques, at the same thresholding levels, using different functionally localised ROI's to investigate which method provided best correspondence between CBF and BOLD responses to task.

It can be seen from Figure 3.3 that CBF measured using dual-echo PASL produces a higher number of significantly correlated voxels with task when averaging across the five subjects at all thresholded levels. The opposite is true when considering the BOLD related changes to task with PCASL providing consistently more activated voxels at all thresholding levels. In both cases the group standard deviation is comparable across techniques when CBF or BOLD is considered. In all cases

the number of active voxels decrease as the significance thresholding decreases, as expected.

The quality of the activation can be measured by calculating the z-score. A higher z-score suggests stronger task related activation and a more sensitive technique. Mean z-scores across the group, calculated in OL at the varying thresholding levels are presented in Figure 3.4. It can be seen that group mean z-score increases with thresholding. This is to be expected as voxels with weaker correlations to the activation are removed with thresholding, thus increasing z-scores. CBF activation detected with dual-echo PASL provides a consistently higher z-score when compared to PCASL as well as considerably lower standard deviations. Group mean z-score calculated using BOLD contrast is higher using the PCASL technique with the standard deviation being smaller.

The main aim of this initial study is to choose an available acquisition method which has the greatest sensitivity to detecting changes in CBF and BOLD for use in calibrated BOLD experiments. Some other considerations that warrant discussion mainly focus around the measurement of CBF. As the signal difference between ASL tag-control images is  $\sim 1\%$  and requires some form of subtraction to weight the time series to perfusion, the intrinsic SNR and temporal resolution of ASL is worse than with BOLD imaging. Therefore detecting task related changes in CBF should be viewed as challenging and a technique proving more capable in this aspect should be given more weight. The short TE of the dual-echo PASL technique provides CBF measures with a marginally higher number of significantly correlated voxels with higher mean z-score at all thresholding levels. This would suggest that PASL with a short TE, acquired as close to  $TE = 0$  ms as possible, is

more sensitive at detecting task-related changes in CBF than a higher SNR tagging module, as in PCASL, with a longer, suboptimal TE. During the 10 minute acquisition time, 272 PASL volumes were acquired compared to 192 PCASL volumes. This is as a result of the shorter TR of the PASL technique when compared to PCASL giving the PASL approach a better temporal resolution which may be an important factor.

It is also important to note that PASL may be favourable to PCASL when choosing a method to measure CBF changes during hypercapnic respiratory manipulations as is the case in calibrated BOLD. Hypercapnia is known to induce changes in the velocity of arterial blood. This change in velocity has been demonstrated using phase-contrast MRI in areas of the arterial tree such as the internal carotid and vertebral arteries where the PCASL labelling plane is typically positioned [73]. This can cause the use of hypercapnia to decrease the tagging efficiency of the PCASL technique and lead to inaccurate estimates of CBF. Failure to correct for decreases in tagging efficiency due to increased velocity of arterial blood lead to overestimation of the tagging efficiency and underestimation of CBF calculated during hypercapnia. Due to the spatial nature of the PASL tag it should be insensitive to such changes. For the QUIPSS II approach used in this study, this assumes that the tag thickness is large enough that the cut-off saturation pulse, used to provide a well defined bolus, does not miss the back of the tagging slab. Methods for correcting changes in PCASL tagging efficiency are available but require additional phase-contrast scans to be performed [73].

Surprisingly the PCASL technique proved more sensitive to detecting task related changes in BOLD. This may be due to the Cartesian EPI readout offering

improved sensitivity to BOLD changes over the spiral readout. The Cartesian sampling scheme samples k-space in a more thorough fashion which involves a longer readout when compared to the spiral readout. To investigate this further, group mean percentage BOLD increase and group mean coefficient of determination were calculated over the OL as determined by the anatomical ROI previously described. Group mean percentage increase were similar for both techniques, PASL =  $0.34 \pm 0.21$  % and PCASL =  $0.32 \pm 0.15$  %. However the PCASL technique demonstrated a higher group mean coefficient of determination ( $R^2$ ), PASL =  $0.08 \pm 0.04$  and PCASL  $0.10 \pm 0.04$ . This would suggest that the improved BOLD sensitivity afforded by the Cartesian EPI readout is due a noisier spiral readout.

Figure 3.5 demonstrates that higher correspondence between CBF and BOLD time-series is achieved when using CBF to localise the signal time-series in both techniques. One reason for this may be the fact that ASL measures the delivery of arterial blood to the capillary beds and better localises the BOLD signal to this region. BOLD signal changes are less specific and arise from venous oxygenation changes. At all thresholding levels, equivalent or better correlation is demonstrated by PASL when compared to PCASL. The improved correlation between CBF and BOLD is also shown by the OL anatomical, ROI. This anatomical ROI analysis has the advantage of not constraining the signal to only task-like voxels and instead includes all signal from the OL.

To summarise the results in Figures 3.3 and 3.4, the dual-echo PASL technique allows CBF measures which are more sensitive to task-related changes with a higher number of active voxels whereas the single-echo PCASL acquisition allows more sensitive BOLD related changes with task. Taking this into consideration

the improved correlation between task-related changes in CBF and BOLD signal afforded by the dual-echo PASL technique can be put down to its superior CBF measure. Although a higher SNR is provided by a PCASL tagging module, the dual-echo PASL approach allows a CBF measurement to be made with a TE as short possible, improving the SNR of the ASL measurement and minimising  $T_2^*$  influences. The dual-echo PASL acquisition also allows an improved temporal resolution, with a TR of 2.2 s compared to 3.1 s, which may contribute towards the better CBF and BOLD correlations.

### 3.5 Conclusion

The sensitivity of two ASL techniques, a dual-echo PASL with spiral EPI read-out and a single-echo PCASL Cartesian EPI readout, were compared for detecting task-related changes in CBF and BOLD with a visual task. The optimised echo time and superior temporal resolution of the PASL technique offered better sensitivity in terms of detecting task related CBF changes whereas the PCASL technique offered better BOLD sensitivity. Better correspondence between CBF and BOLD time-series is achieved when using CBF to localise both perfusion and BOLD task related time-series with PASL again demonstrating higher correlation.

From these results and the fact that PASL tagging is largely insensitive to CBF misestimation related to velocity dependent tagging efficiency errors [78], the dual-echo PASL technique would appear to be the more appropriate acquisition for application in calibrated BOLD, respiratory manipulation style experiments.



## Chapter 4

# Comparison of Dual Calibrated FMRI Respiratory Designs for the Detection of Regional Alterations in Absolute CMRO<sub>2</sub>

### 4.1 Introduction

Oxygen is essential in the supply of energy to the brain. The brain has minimal energy and oxygen reserves so it must be continuously supplied with oxygen rich blood in order to maintain proper, healthy function. The rate at which oxygen is consumed by the brain is referred to as the cerebral metabolic rate of O<sub>2</sub> consumption (CMRO<sub>2</sub>) and is a direct indicator of cerebral activity under the assumption of largely oxidative metabolism [12]. CMRO<sub>2</sub> is closely related to brain function and health and can change regionally with disease or functional activation [19]. The coupling of CMRO<sub>2</sub> with CBF and its relationship with CBV make it an important component in the formation of BOLD contrast, commonly exploited to map neural activity in the brain [32]. Perturbations in cerebral oxygen metabolism are

directly linked to neurodegenerative disorders such as Alzheimer's, Parkinson's and multiple sclerosis [13–15] whilst directly measuring  $\text{CMRO}_2$  can assist in assessing the extent of brain damage after stroke [16] and aid in tumour management and outcome [17]. As a result, techniques capable of producing non invasive, absolute, quantitative maps of  $\text{CMRO}_2$  in the brain provide us with a unique tool to investigate the regional and spatial extent of cerebral oxygen consumption and have a wide range of applications. With appropriate development a technique allowing a robust absolute  $\text{CMRO}_2$  measure would provide a valuable insight into the underlying metabolic changes that accompany normal brain development, ageing and brain disease in which tissue damage or dysfunction alters metabolic activity. Oxygen metabolism presents a functional biomarker which could aid in the diagnosis and development of new treatment pathways of such diseases. A direct measure could also be applied to studies of task-related brain activity by providing a measure of baseline from which brain activity levels are changing, aiding in the interpretation of traditional fMRI studies.

#### 4.1.1 PET

Currently triple oxygen Positron Emission Tomography (PET) is the gold standard for providing detailed oxygen metabolism maps of the brain [19]. This technique requires three separate PET radio-tracer studies to be performed allowing whole brain  $\text{CMRO}_2$  maps to be produced. However this technique is time consuming taking  $\sim 45$  minutes to acquire the relevant data, requires an on-site cyclotron due to the short half-life of the radioisotope used, is expensive to perform and most

importantly exposes the subject to a radiation dose which compromises the ability of PET to be used in longitudinal studies of disease or ageing.

### 4.1.2 MRI

A number of MRI alternatives have been developed in an attempt to avoid using radioisotopes to measure  $\text{CMRO}_2$  in the human brain [45, 46].

#### Relative $\text{CMRO}_2$ and Calibrated BOLD

Calibrated BOLD is an established technique used to determine changes in  $\text{CMRO}_2$  associated with a task by calibrating the blood oxygen level dependent (BOLD) signal using measurements acquired during a respiratory manipulation. As discussed in **Chapter 3**, arterial spin labelling (ASL) can be acquired and processed in a manner which allows simultaneous measures of BOLD and cerebral blood flow (CBF) to be made during a respiratory manipulation such as hypercapnia [45] or hyperoxia [46]. Using an appropriate BOLD signal model and relevant assumptions about the respiratory manipulation, changes in  $\text{CMRO}_2$  can be quantified relative to baseline. However as this technique produces estimates of relative changes in  $\text{CMRO}_2$  from an unknown baseline and is dimensionless, the interpretation of these changes prove problematic where the baseline may be altered in disease or drug states [63].

### Absolute CMRO<sub>2</sub>

MR methods have started to emerge allowing estimates of absolute CMRO<sub>2</sub> to be made in  $\mu\text{mol}$  of O<sub>2</sub> consumed per 100g of tissue per minute ( $\mu\text{mol}/100\text{g}/\text{min}$ ). Methods yielding bulk or whole brain absolute CMRO<sub>2</sub> are based on measurements of CBF and venous oxygen saturation via relaxation measurements of T<sub>2</sub> of venous blood [79] or the pattern of magnetic field distortions around major veins [64]. Velocity selective methods have also been proposed to isolate the T<sub>2</sub> of venous blood and estimate its oxygenation based on a T<sub>2</sub>-oxygenation calibration curve [70, 71]. However, these techniques have low SNR and currently suffer from limited brain coverage. Methods capable of producing whole brain parametric maps capable of detecting regional differences in absolute CMRO<sub>2</sub> are preferable in detecting the extent of disease or functional activation and are analogous to the PET technique discussed previously. A quantitative or qBOLD approach has been demonstrated in which R'<sub>2</sub> is sensitive to CBV and deoxyhaemoglobin concentration [69]. However the distinction between CBV and deoxyhaemoglobin concentration is challenging under normal experimental conditions [68].

#### 4.1.3 Dual Calibrated FMRI

By performing dual hypercapnic-hyperoxic manipulations of CBF and BOLD signals in the same session, it has recently been shown that calibrated BOLD can be extended to estimate absolute CMRO<sub>2</sub> [1, 2]. The technique measures the maximum BOLD signal (M) and estimates the baseline oxygen extraction fraction (OEF<sub>0</sub>) through dual calibration. As this is an absolute measure it provides a

quantitative fMRI measurement for investigating longitudinal changes in cerebral metabolic behaviour, with use as a potential biomarker of disease which has applications in both research and clinical settings.

Further study of the dual calibrated fMRI (dcfMRI) technique involved the investigation of the respiratory manipulation design and the sensitivity of the technique to detecting regional changes in metabolism [3]. Interleaved respiratory manipulations were performed with periods of normocapnia with hyperoxia and hypercapnia with normoxia interleaved with periods of normocapnia with normoxia, similar to the original studies [1, 2]. This respiratory design, lasting 19.5 minutes, was then used in a dcfMRI protocol to detect regional changes in absolute CMRO<sub>2</sub> due to a sustained visual stimulus. The study also introduced a simultaneous respiratory manipulation with periods of hyperoxia which were simultaneously modulated using periods of hypercapnia, lasting 13.5 minutes in total. By simultaneously modulating hyperoxia using hypercapnia, the simultaneous dcfMRI approach provided additional information about the exponents,  $\alpha$  and  $\beta$ , used in the BOLD signal model.  $\alpha$  is the exponent relating relative increases in CBF to relative increases in CBV and  $\beta$  is the exponent relating deoxyhaemoglobin concentration to the transverse relaxation rate  $R_2^*$ . Both of these model parameters are dependent on cerebrovasculature, have the potential to change depending on the underlying physiology and are assumed in the interleaved dcfMRI approach.

The focus of this study is to compare an interleaved respiratory manipulation design to a simultaneous design for the detection of regional changes in metabolism. This study offers a number of refinements to that presented by *Wise et al.* [3]. Both interleaved and simultaneous respiratory manipulations are used to investigate

regional elevations in oxygen metabolism, a visual and motor stimulus is used to regionally elevate oxygen metabolism and optimised interleaved and simultaneous respiratory manipulations are presented.

The interleaved and simultaneous hypercapnic-hyperoxic respiratory manipulations are modified versions of those presented by *Wise et al.* [3]. Modifications made to the interleaved design are shown in Figure 4.1. Periods of normocapnia/normoxia and hyperoxia/normocapnia last one minute each and periods of hypercapnia/normoxia last 2.5 minutes. The reliance on arterial spin labelling (ASL) to measure changes in CBF is considered to be a limiting factor in the dcfMRI routine as the measure of CBF using ASL suffers from low SNR. It can also be seen from Figure 4.1 that changes in CBF are only expected during periods of hypercapnia. In order to increase the SNR of the ASL measure of CBF change, the length of the hypercapnia/normoxia blocks were increased. As no such SNR limitations are placed on the detection of BOLD changes induced during periods of hyperoxia, more frequent, shorter blocks of hyperoxia and normocapnia/normoxia were used. The symmetry and interleaved nature of the design, were also thought to be beneficial in dealing with any drift that may occur during the long scan time duration. To aid in extrapolating measurements of the  $\alpha$  and  $\beta$  exponents from the simultaneously modulated design it was considered best to have many levels of simultaneously varying hypercapnia and hyperoxia in the 18 minute time-course, as shown in Figure 4.2. It was also designed symmetrically to counteract drift with baseline measures being conducted at the beginning, middle and end of the respiratory design. The acquisition time of both respiratory designs was set at 18 minutes.

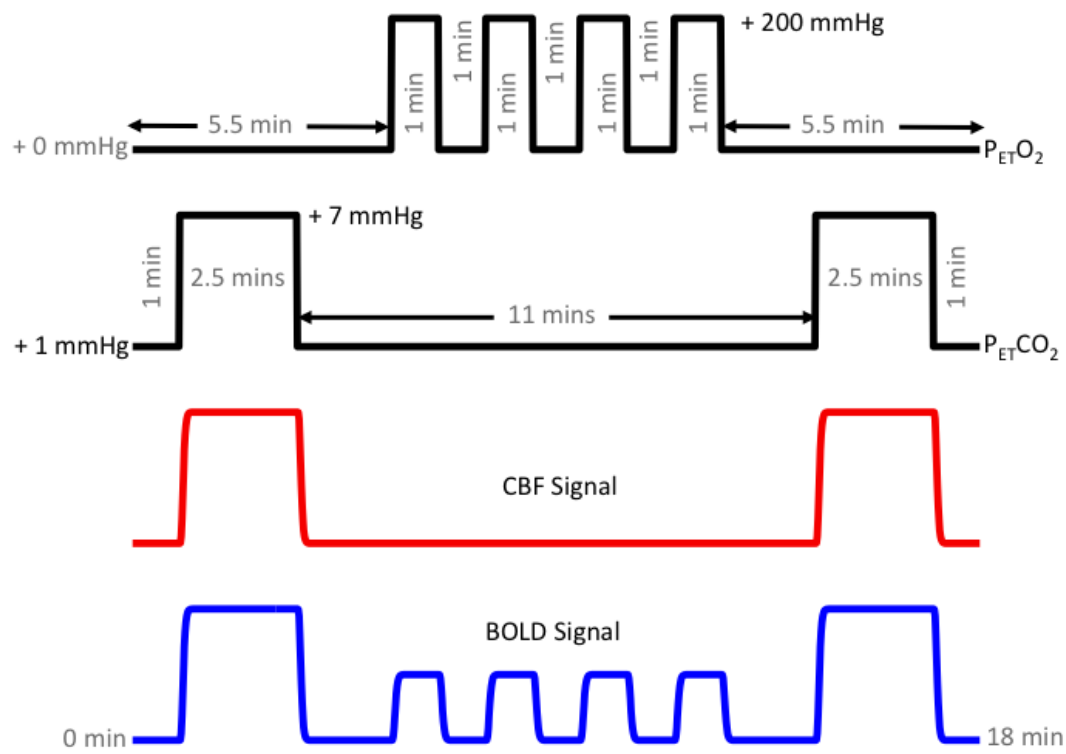


Figure 4.1: Schematic detailing, from top to bottom, target  $P_{ET}O_2$  and  $P_{ET}CO_2$  time courses and expected perfusion and BOLD responses for the interleaved respiratory manipulation.

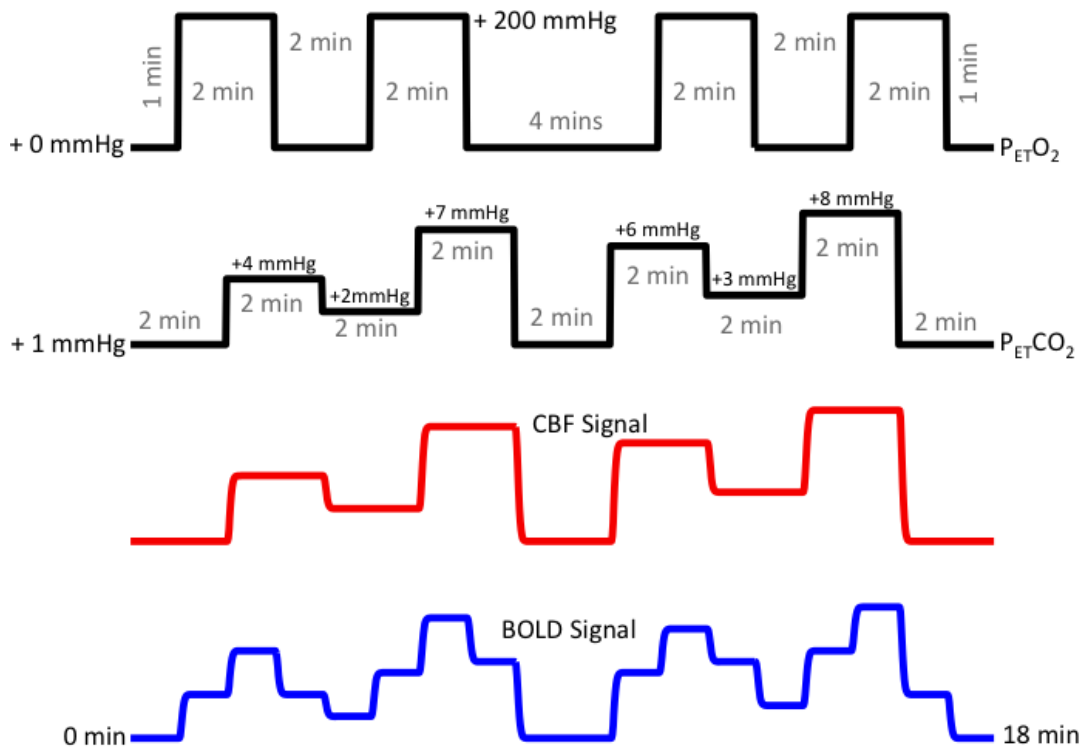


Figure 4.2: Schematic detailing, from top to bottom, target  $P_{ET}O_2$  and  $P_{ET}CO_2$  time courses and expected perfusion and BOLD responses for the simultaneous respiratory manipulation.



Interleaved and simultaneous dcfMRI approaches were then used to investigate regional changes in metabolism due to continuous visual and motor stimulation. This allows us to investigate the sensitivity of the dcfMRI technique for the detection of regional metabolic changes and therefore assess the suitability of the technique for application in the detection, monitoring and treatment of disease.

## 4.2 Methods

### 4.2.1 Participants

8 normal healthy participants (aged 24 - 39; mean age  $33.5 \pm 5.0$ ; 2 female) were recruited and scanned. Experimental procedures were approved by the local institutional ethical review committee.

### 4.2.2 MRI

Scanning was performed on a 3T GE HDx MRI (GE Healthcare, Milwaukee WI) with a body transmit coil and 8-channel head receive coil. All participants had previous whole brain  $T_1$ -weighted structural scans available (fast spoiled gradient recalled echo,  $1 \times 1 \times 1$  mm voxels,  $TI/TR/TE = 450/7.8/3$  ms). Each participant was scanned in two sessions on separate days with protocols lasting approximately 50 minutes. On each day a functional localiser, dcfMRI acquired during baseline and dcfMRI acquired during elevated baseline were acquired. The dcfMRI

acquired during baseline and elevated baseline allowed quantification of absolute  $\text{CMRO}_2$  at baseline and elevated baseline during each session. During the first session the dcfMRI protocol used an interleaved hypercapnic-hyperoxic respiratory manipulation and the second session used a simultaneous hypercapnic-hyperoxic respiratory manipulation, as detailed in Figure 4.3.

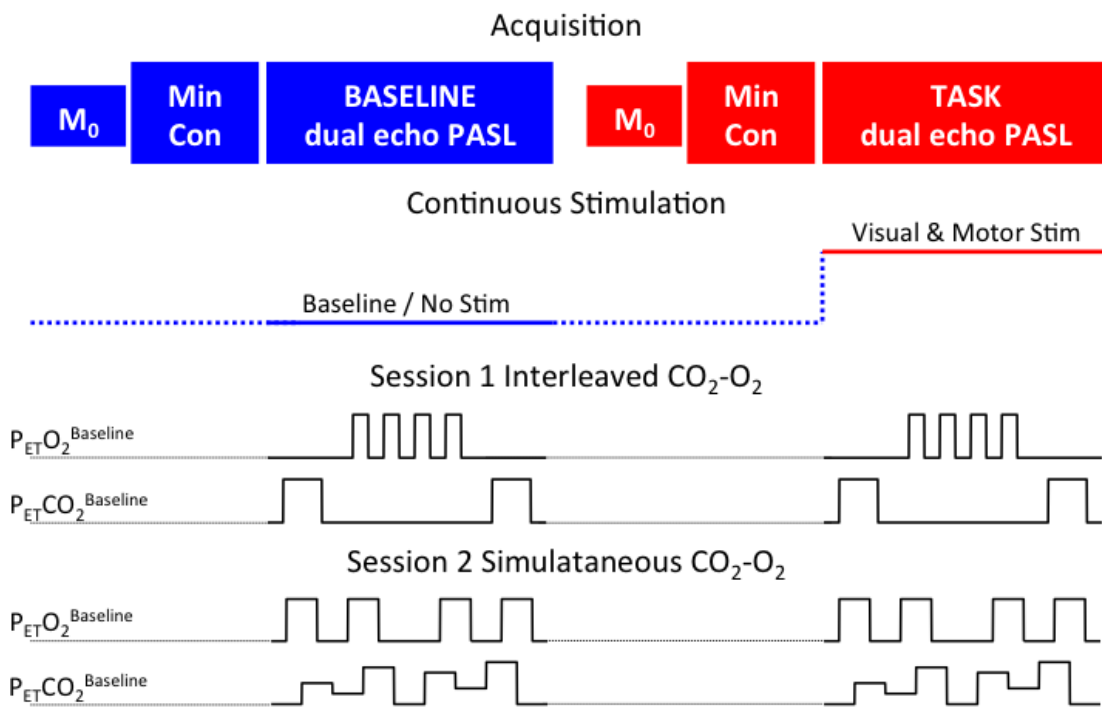


Figure 4.3: Schematic detailing the protocol used to assess the suitability of the interleaved and simultaneous dcfMRI techniques for detecting regional changes in metabolism. Session 1 involved an interleaved dcfMRI acquisition at rest and during continuous visual and motor stimulation while Session 2 consisted of simultaneous dcfMRI acquisition at rest and during continuous visual and motor stimulation. Not shown is the acquisition of the functional localiser (5.5 mins) which was acquired at the start of each session during normocapnia and normoxia.

## CBF and BOLD Acquisition

Simultaneous ASL and BOLD imaging data was collected for the functional localiser and for each of dcfMRI acquisitions in each session using a PASL proximal inversion and control for off-resonance effects (PICORE), quantitative imaging of perfusion using a single subtraction (PICORE QUIPSS II) [37] imaging sequence with a dual-echo gradient echo (GRE) readout and spiral k-space acquisition ( $TE_1 = 3$  ms  $TE_2 = 29$  ms,  $TR = 2.2$  s, flip angle  $90^\circ$ , FOV 22 cm, matrix  $64 \times 64$ , 12 slices of 7 mm thickness with an inter-slice gap of 1 mm acquired in ascending order,  $TI_1 = 700$  ms,  $TI_2 = 1600$  ms for the most proximal slice and was incremented by 54.6 ms for subsequent slices, tag thickness = 20 cm, adiabatic hyperbolic secant inversion pulse, 10 mm gap between labelling slab and bottom slice, 10 cm QUIPSS II saturation band thickness). This resulted in the acquisition of 248 volumes (124 tag-control pairs) for the functional localiser and 488 volumes (244 tag - control pairs) for each of the absolute CMRO<sub>2</sub> acquisitions. A separate single shot ( $M_0$ ) scan was acquired ( $TR = \infty$ ) with the same parameters as the functional run to measure the equilibrium brain tissue magnetisation for purposes of quantifying CBF. A minimum contrast image was also acquired to correct for coil sensitivity with the same acquisition parameters as the ASL run except for  $TE = 11$  ms,  $TR = 2$  s, and 8 interleaves.

### 4.2.3 Stimulus Design

## Functional Localiser

The functional localiser, lasting  $5\frac{1}{2}$  minutes, was used to create ROI's of activated voxels. This consisted of a 30 second baseline, 30 second motor stimulation and 30 second visual stimulation repeated three times ending with a baseline period. The motor stimulation consisted of numbers from 1 to 4 appearing on the screen with the participant responding by pressing the corresponding button on a button box. The button box was positioned in the subjects right hand with index finger corresponding to button 1, middle finger corresponding to button 2 and so on to button 4. Visual stimulation consisted of a full contrast reversing checkerboard pattern. The frequency of the reversing checkerboard was 8 Hz and the motor task 2 Hz.

## Baseline and Elevated Baseline CMRO<sub>2</sub> Conditions

Each participant was then scanned during an 18 minute respiratory challenge for separate rest and continuous task conditions allowing baseline and elevated baseline CMRO<sub>2</sub> to be measured. The elevated baseline condition consisted of a continuous visual and motor task performed for the duration of the entire scan. The task was comprised of the reversing checkerboard pattern overlaid with the changing numbers task that was used in the functional localiser as motor stimulation. During the baseline condition scan, the participant was told to fixate on a cross hair overlaid on a black background. The functional task protocol provided a regional variation in CMRO<sub>2</sub> in corresponding visual and motor regions of the brain between baseline and elevated baseline acquisitions essentially, simulating a disease or treatment-like condition where metabolism changes regionally. The order with

which the baseline and elevated baseline conditions were scanned was randomised to control for order effects.

#### 4.2.4 Respiratory Manipulations

Respiratory challenges were administered using a system of end-tidal forcing [63] which offers independent control of partial pressures of end-tidal oxygen and carbon dioxide ( $P_{ET}O_2$  and  $P_{ET}CO_2$  respectively). The end-tidal forcing system comprised a laptop personal computer using BreatheDmx software (Department of Physiology, Anatomy and Genetics, Oxford University, UK) to monitor end-tidal expired gas levels and calculate the inspired partial pressures required to achieve the desired target. The gas mixtures were delivered at a total flow rate of 30 litres per minute (lpm) through a fast gas mixing system connected to a tight-fitting face-mask worn by the volunteer (Quadralite, Intersurgical, Wokingham, Berkshire, UK). The respiratory circuit included a reservoir on the expired limb to permit re-breathing in the event that the instantaneous inspiratory rate exceeded 30 lpm. Supplies of 10%  $CO_2$  (balance air), 10%  $O_2$  (balance  $N_2$ ), 100%  $O_2$  and medical air were delivered from cylinders to the gas mixing chamber which was placed as close as possible to the volunteer (on the chest) to minimise delays in switching to a new inspiratory mixture. Gas delivery was controlled by four mass flow controllers (MKS Instruments, Wilmington, MA, USA). Tidal gases were sampled from the volunteers facemask and  $P_{ET}O_2$  and  $P_{ET}CO_2$  were measured using rapidly responding gas analysers (AEI Technologies, Pittsburgh, PA, USA). During the functional localiser  $P_{ET}O_2$  and  $P_{ET}CO_2$  were monitored for the

volunteer. Resting  $P_{ET}O_2$  was used as the  $P_{ET}O_2$  target for normoxic periods and resting  $P_{ET}CO_2 + 1\text{mmHg}$  was used as the target  $P_{ET}CO_2$  for normocapnia to allow the end-tidal forcing system to provide control of end-tidal  $CO_2$ . During the functional localiser scan the volunteer breathed medical air only without control of end-tidal  $CO_2$  and  $O_2$ .

### Interleaved and Simultaneous Hypercapnic-Hyperoxic Respiratory Designs

Target profiles for  $P_{ET}O_2$  and  $P_{ET}CO_2$  are shown in Figures 4.1 & 4.2. Figure 4.1 shows an interleaved hypercapnic and hyperoxic respiratory manipulation whereas Figure 4.2 demonstrates a simultaneous hypercapnic and hyperoxic manipulation. Each participant was scanned once with the interleaved design and once with the simultaneous design producing whole brain  $CMRO_2$  measures at baseline and elevated baseline for both designs.

#### 4.2.5 Analysis

##### Preprocessing

All image time-series were motion corrected using *3dvolreg* [74]. Time-series image data acquired from the first echo of the PASL technique were used to calculate CBF, while the data from the second echo was used to examine changes in BOLD signal. Physiological noise correction (a modified RETROICOR), was applied by regressing the first and second harmonics of both the cardiac and respiratory

cycles from the data along with the interaction term of the first cardiac and respiratory harmonics [80,81]. Interpolated surround subtraction of the first-echo, tag and control image time-series was performed to yield a perfusion-weighted time-series [43] which was corrected for coil sensitivity by dividing the CBF time-series by a normalised version of the minimum contrast image [82]. CBF images were calculated using the  $M_0$  of blood (estimated from the cerebrospinal fluid signal in the ventricles of the  $M_0$  image) and the general kinetic model (GKM) [33]. The CBF estimates were adjusted for the likely reduction of the  $T_1$  of arterial blood with increasing plasma concentration of dissolved paramagnetic  $O_2$ , according to the measured partial pressure of arterial  $O_2$  and blood  $T_1$  values quoted in *Bulte et al.* [51]. Interpolated surround averaging of the tag and control images was performed to yield a BOLD weighted time-series.

### Anatomical ROI Timeseries

Subject specific ROI's of global grey matter (GM) were produced using FAST segmentation [83] and registered to the native space of CBF and BOLD images using FLIRT [77]. A binary mask was then created by thresholding the GM mask in native space to keep voxels above 0.5. Occipital lobe (OL, MNI152 atlas (Montreal Neurlogical Institute)) and precentral gyrus (PG, Harvard-Oxford cortical structural atlas) ROI's were transformed to the native space of the CBF and BOLD time-series by registering the relevant whole brain standard space images to the high resolution anatomical in each subject and then registering the high resolution anatomical image to the native space of the CBF and BOLD time-series. The transforms of these registrations were concatenated and applied to the OL and PG

ROI's, as determined in standard space, to transform them from standard space to native space. The OL and PG ROI's, in native space, were then thresholded to produce binary masks and combined with the subject specific GM masks. This analysis was localised to GM as the measurement of white matter perfusion using ASL suffers from low SNR and is therefore unreliable.

### Functionally Localised ROI Timeseries

The CBF time-series for the functional localiser run were analysed to identify significant visual and motor stimulus-induced changes in CBF using a linear modelling approach (*3dDeconvolve* [74]). CBF was chosen to localise the area of activation as *Leontiev et al.* [84] demonstrated that selecting ROI's according to flow activation significantly improves the robustness of measurements available with fMRI. A box-car regressor with on/off periods corresponding to the on/off visual and motor tasks used in the functional localiser task were convolved with gamma haemodynamic response functions and fitted to the data. The resulting visual and motor task activation maps were thresholded at  $p < 0.001$  level to correct for multiple comparisons. Only clusters of voxels greater than 50 were included using *3dclust* [74]. The OL GM and PG GM ROI's were then used to further anatomically constrain the visual and motor activation ROI's respectively.

### Block Averaging

Averaging over the native-space ROI voxels, mean CBF and BOLD time-series were produced for each of the five ROI's. GM, OL and PG ROI's were determined from a standard atlas and functional ROI's in visual cortex (fVC) and motor cortex



(fMC) were determined by the functional localiser as described above. For each ROI, relative CBF signal time-series normalised by baseline ( $\frac{CBF}{CBF_0}$ ) and BOLD signal time-series normalised by baseline ( $\frac{\Delta S}{S_0}$ ) were block averaged. Baseline was calculated by taking the 10<sup>th</sup> percentile CBF and BOLD values from the ROI time-series. Block-averaging was conducted to produce fewer time-points with higher SNR. This was particularly beneficial when fitting the BOLD signal model to the CBF time-series. Block averaging also excluded time-points that were considered to be in transition by only including CBF and BOLD time-points that were considered to have reached steady state. For the interleaved design block averaging periods were calculated for each final 30 second period of each 60 second respiratory block (normocapnia with normoxia and normocapnia with hyperoxia) and 120 seconds of each 150 second block (hypercapnia with normoxia). The final 30 second period of each 60 second respiratory block was used when block averaging the simultaneous design. The mean arterial oxygen content,  $C_aO_2$ , was calculated from the  $P_{ET}O_2$  data for the same time periods.

### Absolute CMRO<sub>2</sub> Quantification

The BOLD model described in *Wise et al.* [3] was fitted to the global GM and regional data using a simple bayesian framework (written in house using Matlab (MathWorks Inc., Natick, MA)) to yield estimates of M and  $S_vO_2$  (interleaved design) and M,  $S_vO_2$ ,  $\alpha$  and  $\beta$  (simultaneous design) for each of the baseline and elevated baseline conditions. Where  $\alpha$  and  $\beta$  were held constant, M and  $S_vO_2$  fitting was repeated for two combinations of previously used  $\alpha$  and  $\beta$ :  $(\alpha, \beta) = (0.38 [50], 1.5 [45])$  and  $(0.14, 0.91 [85])$ . Priors for M and  $S_vO_2$  were generated as

normal probability density functions centred around initial estimates of 0.08 and 0.5 with broad standard deviations of 0.02 and 0.1. When fitting for  $M$ ,  $S_vO_2$ ,  $\alpha$  and  $\beta$  normal probability density functions centred around initial estimates of 0.3 and 1.4 with standard deviations of 0.1 and 0.2 were used as priors for  $\alpha$  and  $\beta$ . By applying Bayes' rule to the first time points of averaged data  $\frac{\Delta S}{S_0}$ ,  $\frac{CBF}{CBF_0}$  and  $C_aO_2$ , posterior probability distributions of the variables,  $[M \text{ and } S_vO_2]$  and  $[M, S_vO_2, \alpha \text{ and } \beta]$ , were generated after integrating over the ranges 0.01 – 0.15 ( $M$ ), 0.2 – 0.8 ( $S_vO_2$ ), 0.1 – 0.5 ( $\alpha$ ) and 0.8 – 2.0 ( $\beta$ ). These were chosen to be beyond the extremes of physiologically plausible values. The posterior distributions were used as the priors for calculations with the second time points of averaged data and so on until a final posterior distribution for each of the two variables was obtained. The maxima of these probability distribution functions provided the estimates of  $M$  and  $S_vO_2$  and  $M, S_vO_2, \alpha$  and  $\beta$  for each subject. Absolute  $CMRO_2$  was then calculated using the equation:

$$CMRO_2 = (1 - S_vO_2) \cdot CBF \cdot C_aO_2 \quad (4.1)$$

.

### Statistical Testing

Testing for significant group increases between baseline (non-stimulated) and elevated baseline (continuously stimulated) were performed in the structural and functional ROI's for CBF,  $S_vO_2$  and  $CMRO_2$  using one-tailed, paired t-tests. *3dtttest++* [74] was used to test for significant regional differences between baseline

and elevated baseline M, CBF,  $S_vO_2$  and  $CMRO_2$ . This was achieved by registering the individual whole brain parameter maps of M, CBF,  $S_vO_2$  and  $CMRO_2$  to MNI152 space [76] through the hi-resolution structural image using FLIRT.

## 4.3 Results

The number of task related voxels identified by the functional localiser in the visual and motor cortex used to make the fVC and fMC ROI's for both the interleaved and simultaneous sessions are shown in Figure 4.4. Group mean number of voxels localised for the interleaved design in visual and motor tasks are  $366 \pm 284$  and  $658 \pm 544$  and for the simultaneous design in visual and motor are  $647 \pm 322$  and  $714 \pm 770$ .

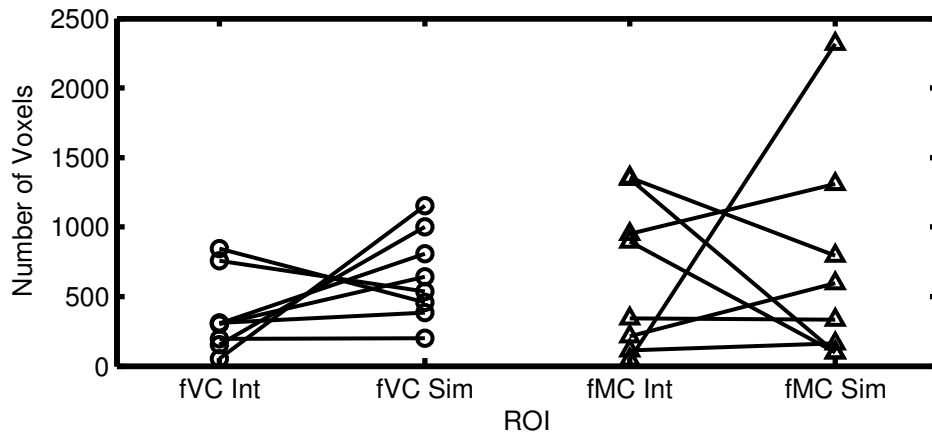


Figure 4.4: Details of the number of voxels identified by the functional localiser to create the fVC and fMC ROI's in the interleaved (Int) and simultaneous (Sim) dcfMRI sessions. Each point represents a single subject. A line connects the corresponding interleaved and simultaneous ROI voxel count for that subject ( $N = 8$ ).

By estimating  $S_vO_2$  and measuring CBF and  $C_aO_2$ , estimates of absolute  $CMRO_2$  were made using Equation 4.1 on all 8 subjects for both respiratory designs.

Measurements of CBF, M,  $S_vO_2$  and consequently  $CMRO_2$  were made in the five regions of interest detailed above at baseline and elevated baseline for both the interleaved and simultaneous design.

Tables 4.1 ( $\alpha = 0.38, \beta = 1.5$ ) and 4.2 ( $\alpha = 0.14, \beta = 0.91$ ) show estimates of M and  $S_vO_2$  made using different combinations of  $\alpha$  and  $\beta$  values present in the literature for the interleaved respiratory design. Significant differences between baseline and elevated baseline CBF were found in OL, fVC and fMC and are marked with (\*). No significant differences were found between baseline and elevated baseline measures of the remaining parameters.

Table 4.3 shows estimates of M,  $S_vO_2$ ,  $\alpha$  and  $\beta$  for the simultaneous respiratory designs again for the five ROI's. Significant differences between baseline and elevated baseline CBF were found in OL, fVC, PG and fMC and are again marked with (\*). Significant increases in  $CMRO_2$  were detected in the functionally localised visual and motor ROI's.

Figure 4.5 shows group averaged, whole brain parameter maps of CBF, M,  $S_vO_2$  and  $CMRO_2$  in standard space at baseline and elevated baseline for the interleaved design. Figure 4.6 shows the equivalent whole brain parameter maps for the simultaneous design of CBF, M,  $S_vO_2$  and  $CMRO_2$  with the addition of  $\alpha$  and  $\beta$ . These whole brain maps were produced by performing the analysis routine described in

ROI		CBF (ml/100g/min)	M	S <sub>v</sub> O <sub>2</sub>	$\alpha$	$\beta$	CMRO <sub>2</sub> ( $\mu$ mol/100g/min)
GM	-Rest	51.8 $\pm$ 7.7	0.035 $\pm$ 0.013	0.53 $\pm$ 0.18	0.38	1.50	196.1 $\pm$ 85.6
	-Task	53.6 $\pm$ 5.3	0.032 $\pm$ 0.010	0.60 $\pm$ 0.13			169.6 $\pm$ 54.7
OL	-Rest	56.7 $\pm$ 8.7	0.032 $\pm$ 0.014	0.53 $\pm$ 0.09			209.7 $\pm$ 46.2
	-Task	64.2 $\pm$ 9.5*	0.030 $\pm$ 0.010	0.55 $\pm$ 0.09			222.5 $\pm$ 37.1
fVC	-Rest	62.3 $\pm$ 11.9	0.045 $\pm$ 0.010	0.50 $\pm$ 0.07			247.8 $\pm$ 58.6
	-Task	84.0 $\pm$ 18.5*	0.036 $\pm$ 0.003	0.58 $\pm$ 0.17			265.3 $\pm$ 83.6
PG	-Rest	45.9 $\pm$ 8.4	0.024 $\pm$ 0.016	0.59 $\pm$ 0.20			152.6 $\pm$ 85.7
	-Task	48.1 $\pm$ 7.1	0.024 $\pm$ 0.014	0.60 $\pm$ 0.20			154.3 $\pm$ 84.6
fMC	-Rest	46.7 $\pm$ 18.8	0.026 $\pm$ 0.023	0.58 $\pm$ 0.14			142.4 $\pm$ 61.4
	-Task	62.3 $\pm$ 9.5*	0.025 $\pm$ 0.010	0.70 $\pm$ 0.17			143.9 $\pm$ 73.6

Table 4.1: Interleaved design, estimating M and S<sub>v</sub>O<sub>2</sub> with traditional ( $\alpha=0.38$ ,  $\beta=1.5$ )  $\alpha$  and  $\beta$  values. \* indicates significant difference,  $p<0.05$ , between baseline (rest) and elevated baseline (task) conditions. This was tested for all ROI's for CBF, S<sub>v</sub>O<sub>2</sub> and CMRO<sub>2</sub>

ROI		CBF (ml/100g/min)	M	S <sub>v</sub> O <sub>2</sub>	$\alpha$	$\beta$	CMRO <sub>2</sub> ( $\mu$ mol/100g/min)
GM	-Rest	51.8 $\pm$ 7.7	0.050 $\pm$ 0.017	0.55 $\pm$ 0.17	0.14	0.91	187.5 $\pm$ 79.4
	-Task	53.6 $\pm$ 5.3	0.046 $\pm$ 0.013	0.61 $\pm$ 0.12			164.6 $\pm$ 50.7
OL	-Rest	56.7 $\pm$ 8.7	0.045 $\pm$ 0.020	0.53 $\pm$ 0.09			207.7 $\pm$ 41.4
	-Task	64.2 $\pm$ 9.5*	0.043 $\pm$ 0.014	0.56 $\pm$ 0.09			218.9 $\pm$ 36.0
fVC	-Rest	62.3 $\pm$ 11.9	0.062 $\pm$ 0.013	0.51 $\pm$ 0.07			243.4 $\pm$ 57.9
	-Task	84.0 $\pm$ 18.5*	0.051 $\pm$ 0.005	0.60 $\pm$ 0.18			253.5 $\pm$ 83.6
PG	-Rest	45.9 $\pm$ 8.4	0.034 $\pm$ 0.023	0.59 $\pm$ 0.20			153.2 $\pm$ 84.3
	-Task	48.1 $\pm$ 7.1	0.034 $\pm$ 0.019	0.62 $\pm$ 0.19			147.0 $\pm$ 77.5
fMC	-Rest	46.7 $\pm$ 18.8	0.035 $\pm$ 0.031	0.58 $\pm$ 0.13			140.8 $\pm$ 54.0
	-Task	62.3 $\pm$ 9.5*	0.036 $\pm$ 0.014	0.70 $\pm$ 0.17			140.6 $\pm$ 74.0

Table 4.2: Interleaved design, estimating M and S<sub>v</sub>O<sub>2</sub> with updated( $\alpha=0.14$ ,  $\beta=0.91$ )  $\alpha$  and  $\beta$  values. \* indicates significant difference,  $p<0.05$ , between baseline (rest) and elevated baseline (task) conditions. This was tested for all ROI's for CBF, S<sub>v</sub>O<sub>2</sub> and CMRO<sub>2</sub>

ROI		CBF (ml/100g/min)	M	S <sub>v</sub> O <sub>2</sub>	$\alpha$	$\beta$	CMRO <sub>2</sub> ( $\mu$ mol/100g/min)
GM	-Rest	49.6 $\pm$ 10.2	0.070 $\pm$ 0.019	0.64 $\pm$ 0.11	0.450 $\pm$ 0.117	0.92 $\pm$ 0.27	137.7 $\pm$ 38.0
	-Task	52.4 $\pm$ 11.0	0.064 $\pm$ 0.022	0.67 $\pm$ 0.11	0.442 $\pm$ 0.109	1.04 $\pm$ 0.19	139.8 $\pm$ 55.9
OL	-Rest	54.1 $\pm$ 10.6	0.064 $\pm$ 0.025	0.64 $\pm$ 0.12	0.458 $\pm$ 0.112	1.00 $\pm$ 0.24	152.5 $\pm$ 40.4
	-Task	63.8 $\pm$ 16.1 *	0.066 $\pm$ 0.026	0.69 $\pm$ 0.08	0.467 $\pm$ 0.062	1.06 $\pm$ 0.29	159.3 $\pm$ 59.3
fVC	-Rest	57.2 $\pm$ 13.1	0.074 $\pm$ 0.024	0.65 $\pm$ 0.11	0.492 $\pm$ 0.097	0.94 $\pm$ 0.22	152.0 $\pm$ 26.0
	-Task	79.3 $\pm$ 21.0 *	0.080 $\pm$ 0.017	0.65 $\pm$ 0.08	0.417 $\pm$ 0.099	1.00 $\pm$ 0.27	213.9 $\pm$ 43.2*
PG	-Rest	43.6 $\pm$ 10.7	0.074 $\pm$ 0.023	0.64 $\pm$ 0.08	0.533 $\pm$ 0.094	0.83 $\pm$ 0.22	121.8 $\pm$ 31.1
	-Task	47.0 $\pm$ 11.0 *	0.062 $\pm$ 0.025	0.70 $\pm$ 0.08	0.517 $\pm$ 0.099	0.98 $\pm$ 0.24	116.5 $\pm$ 51.8
fMC	-Rest	39.7 $\pm$ 14.3	0.076 $\pm$ 0.041	0.66 $\pm$ 0.13	0.517 $\pm$ 0.093	0.75 $\pm$ 0.22	104.4 $\pm$ 45.5
	-Task	59.0 $\pm$ 18.1 *	0.076 $\pm$ 0.029	0.68 $\pm$ 0.08	0.475 $\pm$ 0.079	0.88 $\pm$ 0.26	148.9 $\pm$ 61.3*

Table 4.3: Simultaneous design, fitting for M, S<sub>v</sub>O<sub>2</sub>,  $\alpha$  and  $\beta$ . \* indicates significant difference, p<0.05, between baseline (rest) and elevated baseline (task) conditions. This was tested for all ROI's for CBF, S<sub>v</sub>O<sub>2</sub> and CMRO<sub>2</sub>

the Methods section on a voxel wise basis throughout the brain. Regional elevations in CBF and CMRO<sub>2</sub> are particularly evident in the visual cortex for both techniques.

T-statistic maps produced as a result of the voxelwise t-test analysis are presented in Figure 4.7 reflecting the ROI analysis presented in Tables 4.1, 4.2 and 4.3.

## 4.4 Discussion

In this study a noninvasive, dcfMRI protocol is used to produce absolute, whole brain measures of oxygen metabolism. A BOLD signal model [3] allows estimates of S<sub>v</sub>O<sub>2</sub> and in turn CMRO<sub>2</sub> to be made from perfusion and BOLD data acquired during a dual hypercapnic-hyperoxic challenge. A simple motor and visual task was used to regionally elevate oxygen metabolism to simulate a disease or treatment-like condition and demonstrate the ability of the technique to detect regional changes in baseline CMRO<sub>2</sub>. The implementation of interleaved and simultaneous hypercapnic-hyperoxic challenges allowed the optimisation of the respiratory manipulation to be investigated, at the same time assessing the protocol's ability to detect changes in other physiological parameters which may be affected by the altered metabolic state. Measurements using the interleaved respiratory manipulation are comparable in principal to the work shown by *Gauthier et al.* [2] and *Bulte et al.* [1] and both the interleaved and simultaneous designs are extensions of the work presented by *Wise et al.* [3].



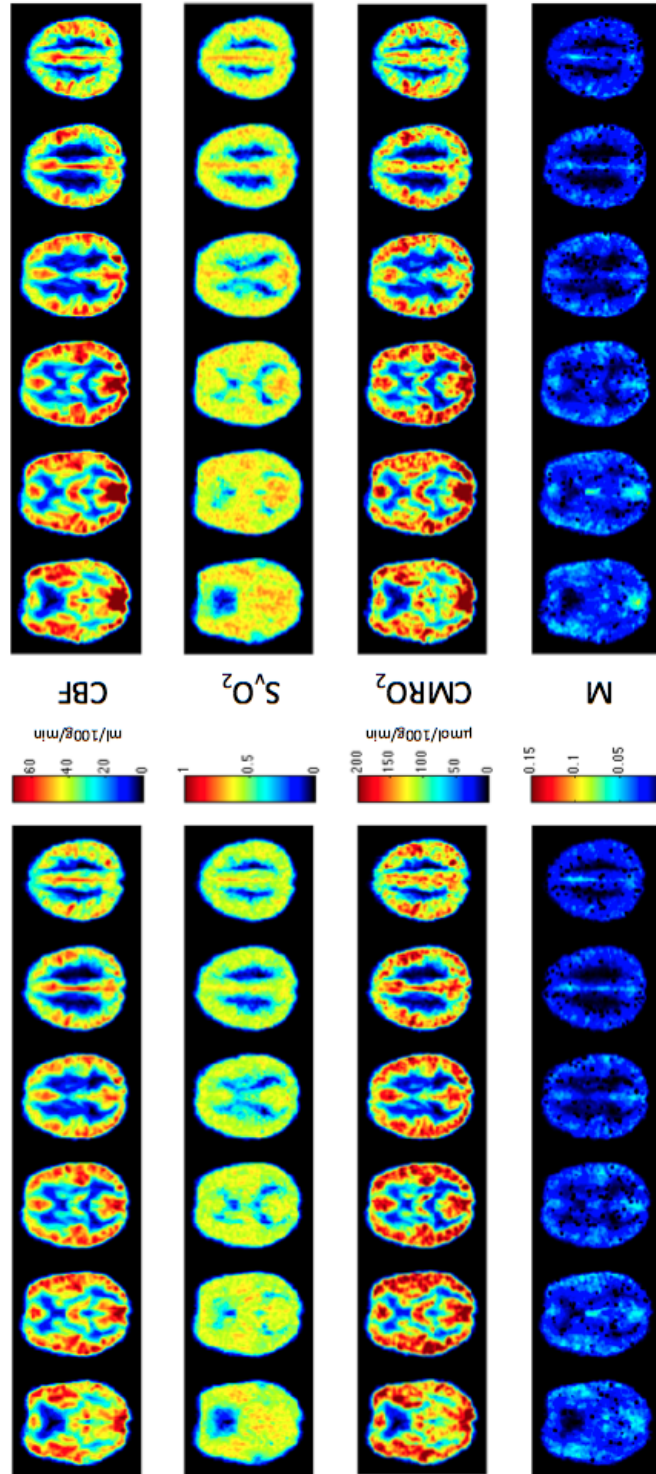


Figure 4.5: Group averaged, whole brain parameter maps acquired using interleaved hypercapnic-hyperoxic respiratory manipulations. Regional differences between baseline and elevated baseline can be clearly assessed due to good whole brain coverage. Measures are limited to grey matter as a result of limitations associated with measuring CBF in white matter using ASL.

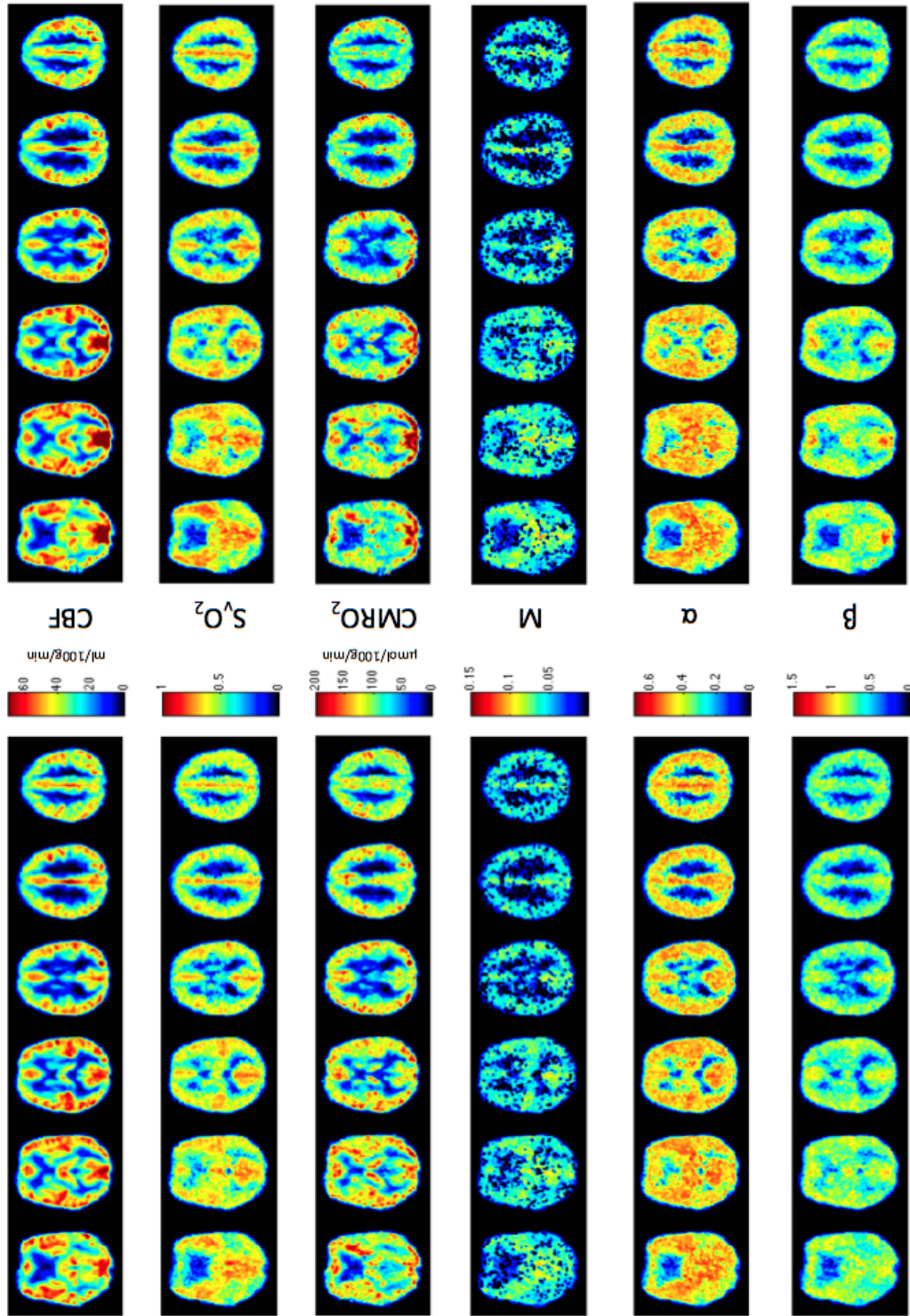


Figure 4.6: Whole brain parameter maps produced using simultaneous hypercapnic-hyperoxic respiratory manipulations. In addition to equivalent parameter maps to those shown in Figure 4.5, simultaneous respiratory manipulation allows for the estimation  $\alpha$  and  $\beta$

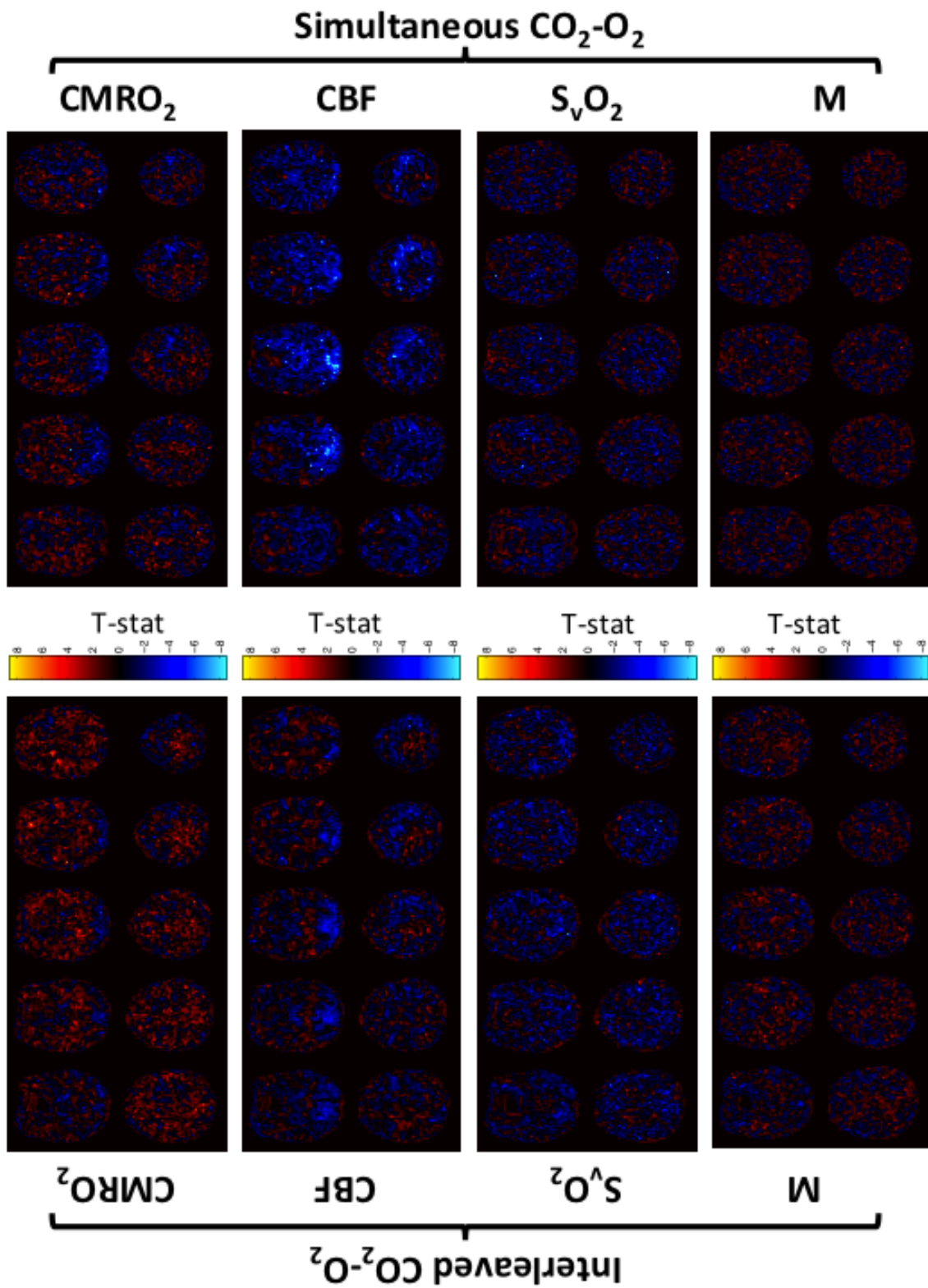


Figure 4.7: T-statistic maps produced as a result of the voxelwise, paired t-test analysis conducted between the baseline and elevated baseline parameter maps for both the interleaved and the simultaneous respiratory designs.

In all 8 subjects, consistent CBF baseline values in the predicted range were achieved across the group in both the rest and task conditions. Spatial variation of CBF values are consistent with literature [3]. In both scan sessions, OL demonstrated the highest regional CBF with respect to the regions measured,  $\sim 55$  ml/100g/min, with PG showing lowest,  $\sim 45$  ml/100g/min, and GM perfusion values of  $\sim 50$  ml/100g/min at rest.

Direct comparison of CMRO<sub>2</sub> measurements made in GM to values established with dcfMRI show the interleaved design,  $187.5 \pm 79.4$   $\mu$ mol/100g/min, overestimates resting CMRO<sub>2</sub> when compared to values reported by *Bulte et al.* [1],  $158 \pm 39$   $\mu$ mol/100g/min and *Gauthier et al.* [2],  $145 \pm 30$   $\mu$ mol/100g/min. CMRO<sub>2</sub> estimates made using simultaneous design agree well with ranges from PET literature of 128-149  $\mu$ mol/100g/min [17] (age and region dependent) and  $136 \pm 10$   $\mu$ mol/100g/min [19] in an older cohort. However it is important to note that the measurement is localised to GM as a result of limitations associated with using ASL to measure CBF. This coupled with the improved spatial resolution afforded by MRI and a relatively young cohort would lead to the expectation that the simultaneous CMRO<sub>2</sub> measures would be higher than those associated with PET.

M is the fractional, maximum BOLD signal change that can occur due to removing all deoxyhemoglobin from a given voxel and is a function of the amount of deoxyhemoglobin present in a given physiological state. Estimates of M made using the simultaneous design,  $0.070 \pm 0.019$ , agree well with established values in the range of 0.06 – 0.088 [46]. However, measures of M made using the interleaved design,  $0.050 \pm 0.017$  and  $0.035 \pm 0.013$ , seem low in comparison. It is interesting to

note the differences between  $M$  estimated using different combinations of  $\alpha$  and  $\beta$ . As these parameters are fixed in the interleaved model and changes in these fixed parameters result in different estimated  $M$ 's, this would suggest that there is some collinearity between  $M$  and  $\alpha$  and  $\beta$ .

At rest, arterial blood is nearly fully oxygenated with approximately 40% of the oxygen extracted during its transit across the capillary bed [86, 87]. Venous oxygenation saturation ( $S_vO_2$ ) represents the amount of oxygen remaining in the blood after it has passed through the capillaries into the venous vasculature. Assuming arterial blood is fully saturated,  $S_vO_2$  is equivalent to  $1 - OEF$ . Therefore  $S_vO_2$  values in the range of 0.55–0.65 are expected in GM. Measures of  $S_vO_2$  using the interleaved,  $0.55 \pm 0.17$ , and simultaneous design,  $0.64 \pm 0.11$ , are within the acceptable range of estimates but at opposite ends of the spectrum. The estimates of  $S_vO_2$  using the interleaved design lead to measures of  $CMRO_2$  that are considered high for GM ( $\sim 200 \mu\text{mol}/100\text{g}/\text{min}$ ). The simultaneous design leads to more agreeable estimates of  $S_vO_2$  and  $CMRO_2$  in GM. This is probably due to the extra degrees of freedom available to the simultaneous design for measuring  $\alpha$  and  $\beta$ . It is important to note that unrealistic parameter estimates of  $M$ ,  $S_vO_2$ ,  $\alpha$  and  $\beta$  were produced when trying to fit for all four parameters using the interleaved design (results not presented here). This is due to the lack of information provided by the single hypercapnic modulation, meaning  $\alpha$  and  $\beta$  cannot be properly determined by the BOLD signal model. As a result, the most likely explanation for the difference between the  $S_vO_2$  values, produced by the interleaved and simultaneous designs, is that the extra degrees of freedom used in the simultaneous design not only allow  $\alpha$  and  $\beta$  to be measured, but also capture some other sources of vari-

ation. These sources of variation are not accounted for in the interleaved model where  $\alpha$  and  $\beta$  are fixed

In a given brain region, it is changes in CBF and OEF that dictate the extent of the BOLD signal. In an activated brain region where CMRO<sub>2</sub> increases, it is expected that increases in S<sub>v</sub>O<sub>2</sub> and CBF also accompany a rise in metabolic demand when compared to the same region at rest. No significant changes were detected for CMRO<sub>2</sub> in the functional ROI's between rest and task conditions for the interleaved design. Significant changes ( $p < 0.05$ ) were detected between baseline and elevated baseline conditions in the visual and motor cortex using the simultaneous design. In the visual cortex a group average increase in CMRO<sub>2</sub> of 61.9  $\mu\text{mol}/100\text{g}/\text{min}$  (40%) with task accompanied a significant increase of 22.1 ml/100g/min (38.5%) in CBF. A significant increase in CMRO<sub>2</sub> of 44.5  $\mu\text{mol}/100\text{g}/\text{min}$  (43%) and CBF of 19.3 ml/100g/min (49%) in the motor cortex was detected with task. Percentage CMRO<sub>2</sub> increases in the visual and motor cortex are larger than expected when compared with calibrated BOLD studies, usually  $\sim 30\%$  [45] and  $\sim 25\%$  [88] respectively. The larger than expected CMRO<sub>2</sub> responses may be due to the constant duration and combined nature of the task coupled with the strength of the flashing checkerboard. The significant regional changes detected using the simultaneous design may again be due to the extra degrees of freedom afforded by this approach.

As previously discussed, the simultaneous approach not only allows  $\alpha$  and  $\beta$  to be measured, but the extra degrees of freedom may allow other sources of variation to be captured. This may make the simultaneous approach more sensitive to detecting changes in CMRO<sub>2</sub> by allowing the BOLD signal model to correctly



deal with changes in  $\alpha$ ,  $\beta$  or other variations that may accompany the regional changes in metabolism. No significant changes in  $S_vO_2$  were detected in either functional ROI suggesting that task related increases in  $CMRO_2$  are mainly driven by increased CBF. This may be because the biological changes in OEF are small compared to the changes in CBF and the proposed technique does not have the required sensitivity to detect such small changes.

The ratio of the fractional changes with activation between CBF and  $CMRO_2$  is often referred to as the coupling of these two terms and can be defined as  $n = (\frac{\Delta CBF\%}{\Delta CMRO_2\%})$ . Calibrated BOLD studies have reported  $n$  in the range of 1.7 - 4.5 for cortical regions including the motor and visual cortex. In the functionally defined ROI's, the simultaneous design produces values of  $n \approx 1$ . These coupling values measured in the functional ROI's are lower than that currently established in literature for similar tasks and are not surprising as we do not detect significant group differences between rest and task  $S_vO_2$  estimates with very small if any group average differences calculated. This would again suggest that  $CMRO_2$  changes with task are mostly CBF driven and the technique requires improvements in sensitivity or a larger cohort of subjects to detect the small changes in  $S_vO_2$  that may occur with the tasks used in this experiment.

For the interleaved design, slightly lower variability in  $CMRO_2$  across subjects was demonstrated for  $\alpha, \beta = 0.14, 0.91$  with estimates of  $M$  and  $S_vO_2$  that are more agreeable with literature produced when compared to estimates made using  $\alpha, \beta = 0.38, 1.5$ . As such values of  $\alpha, \beta = 0.14, 0.91$  are used in the following Chapters when values of  $\alpha$  and  $\beta$  are assumed. However parameter estimates did not change drastically when using these different  $\alpha, \beta$  combinations. The largest differences

in  $\text{CMRO}_2$  found between the two  $\alpha$ ,  $\beta$  combinations were  $\sim 5\%$  found in global GM.

By simultaneously varying arterial concentrations of carbon dioxide and oxygen, the BOLD signal model was exploited to produce estimates of  $\alpha$  and  $\beta$  as well as  $M$  and  $S_v\text{O}_2$ . Interpreting the simultaneous hypercapnic-hyperoxic data using the BOLD signal model leads to estimates of  $\alpha=0.45\pm0.12$  and  $\beta=0.92\pm0.27$  for whole brain GM at rest. The traditional combination of  $\alpha = 0.38$  and  $\beta = 1.5$  were proposed by [50] and [45].  $\alpha$  was originally measured by altering inspired  $\text{CO}_2$  in monkeys and measuring global changes in flow and volume, whereas  $\beta$  was based on approximations made using Monte Carlo simulations of a BOLD signal model. More recently, *Griffeth et al.* [85] proposed a new combination of values,  $\alpha=0.14$  and  $\beta=0.91$ , based on the optimisation of the exponents in relation to a complex, compartmental BOLD model for a range of BOLD and CBF signal changes. However, these comparisons with a complex signal model suggest  $\alpha$  and  $\beta$  potentially lose their original physiological meanings as intended in the Davis model. Instead,  $\alpha$  and  $\beta$  are effectively capturing several sources of variation arising in the detailed model, and they should just be regarded as fitting parameters. It is therefore difficult to make a physical interpretation of the  $\alpha$  and  $\beta$  values presented in Table 4.3. The main focus should instead be on the fact that the simultaneous design allows a certain degree of flexibility by allowing the  $\alpha$  and  $\beta$  terms to be determined through the model. This is advantageous as these exponential terms may take account of a number of underlying physiological processes which the BOLD signal model cannot take into account when  $\alpha$  and  $\beta$  are fixed. This allows for changes in these underlying, unknown effects due to



altered states of activation, disease or treatment to be accounted for by adding an additional degree of freedom. However as estimating these parameters may not have a direct physiological interpretation there may be room for optimisation of the BOLD signal model presented in *Wise et al.* [3].

The group averaged, whole brain parameter maps presented in Figures 4.5 and 4.6 demonstrates the potential of this technique to detect regional, localised changes in physiological parameters. Increases in  $\text{CMRO}_2$  can be seen in visual cortex between baseline and elevated baseline images in both Figures 4.5 and 4.6. To investigate this further groupwise T-statistic maps are shown in Figure 4.7. For both the interleaved and simultaneous designs, differences in the visual and motor cortex can be seen in the  $\text{CMRO}_2$  T-statistic maps as regions of blue and with differences more evident in the simultaneous design. On visual inspection of the CBF and  $\text{S}_v\text{O}_2$  T-statistic maps it is interesting to note that the task related changes detected in  $\text{CMRO}_2$  seem to be driven by CBF and that larger more significant task related group changes were detected in visual and motor cortex with the simultaneous design. There does not appear to be a strong group, regional change in  $\text{S}_v\text{O}_2$  detected with either technique. The T-statistic maps demonstrate the ability of this technique to provide detailed regional information about changes in cerebral metabolism and related haemodynamic parameters which reflect the ROI analysis presented in Tables 4.1, 4.2 and 4.3.

## 4.5 Conclusion

We have demonstrated the use of an absolute CMRO<sub>2</sub> quantification routine by implementing a dual hypercapnic-hyperoxic manipulation during which BOLD and CBF time courses are measured. When compared to an interleaved respiratory manipulation, a simultaneous approach is capable of detecting significant regional alterations in absolute CMRO<sub>2</sub> (induced using sensory and motor stimulus of the visual and motor cortex respectively) that produces agreeable estimates of CMRO<sub>2</sub> in global grey matter compared with a range of established values. The technique also circumvents the complication of pre-allocating values to the exponents of the BOLD signal model,  $\alpha$  and  $\beta$ , by allowing them to be made using the signal model and simultaneous hypercapnic-hyperoxic manipulation. The ability to infer absolute measures of CMRO<sub>2</sub> using fMRI-based methods increases the potential of fMRI to quantify an important clinical biomarker that is implicated in numerous neurological diseases and, at the same time, can improve our understanding of metabolic processes in the brain. However, in order for this technique to become clinically relevant, it is important to make the measure as robust as possible. This requires the investigation of within and between session reproducibility and repeatability which is the subject of the following chapters.

## Chapter 5

# Test-Retest Repeatability of Dual Calibrated fMRI Measures of Oxygen Metabolism in the Brain.

### 5.1 Introduction

The brain requires an uninterrupted supply of oxygen in order to extract the energy it needs from glucose. The rate at which oxygen is consumed in the brain to produce this energy is referred to as the cerebral metabolic rate of oxygen consumption ( $\text{CMRO}_2$ ).  $\text{CMRO}_2$  can be related to oxygen concentration levels in blood, cerebral blood flow (CBF) and oxygen extraction fraction (OEF) and therefore can be measured if these parameters are known.  $\text{CMRO}_2$  can become altered due to activation, disease and drug related interventions and is therefore a good indicator of cerebral health. This makes  $\text{CMRO}_2$  a desirable biomarker to quantify and map in the human brain.

An established class of PET techniques using oxygen isotopes ( $^{15}\text{O}$ ) [19] are currently considered the gold standard for producing whole brain, oxygen metabolism maps. However these techniques are invasive and expose the subject to a radiation

dose meaning they are not ideal for conducting longitudinal tracking of cerebral metabolic variables.

Recently, dual calibrated FMRI (dcFMRI) has been demonstrated as being capable of producing whole brain maps of absolute CMRO<sub>2</sub> by measuring venous oxygen saturation, S<sub>v</sub>O<sub>2</sub>, cerebral blood flow (CBF) and maximum BOLD signal change, M [1–3]. The measurement relies on detecting CBF and BOLD signal changes made during a dual respiratory manipulation, using arterial spin labelling (ASL). The induced signal changes are interpreted using a BOLD signal model. The dual respiratory manipulation involves increasing levels of inspired carbon dioxide (CO<sub>2</sub>) and oxygen (O<sub>2</sub>), inducing hypercapnia and hyperoxia respectively. These calibrated FMRI techniques are therefore an extension of the methods introduced by *Davis et al.* and *Chiarelli et al.* [45, 46]. The BOLD signal model used for the absolute quantification of CMRO<sub>2</sub> is an amalgamation of the models presented in these studies and can be found in [3]. dcFMRI has the potential to become a robust clinical and research tool. With no radiation burden attached this technique would lend itself to the longitudinal study and monitoring of metabolic changes in the brain associated with development and ageing, disease, trauma and drug efficacy and targeting.

However, before dcFMRI can be applied to longitudinally monitor metabolic changes in the brain, it is important that the test-retest repeatability of the technique is first assessed to understand the limitations of the technique. Test-retest repeatability studies have been conducted for <sup>15</sup>O PET [89, 90] and a recently introduced regional MR technique named TRUST (T<sub>2</sub>-relaxation-under-spin-tagging) [91]. The aim of this study is to establish reference data on the test-retest repeatability

of absolute  $\text{CMRO}_2$  measures made using dcfMRI. The test-retest repeatability of the CBF, M and  $\text{S}_v\text{O}_2$  measures allowing the calculation of  $\text{CMRO}_2$  will also be assessed. Two respiratory manipulation designs were compared, an interleaved hypercapnic-hyperoxic design and a simultaneous hypercapnic-hyperoxic design as presented in **Chapter 4**. Resting measures of oxygen metabolism related parameters made using dcfMRI were compared in a cohort of subjects for each technique, within session where subjects were scanned back-to-back with the same protocol and between session where resting measures were repeated on a separate scan day. This allowed the intrasession, intersession and intersubject variability to be investigated. The repeatability of the interleaved and simultaneous designs were compared by calculating intraclass correlation coefficient's (ICC's).

## 5.2 Methods

### 5.2.1 Participants

8 normal healthy participants (aged 24 - 39; mean age  $33.5 \pm 5.0$ ; 2 female) were recruited and scanned having given written consent. Experimental procedures were approved by the local institutional ethical review committee.

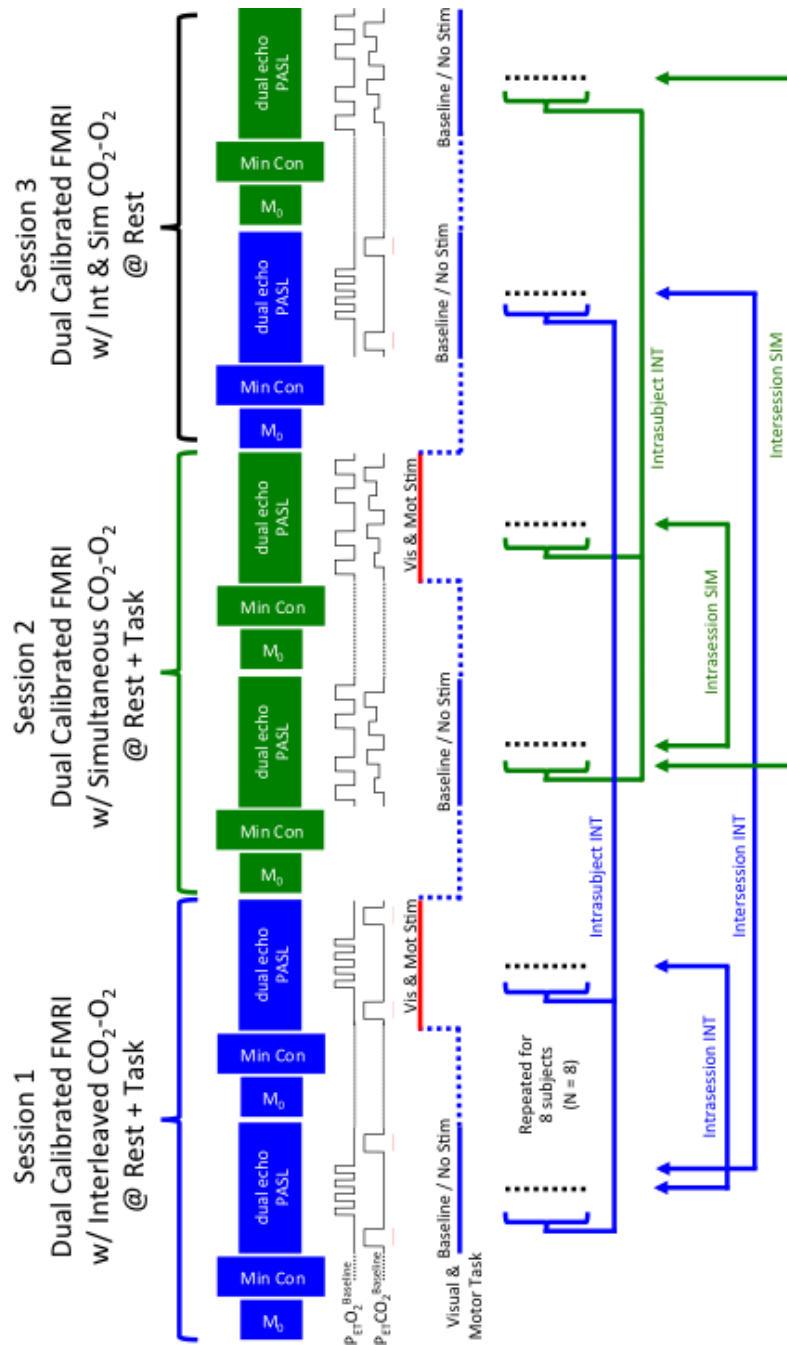


Figure 5.1: Schematic detailing the acquisition strategy used to investigate test-retest repeatability of physiological parameters measured using dcfMRI with interleaved and simultaneous respiratory manipulations. Calibration scans ( $M_0$  and Min Con) and dual echo PASL were acquired during respiratory manipulations in order to quantify oxygen metabolism related physiological parameters. Additional functional localisers acquired during Session 1 (interleaved) and Session 2 (simultaneous) are not shown in the schematic. Localisers were used to remove task related effects from the visual and motor stimulated scans to create a second "rest" scan for intrasession comparisons. Repeat rest measures of interleaved and simultaneous designs were conducted during Session 3. The bottom of the schematic details intrasession, intersession and intersubject groupings for the interleaved (blue) and simultaneous (green) designs.

### 5.2.2 MRI

Scanning was performed on a 3T GE HDx MRI (GE Healthcare, Milwaukee WI) with a body transmit coil and 8-channel head receive coil. All participants had previous whole brain  $T_1$ -weighted structural scans available (fast spoiled gradient recalled echo, 1x1x1 mm voxels,  $TI/TR/TE = 450/7.8/3$  ms). dcfMRI acquisitions lasted 18 minutes each. Details of the dual echo PASL protocol, including  $M_0$  and minimum contrast (Min Con) ASL calibration scans, used to simultaneously measure CBF and BOLD signal time-series during localiser and dcfMRI scans can be found in **Chapter 4** alongside details of the interleaved and simultaneous hypercapnic-hyperoxic respiratory manipulations.

### 5.2.3 Acquisition Overview

Each participant was scanned during three scanning sessions performed on separate days. Each session consisted of two dcfMRI acquisitions. In the first session a dcfMRI acquisition was performed using an interleaved hypercapnic-hyperoxic respiratory manipulation during rest and combined, continuous visual/motor stimulation. The second session was equivalent to the first apart from using a simultaneous hypercapnic-hyperoxic respiratory manipulation during the dcfMRI acquisition. A comparison of interleaved and simultaneous respiratory manipulations for the quantification of oxygen metabolism related parameters is demonstrated in **Chapter 4**. During the third session a repeat measure of the interleaved and simultaneous dcfMRI acquisition at rest was performed. During rest scans the participant was presented with a crosshair on a black background and instructed to

keep their eyes open. This allowed the baseline state of the physiological variables to be measured. During combined visual and motor stimulation the subject was presented with a continuous flashing checkerboard and finger tapping task corresponding to numbers between 1 and 4 presented on the screen. This allowed an elevated baseline state of the physiological variables to be measured in visual and motor cortex. During session 1 and 2 a functional localiser, lasting  $5\frac{1}{2}$  minutes, was used to create ROI's of activated voxels during visual and motor stimulation. This consisted of a 30 second baseline, 30 second motor stimulation and 30 second visual stimulation repeated three times ending with a baseline period. A schematic layout of the 3 scan sessions, excluding the functional localiser runs in session 1 and 2 can be seen in Figure 5.1.

To investigate test-retest repeatability all dcfMRI scans would ideally be conducted at rest. However a subset of the data (session 1 and 2) was used to investigate the sensitivity of dcfMRI for detecting regional changes in physiologic parameters. In an attempt to manufacture a second intrasession "rest" measure, processing steps described in Section 5.2.5 were performed to remove significantly activated voxels from the task datasets in sessions 1 and 2 as shown in Figure 5.1.

#### 5.2.4 Data Preprocessing

The image time-series produced by the dual-echo PASL sequence were motion corrected using *3dvolreg* [74]. Time-series image data acquired from the first echo of the PASL technique were used to calculate CBF, while the data from the second



echo were used to examine changes in BOLD signal. Interpolated surround subtraction of the ASL tag and control image time-series was performed to yield a perfusion-weighted time-series [43] which was corrected for coil sensitivity. CBF images were calculated using the  $M_0$  of blood, estimated from the cerebrospinal fluid signal of the  $M_0$  image and the general kinetic model (GKM) [33]. The CBF estimates were adjusted for the likely reduction of the  $T_1$  of arterial blood with increasing plasma concentration of paramagnetic  $O_2$ , according to the blood  $T_1$  values quoted in [51]. Interpolated surround averaging of the tag and control images was performed to yield a BOLD weighted time-series.

### 5.2.5 Regions of Interest (ROI's)

ROI's of global grey matter (GM) were produced using FAST segmentation [83] of the high resolution anatomical images. A second modified GM ROI was produced in an attempt to gain useful information about intrasession repeatability. This was done by removing voxels from GM that were deemed to respond significantly to the visual and motor tasks.

Two functional localisers were performed on each subject during session 1 and 2. The BOLD time-series acquired during each functional localiser task was fitted with baseline, drift and activation regressors using *3dDeconvolve* [74] in order to produce  $\beta$ -weight maps of visual and motor activation. All  $\beta$ -weight maps were registered to MNI152 space (Montreal Neurlogical Institute) [76] through the high-resolution structural image using FLIRT. *3dttest++* [74] was used to test on a voxel-wise basis whether the mean across the group significantly differed from zero.

This significance map was liberally thresholded at  $p = 0.01$  and was transformed back to the native space of the subject through the high-resolution anatomical image. This mask was then removed from the global GM mask to produce a mask of GM without task (GM-NoTask) and transformed to native space of the CBF and BOLD time-series.

### Quantification of Physiological Parameters

CBF and BOLD time-series were produced in GM and GM-NoTask ROI's for each subject. For each ROI's time-series, time averaged relative CBF ( $\frac{CBF}{CBF_0}$ ) and BOLD signal ( $\frac{\Delta S}{S_0}$ ) were block averaged. For the interleaved design block averaging periods were calculated for each final 30 second period of each 60 second respiratory block (normocapnia with normoxia and normocapnia with hyperoxia) and 120 seconds of each 150 second block (hypercapnia with normoxia). The final 30 second period of each 60 second respiratory block was used when block averaging the simultaneous design. The mean arterial oxygen content,  $C_aO_2$ , was calculated from the  $P_{ET}O_2$  data for the same time periods. The model described by *Wise et al.* [3] was fitted to the CBF and BOLD time-series using a simple bayesian framework to yield estimates of  $M$  and  $S_vO_2$  for the interleaved design and  $M$ ,  $S_vO_2$ ,  $\alpha$  and  $\beta$  for the simultaneous design. This was done in both the interleaved and simultaneous respiratory designs, permitting calculation of absolute  $CMRO_2$ . Where  $\alpha$  and  $\beta$  were held constant in the interleaved design,  $M$  and  $S_vO_2$  fitting was performed using  $\alpha, \beta = 0.14, 0.91$  [85]. Priors for  $M$  and  $S_vO_2$  were generated as normal probability density functions centred around initial estimates of 0.08 and 0.5 with broad standard deviations of 0.02 and 0.1. When fitting for  $M$ ,  $S_vO_2$ ,  $\alpha$  and  $\beta$

for the simultaneous design, normal probability density functions centred around initial estimates of 0.3 and 1.4 with standard deviations of 0.1 and 0.2 were used as priors for  $\alpha$  and  $\beta$  and the same priors were used for M and  $S_vO_2$  in the simultaneous design. By applying Bayes' rule to the first time points of averaged data  $\frac{\Delta S}{S_0}$ ,  $\frac{CBF}{CBF_0}$  and  $C_aO_2$ , posterior probability distributions of the variables M and  $S_vO_2$  (interleaved design) and M,  $S_vO_2$ ,  $\alpha$  and  $\beta$ , were generated after integrating over the ranges 0.01 – 0.15 (M), 0.2 – 0.8 ( $S_vO_2$ ) and 0.1 – 0.5 ( $\alpha$ ) and 0.8 – 2.0 ( $\beta$ ) where relevant in the simultaneous design. These were chosen to be beyond the extremes of physiologically plausible values. The posterior distributions were used as the priors for calculations with the second time points of averaged data and so on until a final posterior distribution for each of the two variables was obtained. The maxima of these probability distribution functions provided the estimates of M and  $S_vO_2$  for each subject. Assuming that arterial blood is fully saturated with oxygen, oxygen extraction fraction (OEF) =  $1 - S_vO_2$  and absolute  $CMRO_2$  can be calculated using the equation:

$$CMRO_2 = OEF \cdot CBF \cdot C_aO_2 \quad (5.1)$$

### 5.2.6 Statistical Analysis

#### Coefficients of variation

For dcfMRI acquisitions using both interleaved and simultaneous respiratory manipulations, intrasession, intersession and intersubject coefficients of variation

(CV) were calculated for M,  $S_vO_2$ , CBF and  $CMRO_2$  from the data collected in the three sessions as shown in Figure 5.1.

Intrasession CV was calculated as:

$$CV_{intrasession} = \frac{1}{N} \sum_n \frac{|M_{n1} - M_{n2}|}{\sqrt{2} \cdot Mean(M_{n1}, M_{n2})} \quad (5.2)$$

where  $M_{n1}$  and  $M_{n2}$  represent measurement #1 and #2 made in the same session for Subject #n ( $n = 1, 2 \dots, N$ ). When referring to interleaved dcfMRI this is calculated using the two measures made in Session 1 and when referring to simultaneous dcfMRI this refers to the two measures made in Session 2.

Intersession CV was calculated as:

$$CV_{intersession} = \frac{1}{N} \sum_n \frac{|M_{nk1} - M_{nk2}|}{\sqrt{2} \cdot Mean(M_{nk1}, M_{nk2})} \quad (5.3)$$

where  $M_{nk1}$  and  $M_{nk2}$  represent the rest measurements from separate sessions. In the case of the interleaved design this refers to rest measures made in Session 1 ( $k_1$ ) and 3 ( $k_2$ ) and for the simultaneous design this is the rest measures made in Session 2 ( $k_1$ ) and 3 ( $k_2$ ).

Intersubject CV was calculated as:

$$CV_{intersubject} = \frac{1}{N \cdot K} \sum_n \sum_{k=1,2,3} \frac{SD_n(M_{nk})}{Mean_n(M_{nk})} \quad (5.4)$$

where  $SD_n$  and  $Mean_n$  represent standard deviation and mean across subjects. These were calculated across all subjects for the relevant measures made in Sessions 1 ( $k_1, k_2$ ) and 3 ( $k_3$ ) for the interleaved design and Sessions 2 ( $k_1, k_2$ ) and 3 ( $k_3$ ) for the simultaneous design.

As presented by *Liu et al.* [91], the value of  $CV_{intersession}$  is expected to contain additional variance due to subject repositioning and day-to-day differences in physiological state compared to  $CV_{intrasession}$  and can be calculated as  $CV_{Day-to-Day} = \sqrt{CV_{intersession}^2 - CV_{intrasession}^2}$ . An additional confound in the case of this study is that intrasession measures compare a rest condition scan with a task condition scan. However as mentioned previously processing steps were taken to remove the influence of the task on the measure. Similarly, compared to  $CV_{intersession}$ ,  $CV_{intersubject}$  contains additional intersubject physiological differences and can be calculated as  $CV_{IntersubPhysiology} = \sqrt{CV_{intersubject}^2 - CV_{intersession}^2}$ .

### Intraclass Correlation

ICC's were used to assess the intra- and inter- session repeatability of measurements of M,  $S_vO_2$ , CBF and  $CMRO_2$  using the same groupings as described for the CV calculations for both interleaved and simultaneous hypercapnic-hyperoxic dcfMRI. There are multiple forms of the ICC. ICC(2,1) was chosen and its calculation is described in detail by *Shrout and Fleiss* [92]. ICC's reflect the ratio between the variability of measurement on the same subject (intra or inter - session in this case) and the total data variance across all subjects and all measurements. These comparisons were performed within technique, that is intra or inter - session for both the interleaved and simultaneous dual calibrated approaches.

## 5.3 Results

Eight participants were scanned during three sessions. Each session involved two dcfMRI acquisitions. This resulted in each subject having three dcfMRI acquisitions acquired using both the interleaved and the simultaneous respiratory manipulations.

### 5.3.1 Coefficients of Variation

Intrasession, intersession and intersubject CV's, calculated using Equations 5.2, 5.3 and 5.4, are presented for the measured physiological parameters in both global GM and GM-NoTask, Table 5.1. Lower CV's represent less variance in the measure with the interleaved design demonstrating lower CV's for intra and intersession CMRO<sub>2</sub> measures. In all cases inter subject variance is higher than intersession variance suggesting that the technique has sensitivity to detect intersubject differences.

### 5.3.2 Intraclass Correlation

Intrasession and intersession comparisons are presented in Figure 5.2 (GM) and 5.3 (GM-NoTask). ICC's are calculated for these relations and presented in Table 5.2 with the interleaved design demonstrating superior intra and intersession ICC's for all parameters except for CBF. ICC's of higher value represent better repeatability with values above 0.6 showing good repeatability.



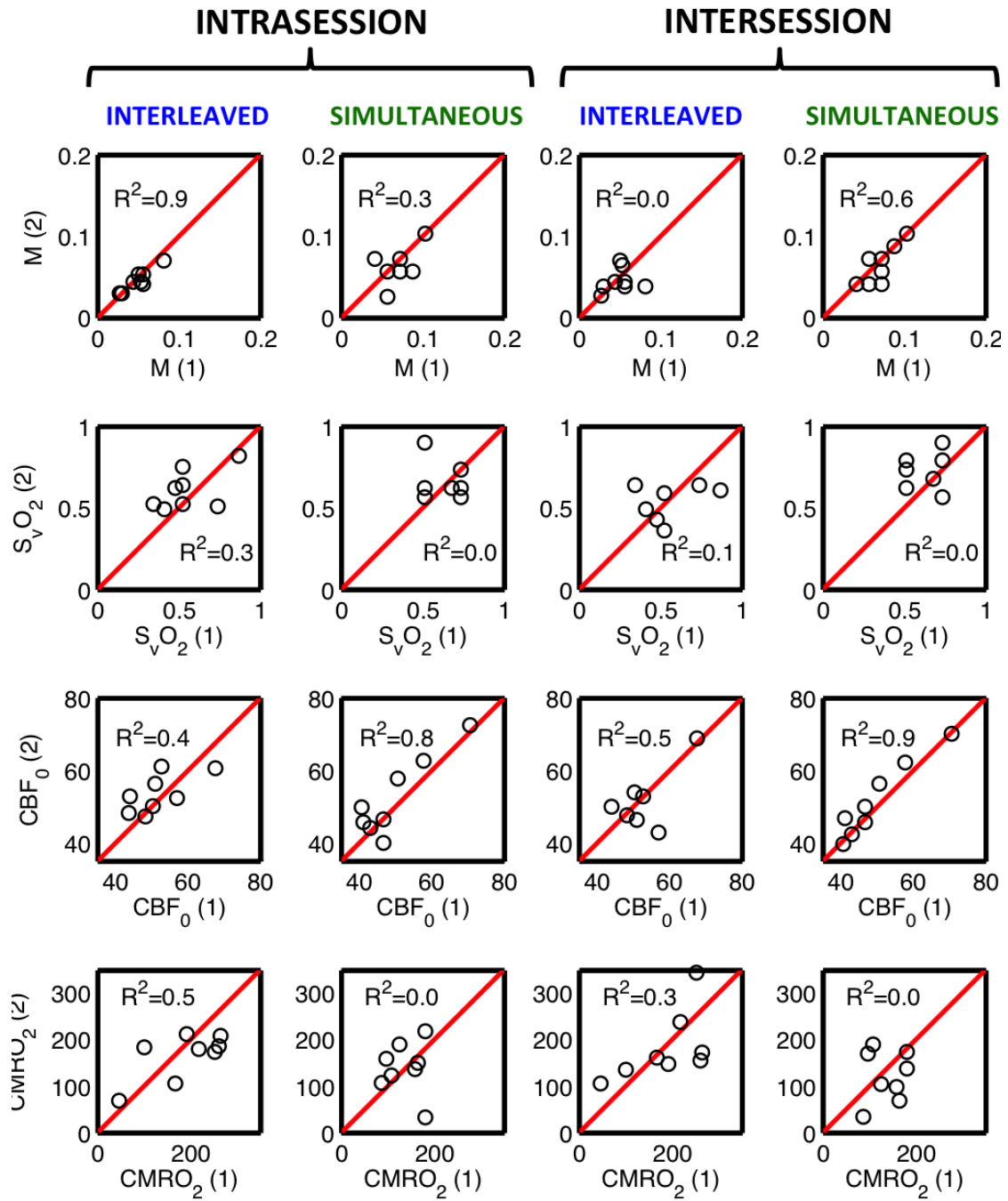


Figure 5.2: Scatterplots of measured physiological variables,  $M$ ,  $S_vO_2$ ,  $CBF$  and  $CMRO_2$  presented intra- and inter-session for both the interleaved and simultaneous dcfMRI acquisition. Scatterplots presented in this figure were produced using global GM ROI. ICC's describing the relations demonstrated in these plots are presented Table 5.2



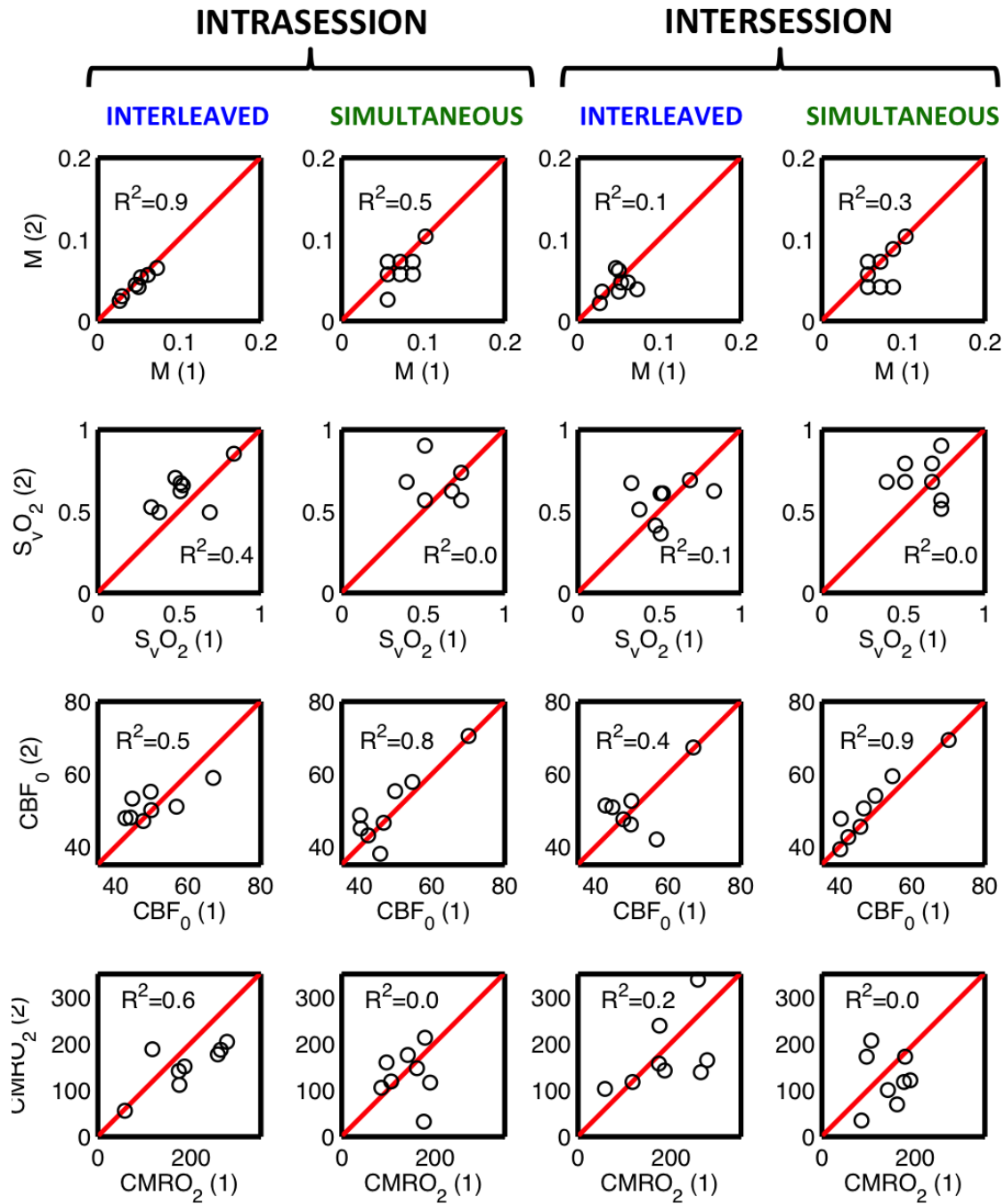


Figure 5.3: Scatterplots of measured physiological variables, M,  $S_vO_2$ , CBF and  $CMRO_2$  presented intra- and inter- session for both the interleaved and simultaneous dcfMRI acquisition. Scatterplots presented in this figure were produced using GM-NoTask ROI. ICC's describing the relations demonstrated in these plots are presented Table 5.2.

	Intrasession (ICC)		Intersession (ICC)	
	INT	SIM	INT	SIM
	<u>GM</u>			
M	0.90*	0.52	0.21	0.78*
$S_vO_2$	0.51	-0.16	0.26	-0.05
$CBF_{base}$	0.60*	0.89*	0.71*	0.96*
$CMRO_2$	0.62*	-0.02	0.58	0.10
	<u>GM-NoTask</u>			
M	0.97*	0.66*	0.36	0.52
$S_vO_2$	0.57	-0.18	0.25	-0.11
$CBF_{base}$	0.60*	0.88*	0.60*	0.95*
$CMRO_2$	0.68*	-0.01	0.50	0.01

Table 5.2: Intraclass correlation coefficient's (ICC) calculated intra- and intersession for the measured physiological variables, M,  $S_vO_2$ ,  $CBF$  and  $CMRO_2$ . ICC's are calculated for both GM and GM-NoTask ROI's and \*'s mark ICC's  $\geq 0.6$  (See Section 5.4.2 for information on interpreting ICC's).

## 5.4 Discussion

dcfMRI is a technique capable of producing whole-brain maps of  $CMRO_2$  as well as other physiological parameters associated with oxygen metabolism in the brain. It has been shown to produce similar estimates of  $CMRO_2$  when compared to other quantitative techniques and is sensitive to detecting regional changes in oxygen metabolism, [1–3] and **Chapter 4**. dcfMRI has the potential to provide a practical technique capable of implementation in clinical and research settings to investigate regional and longitudinal changes in  $CMRO_2$ . However before this technique can be implemented into such studies it is important to assess it's test-retest repeatability.

### 5.4.1 CV's

Intrasession, intersession and intersubject CV's are presented in Table 5.1 for both interleaved and simultaneous hypercapnic-hyperoxic dcfMRI using GM and GM-NoTask ROI's. Calculating the CV's in this manner provides an important reference for future studies. It also presents a useful comparison with other CMRO<sub>2</sub> measurement techniques which have investigated test-retest repeatability using these indices. These studies investigated test-retest repeatability of <sup>15</sup>O PET [89, 90] and a recently proposed MR protocol, TRUST [91]. For comparison with Table 5.1 a summary of CV's from these studies is presented in Table 5.3.

It can be seen that the CV's presented in this study are larger than those presented in Table 5.3. However as intersubject CV is greater than intersession CV in both cases the technique should have some sensitivity allowing it to determine differences between subjects taking into account intersession variability. dcfMRI also provides some distinct advantages over these techniques. TRUST is limited in terms of spatial resolution and only provides a whole brain measure. It therefore is not useful for investigating regional changes in oxygen metabolism. <sup>15</sup>O PET techniques are capable of producing whole brain maps of oxygen metabolism related parameters such as CMRO<sub>2</sub> but suffer from disadvantages associated with the use of radioisotopes. <sup>15</sup>O PET requires an on site cyclotron for the preparation of specialised radiotracers with a short half-life, is expensive to perform and invasive. Longitudinal studies of metabolism using PET are also limited as such studies require participants to receive multiple radiation doses.

	PET [89]	PET [90]	TRUST [91]
<u>OEF (%)</u>			
Intrasession CV	$5.7 \pm 4.4$	-	$3.2 \pm 1.2$
Intersession CV	-	9.3	$8.2 \pm 4.5$
Intersubject CV	$7.3 \pm 1.2$	21.4	15.6
<u>CBF (ml/100g/min)</u>			
Intrasession CV	$8.4 \pm 7.6$	-	$2.8 \pm 0.8$
Intersession CV	-	8.8	$7.4 \pm 3.0$
Intersubject CV	$13.5 \pm 1.4$	13.1	17.4
<u>CMRO<sub>2</sub> (<math>\mu</math>mol/100g/min)</u>			
Intrasession CV	$5.3 \pm 3.9$	-	$3.8 \pm 1.4$
Intersession CV	-	5.3	$6.6 \pm 1.6$
Intersubject CV	$12.8 \pm 1.1$	7.1	8.8

Table 5.3: Intrasession, intersession and intersubject CV's calculated in test-retest repeatability studies of quantitative oxygen metabolism techniques involving  $^{15}\text{O}$  PET [89,90] and MR TRUST [91]

### 5.4.2 ICC's

Variations on the dcfMRI, hypercapnic-hyperoxic respiratory manipulation used for absolute CMRO<sub>2</sub> quantification were introduced by *Wise et al.* [3]. The interleaved design performs hyperoxia during normocapnia and hypercapnia during normoxia whilst the simultaneous design concurrently varies levels of hypercapnia and hyperoxia as shown in Fig. 5.1 and described in more detail in **Chapter 4**. The simultaneous design also has the advantage of being able to measure values of  $\alpha$  and  $\beta$  which must be assumed when using the interleaved respiratory design, as discussed in **Chapter 4**.

To investigate if the type of respiratory manipulation used is advantageous in terms of repeatability, ICC's were calculated for the measured physiological parameters intrasession and intersession for both respiratory designs. For the interpretation of ICC's the stratification approach suggested by *Cicchetti et al.* [93] is considered. This proposed ICC groupings of poor (<0.4), fair (0.41-0.59), good (0.60-0.74) or excellent (>0.75) repeatability. This approach has previously been adopted by [94–96].

Considering the global GM and GM-NoTask ROI's, intrasession measures are more relevant for the GM-NoTask whereas intersession is most relevant in GM. GM-NoTask ROI is required for the intrasession comparison as one of the measurements is confounded by a task as shown in Figure 5.1 and the mask attempts to exclude regions engaged in the task. Both intersession measures were conducted at rest and therefore GM is appropriate for use here.

Intrasession, interleaved measurements of  $\text{CMRO}_2$  (GM-NoTask) are considerably more reproducible than simultaneous measurements which do not seem to have any appreciable correlation ( $\approx 0$ ). As  $\text{CMRO}_2$  is calculated from  $\text{S}_v\text{O}_2$  and CBF, these parameters also show high significant, or close to significant ICC's ( $p \approx 0.05$ ) when compared to the simultaneous approach. Comparing GM calculations to GM-NoTask, it is interesting to note that the measured ICC's generally increase slightly when the task is removed, as is expected intrasession, demonstrating that the task-related areas are confounding the results.

Intersession ICC's (GM) are better, in the case of the simultaneous design, than the intrasession ICC's. This is surprising, as intersession comparisons would be expected to contain extra sources of variance when compared to intrasession measures. It is a possibility that the intrasession comparisons, particularly in the case of the simultaneous design, are influenced by the presence of the task leading to the higher intrasession ICC's. For the interleaved design an expected decrease in ICC's is seen between intra and intersession except for the case of CBF. This may be due to the smaller ROI (reduced SNR) used to calculate the GM-NoTask.

The initial impression given by the ICC's, shown in Table 5.2, suggest that  $\text{S}_v\text{O}_2$  is considerably more reproducible using the interleaved design leading to more reproducible measures of  $\text{CMRO}_2$  at rest. However it is interesting to note that in **Chapter 4** the simultaneous design detected significant differences between baseline (rest) and elevated baseline states (continuous task) in visual and motor cortex for  $\text{CMRO}_2$  where the interleaved design did not. This might suggest that the interleaved design demonstrates higher repeatability due to the insensitivity of the technique to detect changes in  $\text{CMRO}_2$  possibly related to fixing the  $\alpha$  and

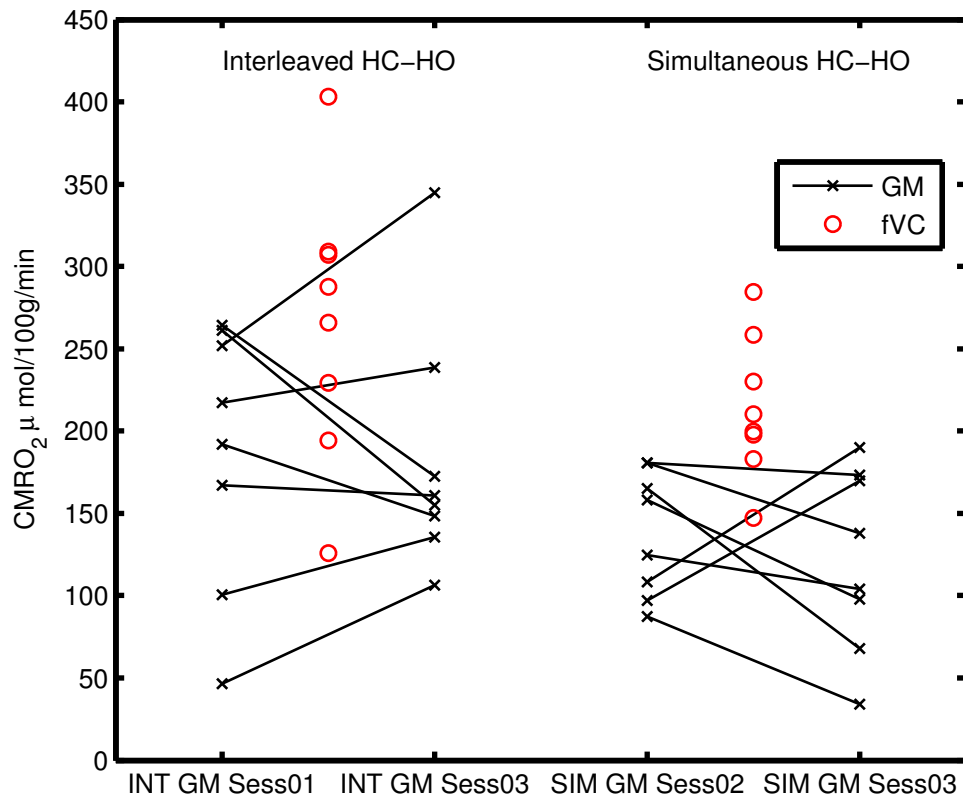


Figure 5.4: Difference between resting CMRO<sub>2</sub> measures made in global GM (Black) compared to elevated baseline CMRO<sub>2</sub> measures, from **Chapter 4**, that were functionally localised in the visual cortex (Red) for both the interleaved and simultaneous HC-HO design. This visually demonstrates the argument that the interleaved design has better repeatability (ICC) but may not be sensitive enough to detect changes in CMRO<sub>2</sub>, demonstrated by the overlap between GM and fVC measures. For the simultaneous design there is less overlap between GM and fVC and it is therefore more sensitive to detecting changes in CMRO<sub>2</sub>.

$\beta$  parameters. Figure 5.4 attempts to visualise this in terms of intersession resting CMRO<sub>2</sub> GM measures compared to the elevated baseline measures that were functionally localised to the visual cortex (made in **Chapter 4**). However, in order to thoroughly investigate this, a test-retest repeatability investigation of regional and global changes in oxygen metabolism would need to be conducted. This could be done by performing back to back baseline and elevated baseline dcfMRI measures, essentially repeating within session the experiment that was conducted in **Chapter 4**. This procedure would then be repeated on a separate scanning day allowing intrasession and intersession repeatability of baseline and elevated baseline measures to be assessed. This would allow the sensitivity of the techniques to detecting changes in absolute CMRO<sub>2</sub> to be assessed. The repeatability of the task itself must be investigated and the ideal elevated baseline paradigm may not necessarily be a continuous visual or motor task as used in **Chapter 4**.

It is also important to note that the sample size and number of repeat measurements used in this study is small. 8 subjects had 3 acquisitions of each type, interleaved and simultaneous, repeated once within session and once between session. A more thorough approach could be taken, similar to that used to investigate the test-retest repeatability of TRUST [91], where 7 subjects were scanned in 5 different sessions and within sessions were two repeats of the same measure. By increasing the number of subjects and/or the number of measurements a more rigorous characterisation of the distribution of measures intersubject, intra and inter-session would be provided.



## 5.5 Conclusion

Test-retest repeatability of dcfMRI using interleaved and simultaneous hypercapnic-hyperoxic respiratory manipulations was assessed by scanning 8 participants in three separate sessions. Each session consisted of two separate dcfMRI acquisitions. Intrasection, intersession and intersubject variation was determined for both interleaved and simultaneous designs and provides useful reference data for future studies. Physiological parameters measured at rest using interleaved and simultaneous designs were further compared for intrasection and intersession repeatability using ICC's. The interleaved design results in more reproducible measures of  $\text{CMRO}_2$ . However, questions remain over the sensitivity of the technique to detect changes in oxygen metabolism and associated parameters.

## Chapter 6

# Optimisation of Acquisition Time for a Dual Calibrated fMRI Protocol

## 6.1 Introduction

Dual calibrated fMRI (dcfMRI) is a promising technique capable of providing whole brain maps of absolute  $\text{CMRO}_2$  and related physiological variables. The technique is an extension of the calibrated BOLD methodology [45, 46] and uses a BOLD signal model to quantify baseline  $\text{S}_v\text{O}_2$  from induced changes in cerebral blood flow (CBF) and BOLD using combined hypercapnic and hyperoxic respiratory challenges. As dcfMRI is a recently introduced technique limited literature presenting its use is available. The duration and design of the hypercapnic-hyperoxic respiratory manipulations presented in these studies differ somewhat with total acquisition times as short as 13.5 minutes and as long as 19.5 minutes being presented. *Wise et al.* [3] presented acquisition routines lasting, 13.5 minutes (simultaneous) and 19.5 minutes (interleaved), while *Bulte et al.* [1], *Gauthier et al.* [2] and **Chapter 4** from this text present designs lasting 18 minutes. The details of the duration of the individual respiratory stimulations also vary between studies along with the concentrations of gas used.

### 6.1.1 Reducing Acquisition Time

In order to make the dcfMRI protocol an appealing technique to implement in clinical and research scan protocols it is necessary to produce reliable measures of absolute  $\text{CMRO}_2$  and related physiological parameters in as short a scan time as possible. Aside from the obvious advantages afforded by a shorter acquisition such as reductions in valuable scan time, improvements in subject comfort and realistic implementation in larger scanning protocols, it would also reduce the susceptibility of the technique to motion related errors and there would be less potential for change or drift in CBF and BOLD signals as well as the underlying physiological parameters being measured.

However, reducing scan time must be done carefully as it is important to establish that the parameter measurements compare favourably with those made using longer acquisition times. To understand where reductions in acquisition time can feasibly be made the reasoning behind the current respiratory designs presented in this study are discussed along with relevant details on elements of the post-processing pipeline. Using data acquired in a previous study a number of analytical approaches are then proposed to investigate if the acquisition time of the dual calibrated approach can feasibly be reduced and in what areas these reductions might take place. The respiratory manipulations investigated in this work have been presented in **Chapter 4** as the interleaved and simultaneous hypercapnic-hyperoxic respiratory manipulations and data acquisition lasted 18 minutes in total.

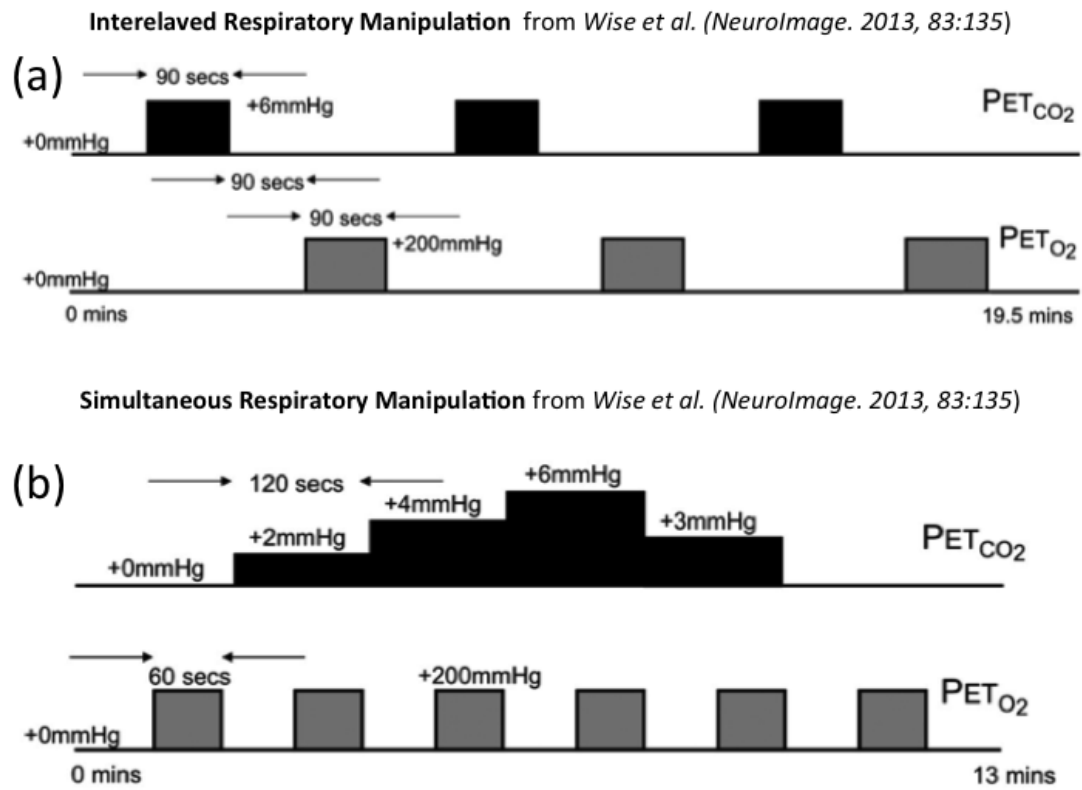


Figure 6.1: Interleaved and simultaneous hypercapnic-hyperoxic respiratory manipulations as presented by *Wise et al.* [3]

### 6.1.2 Interleaved Hypercapnic-Hyperoxic Respiratory Design

The design of the interleaved hypercapnic-hyperoxic respiratory manipulation was based on that presented by *Wise et al.* [3], shown in Figure 6.1a, with some modifications. During the interleaved design, BOLD and CBF changes are measured during periods of normocapnia and normoxia (baseline), hypercapnia and normoxia (HC) and hyperoxia and normocapnia (HO). As can be seen in Figure 6.2 baseline and HO periods last one minute each and periods of HC last 2.5 minutes. The reliance on arterial spin labelling (ASL) to measure changes in CBF is likely to be a limiting factor in the dcfMRI routine as the measure of CBF using ASL suffers from low SNR. It can also be seen from Figure 6.2 that changes in CBF are only expected during periods of HC. In order to increase the accuracy of the ASL measure of CBF change, the length of the HC blocks were increased in comparison to HO where no CBF change need be detected. As no such SNR limitations are placed on the detection of BOLD changes induced during periods of HO, more frequent, shorter blocks of HO and baseline were used. The symmetry and interleaved nature of the design, with baseline and HO blocks being bookended by long blocks of HC, were also thought to be beneficial in dealing with any drift that may occur during the long scan time duration.

### 6.1.3 Simultaneous Hypercapnic-Hyperoxic Respiratory Design

The concept of the simultaneous hypercapnic-hyperoxic respiratory design was introduced by *Wise et al.* [3] and the design of the simultaneous hypercapnic-hyperoxic respiratory manipulation used in this study was based on this, shown

in Figure 6.1b, with some modifications. It involves modelling CBF and BOLD changes during hyperoxic stimulation which is simultaneously modulated using varying levels of hypercapnia (HC-HO) as well as measuring baseline periods conducted during normocapnia and normoxia. A schematic of the design used in this study is shown in Figure 6.3. Using the simultaneous approach information about the exponents,  $\alpha$  and  $\beta$ , used in the BOLD signal model can be measured.  $\alpha$  is the exponent relating relative increases in CBF to blood volume and  $\beta$  is the exponent relating deoxyhaemoglobin concentration to the relaxation rate  $R2^*$ . Both of these model parameters are dependent on cerebrovasculature and have the potential to change depending on the underlying physiology. To aid in extrapolating measurements of these exponents from the simultaneously modulated CBF and BOLD data, it was considered advantageous to have many levels of simultaneously varying HC-HO in the 18 minute time-course. It was also designed symmetrically to counteract drift with baseline measures being conducted at the beginning, middle and end of the respiratory protocol.

#### 6.1.4 Block Averaging Time-Points

To increase the accuracy of the measurements made during each respiratory period, block averaging was performed over designated window widths as shown in Figure 6.2 and 6.3. This provided fewer points than fitting the CBF and BOLD time-series on a volume by volume basis and improved accuracy of each CBF measurement entered into the fitting in particular. The block averaging approach also allowed periods of transition between conditions to be disregarded as the BOLD

signal model assumes a steady state. In each respiratory block the first 30 seconds was removed to allow the physiological measures reach such a steady state. From observations of transitions of inspired gases during the experiments this was considered liberal and more than enough time to allow the effect of transitions to be minimised.

### 6.1.5 Analytical Approach

#### Timecourse Splitting

The 18 minute interleaved and simultaneous respiratory manipulations were designed symmetrically allowing the data acquired to be split into two, symmetrical 9 minute chunks which were used to provide estimates of the physiological variables during these periods. This allowed a comparison of estimates of absolute  $\text{CMRO}_2$  and associated physiological parameters to be made using the 1<sup>st</sup> 9 minutes, 2<sup>nd</sup> 9 minutes and all 18 minutes of data.

#### Varying Block Average Window Sizes

As described above, block averaging was used to decrease the number of time-points used in the fitting routine but increase the accuracy of these block averaged data-points. The effect of decreasing time-points in each block averaged point on the final variable estimates was investigated by making the window sizes smaller. This leads to less data being averaged in each block averaged point decreasing the SNR. By taking this approach we attempt to determine if a smaller window

size would provide parameter estimates comparable to those made using the full window size. In practice if a smaller window size was shown to produce comparable estimates to a larger window size, the extra data used in the larger window might be considered surplus and the length of that respiratory block could be decreased.

### Block Averaged Time-Point Resampling

The block averaged time-point resampling routine attempts to determine if the acquisition time can be made shorter by acquiring fewer respiratory blocks. In practice this is done by defining a number of time-based groupings for the interleaved and simultaneous design which require a designated number of block-averaged data-points of a certain type (baseline, HC, HO or HC-HO) as shown in Figure 6.4. The designated number of block averaged data-points are then randomly chosen from those available in the subjects time-series. The randomly chosen BOLD, CBF and  $P_{ET}O_2$  block averaged data-points are then fitted with the BOLD-signal model to determine absolute  $CMRO_2$  and related physiological variables. This process is then repeated 1,000 times in each subject, for each time based grouping giving a distribution of measured physiological parameters. By comparing the distributions of parameters calculated in the time-based groupings we can investigate at what stage enough block averaged data-points are used to make reliable parameter estimates.



### Interleaved CO<sub>2</sub>-O<sub>2</sub>

#### Varying Block Average Window:

- Dotted lines mark the center of a respiratory block.

- 100% windows:

■ = 30 s window ■ = 45 s window ■ = 70 s window

- The effect of variable window sizes is investigated by taking 100% to 10% (in steps of 10%) of these windows.

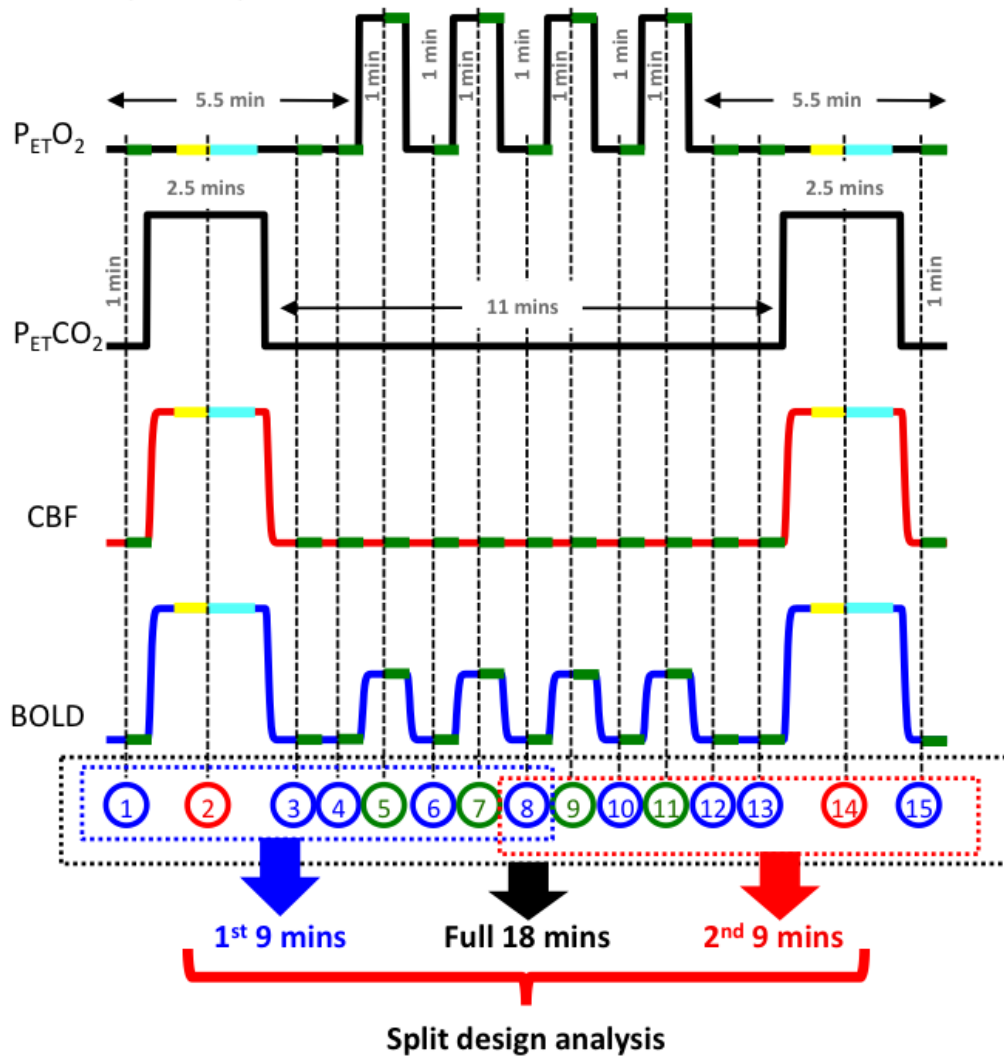


Figure 6.2: Schematic of interleaved hypercapnic-hyperoxic respiratory challenge used during the dcfMRI protocol. Details of the block averaging windows described in Section 6.2.6 are shown with dotted lines marking the centre of the respiratory block. BOLD, CBF and  $P_{ET}O_2$  block averaged data-points used in the split design analysis described in Section 6.2.7 are detailed at the bottom.

### Simultaneous CO<sub>2</sub>-O<sub>2</sub>

#### Varying Block Average Window:

- Dotted lines mark the center of a respiratory block.
- 100% windows:            = 30 s window
- The effect of variable window sizes is investigated by taking 100% to 10% (in steps of 10%) of these windows.

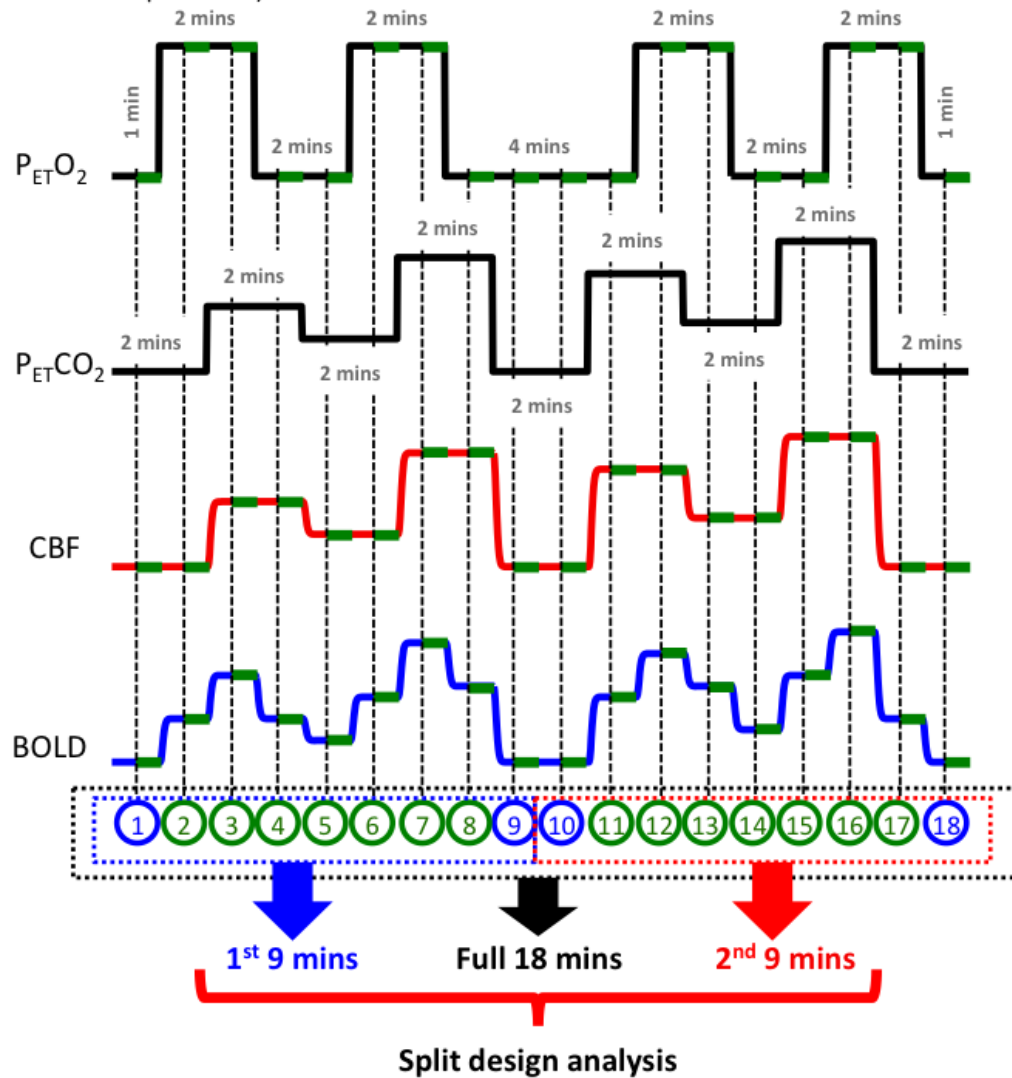


Figure 6.3: Schematic of simultaneous hypercapnic-hyperoxic respiratory challenge used during the dcfMRI protocol. Details of the block averaging windows described in Section 6.2.6 are shown with dotted lines marking the centre of the respiratory block. BOLD, CBF and  $P_{ET}O_2$  block averaged data-points used in the split design analysis described in Section 6.2.7 are detailed at the bottom.

### Timepoint Resampling

#### Interleaved CO<sub>2</sub>-O<sub>2</sub>:

- = Normocapnia & Normoxia (Baseline)
- = Hypercapnia & Normoxia (HC)
- = Normocapnia & Hyperoxia(HO)

Random combinations of block averaged CBF, BOLD and P<sub>ET</sub>O<sub>2</sub> timepoints taken and used to calculate M, S<sub>v</sub>O<sub>2</sub> and CMRO<sub>2</sub>.

<span style="color: blue;">○</span> x 1,	<span style="color: red;">○</span> x 1,	<span style="color: green;">○</span> x 1	= 4.5 mins
<span style="color: blue;">○</span> x 1,	<span style="color: red;">○</span> x 2,	<span style="color: green;">○</span> x 1	= 7 mins
<span style="color: blue;">○</span> x 5,	<span style="color: red;">○</span> x 1,	<span style="color: green;">○</span> x 2	= 9.5 mins
<span style="color: blue;">○</span> x 5,	<span style="color: red;">○</span> x 2,	<span style="color: green;">○</span> x 2	= 12 mins
<span style="color: blue;">○</span> x 7,	<span style="color: red;">○</span> x 1,	<span style="color: green;">○</span> x 4	= 13.5 mins
<span style="color: blue;">○</span> x 7,	<span style="color: red;">○</span> x 2,	<span style="color: green;">○</span> x 4	= 16 mins
<span style="color: blue;">○</span> x 9,	<span style="color: red;">○</span> x 2,	<span style="color: green;">○</span> x 4	= 18 mins (ALL)

#### Simultaneous CO<sub>2</sub>-O<sub>2</sub>:

- = Normocapnia & Normoxia (Baseline)
- = Hypercapnia & Hyperoxia (HC-HO)

Random combinations of block averaged timepoints CBF, BOLD and P<sub>ET</sub>O<sub>2</sub> taken and used to calculate M, S<sub>v</sub>O<sub>2</sub>,  $\alpha$ ,  $\beta$  and CMRO<sub>2</sub>.

<span style="color: blue;">○</span> x 1,	<span style="color: green;">○</span> x 3	= 4 mins
<span style="color: blue;">○</span> x 4,	<span style="color: green;">○</span> x 3	= 7 mins
<span style="color: blue;">○</span> x 1,	<span style="color: green;">○</span> x 8	= 9 mins
<span style="color: blue;">○</span> x 4,	<span style="color: green;">○</span> x 8	= 12 mins
<span style="color: blue;">○</span> x 1,	<span style="color: green;">○</span> x 12	= 13 mins
<span style="color: blue;">○</span> x 4,	<span style="color: green;">○</span> x 12	= 16 mins
<span style="color: blue;">○</span> x 4,	<span style="color: green;">○</span> x 14	= 18 mins (ALL)

Figure 6.4: Schematic detailing the time-based groupings and type of block averaged data-points used in the block averaged time-point resampling analysis for both the interleaved and simultaneous respiratory manipulations.

## 6.2 Methods

The data used in this study is a subset of data presented in **Chapter 4**.

### 6.2.1 Participants

Eight normal healthy participants (aged 24 - 39; mean age  $33.5 \pm 5.0$ ; 2 female) were recruited and scanned having given written consent. Experimental procedures were approved by the local institutional ethical review committee.

### 6.2.2 MRI

Scanning was performed on a 3T GE HDx MRI (GE Healthcare, Milwaukee WI) with a body transmit coil and 8-channel head receive coil. All participants had previous whole brain  $T_1$ -weighted structural scans available (fast spoiled gradient recalled echo, 1x1x1 mm voxels, TI/TR/TE = 450/7.8/3 ms).

Two dcfMRI protocols were performed in each subject on separate days allowing the estimation of absolute  $CMRO_2$  and associated physiological variables. During day one an interleaved respiratory manipulation was used and during day two a simultaneous respiratory manipulation. These scans were conducted during rest (eyes open, fixating on a cross hair on a black background) and details of the interleaved and simultaneous respiratory manipulations are presented in **Chapter 4**.

Simultaneous perfusion and BOLD imaging data was collected for each dcfMRI acquisition using a PASL proximal inversion and control for off-resonance effects (PICORE), quantitative imaging of perfusion using a single subtraction (PICORE QUIPSS II) [37] imaging sequence with a dual-echo gradient echo (GRE) readout and spiral k-space acquisition ( $TE_1 = 3$  ms  $TE_2 = 29$  ms,  $TR = 2.2$  s, flip angle  $90^\circ$ , FOV 22 cm, matrix  $64 \times 64$ , 12 slices of 7 mm thickness with an inter-slice gap of 1 mm acquired in ascending order,  $TI_1 = 700$  ms,  $TI_2 = 1600$  ms for the most proximal slice and was incremented for the subsequent slices, tag thickness = 20 cm, adiabatic hyperbolic secant inversion pulse, 10 mm gap between labelling slab and bottom slice, 10 cm QUIPSS II saturation band thickness). This resulted in the acquisition of 488 volumes (244 tag - control pairs) for each of the dcfMRI experiment. A separate single shot ( $M_0$ ) scan was acquired ( $TR = \infty$ ) with the same parameters as the functional run to measure the equilibrium brain tissue magnetisation for purposes of quantifying CBF. A minimum contrast image was also acquired to correct for coil sensitivity.

### 6.2.3 Respiratory Manipulation

Respiratory challenges were administered using a system of end-tidal forcing [63] which offers independent control of partial pressures of end-tidal oxygen and carbon dioxide ( $P_{ET}O_2$  and  $P_{ET}CO_2$  respectively). The end-tidal forcing system comprised a laptop personal computer using BreatheDmx software (Department of Physiology, Anatomy and Genetics, Oxford University, UK) to monitor end-tidal expired gas levels and calculate the inspired partial pressures required to

achieve the desired target. The gas mixtures were delivered at a total flow rate of 30 litres per minute (lpm) through a fast gas mixing system connected to a tight-fitting face-mask worn by the volunteer (Quadralite, Intersurgical, Wokingham, Berkshire, UK). The respiratory circuit included a reservoir on the expired limb to permit re-breathing in the event that the instantaneous inspiratory rate exceeded 30 lpm. Supplies of 10% CO<sub>2</sub> (balance air), 10% O<sub>2</sub> (balance N<sub>2</sub>), 100% O<sub>2</sub> and air were delivered from cylinders to the gas mixing chamber which was placed as close as possible to the volunteer (on chest) to minimise delays in delivery. Gas delivery was controlled by four mass flow controllers (MKS Instruments, Wilmington, MA, USA). Tidal gases were sampled from the volunteers facemask and  $P_{ET}O_2$  and  $P_{ET}CO_2$  were measured using rapidly responding gas analysers (AEI Technologies, Pittsburgh, PA, USA). During set-up  $P_{ET}O_2$  and  $P_{ET}CO_2$  were monitored for the volunteer. Resting  $P_{ET}O_2$  was used as the  $P_{ET}O_2$  target for normoxic periods and resting  $P_{ET}CO_2 + 1\text{mmHg}$  was used as the target  $P_{ET}CO_2$  for normocapnia to allow the end-tidal forcing system to provide control of end-tidal CO<sub>2</sub>. Target profiles for  $P_{ET}O_2$  and  $P_{ET}CO_2$  are shown in Figures 6.2 & 6.3.

#### 6.2.4 Preprocessing

All image time-series were motion corrected using *3dvolreg* [74]. Time-series image data acquired from the first echo of the PASL technique was used to calculate CBF, while the data from the second echo was used to examine changes in BOLD signal. Physiological noise correction (a modified RETROICOR), was applied

with the first and second harmonics of both the cardiac and respiratory cycles being regressed from the data along with the interaction term of the first cardiac and respiratory harmonics [80,81]. Interpolated surround subtraction of the ASL tag and control image time-series was performed to yield a perfusion-weighted time-series [43] which was corrected for coil sensitivity [82]. CBF images were calculated using the  $M_0$  of blood, estimated from the cerebrospinal fluid signal of the  $M_0$  image and the general kinetic model (GKM) [33]. The CBF estimates were adjusted for the likely reduction of the  $T_1$  of arterial blood with increasing plasma concentration of paramagnetic  $O_2$ , according to the blood  $T_1$  values quoted in *Bulte et al.* [51]. Interpolated surround averaging of the tag and control images was performed to yield a BOLD weighted time-series.

### 6.2.5 ROI's

Subject specific ROI's of global grey matter (GM) were produced using FAST segmentation on the high resolution structural images [83] and registered to the native space of CBF and BOLD images using FLIRT [77]. Partial voluming of GM was removed by thresholding the mask to include only voxels that were deemed to contain all grey matter. Mean CBF and BOLD time-series for GM were produced by averaging over the voxels in GM using the ROI mask.

### 6.2.6 Block Averaging

Relative CBF ( $\frac{CBF}{CBF_0}$ ) and BOLD signal ( $\frac{\Delta S}{S_0}$ ) timeseries were block averaged to remove periods of transition from the analysis where the BOLD signal model is not applicable. For the interleaved design, block averaging periods were calculated for each final 30 second period of each 60 second respiratory block (normocapnia with normoxia and normocapnia with hyperoxia) and 120 seconds of each 150 second block (hypercapnia with normoxia). The final 30 second period of each 60 second respiratory block was used when block averaging the simultaneous design. The mean arterial oxygen content,  $C_aO_2$ , was calculated from the  $P_{ET}O_2$  data for the same time periods. Periods of block averaging are shown in Figure 6.2 & 6.3.

### 6.2.7 Split Design Analysis

A split design analysis provided a crude way to investigate reducing scan time, allowing data acquired in equivalent scan times to be compared. Due to the symmetrical design of the respiratory manipulations this was possible. The relative block averaged time-series were analysed in terms of the 1<sup>st</sup> 9 minutes, the 2<sup>nd</sup> 9 minutes and the full 18 minutes. For the interleaved design, CBF, BOLD and  $P_{ET}O_2$  block averaged data-points from 1 to 8 were used for the 1<sup>st</sup> 9 minutes, 8 to 15 for the 2<sup>nd</sup> 9 minutes and 1 to 15 for the full 18 minutes as shown in Figure 6.2. For the simultaneous design block averaged data-points from 1 to 9 were used for the 1<sup>st</sup> 9 minutes, 10 to 18 for the 2<sup>nd</sup> 9 minutes and 1 to 18 for the full 18 minutes as shown in Figure 6.3.



### 6.2.8 Block Averaging using Varying Window Duration

The effect of reducing the amount of time-series data used to calculate each block averaged time-point was investigated by varying the duration of the block average windows. Block average windows of 100% duration are described in Section 6.2.6 and can be visualised in Figures 6.2 & 6.3. The block averaging windows were then reduced by 10% increments down to 10% of the original block averaging window size. All block averaging windows begin at the centre of the respiratory block (dotted lines Figures 6.2 & 6.3). By decreasing the percentage size of the block average windows, fewer time points are used to average before and after the dotted line.

### 6.2.9 Block Averaged Time-Point Resampling

To demonstrate the effect the number of block averaged data-points has on parameter estimation a block-averaged time-point resampling routine was used. The block averaged data-points calculated for the interleaved and simultaneous designs using the 100% block averaging windows were used. For each subject block averaging produced BOLD, CBF and  $P_{ET}O_2$  block averaged data-points made during 9 baseline (normocapnia and normoxia), 2 HC (hypercapnia during normoxia) and 4 HO (hyperoxia during normocapnia) in the interleaved design and 4 baseline and 14 HC-HO (hypercapnia with hyperoxia of varying degrees) in the simultaneous design. Time-based groupings can be seen at the bottom of Figures 6.2 & 6.3.

For the interleaved design the minimum requirement to estimate absolute  $\text{CMRO}_2$  are BOLD, CBF and  $\text{P}_{\text{ET}}\text{O}_2$  measures made at baseline (duration = 1 minute), HO (duration = 1 minute) and HC (duration = 2.5 minutes). Summing the durations of these three block averaged data-points gives a minimum acquisition time of 4.5 minutes using the block averaging technique defined in Section 6.2.6.

Seven time-based groupings related to length of acquisition were then defined. For the interleaved design these were 4.5, 7, 9.5, 12, 13.5, 16 and 18 minutes. The increasing group timings were achieved by incrementally introducing more baseline, HO and HC block averaged data-points of BOLD, CBF and  $\text{P}_{\text{ET}}\text{O}_2$  as described in the schematic in Figure 6.4.

Time-based groupings of 4, 7, 9, 12, 13, 16 and 18 minutes were used for the simultaneous design to try to closely mirror the total times used in the groupings of the interleaved design. Again the increasing group timings were achieved by incrementally introducing more baseline and HO-HC block averaged data-points of BOLD, CBF and  $\text{P}_{\text{ET}}\text{O}_2$  as described in the schematic in Figure 6.4.

Using these grouping definitions, a block averaged time-point resampling routine was performed for each subject for both the interleaved and simultaneous design. As defined in Figure 6.4 each grouping has a required number of block averaged BOLD, CBF and  $\text{P}_{\text{ET}}\text{O}_2$  time-points made during a certain respiratory state which is required. For example the interleaved 9.5 minute grouping requires 5 BOLD, CBF and  $\text{P}_{\text{ET}}\text{O}_2$  block averaged data-points made during baseline (total duration = 5 minutes), 2 during HO (total duration = 2 minutes) and 1 during HC (total duration = 2.5 minutes). To perform the block averaged time-point resampling

routine the BOLD, CBF and  $P_{ET}O_2$  block averaged data-points are randomly chosen within the requirements of the time-based grouping. For the interleaved 9.5 minute example, 5 baseline points are randomly chosen from the 9 available, 2 HO block averaged data-points are randomly chosen from the 4 available and 1 HC block averaged time-point was randomly chosen from the 2 available. The physiological measures made at these block averaged data-points were then concatenated to make BOLD, CBF and  $P_{ET}O_2$  time-series containing information from 5 block averaged time points made at baseline, 2 during HO and 1 during HC giving a time-series taking 9.5 minutes to acquire. The BOLD, CBF and  $P_{ET}O_2$  block averaged time-series were then used to estimate absolute  $CMRO_2$  and related physiological parameters using the fitting routine described in Section 6.2.10. This was then repeated 1,000 times in each subject for each grouping. During each iteration the designated number of baseline, HC and HO block averaged data-points for that grouping were randomly chosen from those available in the subjects physiological time-series and absolute  $CMRO_2$  and related physiological variables recalculated producing a distribution of parameter estimates.

The block averaged time-point resampling routine was the same for the simultaneous design with the simultaneous time-based groupings being described in Figure 6.4 with block averaged data-points being randomly chosen from the baseline and HC-HO block averaged data-points available in each subjects time-series during each iteration and recalculated using the  $CMRO_2$  quantification routine described in Section 6.2.10.

### 6.2.10 Calculating Absolute CMRO<sub>2</sub>

The BOLD signal model described in [3] was fit to the global GM, mean CBF and BOLD block averaged time-series produced from the different analysis approaches described in Sections 6.2.7, 6.2.8 and 6.2.9. This was done using a simple bayesian framework to yield estimates of M and S<sub>v</sub>O<sub>2</sub> (interleaved) and M, S<sub>v</sub>O<sub>2</sub>,  $\alpha$  and  $\beta$  (simultaneous) at baseline permitting calculation of absolute CMRO<sub>2</sub>.  $\alpha = 0.14$  and  $\beta = 0.91$  were chosen from [85] when fitting the interleaved design. Priors for M and S<sub>v</sub>O<sub>2</sub> were generated as normal probability density functions centred around initial estimates of 0.08 and 0.5 with broad standard deviations of 0.02 and 0.1. When fitting for M, S<sub>v</sub>O<sub>2</sub>,  $\alpha$  and  $\beta$ , normal probability density functions centred around initial estimates of 0.3 and 1.4 with standard deviations of 0.1 and 0.2 were used as priors for  $\alpha$  and  $\beta$ . By applying Bayes' rule to the first block averaged time points of  $\frac{\Delta S}{S_0}$ ,  $\frac{CBF}{CBF_0}$  and C<sub>a</sub>O<sub>2</sub>, posterior probability distributions of the variables, M and S<sub>v</sub>O<sub>2</sub> and M, S<sub>v</sub>O<sub>2</sub>,  $\alpha$  and  $\beta$ , were generated after integrating over the ranges 0.01 – 0.15 (M), 0.2 – 0.8 (S<sub>v</sub>O<sub>2</sub>), 0.1 – 0.5 ( $\alpha$ ) and 0.8 – 2.0 ( $\beta$ ). These were chosen to be beyond the extremes of physiologically plausible values. The posterior distributions were used as the priors for calculations with the second time points of averaged data and so on until a final posterior distribution for each of the two variables was obtained. The maxima of these probability distribution functions provided the estimates of M and S<sub>v</sub>O<sub>2</sub> and M, S<sub>v</sub>O<sub>2</sub>,  $\alpha$  and  $\beta$  for each subject. Absolute CMRO<sub>2</sub> was then calculated using:

$$CMRO_2 = OEF \cdot CBF \cdot C_aO_2 \quad (6.1)$$

## 6.3 Results

### 6.3.1 Split Design Analysis

As described in Section 6.2.7 the CBF, BOLD and  $P_{ET}O_2$  block averaged data-points were split into the 1<sup>st</sup> 9 minutes and 2<sup>nd</sup> 9 minutes to investigate if differences could be detected between these measures and a full 18 minute acquisition in terms of absolute  $CMRO_2$ , CBF and  $S_vO_2$  in GM at rest. The partitioning of the block averaged data-points used to achieve these measures are shown at the bottom of Figure 6.2 for the interleaved design and Figure 6.3 for the simultaneous design. The group mean  $\pm$  standard deviation  $CMRO_2$ , CBF and  $S_vO_2$  were calculated in GM at rest from data partitioned into the 1<sup>st</sup> 9 minutes, 2<sup>nd</sup> 9 minutes and full 18 minutes and is presented in Figure 6.5. Similar data is presented in Figure 6.6 depicting intersubject coefficients of variation (CV) and Figure 6.7 showing ICC's to investigate the reproducibility of the measures being made using different data partitioning. Background to the use of ICC's for assessing reproducibility are explained in **Chapter 5**.

### 6.3.2 Varying Window Duration Analysis

A comparison of the total amount of acquisition time used to calculate each window size for both the interleaved and simultaneous designs is shown in Figure 6.8. The 100% acquisition times are less than 18 minutes as transitional periods have been removed as discussed in the Section 6.2.6. Changes in group mean and standard

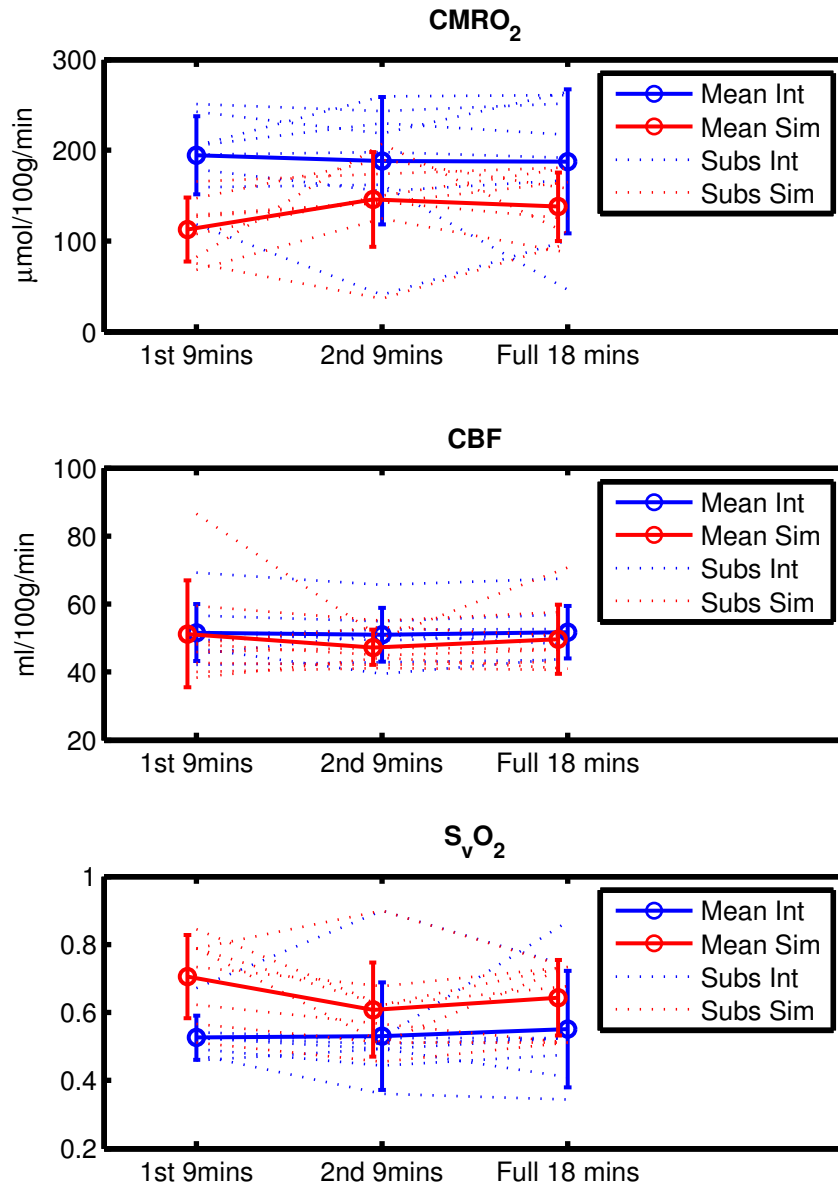


Figure 6.5: Group mean  $\pm$  standard deviation ( $N = 8$ ) (Solid blue and red lines) of absolute  $\text{CMRO}_2$ , baseline CBF and  $\text{S}_v\text{O}_2$  calculated for the 1<sup>st</sup> 9 minutes, 2<sup>nd</sup> 9 minutes and full 18 minutes of the interleaved and simultaneous respiratory manipulations as described in Figures 6.2 & 6.3 and Section 6.2.7. Measurements for individual subjects are shown in the dashed blue and red lines.

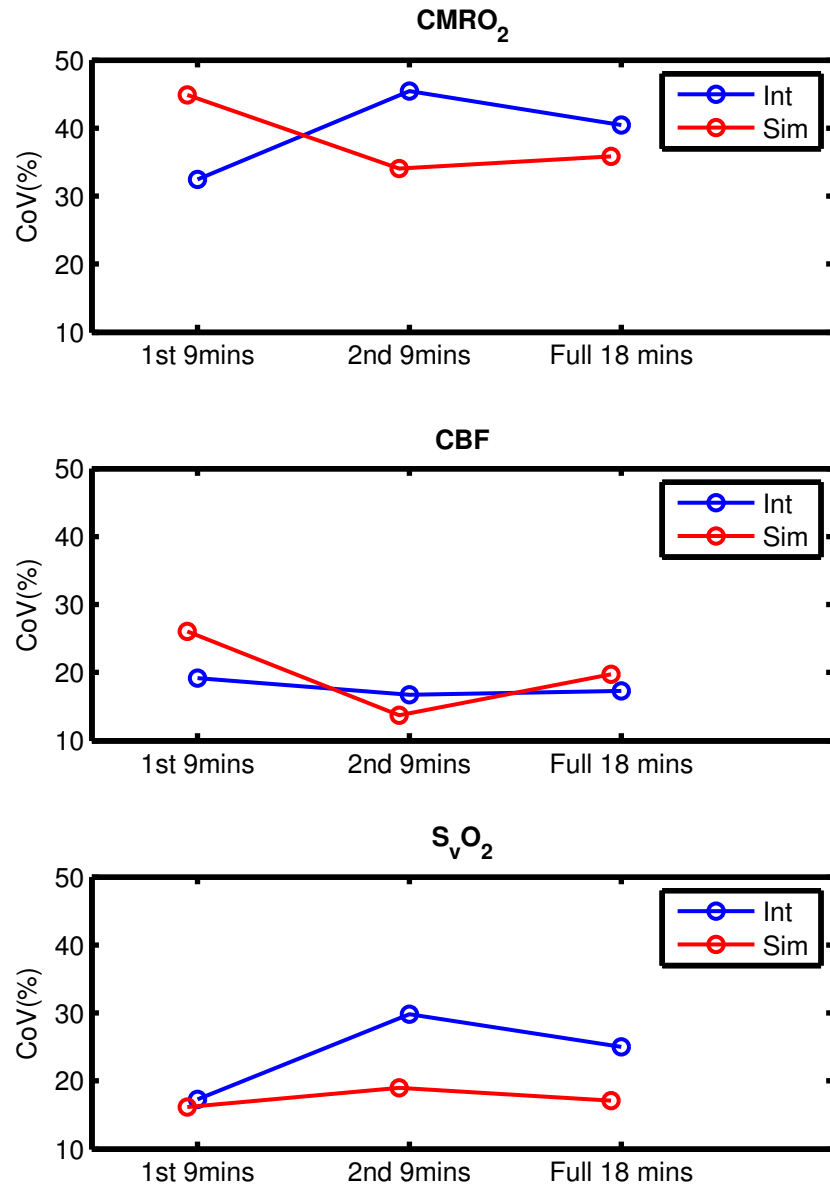


Figure 6.6: Intersubject CV's ( $= \frac{GroupStandardDeviation}{GroupMean}$ ) ( $N = 8$ ) for absolute CMRO<sub>2</sub>, baseline CBF and S<sub>v</sub>O<sub>2</sub> calculated in GM from the 1<sup>st</sup> 9 minutes, 2<sup>nd</sup> 9 minutes and full 18 minutes of the interleaved and simultaneous respiratory manipulations.

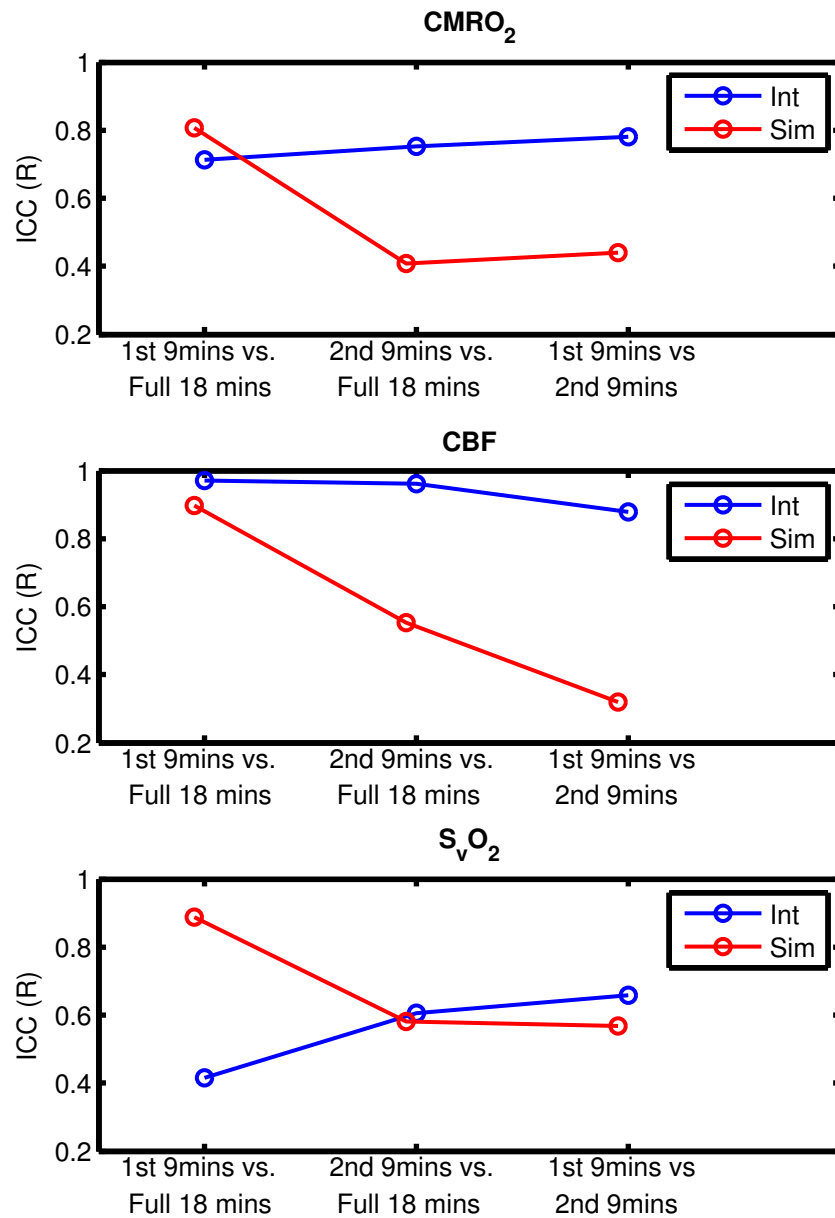


Figure 6.7: Intraclass correlation coefficient (ICC's) calculated for 8 subjects between the 1st 9 minutes and full 18 minutes, 2nd 9 minutes and full 18 minutes and the 1st 9 minutes and 2nd 9 minutes.



deviation  $\text{CMRO}_2$ ,  $\text{S}_v\text{O}_2$  and  $M$  with varying window size changes are presented in Figure 6.9. Intraclass correlation coefficient's (ICC) were calculated by testing the parameter estimates at a given window size with those made at 100%.

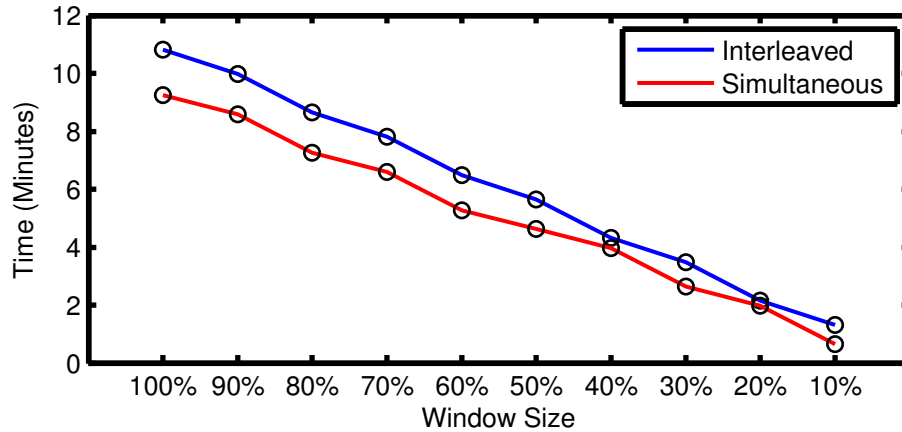


Figure 6.8: Amount of time used in block averages plotted as a function of window size for both the interleaved and simultaneous respiratory designs. Each acquisition took 18 minutes and periods used for block averaging to avoid transitions are shown in Figure 6.2 & 6.3. Window sizes of varying duration (10 - 100%) all begin at the dotted lines positioned at the centre of the respiratory blocks as shown in Figures 6.2 & 6.3.

### 6.3.3 Block Averaged Time-Point Resampling

Results of the block averaged time-point resampling routine as applied to the interleaved and simultaneous respiratory designs are presented in Figure 6.11. Subject means were calculated from the 1,000 randomly sampled iterations at each time-based grouping and the group mean and standard deviation was then calculated from these means across subjects for  $\text{CMRO}_2$ ,  $\text{S}_v\text{O}_2$  and  $M$ . The full 18 minute time-based grouping does not demonstrate any variation as all block averaged data-points were used to calculate the end physiological variables as the random

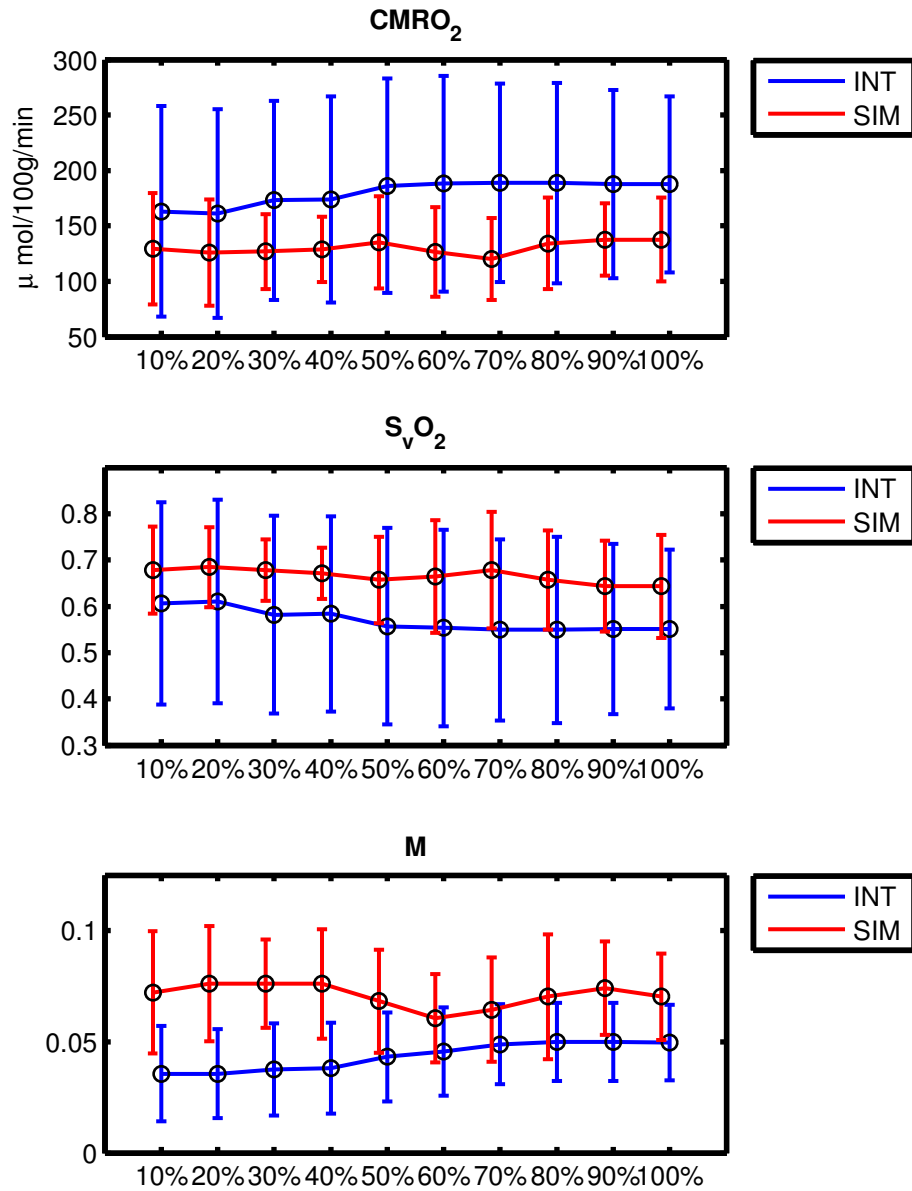


Figure 6.9: Group mean  $\pm$  standard deviation (N = 8) of absolute  $CMRO_2$ ,  $M$  and  $S_vO_2$  calculated for the interleaved and simultaneous respiratory manipulations using block averaging windows ranging from 10% to 100% of those shown in Figures 6.2 & 6.3.

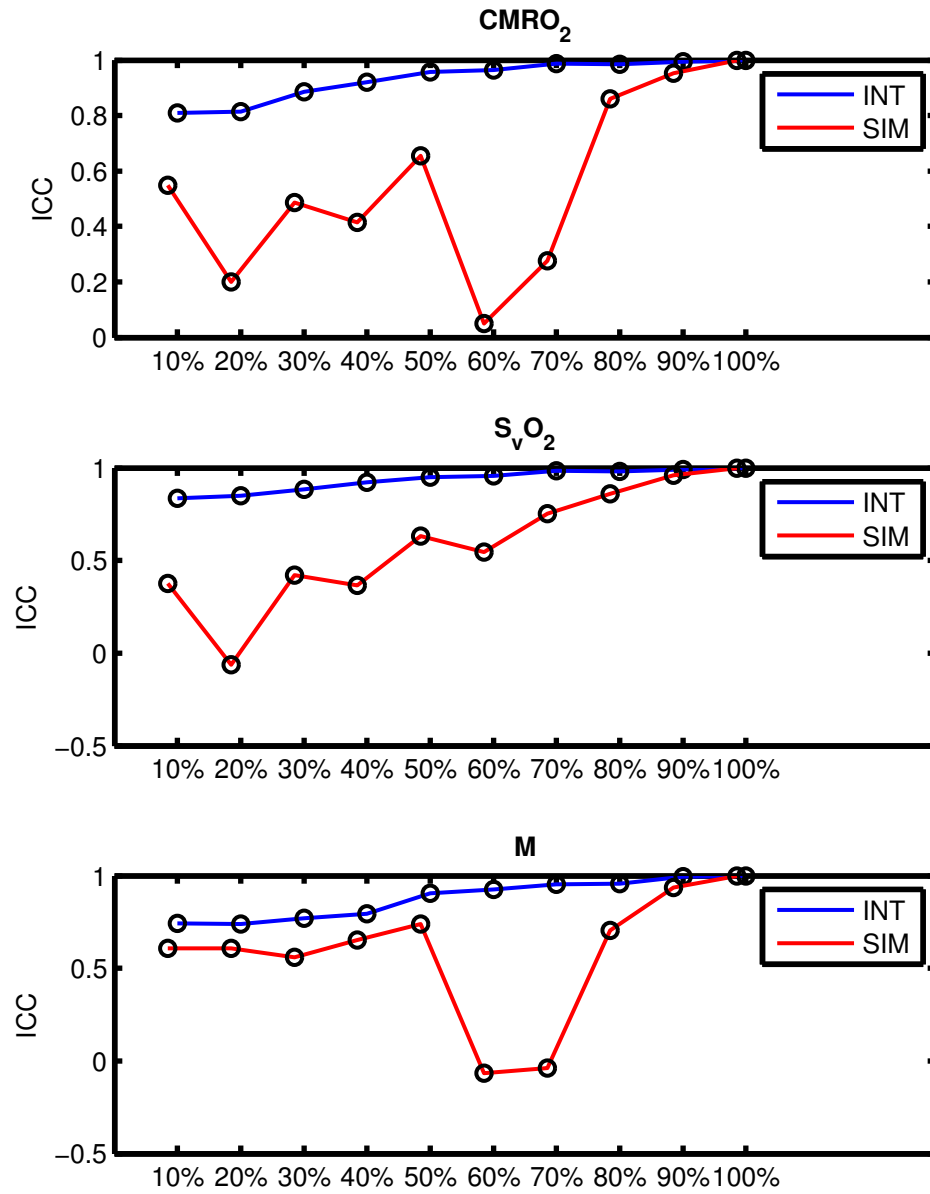


Figure 6.10: Intraclass correlation coefficients calculated by correlating across subjects, the parameter estimates at a given window size with those made at 100%

reordering of the block averaged data-points employed by the block averaged time-point resampling routine does not influence the end result.

## 6.4 Discussion

BOLD, CBF and  $P_{ET}O_2$  block averaged time-series data was acquired in 8 subjects during an interleaved and simultaneous hypercapnic-hyperoxic challenge on separate days. Each scan lasted 18 minutes and was conducted at rest allowing measurements of  $M$ ,  $S_vO_2$  and absolute  $CMRO_2$  to be made using both techniques. Three separate analytical approaches were performed on the data to determine the viability of a shortened acquisition time for quantification of absolute  $CMRO_2$  and related physiological measures.

### 6.4.1 Split Design Comparison

The split analysis approach involved splitting the data collected for each 18 minute acquisition into the 1<sup>st</sup> 9 minutes of data and the 2<sup>nd</sup> 9 minutes. The BOLD signal model was fit to the portioned data to provide estimates of  $M$ ,  $S_vO_2$  and absolute  $CMRO_2$ .

From Figure 6.5, group mean CBF values are stable across all data portions. Measurements of  $S_vO_2$  appear to decrease in the 2<sup>nd</sup> 9 minutes using the simultaneous design but appear to be stable using the interleaved design. This leads to an increase in absolute  $CMRO_2$  detected between the 1<sup>st</sup> 9 minutes and the 2<sup>nd</sup> 9 minutes of data when looking at the simultaneous design. The group aver-

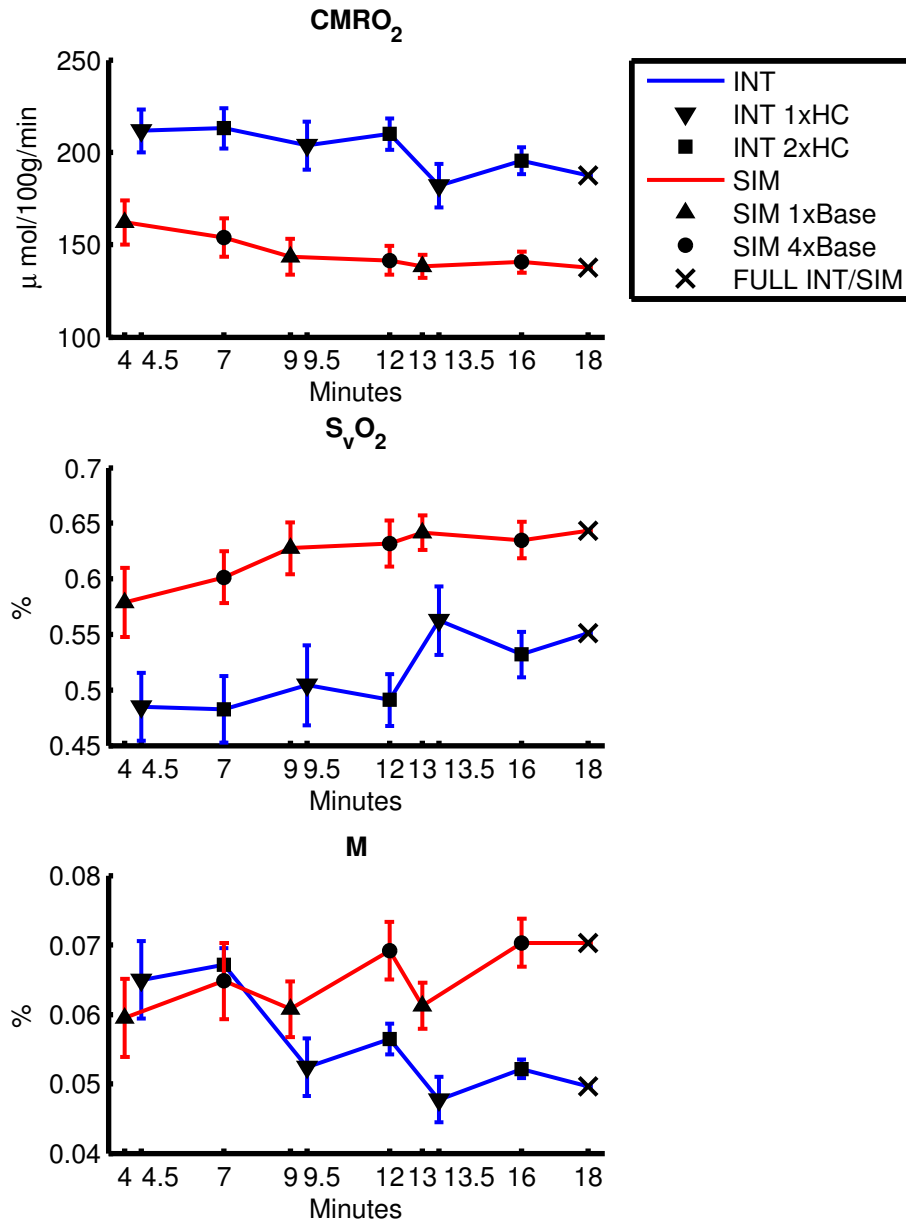


Figure 6.11: Group mean  $\pm$  standard deviation ( $N = 8$ ) of absolute CMRO<sub>2</sub>, baseline CBF and S<sub>v</sub>O<sub>2</sub> plotted as a function of the time based groupings shown in Figure 6.4. For each time based grouping the mean of 1,000 iterations of the random block averaged time-point resampling routine was calculated in each subject. The mean and standard deviation of these means across the group was then calculated and presented here. No variation is seen in the full 18 minute time-based grouping as all block averaged data-points were used to calculate the physiological variables and random reordering of the block averaged data-points does not influence the end result.

age  $\text{CMRO}_2$  value calculated for the 1<sup>st</sup> 9 minutes of the simultaneous design is unrealistically low ( $\approx 100 \mu\text{mol}/100\text{g}/\text{min}$ ).

CV values for  $\text{CMRO}_2$ , CBF and  $\text{S}_v\text{O}_2$  presented in Figure 6.6 suggest intersubject variation in the  $\text{CMRO}_2$  measure is mainly due to variation in  $\text{S}_v\text{O}_2$  in the interleaved design and variation in CBF in the simultaneous design.

ICC's calculated between the 1<sup>st</sup> 9 minutes and full 18 minutes, 2<sup>nd</sup> 9 minutes and full 18 minutes and the 1<sup>st</sup> 9 minutes and 2<sup>nd</sup> 9 minutes for both the interleaved and simultaneous hypercapnic and hyperoxic challenges are presented in Figure 6.7. Comparison with intrasession ICC values calculated in **Chapter 5**, (Interleaved:  $\text{CMRO}_2 = 0.68$ ;  $\text{CBF} = 0.60$ ;  $\text{S}_v\text{O}_2 = 0.57$  and Simultaneous:  $\text{CMRO}_2 = -0.01$ ;  $\text{CBF} = 0.88$ ;  $\text{S}_v\text{O}_2 = -0.18$ ) the interleaved design shows similar ICC values for all comparisons in all physiological values. The simultaneous design demonstrates generally lower ICC values but they are considerably higher than the intrasession ICC values from **Chapter 5**.

Differences between the parameter measures made in the two 9 minute periods may be due to changes occurring over the course of the 18 minute scan. Drift in the BOLD and CBF signal may occur due to scanner instabilities or changes in the underlying physiology causing differences in the parameters measured from the 1<sup>st</sup> 9 minutes and the 2<sup>nd</sup> 9 minutes. Physiological changes may be caused by acclimatisation of the subject to the respiratory tasks and to resting in the scanner. Differences in parameter measures are also likely to be related to measurement noise and repeatability which is investigated in **Chapter 5**.

Although the approach of splitting the design into two 9 minute chunks allows a like-for-like comparison, it is a crude way of investigating shorter acquisition times. The varying window analysis and block averaged time-point resampling routines provide more subtle approaches to determining appropriate shortened acquisition routines.

### 6.4.2 Varying Window Size for Block Averaging

The total amount of time used to calculate the physiological variables as a function of varying block-average window size is shown in Figure 6.8 for both the interleaved and simultaneous design. The graph demonstrates that slightly less data is used in the simultaneous design for all window sizes with the difference decreasing as the windows get smaller. Total scan times using the 100% block average windows are less than 18 minutes as data acquired during transitions was removed as described in Section 6.2.6. After removing the transition periods and using the 100% block averaged windows the interleaved design uses  $\sim 10.5$  minutes of data whereas the simultaneous design uses  $\sim 9$  minutes.

Figure 6.9 shows the group mean  $\pm$  standard deviation of  $\text{CMRO}_2$ ,  $\text{S}_v\text{O}_2$  and  $\text{M}$  calculated at varying block average window widths for both the interleaved and simultaneous designs. The same baseline CBF was used despite the varying window width as this value was used to normalise the CBF trace before block averaging was performed. Group standard deviations calculated for  $\text{S}_v\text{O}_2$  and  $\text{CMRO}_2$  are consistently smaller for all window sizes using the simultaneous design. Differences between group mean  $\text{S}_v\text{O}_2$  and  $\text{CMRO}_2$  calculated using the interleaved and

simultaneous design are discussed in **Chapter 4** but differences between the two measures remain consistent for all window sizes. This may be due to the fact that all transitions were removed from the block averaged design and all block averaging windows began at the same point at the centre of the respiratory manipulation and the respiratory challenges were allowed to reach a steady state.

In both interleaved and simultaneous design reasonable estimates of  $S_vO_2$  and absolute  $CMRO_2$  are made even at the smallest window size (10%). The affect of smaller window sizes was to underestimate group mean  $CMRO_2$  by a maximum of  $\sim 15\%$  for both approaches with group  $S_vO_2$  being overestimated by a maximum of  $\sim 10\%$  for the interleaved design and  $\sim 5\%$  for the simultaneous approach.

The interleaved and simultaneous designs achieve group parameter estimates that agree well with those calculated using a 100% block averaging window at a window duration of 50%. Estimates calculated using the interleaved design remain stable for increasing window duration after this point. However considering estimates calculated using the simultaneous design become unstable after this point, using the simultaneous design with window sizes less than 80-90% of those currently being used could lead to unreliable parameter estimates. This can be put down to the reduced accuracy of block averaged data-points using reduced window sizes.

For smaller window sizes, the group standard deviations for the interleaved design remain around 20% higher than that calculated using the 100% block averaged window. The group standard deviation only begins to converge to the lower value measured using the 100% window at around 70% of it's size. Group standard deviations converge earlier with smaller window sizes for the simultaneous design.



ICC's presented in Figure 6.10 were calculated by correlating the parameter estimates at a given window size with those made with 100% windows. From this it can be seen that the parameter estimates are reliable when made with a window size 50% of the size currently being used. However simultaneous parameter estimates are unreliable until they reach  $\sim 90\%$  of the width currently being used.

From this analysis the interleaved block averaging windows could be reduced to 50% of those currently being used and still produce comparable parameter estimates to those made using 100% block-average windows. This would reduce the overall scan time by  $\sim 5$  minutes meaning reliable parameter estimates could be made in around 13 minutes. In this study 30 second periods were removed at the start of each block to remove transition periods. This may be considered liberal and by optimising the removal of periods related to transitions further savings in scan time could be made. An alternative approach would be to modify the BOLD signal model to account for transition periods.

The unreliable estimates produced using smaller window sizes in the simultaneous design may be due to a number of factors related to the CBF measurement. For the simultaneous design, accurate measurements of CBF may be difficult to achieve particularly with the smaller window sizes compared to the interleaved approach and the rapidly changing nature of the design. The interleaved design was purposely designed with large hypercapnic blocks to increase the accuracy of the CBF measure giving a 2 minute continuous measure when a 100% window is used and transitions were removed. Comparatively the simultaneous approach uses block averaging of 30 seconds during periods of hypercapnia. By reducing the window size below 90 % the accuracy of the block averaged CBF signal may

decrease to a level where measurements are erratic leading to unreliable parameter estimates when fitting with the BOLD signal model.

### 6.4.3 Block Averaged Time-Point Resampling

The block averaged time-point resampling routine attempts to determine how many block averaged data-points are required to produce reliable estimates that agree well with parameter estimates made using all the block averaged data points from the full 18 minutes.

In Figure 6.11 each data point is the mean parameter estimate from 8,000 (1,000 x 8 subjects) randomly sampled time-series fitted with the BOLD signal model. It can be seen that group mean differences between  $S_vO_2$  and  $CMRO_2$  are still present between the interleaved and simultaneous designs.

From Figure 6.11 it can be seen that the simultaneous design converges on a group mean which deviates by  $\sim 5\%$  from the parameters calculated using the full 18 minutes of block averaged points using a time-based grouping of 9 minutes (1 baseline and 8 HC-HO block-averaged time-points) or more.

Applying a similar approach to the interleaved design reasonable parameter estimates seem to be achieved at a time based grouping of 13.5 minutes. However it is also interesting to note the effect of randomly choosing the hypercapnic block averaged time-point versus including both hypercapnic block averaged data-points for the interleaved design. This is represented in Figure 6.11 as triangular and square data points respectively. By randomly choosing the hypercapnic block av-

eraged time-point to be included, the standard deviation across the 8,000 samples becomes larger. It is therefore suggested that reducing the acquisition time of the interleaved design is best done using shorter respiratory blocks but keeping the same number of blocks.

## 6.5 Conclusion

By using windows of varying sizes to block average the BOLD, CBF and  $P_{ET}O_2$  time-series it was found that reliable parameter estimates could be produced using windows 50% the width of those currently being used in the interleaved design. In practise the extra 50% of surplus data would not be acquired allowing a faster acquisition and measurement of  $CMRO_2$ . However this shortened acquisition still requires experimental confirmation. This would allow reliable parameter estimates to be produced using the interleaved approach with shorter respiratory blocks in  $\sim 13$  minutes.

Using the same analytical approach on the simultaneous respiratory design it was found that reducing the duration of the respiratory challenge blocks in this manner would not be advisable. However the block averaged time-point resampling routine suggests that half the simultaneous design could be conducted using any of the time-based groupings lasting 9 minutes or more. This would mean retaining the size of the respiratory blocks currently being used but reducing the number of respiratory blocks to shorten the acquisition.

Future work to further shorten these acquisition routines should focus on minimising the amount of data disregarded due to transitions or alternatively adding terms to the BOLD signal model to correctly model these transitions.

## Chapter 7

# Investigation of Changes in OEF due to Hypocapnia Induced by Voluntary Hyperventilation Measured using Dual Calibrated fMRI

## 7.1 Introduction

Regional measurements of oxygen extraction fraction (OEF) can be used to assess compensatory responses made by the brain due to alterations in cerebral blood flow (CBF). CBF plays a vital role in oxygen and metabolite delivery allowing the brain to maintain proper function. In healthy brain tissue, CBF is closely matched to the cerebral metabolic rate of  $O_2$  ( $CMRO_2$ ) with little regional variation in OEF. In order to maintain acceptable oxygen levels within brain tissue, reductions in CBF can lead to progressive increases in OEF. Severe reductions in CBF can be implicated in chronic disease, brain trauma and particularly stroke [9] where mismatches in OEF may mean that sufficient levels of oxygen are not maintained leading to cell dysfunction and ischaemia.

### 7.1.1 Dual Calibrated FMRI

Dual calibrated FMRI (dcfMRI) [1–3] allows mapping of venous oxygen saturation ( $S_vO_2$ ) across the brain. Assuming arterial blood is fully saturated, OEF can be estimated as  $1-S_vO_2$  and absolute  $CMRO_2$  can be calculated from Fick’s principle by combining OEF with a measure of CBF. This technique is non-invasive, radioisotope free and is based on combining calibrated BOLD methodologies that traditionally use hypercapnic [45] or hyperoxic [46] challenges allowing estimates of relative change in  $CMRO_2$ . To quantify  $S_vO_2$ , dcfMRI measures blood flow and blood oxygen level dependent (BOLD) signal changes during hypercapnic and hyperoxic respiratory manipulations in the same session and analyses the changes using a BOLD signal model. As this technique provides a method to map  $S_vO_2$ , and hence OEF throughout the brain it is well suited for a wide range of clinical and research applications. However, to become a useful quantitative neuroimaging tool the technique must demonstrate sensitivity in detecting disease or treatment induced changes in  $S_vO_2$ .

### 7.1.2 Hyperventilation and Hypocapnia

Carbon dioxide ( $CO_2$ ) is a known vasodilator. Hypocapnia is a state of reduced  $CO_2$  in blood which causes relative vasoconstriction and is known to globally lower CBF [97–102]. It occurs when arterial partial pressure of carbon dioxide ( $P_aCO_2$ ) in blood is lower than normal.  $P_aCO_2$  describes the amount of  $CO_2$  dissolved in arterial blood and can be inferred by measuring the partial pressure of end tidal  $CO_2$  ( $P_{Et}CO_2$ ). Hypocapnia can be induced as a result of hyperventilation where

the rate and quantity of  $\text{CO}_2$  ventilated from the body exceeds the amount of  $\text{CO}_2$  produced by the body therefore reducing  $P_a\text{CO}_2$ . This can be achieved voluntarily by increasing the depth and frequency of breathing.

Hypocapnia is known to reduce CBF, decreasing the rate of delivery of oxygen available to brain tissue in arterial blood. It is suspected that decreasing blood flow is counteracted by an increase in OEF in an attempt to maintain acceptable  $\text{CMRO}_2$  [103]. However it is unclear if  $\text{CMRO}_2$  changes during hypocapnia, as current studies are complicated by the use of sedation/anaesthesia [104, 105].

Hypocapnia presents a useful physiological state with which to evaluate changes in cerebrovascular and cerebral metabolic function. By performing dual-calibrated fMRI using a modified interleaved respiratory manipulation incorporating hyperventilation, the sensitivity of the technique can be assessed with respect to detecting decreases in  $S_v\text{O}_2$  during a global decrease in CBF. This allows the suitability of the technique for implementation in studies of chronic disease, brain trauma and stroke to be investigated, where changes in regional OEF are of interest. This study will also provide further insight into the behaviour of underlying physiological variables, such as  $\text{CMRO}_2$  and maximum BOLD signal change (M), which contribute towards the BOLD signal during hypocapnia and have previously been the focus of investigation [102, 106, 107].

## 7.2 Methods

### 7.2.1 Participants

Six normal healthy participants (aged 24-40; mean age  $33.5 \pm 5.7$ ; 1 female) were recruited and scanned having given written consent. Experimental procedures were approved by the local institutional ethical review committee. All participants had previous experience performing respiratory manipulations during MR scanning.

### 7.2.2 MRI

Scanning was performed on a 3T GE HDx MRI (GE Healthcare, Milwaukee WI) with a body transmit coil and 8-channel head receive coil. All participants had previous whole brain  $T_1$ -weighted structural scans available (fast spoiled gradient recalled echo, 1x1x1 mm voxels, TI/TR/TE = 450/7.8/3 ms). The scan session lasted approximately one hour and consisted of two interleaved hypercapnic-hyperoxic dcfMRI protocols similar to **Chapter 4**. The first dcfMRI protocol was performed at baseline allowing measurements of  $S_vO_2$  to be made at normal baseline CBF. The second dcfMRI protocol was performed during hypocapnia, providing a new low flow baseline from which changes in  $S_vO_2$  could be compared with the baseline scan. fMRI acquisition for each protocol lasted eighteen minutes with an additional minute for calibration scans. During these protocols simultaneous perfusion and BOLD imaging data was collected using a PASL proximal



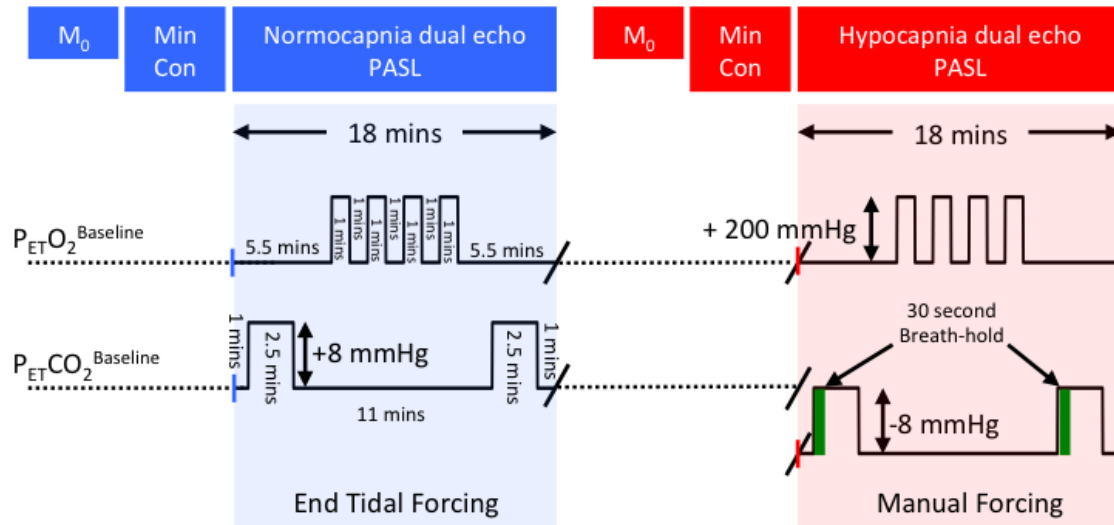


Figure 7.1: Schematic detailing the acquisition strategy for normocapnic (blue) and hypocapnic (red) dcfMRI acquisitions. Calibration ( $M_0$  and minimum contrast) scans were acquired prior to the ASL acquisition. Dual echo PASL was used to simultaneously measure CBF and BOLD changes during an 18 minute measurement. Target end tidal  $O_2$  and  $CO_2$  values for the respiratory manipulations are shown. The normocapnic session was conducted with a system of end tidal forcing. Hypocapnic baseline ( $P_{Et}CO_2 - 8$  mmHg) was achieved using voluntary hyperventilation and an  $EtCO_2$  feedback task. A manual forcing system was employed during the hypocapnic acquisition and was used to deliver the periods of hyperoxia. A 30 second breath-hold (green) was introduced to aid recovery of  $P_{Et}CO_2$  from hypocapnic baseline back to normocapnia.

inversion and control for off-resonance effects (PICORE), quantitative imaging of perfusion using a single subtraction (PICORE QUIPSS II) [37] imaging sequence with a dual-echo gradient echo (GRE) readout and spiral k-space acquisition ( $TE_1 = 3$  ms,  $TE_2 = 29$  ms,  $TR = 2.2$  s, flip angle  $90^\circ$ , FOV 22 cm, matrix  $64 \times 64$ , 12 slices of 7 mm thickness with an inter-slice gap of 1 mm acquired in ascending order,  $TI_1 = 700$  ms,  $TI_2 = 1600$  ms for the most proximal slice and was incremented for the subsequent slices, tag thickness = 20 cm, adiabatic hyperbolic secant inversion pulse, 10 mm gap between labelling slab and bottom slice, 10 cm QUIPSS II saturation band thickness). This resulted in a 490 volume acquisition (245 tag - control pairs) for each of the dcfMRI acquisitions. The calibration scans consisted of a separate single shot,  $M_0$  scan ( $TR = \infty$ ) with the same parameters as the functional run to measure the equilibrium brain tissue magnetisation for purposes of quantifying CBF and a minimum contrast image used to correct for coil sensitivity [82].

### 7.2.3 Respiratory Manipulations

During the baseline condition scan the participant was told to fixate on a cross hair overlaid on a black background allowing resting measures of CBF,  $S_vO_2$ , M and  $CMRO_2$  to be made. The baseline interleaved hypercapnic-hyperoxic respiratory manipulation paradigm is shown in Figure 7.1 highlighted in blue and was administered using a system of end-tidal forcing [63] which offers independent control of partial pressures of end-tidal oxygen and carbon dioxide ( $P_{Et}O_2$  and  $P_{Et}CO_2$  respectively). Details of the respiratory circuit and gas concentrations used can be

found in **Chapter 4**. At the beginning of the scan session the volunteer breathed medical air only without control of  $P_{Et}CO_2$  and  $P_{Et}O_2$  allowing baseline  $P_{Et}CO_2$  and  $P_{Et}O_2$  to be measured. Target profiles for  $P_{Et}O_2$  and  $P_{Et}CO_2$  for the baseline acquisition are also highlighted in blue in Figure 7.1.

The hypocapnic condition scan was performed by decreasing baseline  $P_{Et}CO_2$  by 8 mmHg from that measured in the baseline condition described above. Periods of normocapnia ( $P_{Et}CO_2^{base}$ ) and hypercapnia ( $P_{Et}CO_2^{base} + 8\text{mmHg}$ ) in the baseline conditioned scan correspond to periods of hypocapnia ( $P_{Et}CO_2^{base} - 8\text{mmHg}$ ) and normocapnia ( $P_{Et}CO_2^{base}$ ) respectively in the hypocapnic conditioned scan. Target profiles of  $P_{Et}CO_2$  for the hypocapnic acquisition are shown in Figure 7.1 highlighted in red. Participants were given 2 minutes before the start of the hypocapnic acquisition to reach hypocapnic baseline using voluntary hyperventilation.

In order to achieve a hypocapnic baseline of  $P_{Et}CO_2^{base} - 8\text{mmHg}$  an  $EtCO_2$  feedback task, similar to that used by *Pattinson et al.* [108], was employed. The participant's  $P_{Et}CO_2$  was displayed on a screen along with a target  $P_{Et}CO_2$  shown beside it. Target  $P_{Et}CO_2$  corresponded to  $P_{Et}CO_2^{base} - 8\text{mmHg}$  during periods of hypocapnia and  $P_{Et}CO_2^{base}$  during periods of normocapnia as shown in Figure 7.1 red. To decrease displayed  $P_{Et}CO_2$  participants were instructed to voluntarily hyperventilate by increasing the depth and frequency of breaths. It took participants less than one minute of mild hyperventilation to achieve the hypocapnic baseline ( $P_{Et}CO_2^{base} - 8\text{mmHg}$ ). It was noted during pilot testing that participants took a considerable time,  $>5$  minutes, to return back to normocapnia ( $P_{Et}CO_2^{base}$ ) after a period of time at hypocapnic baseline. To increase scan time efficiency and maintain symmetry between the hypocapnic and baseline respiratory manipulations, 30

second breathholds were introduced. Breath-holding offers a convenient method for elevating  $P_a\text{CO}_2$  by allowing  $\text{CO}_2$  levels in the lungs and blood to increase [109]. This facilitated a rapid return to normocapnia where participants were instructed to resume normal breathing patterns. All participants were trained in  $\text{EtCO}_2$  manipulation by performing several test runs of the  $\text{EtCO}_2$  feedback task outside the scanner until proficiency was proved. These testing sessions took place on separate days prior to the scan session.

The gas delivery system was switched from the end-tidal forcing system to a manually operated system of valves for the hypocapnic condition. This manual forcing was performed as the end-tidal forcing system relies on the accurate detection of inspired and expired breaths. Due to the complexity of the breathing patterns introduced by the hypocapnic paradigm, increased frequency during hyperventilation and periods of breathholding, the forcing system had difficulty accurately detecting inspired and expired breathes. Medical air was delivered to the participants throughout the hypocapnic session and one minute blocks of hyperoxia were delivered manually according to Figure 7.1. If participant's struggled to maintain normocapnia after breathholding a small amount of hypercapnic mixture (10%  $\text{CO}_2$ , balance air) was manually administered.

An interleaved rather than simultaneous hypercapnic-hyperoxic respiratory manipulation was chosen for this study as the complexity of the simultaneous design, with varying levels of hypercapnia during hyperoxia, would have required a higher level of training in participants and increased the likelihood of operator and subject error in performing the respiratory manipulation correctly.

### 7.2.4 Analysis

#### Preprocessing

All image time-series were motion corrected using *3dvolreg* [74]. Time-series image data acquired from the first echo of the PASL technique were used to calculate CBF, while the data from the second echo were used to examine changes in BOLD signal. Physiological noise correction (a modified RETROICOR), was applied by regressing the first and second harmonics of both the cardiac and respiratory cycles from the data along with the interaction term of the first cardiac and respiratory harmonics [80, 81]. Interpolated surround subtraction of the ASL tag and control image time-series was performed to yield a perfusion-weighted time-series [43] which was corrected for coil sensitivity [82]. CBF images were calculated using the  $M_0$  of blood, estimated from the cerebrospinal fluid signal of the  $M_0$  image and the general kinetic model (GKM) [33]. The CBF estimates were adjusted for the likely reduction of the  $T_1$  of arterial blood with increasing plasma concentration of paramagnetic  $O_2$ , according to the blood  $T_1$  values quoted in [51]. Interpolated surround averaging of the tag and control images was performed to yield a BOLD weighted time-series.

#### Grey Matter Analysis

Subject specific ROI's of global grey matter (GM) were produced using FAST segmentation on the high resolution structural images [83] and registered to the native space of CBF and BOLD images using FLIRT [77]. Partial voluming of grey matter was removed by thresholding the GM segmented mask to include

only voxels that were deemed to contain all grey matter. Mean CBF and BOLD timeseries for GM were produced by averaging over the voxels in GM using the ROI mask. Time averaged relative CBF ( $\frac{CBF}{CBF_0}$ ) and BOLD signal ( $\frac{\Delta S}{S_0}$ ) were block averaged to remove periods of transition from the analysis where the BOLD signal model is not applicable. The interleaved design block averaging periods were calculated for each final 30 second period of each 60 second respiratory block (normocapnia with normoxia and normocapnia with hyperoxia in the baseline acquisition and hypocapnia with normoxia and hypocapnia with hyperoxia for the hypocapnic acquisition) and 90 seconds of each 120 second block (hypercapnia with normoxia (baseline) and normocapnia with normoxia (hypocapnic)). The periods of breath-holding were excluded from block averaging. The mean arterial oxygen content,  $C_aO_2$ , was calculated from the  $P_{ET}O_2$  data for the same time periods using Equation A11 from [3].

The BOLD signal model described in [3] was fitted to the global GM, mean CBF and BOLD timeseries using a simple bayesian framework to yield estimates of  $M$  and  $S_vO_2$  for the baseline and hyperventilation conditions permitting calculation of absolute  $CMRO_2$ .  $\alpha = 0.14$  and  $\beta = 0.91$  were chosen from [85]. Priors for  $M$  and  $S_vO_2$  were generated as normal probability density functions centred around initial estimates of 0.08 and 0.5 with broad standard deviations of 0.02 and 0.1. By applying Bayes' rule to the first time points of averaged data  $\frac{\Delta S}{S_0}$ ,  $\frac{CBF}{CBF_0}$  and  $C_aO_2$ , posterior probability distributions of the variables,  $M$  and  $S_vO_2$ , were generated after integrating over the ranges  $0.01 - 0.15$  ( $M$ ) and  $0.2 - 0.8$  ( $S_vO_2$ ). These were chosen to be beyond the extremes of physiologically plausible values. The posterior distributions were used as the priors for calculations with the second time points

of averaged data and so on until a final posterior distribution for each of the two variables was obtained. The maxima of these probability distribution functions provided the estimates of  $M$  and  $S_vO_2$  for each subject. Absolute  $CMRO_2$  was then calculated using the equation:

$$CMRO_2 = OEF \cdot CBF \cdot C_aO_2 \quad (7.1)$$

### Whole Brain Analysis

Whole brain parameter maps of  $M$ ,  $S_vO_2$  and  $CMRO_2$  at normocapnia and hypocapnia, Figure 7.3, were produced by following the analysis pipeline and fitting routine outlined. The whole brain CBF and BOLD timeseries were analysed on a voxel-wise basis to obtain estimates of  $M$ ,  $S_vO_2$  and  $CMRO_2$  for each voxel.

### Statistical Analysis

From the mean GM ROI measures in Table 7.1, tests for group decreases in CBF and  $S_vO_2$  between normocapnia and hypocapnia were performed using one-tailed, paired t-tests as it was hypothesised that hypocapnia would cause global decreases in both parameters. Tests for group differences between normocapnia and hypocapnia in  $M$  and  $CMRO_2$  were performed using a two-tailed paired t-test. Tests for regional differences between normocapnic and hypocapnic  $M$ , CBF,  $S_vO_2$  and  $CMRO_2$  were performed using *3dttest++* [74]. This was achieved by registering the individual whole brain parameter maps of  $M$ , CBF,  $S_vO_2$  and  $CMRO_2$  to MNI152 space (Montreal Neurlogical Institute) [76] through the hi-resolution

structural image using FLIRT. T-statistic maps produced as a result of this analysis are presented in Figure 7.4.

## 7.3 Results

### 7.3.1 Hypocapnic $P_{Et}CO_2$

The mean group  $P_{Et}CO_2$  for normocapnic baseline was  $43.7 \pm 1.9$  mmHg and hypocapnic baseline was  $35.1 \pm 2.6$  mmHg. Normalised  $P_{Et}CO_2$  ( $\frac{P_{Et}CO_2^{measured}}{P_{Et}CO_2^{targetbase}}$ ) for the hypocapnic run are shown in Figure 7.2. All six participants were successful in using mild voluntary hyperventilation to reach and maintain hypocapnic baseline. As noted the most difficult part of the task was returning to normocapnia. The thirty second breath-holds introduced to speed up the transition from hypocapnia worked well and participants who still struggled to return to normocapnia were administered a small amount of hypercapnic mixture manually.

### 7.3.2 Global Grey Matter Analysis

Table 7.1 presents the whole brain grey matter CBF, M,  $S_vO_2$  and  $CMRO_2$  measures made using dcfMRI at baseline normocapnia and hypocapnia. Group average values were calculated including and excluding an outlier which produced unrealistic measures of  $S_vO_2$  at rest. Excluding the outlier, significant differences were detected with hypocapnia in all parameters except  $CMRO_2$ .



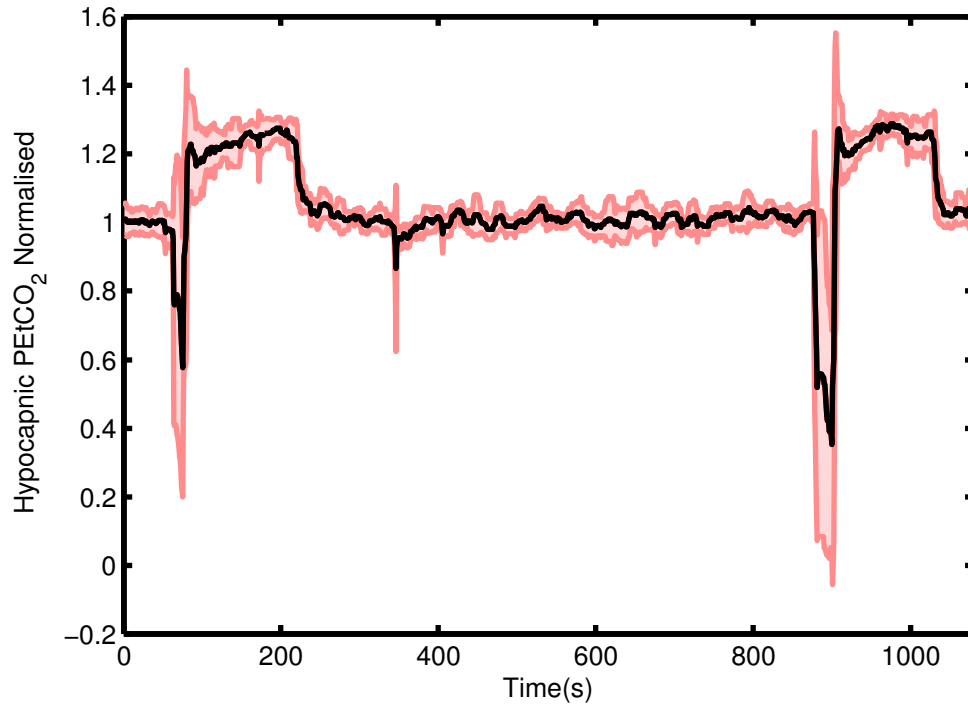


Figure 7.2: Mean normalised  $P_{Et}CO_2$  ( $\frac{P_{Et}CO_2^{measured}}{P_{Et}CO_2^{target}}$ ) (black) for the hypocapnic condition with standard deviation shown in red. The dips in transition between hypocapnia and normocapnia are due to the breath holds employed to aid sharper transition back to normocapnia. These periods were excluded from block-averaging. The mean, group target  $P_{Et}CO_2$  for hypocapnic baseline was  $35.3 \pm 2.5$  mmHg.

Subject	M		$S_vO_2$		$CBF_{base}$		$CMRO_2$	
	Normo	Hypo	Normo	Hypo	Normo	Hypo	Normo	Hypo
1	0.04±0.00	0.01±0.00	0.64±0.07	0.48±0.08	50.0	31.9	141.3	129.9
2	0.04±0.00	0.02±0.00	0.49±0.05	0.43±0.07	45.4	36.8	181.6	163.9
3	0.06±0.00	0.02±0.00	0.43±0.05	0.41±0.07	44.8	35.0	206.8	157.5
4	0.05±0.00	0.02±0.00	0.51±0.05	0.41±0.07	57.6	45.2	222.0	209.9
5	0.05±0.00	0.02±0.00	0.52±0.07	0.46±0.07	40.0	33.9	149.9	142.2
6	0.05±0.00	0.02±0.00	0.85±0.00	0.46±0.08	40.0	30.3	46.5	127.6
Mean±std	0.05±0.01	0.02±0.01 *	0.57±0.15	0.44±0.03 *	46.3±6.7	35.5±5.2 *	158.0±62.9	155.2±30.5
Mean±std†	0.05±0.01	0.02±0.01 *	0.52±0.08	0.44±0.03 *	47.5±6.6	36.6±5.1 *	180.3±34.9	160.7±30.6

Table 7.1: Comparison of physiological variables measured during normocapnia and hypocapnia in global GM ROI's for  $\alpha=0.14$  and  $\beta=0.91$ . Estimates of M and  $S_vO_2$  and their measurement error were made from the posterior distributions produced by the fitting routine.  $CMRO_2$  was calculated using Equation 7.1.

† = subject 6 removed from group analysis.

\* = significant ( $p<0.05$ ) difference between normocapnia and hypocapnia were tested for in the case of M and  $CMRO_2$  (two-tailed, paired t-test) and decreases were hypothesised in the case of CBF and  $S_vO_2$  (one-tailed, paired t-test)

### 7.3.3 Whole Brain Parameter Maps

Group averaged ( $n = 6$ ), whole brain parameter maps acquired at normocapnia (left) and hypocapnia (right) using interleaved hypercapnic-hyperoxic respiratory manipulations are presented in Figure 7.3. Target end tidal values for both respiratory manipulations can be seen in Figure 7.1. An end tidal forcing system was used for the normocapnic session and manual forcing and an EtCO<sub>2</sub> feedback task was used during the hypocapnia session. Whole brain reductions in all four parameters due to hypocapnia can be visualised and agree well with ROI measures presented in Table 7.1. It is important to note that measures are limited to grey matter as a result of limitations associated with measuring CBF using ASL.

T-statistic maps presented in Figure 7.4 were produced by voxelwise, paired t-test analysis (normocapnia - hypocapnia) conducted between the normocapnic and hypocapnic parameter maps. Grey matter structure is visible in the CBF statistical map and to an extent in the CMRO<sub>2</sub> and M statistical maps but no clear pattern or structure is perceptible in the S<sub>v</sub>O<sub>2</sub> statistical map.

## 7.4 Discussion

In this study we have investigated cerebrovascular and cerebral metabolic indicators during normocapnia and hypocapnia. This was achieved by measuring M, S<sub>v</sub>O<sub>2</sub>, CBF and CMRO<sub>2</sub> using dcfMRI in both states. Normocapnic measures were made using a system of end tidal forcing. The hypocapnic state was achieved using an EtCO<sub>2</sub> feedback task similar to that used by *Pattinson et al.* [108] and a

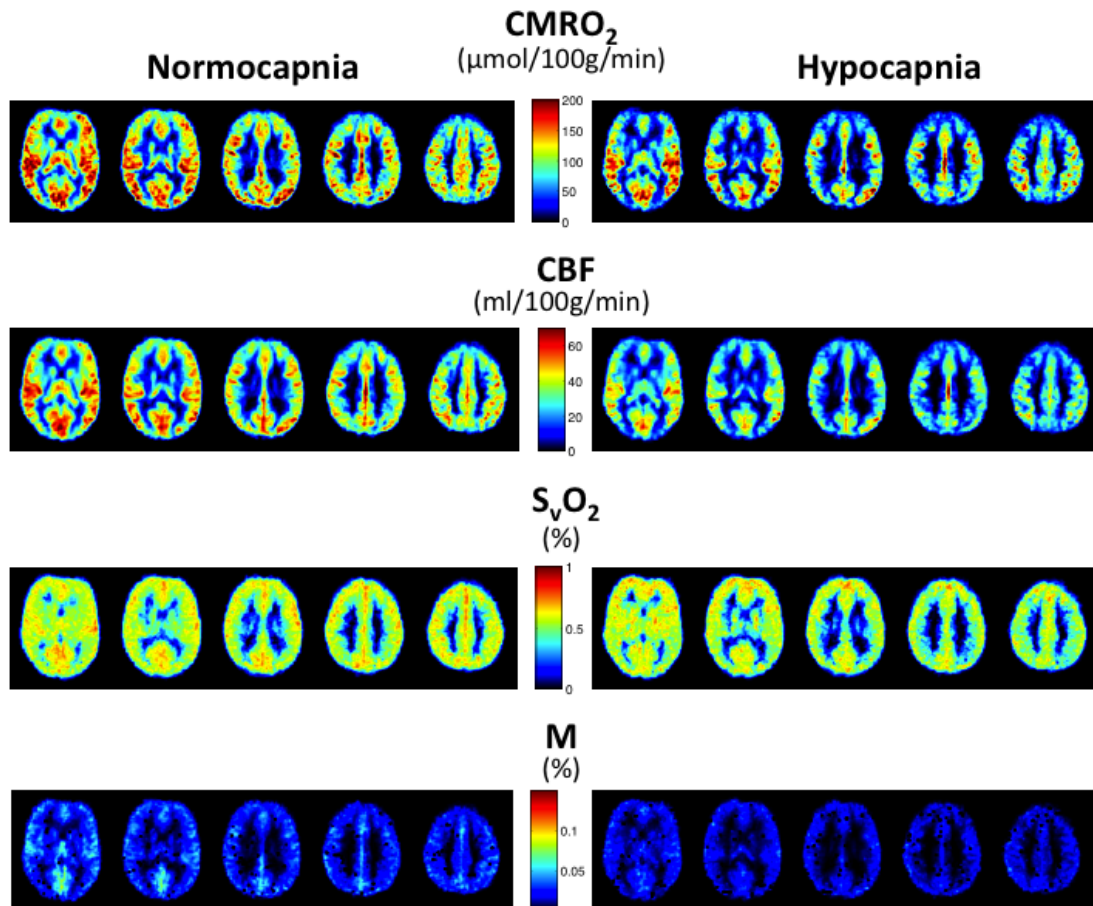


Figure 7.3: Group averaged (n=6), whole brain parameter maps acquired at normocapnia (left) and hypocapnia (right) using interleaved hypercapnic-hyperoxic respiratory manipulations.

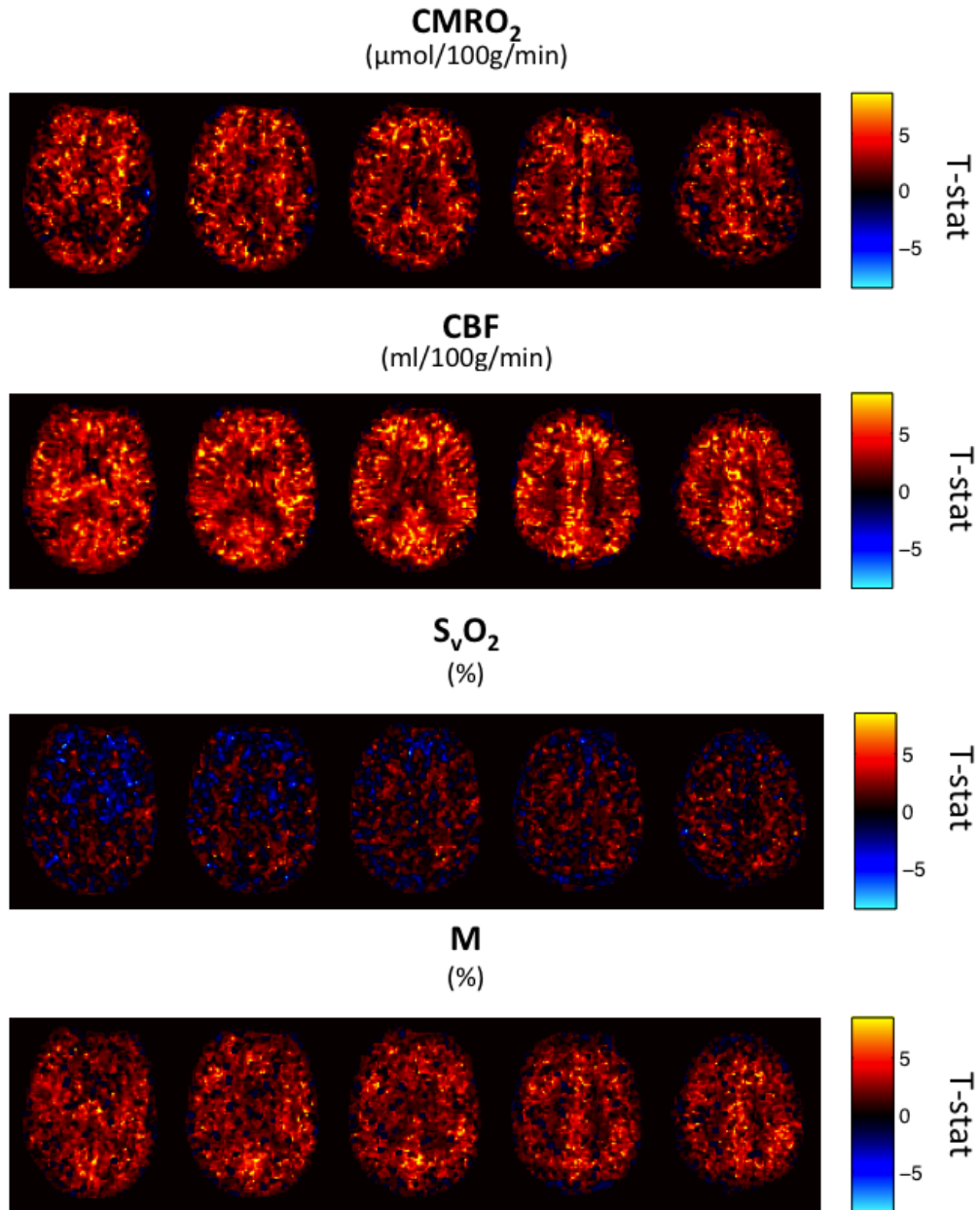


Figure 7.4: T-statistic maps produced as a result of the voxelwise, paired t-test analysis (normocapnia - hypocapnia) conducted between the normocapnic and hypocapnic parameter maps.

manual forcing system to achieve a hypocapnic baseline of  $P_{Et}CO_2^{normocapnia} - 8$  mmHg.

A regional analysis of global GM produced estimates of CBF, M,  $S_vO_2$  and  $CMRO_2$  in all six participants during normocapnia and hypocapnia is shown in Table 7.1. Tenable estimates were produced by the fitting routine for all but one participant. It can be seen from Table 7.1 that subject 6 produced an unrealistic estimate of  $S_vO_2$  in normocapnia (0.85). This is considerably above the accepted range of  $S_vO_2$  values (0.7 - 0.55) and resulted in an unrealistic estimate of  $CMRO_2$  in grey matter of  $46.5 \mu\text{mol}/100\text{g}/\text{min}$ . Therefore group mean and standard deviations for each variable including and excluding subject 6 are displayed at the bottom of Table 7.1. Parameters estimated during normocapnia and hypocapnia, including and excluding subject 6 were also tested for significant differences, in the case of M and  $CMRO_2$  and decreases, in the case of  $S_vO_2$  and CBF. Significant decreases with hypocapnia of M,  $S_vO_2$  and CBF were detected including and excluding the outlier. A non significant decrease ( $p = 0.06$ ) in  $CMRO_2$  of  $19.6 \mu\text{mol}/100\text{g}/\text{min}$  (10.9%) was found when subject 6 was excluded from statistical testing. No significant difference was present when the outlier subject was included.

CBF demonstrated a decrease of  $2.9 \pm 0.9 \text{ \%/mmHg}$  (subject 6 included) and  $2.8 \pm 1.0 \text{ \%/mmHg}$  (subject 6 excluded). These values agree well with those reported in PET literature, with *Ito et al.* [99] reporting decreases in CBF of  $3.5 \pm 0.6 \text{ \%/mmHg}$  with hypocapnia in the cerebral cortex and *Yokoyama et al.* [101] reporting decreases of  $3.0 \pm 1.1 \text{ \%/mmHg}$  for the whole brain. An MRI based study by *Chen & Pike* [102] reported larger decreases with hypocapnia of between  $4.7 \pm 0.8 \text{ \%/mmHg}$  and  $5.2 \pm 0.7 \text{ \%/mmHg}$  in GM using ASL.

Estimates of  $S_vO_2$  at normocapnia ( $0.52 \pm 0.08$ ) agree well with previous measures made using the same interleaved respiratory manipulation in **Chapter 4** and **Chapter 5**. However as discussed in **Chapter 4** and in reference [3] this technique yields estimates of  $S_vO_2$  that are on the low end of the spectrum when compared to other dcfMRI studies by *Bulte et al.* (0.62) [1] and *Gauthier & Hoge* (0.65) [2].  $S_vO_2$  experienced a significant decrease from 0.52 to 0.44 excluding the outlier subject who measured 0.85 at normocapnia. This is a  $14.9 \pm 8.0$  % decrease in  $S_vO_2$  with an 8 mmHg challenge. In a previous investigation of hypocapnia with MR, *Chen & Pike* [102] estimated whole brain  $S_vO_2$  from venous blood  $T_2$  in the jugular vein and reported decreases of 2.2 - 2.6 %/mmHg suggesting a 17.6 - 20.8 % decrease for an 8 mmHg decrease in  $P_{Et}CO_2$ .

Significant decreases in the maximum BOLD signal were observed with M decreasing from 0.049 to 0.017 with hypocapnia. This is a large decrease of  $63.9 \pm 9.9$  % or 8 %/mmHg. M is related to baseline cerebral blood volume ( $CBV_0$ ) and deoxy-hemoglobin concentration ( $[dHb]_0$ ) through the equation  $M = TE\kappa CBV_0[dHb]_0^\beta$  [45, 49]. If we consider that  $[dHb]_0 = [Hb](1-S_vO_2)$  a drop in baseline  $S_vO_2$  as is the case with hypocapnia should result in an increase in  $[dHb]_0$ . However investigations with PET [99] reported a decrease in CBV of  $1.3 \pm 1.0$  %/mmHg. These observations do not explain the large decrease in M that is measured with hypocapnia.

However M is also dependent on  $\kappa$  and  $\beta$ . These constants are both field dependent with  $\kappa$  incorporating vessel geometry and susceptibility differences between vessels and tissue and  $\beta$  incorporating vessel size and diffusion effects. If these presumed constants vary due to hypocapnia these changes will not be accounted for in the

model outside of  $M$ , as  $\beta$  is fixed and may manifest itself as a decrease in  $M$ . Further investigation is needed to explore the effect of changes of  $\kappa$  and  $\beta$  in the model and the effect this will have on the estimation of  $M$ .  $M$  may no longer represent just the maximum BOLD signal change and may be better explained as simply a fitting parameter capable of capturing several sources of physiological variation, much in the same way as the new values of  $\alpha$  and  $\beta$  are described by *Griffeth et al.* [85]. It is also worth noting that if collinearity exists between  $\alpha$  and  $\beta$ , changes in  $\alpha$  with hypocapnia could result in changes in  $M$ .

Excluding the outlying subject, group average  $CMRO_2$  estimates at rest agree well with those already published using this technique. Resting measurements are high relative to other MR and PET studies as a result of low estimates of  $S_vO_2$  discussed above. As previously noted a non-significant decrease ( $p = 0.06$ ) in  $CMRO_2$  of  $19.6 \pm 17.0 \mu\text{mol}/100\text{g}/\text{min}$  ( $10.4 \pm 7.7 \%$ ) was detected due to hypocapnia leading to a  $1.3 \%/mmHg$  decrease in  $CMRO_2$ . Although the decrease in  $CMRO_2$  is not significant the trend in decreasing  $CMRO_2$  with hypocapnia is apparent from Table 7.1 This noticeable effect of hypocapnia on  $CMRO_2$  is in contrast to the limited reports of hypocapnia and  $CMRO_2$  in the literature. *Chen & Pike* [102] reported a  $2.2 - 3.5 \%/mmHg$  increase in whole brain  $CMRO_2$  with hypocapnia using MRI. *Kety & Schmidt* [97] reported a group average increase of  $14 \%$  in  $O_2$  consumption using voluntary hyperventilation and a direct blood sampling technique. However this was over a much greater decrease in  $CO_2$  of  $18 \text{ mmHg}$  leading to an increase in  $CMRO_2$  of  $0.8 \%/mmHg$ . *McPherson et al.* [104] reported no change of  $CMRO_2$  in anaesthetised canines with hypocapnia using radio labelled microspheres and a PET study by *Gjedde et al.* [103] which did not employ hypocapnia



but instead used indomethacin, a non-steroidal anti-inflammatory drug, to reduce CBF significantly by 34 % leading to a 8 % non-significant decrease in  $\text{CMRO}_2$ . EEG [110] and MEG [111] studies have also been used to measure negative DC-shifts with hyperventilation, reflecting increased excitatory synaptic transmission suggesting increases in  $\text{CMRO}_2$ . Evidence from these studies point in the direction of increases in  $\text{CMRO}_2$  with hypocapnia. The results shown in this study of decreasing  $\text{CMRO}_2$  with hypocapnia could be due to a bias in the BOLD signal model. Refinement of the model is an area for future improvement, however it is encouraging to see that the direction of change in  $\text{S}_v\text{O}_2$  and CBF agree well with what is expected. As has been suggested by results presented in [97, 102] there may be a nonlinear relationship between the degree of hypocapnia and its effect on the physiological variables measured. This could be further investigated using the approach presented in this study by modifying the  $\text{EtCO}_2$  feedback task to achieve hypocapnic baselines of different levels.

The T-statistic maps presented in Figure 7.4 were thresholded and clustered to investigate if there were any obvious regional differences as a result of hypocapnia induced changes in CBF, M,  $\text{S}_v\text{O}_2$  and  $\text{CMRO}_2$ . After thresholding and clustering at a number of different p-values and cluster thresholds no evident regional change was noticeable. It is interesting to note that grey matter structure is visible in the CBF statistical map and to an extent in the  $\text{CMRO}_2$  and M statistical maps but no clear pattern or structure is perceptible in the  $\text{S}_v\text{O}_2$  statistical map. As only 5 subjects are used in this analysis, a larger group size may be needed to investigate if changes in the physiological parameters with hypocapnia have any regional variation or bias.

Further limitations are associated with the use of a task to achieve hypocapnia. Neural activity caused by the performance of the EtCO<sub>2</sub> feedback task may influence the measured physiological parameters. It is also worth noting that inaccuracies may be present in the CBF measurement. The use of ASL with a single imaging time may not accurately measure the CBF differences between the normocapnic and hypocapnic states if there are large enough differences in the arterial arrival times (AAT) of these two states. This could be overcome using multi-TI ASL approach to accurately model the discrepancies in AAT.

## 7.5 Conclusion

dcfMRI was used to successfully acquire measures of CBF, M, S<sub>v</sub>O<sub>2</sub> and CMRO<sub>2</sub> during normocapnia and hypocapnia in 5 of 6 participants. Decreases in all measured variables were detected in GM, with all but CMRO<sub>2</sub> showing significant differences. The data demonstrate a clear trend in CBF, M, S<sub>v</sub>O<sub>2</sub> and CMRO<sub>2</sub> between normocapnia and hypocapnia in global grey matter. This demonstrates the sensitivity of the dcfMRI protocol to detect changes in OEF and suggests that the technique is appropriate for clinical application in areas such as stroke or vascular dysfunction in which flow is impaired.

## Chapter 8

# Comparison of Asymmetric Spin Echo with Dual Calibrated fMRI using Hypercapnic-Hyperoxic Respiratory Challenges

### 8.1 Introduction

Oxygen metabolism is the principle form of energy production in the brain and techniques allowing quantitative measurement of this process provide valuable information on neural energy consumption. Dual calibrated fMRI (dcfMRI) [1–3] is a recent extension of the calibrated BOLD methodology [45,46]. Calibrated BOLD utilises a single respiratory manipulation such as hypercapnia or hyperoxia to allow relative, task related changes in the cerebral metabolic rate of oxygen ( $\text{CMRO}_2$ ) consumption to be quantified. Similarly dcfMRI relies on relating changes in cerebral blood flow (CBF) and blood oxygen level dependent (BOLD) signals during respiratory manipulations to a BOLD signal model. However by using both hypercapnic and hyperoxic challenges, quantification of absolute baseline  $\text{CMRO}_2$

can be made. dcfMRI offers a radioisotope free, noninvasive, MRI based technique that is capable of investigating the regional and spatial extent of cerebral oxygen metabolism. By providing quantitative physiological measures that can be tracked longitudinally, this technique broadens the appeal of fMRI making it a more useful clinical and research based tool.

### 8.1.1 Hypercapnia

Hypercapnia was used in the original calibrated BOLD methodology which allowed the estimation of relative changes in  $\text{CMRO}_2$  [45]. However a number of disadvantages have been discussed in literature regarding the use of hypercapnia. *Chiarelli et al.* [46] cited onset of breathlessness and the potential intolerability in distressed or infirm subjects as some of the reasons for the introduction of the alternative hyperoxic calibration methodology. *Mohtasib et al.* [112] made reference to the hyperoxic calibration technique as being more comfortable and better tolerated when implementing calibrated BOLD for studying an ageing population. Concerns over the potential of a hypercapnic challenge to cause sensory stimulation due to air hunger have also been expressed [113]. As a result it would be useful to have an alternative calibration technique to use in conjunction with hyperoxia in the dcfMRI framework to avoid the use of hypercapnia for the estimation of absolute  $\text{CMRO}_2$ .

### 8.1.2 Relaxometry and Quantitative BOLD

A model for the quantification of the haemodynamic properties of the brain was proposed by *Yablonskiy et al.* [114]. The method presented in this study relates the reversible transverse relaxation rate ( $R'_2$ ) to cerebral blood volume (CBV) and the deoxyhaemoglobin concentration ( $[dHb]$ ) of the blood present. Techniques measuring the time signal decay of a gradient echo (GE) and spin echo (SE) have been able to utilise this mathematical model to estimate measures of venous oxygen saturation ( $S_vO_2$ ) and CBV in techniques dubbed quantitative BOLD (qBOLD) [115].

However these techniques involve the fitting of a complex model to the time dependent signal decay and it has been demonstrated through simulation and phantom studies that these techniques require very high SNR in order to distinguish between CBV and  $S_vO_2$  as there is a strong interdependence between the two parameters [116]. It has been pointed out that this interdependence of the two parameters may require the independent estimation of one variable to determine reliable values of the other [117].

The qBOLD approach has progressively become more complex with multi-parametric approaches being employed to estimate relevant variables [118, 119] and more intensive modelling being applied [120]. *Blockley et al.* [69, 121] has recently proposed that qBOLD style techniques could be used for the estimation of the maximum BOLD signal change ( $M$ ) and demonstrated the feasibility of this approach through numerical simulation.  $M$  is the desirable parameter measured in a calibrated BOLD experiment which facilitates the quantitation of relative  $CMRO_2$

changes. Subsequently  $M$  is a key parameter requiring estimation in the dcfMRI methodology allowing calculation of absolute  $\text{CMRO}_2$ . Although  $M$  is dependent on  $\text{CBV}$  and  $S_v\text{O}_2$  its estimation doesn't require the independent determination of either parameter and can instead be measured together in one grouped term. This overcomes the problem of trying to disentangle two interdependent variables from the data.

The aim of this chapter is to evaluate the use of  $R'_2$  relaxometry for the measurement of maximum BOLD signal change ( $M_{R'_2}$ ) and compare it to maximum BOLD signal change determined by hypercapnic calibrated BOLD ( $M_{hc}$ ) and hyperoxic calibrated BOLD ( $M_{ho}$ ) as well as the  $M$  measured using dcfMRI ( $M_{dcfMRI}$ ).  $M_{R'_2}$  is then integrated into the hyperoxic calibrated BOLD technique allowing measures of absolute  $\text{CMRO}_2$  in grey matter (GM) to be made in a manner analogous to dcfMRI. The results are then compared to a more traditional dcfMRI approach using an interleaved hypercapnic-hyperoxic set up, the details of which are presented in **Chapter 4**. The *Background and Theory* section (Section 8.2) introduces the original BOLD signal model proposed by *Davis* [45] and *Hoge* [49]. The derivation of  $M$  is demonstrated and the simplification of the model in the case of individual hypercapnic and hyperoxic calibrations is presented. The combination of hypercapnic and hyperoxic challenges for dual calibration is then discussed allowing the measurement of  $S_v\text{O}_2$  and in turn absolute  $\text{CMRO}_2$ . Finally the relationship of  $R'_2$  with  $M$  is considered and a framework for measuring  $S_v\text{O}_2$  and in turn absolute  $\text{CMRO}_2$  is proposed by combining  $M_{R'_2}$  and hyperoxic calibrated BOLD.

## 8.2 Background and Theory

FMRI is a well established technique most frequently used to investigate regions of increased task related, neuronal function. This is performed by measuring relative changes in BOLD signal from an unquantified baseline state. The magnitude of BOLD signal change is a function of underlying physiological processes, CBF and  $\text{CMRO}_2$ , as well as being dependent on the unknown baseline state defined by  $[\text{dHb}]_0$  and  $\text{CBV}_0$ . Subscript 0 is used in this case to denote the baseline state of the given physiological variable. As a result of the non-quantitative nature and complicated dependence on the previously described physiological variables the interpretation of BOLD signal changes can become difficult.

### 8.2.1 Calibrated BOLD

The calibrated BOLD methodology was introduced to improve interpretability of task related changes in BOLD. This is achieved by estimating  $M$  for the current baseline state allowing estimates of relative change in  $\text{CMRO}_2$  to be inferred from task related changes in BOLD and CBF. To measure  $M$ , a calibration scan is performed where BOLD signal changes are induced by increasing venous  $[\text{dHb}]$ . This can be done by inducing mild hypercapnia [45] or hyperoxia [46] in the participant. The respiratory challenges are considered to be isometabolic and as such do not alter brain metabolism [102]. Hypercapnia involves increasing inspired  $\text{CO}_2$  causing an isometabolic increase in CBF. Hyperoxia is an increase in inspired  $\text{O}_2$  and increases the arterial oxygen content ( $C_a\text{O}_2$ ). The induced BOLD signal changes

can then be interpreted using a simple BOLD signal model derived by *Davis et al.* [45] and *Hoge et al.* [49].

BOLD signal changes depend on changes in [dHb]. Due to its paramagnetic nature and presence in blood vessels, deoxyhaemoglobin (dHb) creates a susceptibility difference with surrounding brain tissue resulting in local signal decreases due to the enhanced relaxation rate. This is dependent on the amount of dHb present and can be related to  $R_2^*$ , the transverse relaxation rate.  $R_2^*$  is also dependent on the volume of blood present described as CBV by [29]. Considering a voxel with a normal resting  $R_2^*$ , removing all dHb from that voxel causes a change in  $R_2^*$  that can be described by  $\delta R_2^*$ , Equation 8.1, where constants  $\kappa$  and  $\beta$  are both field dependent constants and  $\beta$  is dependent on vessel size and geometry.

$$\delta R_2^* = \kappa CBV_0 [dHb]_0^\beta \quad (8.1)$$

Maximum BOLD signal change (M) can then be calculated as:

$$M = TE \cdot \kappa CBV_0 [dHb]_0^\beta = TE \cdot \delta R_2^* \quad (8.2)$$

Changes in BOLD signal can be described as  $\Delta R_2^*$ :

$$\Delta R_2^* = \kappa CBV [dHb]^\beta - \kappa CBV_0 [dHb]_0^\beta \quad (8.3)$$



Small changes in  $\Delta R_2^*$ , such as those that are experienced during an FMRI experiment can be approximated by Equation 8.4 where  $\frac{\Delta S}{S_0}$  is the fractional increase in BOLD signal which takes the echo time (TE) of the acquisition sequence into account.

$$\frac{\Delta S}{S_0} = e^{-TE\Delta R_2^*} - 1 \approx -TE\Delta R_2^* \quad (8.4)$$

Substituting Equation 8.3 for  $\Delta R_2^*$  in Equation 8.4 gives:

$$\frac{\Delta S}{S_0} = TE\kappa CBV_0 [dHb]_0^\beta \left( 1 - \left( \frac{CBV}{CBV_0} \right) \left( \frac{[dHb]}{[dHb]_0} \right)^\beta \right) \quad (8.5)$$

Substituting Equation 8.2 into Equation 8.5 the term for maximum BOLD signal change can be incorporated into the model:

$$\frac{\Delta S}{S_0} = M \left( 1 - \left( \frac{CBV}{CBV_0} \right) \left( \frac{[dHb]}{[dHb]_0} \right)^\beta \right) \quad (8.6)$$

In the case of hypercapnia Equation 8.6 reduces to Equation 8.7 where increases in inspired  $\text{CO}_2$  are assumed to cause isometabolic CBF changes.  $\alpha$  is the Grubb constant [50], a value taken from literature, and relates changes in CBF to changes in CBV as  $\left[ \frac{CBF}{CBF_0} \right]^\alpha = \left[ \frac{CBV}{CBV_0} \right]$ .

$$\frac{\Delta S}{S_0} = M \left( 1 - \left( \frac{CBF}{CBF_0} \right)^{\alpha-\beta} \right) \quad (8.7)$$

In the case of hyperoxia an isometabolic increase in  $C_aO_2$  is assumed to have no effect on CBF and Equation 8.6 is simplified to:

$$\frac{\Delta S}{S_0} = M \left( 1 - \left( 1 - \frac{\Delta C_a O_2}{\phi[Hb](1 - S_v O_2)} \right)^\beta \right) \quad (8.8)$$

Both equations can then be solved for M with all other parameters being measured or assumed. However it is important to note that hyperoxic calibration requires a value for  $S_v O_2$  to be assumed.

### 8.2.2 Dual Calibrated fMRI

dcfMRI uses a two point calibration, inducing BOLD and CBF changes by hypercapnic and hyperoxic respiratory manipulations which are performed in the same session. In it's simplest form, as described by *Bulte et al.* [1], M can be calculated using the hypercapnic calibrated BOLD approach, meaning  $S_v O_2$  no longer needs to be assumed in the hyperoxic calibration. Instead the equation can now be solved for  $S_v O_2$ . Assuming arterial blood is fully saturated the oxygen extraction fraction can be calculated as  $OEF = 1 - S_v O_2$  and  $CMRO_2$  measured using Fick's equation:

$$CMRO_2 = OEF \cdot CBF \cdot C_a O_2 \quad (8.9)$$

The approach of *Gauthier et al.* [2] and *Wise et al.* [3] to dcfMRI differ only in the application of the BOLD signal model. Instead of estimating M independently

using hypercapnic calibration and determining  $S_vO_2$  using hyperoxic calibration, the *Davis/Hoge* model (Equation 8.6), is expanded to accommodate simultaneous modulations of CBF and  $C_aO_2$ . The model reduces to the hypercapnic (Equation 8.7) and hyperoxic (Equation 8.8) based models when arterial oxygen levels and CBF are held constant respectively. However  $M$  and  $S_vO_2$  are estimated by simultaneously optimising these parameters to the data through the expanded model. The approach taken by *Bulte et al.* [1] suggests that if  $M$  is known,  $S_vO_2$  and in turn absolute  $CMRO_2$  can be measured using a hyperoxic calibration technique and it is this approach that we exploit in this chapter.

### 8.2.3 $R_2'$

$[dHb]$  can also be inferred by directly quantifying the relaxation properties of brain tissue. As noted above  $dHb$  present in blood vessels causes a susceptibility difference with surrounding tissue resulting in attenuation of the transverse relaxation rate,  $R_2^*$ .  $R_2^*$  can be expressed as the sum of reversible ( $R_2'$ ) and irreversible ( $R_2$ ) dephasing with relation to spin echo refocussing (Equation 8.10).  $R_2'$  is dephasing caused by local magnetic field inhomogeneities that can be refocused by a spin echo whereas  $R_2$  is dephasing due to the thermal motion of molecules, referred to as spin-spin interactions, and cannot be refocused by a spin echo.

$$R_2^* = R_2' + R_2 \quad (8.10)$$

*Yablonskiy et al.* [114] demonstrated that  $R'_2$  can be related to  $CBV_0$  and  $[dHb]_0$ . From Equation 8.1,  $R_2^*$  describes the amount of dHb present in blood vessels and is given by:

$$R_2^* = \kappa CBV_0 [dHb]_0^\beta \quad (8.11)$$

Assuming that BOLD effects are solely described by  $R'_2$  and reversible transverse relaxation, Equation 8.10 becomes:

$$R_2^* = R'_2 \quad (8.12)$$

Substituting Equation 8.12 into Equation 8.11 gives:

$$R'_2 = \kappa CBV_0 [dHb]_0^\beta \quad (8.13)$$

From Equation 8.2,  $M$  can now be described in terms of  $R'_2$  as:

$$M = TE \cdot R'_2 \quad (8.14)$$

However effects contributing to BOLD signal change ( $\Delta R_2^*$ ) are not considered to be solely reversible. As suggested by simulations irreversible components may contribute towards the signal [122], however further simulations suggest BOLD signal changes can be directly scaled with  $R'_2$  [69].

### Asymmetric Spin Echo (ASE) for Measuring $R'_2$

A single shot ASE can be implemented to provide a measure of  $R'_2$ . In a traditional spin echo experiment a  $180^\circ$  refocusing pulse is applied at  $\frac{TE}{2}$  and a re-phased spin echo is formed at TE where the signal is acquired. In an ASE experiment the signal is still acquired at TE but the  $180^\circ$  refocusing pulse is shifted by  $\frac{\tau}{2}$  so that the re-phased echo is shifted by  $TE - \tau$  with respect to the centre of the signal acquisition window, as shown in Figure 8.1.

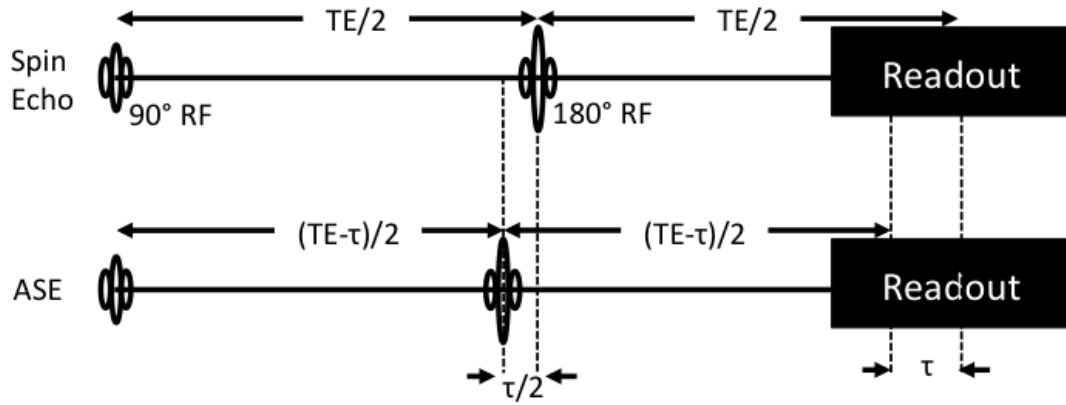


Figure 8.1: Comparison of a spin echo (SE) and asymmetric spin echo (ASE) pulse sequence. In the ASE approach the  $180^\circ$  refocusing pulse is shifted asymmetrically by  $\frac{\tau}{2}$  with respect to the SE refocusing pulse.

The signal refocused by a symmetric SE at a given TE can be described by Equation 8.15 where  $S_0$  is the signal acquired at  $TE = 0$  and is dependent on  $R_2$ , the irreversible decay.

$$S_{SE} = S_0 e^{-TE \cdot R_2} \quad (8.15)$$

By shifting the refocused spin echo by  $-\tau$  with respect to the acquisition time (TE), the signal attains additional attenuation due to  $R'_2$  dephasing. The signal acquired using ASE at TE has an extra attenuation term which describes the  $R'_2$  dephasing, that occurs during time  $\tau$ , as a result of shifting the refocusing pulse by  $\frac{\tau}{2}$ :

$$S_{ASE} = S_0 e^{-TE \cdot R_2} e^{-\tau \cdot R'_2} \quad (8.16)$$

To ensure that measures of  $R'_2$  are localised to the dephasing occurring as a result of susceptibility differences between blood vessels and brain tissue due to dHb, attenuation of the ASE signal due to larger scale magnetic field inhomogeneities must be accounted for. These larger scale magnetic field inhomogeneities occur because of susceptibility differences at tissue/air and tissue/bone interfaces and can be corrected. This can be done by acquiring high-resolution field maps and calculating the frequency difference across voxels in the slice direction ( $\Delta\omega$ ). Although there is the potential for in plane dephasing to also occur, these signal attenuations were deemed to be small when compared to through slice dephasing due to the relative strength of the gradients used.

$$\Delta\omega = \gamma G_z \Delta z \quad (8.17)$$

An attenuation correction factor for differences due to large scale magnetic field inhomogeneities can then be corrected using a  $\tau$  dependent sinc function:

$$F(\tau) = \text{sinc}\left(\frac{\tau\Delta\omega}{2}\right) \quad (8.18)$$

For single shot ASE, TE doesn't change and therefore  $R_2$  weighting is constant. Once  $S_{ASE}$  is corrected for additional signal decay by multiplication with  $F(\tau)$ , changes in  $S_{ASE}$  with  $\tau$  can be used to calculate  $R'_2$  of the resting baseline state of the brain (Equation 8.16) and used to calculate  $M$  (Equation 8.14).  $M_{R'_2}$  can then be used within the hyperoxic calibration to allow Equation 8.8 to be solved for  $S_vO_2$ . If we consider the approach taken by *Bulte et al.* [1] to dcfMRI,  $M_{R'_2}$  effectively replaces  $M_{hc}$  allowing absolute  $CMRO_2$  to be calculated using Equation 8.9. This means that a dcfMRI approach can be performed without the need for a hypercapnic respiratory manipulation. This allows measures of absolute  $CMRO_2$  to be made without the drawbacks associated with hypercapnic respiratory challenge such as air hunger, intolerability and sensory stimulation. This demonstrates a practical improvement for the implementation of the dcfMRI approach and aids in the transition of the technique to a clinical setting.

## 8.3 Methods

### 8.3.1 Participants

Eight normal healthy participants (aged 24 - 39; mean age  $33.5 \pm 5.0$ ; 2 female) were recruited and scanned having given written consent. Experimental procedures were approved by the local institutional ethical review committee. All par-

ticipants had previous experience of performing respiratory manipulations during MR scanning.

### 8.3.2 MRI

Scanning was performed on a 3T GE HDx MRI (GE Healthcare, Milwaukee WI) with a body transmit coil and 8-channel head receive coil. All participants had previous whole brain T<sub>1</sub>-weighted structural scans available (fast spoiled gradient recalled echo, 1x1x1 mm voxels, TI/TR/TE = 450/7.8/3 ms). The data presented in this study is a subset of data acquired during a scanning session that lasted approximately an hour. Only the details of relevant acquisitions to this study are presented from here on. Throughout the scan session participants were presented with a cross hair overlaid on a black background and instructed to keep their eyes open for the duration of the scan.

### Dual Calibrated fMRI

An interleaved hypercapnic-hyperoxic dcfMRI protocol was performed lasting eighteen minutes with an additional minute for calibration scans. Details of the dual-echo spiral EPI sequence used to collect simultaneous perfusion and BOLD imaging data can be found in **Chapter 4** alongside details of the interleaved hypercapnic-hyperoxic respiratory manipulation used.



## Asymmetric Spin Echo

The same anatomical area / prescription was scanned using a single shot ASE-EPI sequence with different asymmetric or  $\tau$  weightings. An SE ( $\tau = 0$  ms) was first acquired followed by asymmetric SE's at  $\tau = 20, 25$  and  $30$  ms. The  $\tau$  times were chosen to be greater than  $15$  ms in order to stay in the monoexponential regime of the signal model [69]. A single-echo, gradient echo (GRE) readout with spiral k-space acquisition was used ( $TE = 44$  ms,  $TR = 3.0$  s, flip angle  $90^\circ$ ) with one interleave being acquired. The anatomical prescription used during the dual-calibrated fMRI was copied to ensure that the same brain regions were covered. In-plane resolution was kept the same as before (FOV  $22$  cm and matrix  $64 \times 64$ ) but  $32$  slices with  $2$  mm thickness and an inter-slice gap of  $1$  mm were acquired. The smaller slice thickness was used to reduce the effect of  $B_0$  inhomogeneities while conserving good signal-to-noise ratio as demonstrated in [119, 123]. Each  $\tau$  acquisition took  $1$  minute  $6$  seconds with two dummy pulses followed by  $20$  volumes being acquired. Although spiral image acquisition helps overcome some of the signal loss and image distortion caused by the presence of  $B_0$  inhomogeneities the use of a spiral in/out [124] or spiral in/in [125] acquisition or other multiple spiral acquisitions, such as that presented by *Brewer et al.* [126], would ideally minimise macroscopic field dephasing effects. To calculate the attenuation correction function,  $F(\tau)$ , two GRE acquisitions were used with the same prescription as the single shot SE acquisition described previously. The GRE's were collected at  $TE = 7$  and  $9$  ms with phase maps for each echo time being output from the raw data.

### 8.3.3 Analysis

All image time-series were motion corrected using *3dvolreg* [74].

#### $M_{R'_2}$ , ASE

Each of the four  $\tau$  shifted ASE acquisitions were averaged over the 20 volumes acquired to give the mean signal map ( $S_{ASE}$ ). 3D phase unwrapping was performed using PRELUDE, (part of the FSL toolbox) on the phase maps acquired for the GRE acquisition (TE = 7 and 9 ms) and the phase difference (rads/s) was calculated by subtracting the unwrapped phase maps on a voxel by voxel basis. The difference image was then demeaned and smoothed using a 2 mm Gaussian smoothing kernel. The demeaned difference images were taken into MATLAB using the AFNI MATLAB toolbox [74] and phase difference was calculated in the slice direction using the "diff.m" function. This provided the frequency difference across each voxel in the slice direction ( $\Delta\omega$ ) and allowed the attenuation correction function  $F(\tau)$  to be calculated individually for each  $\tau$  (Equation 8.18). The signal intensity,  $S_{ASE}$ , for each  $\tau$  was corrected for signal attenuation due to macroscopic field inhomogeneity. Voxels with signal attenuations greater than 10% (i.e.  $F < 90\%$ ) were not included in further analysis and thresholded out. This thresholding was considered liberal and was done to ensure the influence of macroscopic magnetic field inhomogeneity was removed from the measured  $R'_2$ .

Subject specific ROI's of global grey matter (GM) were produced using FAST segmentation on the high resolution images [83] and registered to the native space of each  $\tau$  image using FLIRT [77]. Mean GM signal was calculated across these

ROI's for each of the four attenuation corrected and thresholded  $\tau$  weighted ASE images.

Four M values were calculated using Equations 8.16 and 8.14. Individual estimates of M were made using the GM averaged signal at each of the three  $\tau$  shifted ASE acquisitions ( $\tau = 20, 25$  and  $30$  ms) and the symmetric SE ( $\tau = 0$ ). These estimates are referred to as  $M_{\tau=20ms}$ ,  $M_{\tau=25ms}$  and  $M_{\tau=30ms}$ . A fourth estimate of M was made by estimating a value for  $R'_2$  from all the ASE data acquired in a subject. A line was fit ( $-\log(\frac{S_{\tau=20,25,30}}{S_0})$  vs.  $\tau$ ) to estimate  $R'_2$  and  $M_{\tau fit}$  was determined from this.

## Respiratory Manipulated FMRI

The first and second echo time-series image data acquired by the dual-echo PASL sequence during the dcFMRI protocol was corrected for physiological noise using a modified RETROICOR approach. The first and second harmonics of both the cardiac and respiratory cycles were regressed from the data along with the interaction term of the first cardiac and respiratory harmonics [80, 81]. The first echo acquired was used to calculate CBF, while the data from the second echo was used to examine changes in BOLD signal. Interpolated surround subtraction of the ASL tag and control image time-series was performed to yield a perfusion-weighted time-series [43] which was corrected for coil sensitivity [82]. CBF images were calculated using the  $M_0$  of blood, estimated from the cerebrospinal fluid signal of the  $M_0$  image and the general kinetic model (GKM) [33]. The CBF estimates were adjusted for the likely reduction of the  $T_1$  of arterial blood with increasing plasma concentration of paramagnetic  $O_2$ , according to the blood  $T_1$  values quoted by

*Bulte et al.* [51]. Interpolated surround averaging of the tag and control images was performed to yield a BOLD weighted time-series.

The subject specific ROI's of global GM produced by FAST segmentation were registered to the native space of CBF and BOLD images using FLIRT [77]. Partial voluming of GM was removed by thresholding the mask to include only voxels that were deemed to contain all GM. Mean CBF and BOLD timeseries for GM were produced by averaging over the voxels in GM using the ROI mask. Time averaged relative CBF ( $\frac{CBF}{CBF_0}$ ) and BOLD signal ( $\frac{\Delta S}{S_0}$ ) were block averaged to remove periods of transition from the analysis where the BOLD signal model is not applicable. The interleaved design, block averaging periods were calculated for each final 30 second period of each 60 second respiratory block (normocapnia with normoxia and normocapnia with hyperoxia in the baseline acquisition ) and 120 seconds of each 150 second block (hypercapnia with normoxia). The mean arterial oxygen content,  $C_aO_2$ , was calculated from the  $P_{ET}O_2$  data for the same time periods using Equation A11 from [3].

## M, Calibrated BOLD

The data acquired for the dcfMRI acquisition was divided up in such a way as to allow the calculation of  $M_{hc}$  and  $M_{ho}$  using the calibrated BOLD approach. For the calculation of M using the hypercapnic approach ( $M_{hc}$ ), Equation 8.7 was used. From the block averaged data, periods of hypercapnia and normoxia were used to estimate CBF and BOLD increases from baseline. During the hyperoxic calibration ( $M_{ho}$ ) no change in CBF was assumed. Periods which were hyperoxic and normocapnic were used to estimate BOLD and  $C_aO_2$  changes from baseline.

Constants assumed in Equation 8.8 are  $S_vO_2 = 0.3$  [46],  $\phi = 1.34$  ml/g and  $Hb = 0.15$  g/ml. In both cases baseline was calculated from periods of normocapnia and normoxia.

### Dual Calibrated FMRI

The BOLD signal model described in [3] was fitted to the block averaged global GM, mean CBF and BOLD timeseries using a simple bayesian framework to yield estimates of  $M_{dcFMRI}$  and  $S_vO_2$  permitting calculation of absolute  $CMRO_2$ .  $\alpha = 0.14$  and  $\beta = 0.91$  were chosen from [85]. Priors for  $M$  and  $S_vO_2$  were generated as normal probability density functions centred around initial estimates of 0.08 and 0.5 with broad standard deviations of 0.02 and 0.1. By applying Bayes' rule to the first time points of averaged data  $\frac{\Delta S}{S_0}$ ,  $\frac{CBF}{CBF_0}$  and  $C_aO_2$ , posterior probability distributions of the variables,  $M$  and  $S_vO_2$ , were generated after integrating over the ranges 0.01 - 0.15 ( $M$ ) and 0.2 - 0.8 ( $S_vO_2$ ). These were chosen to be beyond the extremes of physiologically plausible values. The posterior distributions were used as the priors for calculations with the second time points of averaged data and so on until a final posterior distribution for each of the two variables was obtained. The maxima of these probability distribution functions provided the estimates of  $M$  and  $S_vO_2$  for each subject. Absolute  $CMRO_2$  was then calculated using:

$$CMRO_2 = OEF \cdot CBF \cdot C_aO_2 \quad (8.19)$$

### 8.3.4 ASE- $R'_2$ and Hyperoxic Calibrated BOLD

Using the same subset of BOLD data described for the hyperoxic calibrated BOLD approach,  $M$  measured using ASE can be substituted into Equation 8.8 and the problem can be solved for  $S_vO_2$ . Combining  $S_vO_2$  with a baseline measure of CBF, absolute  $CMRO_2$  can be estimated using Equation 8.19.

## 8.4 Results

### 8.4.1 ASE Signal Attenuation Correction, $F(\tau)$

To help correct for macroscopic magnetic field inhomogeneities and ensure that measurement of  $R'_2$  can be directly related to  $[dHb]$  the signal attenuation factor  $F$ , described as a function of  $\tau$  in Equation 8.18, is used to correct the signal intensity of the ASE images acquired at different  $\tau$ .  $F$  was further thresholded at 90% effectively excluding any voxel signals which differed from their measured value by more than 10% due to signal distortion. This was an arbitrary thresholding value that was considered cautious. Details of  $F$  thresholding in terms of voxel exclusion are given in Table 8.1. It can be seen that the number of voxels removed increases with  $\tau$  as expected.

	Total voxels GM	Thresholded voxels GM	% Thresholded
$\tau = 20$ ms	$14776 \pm 703$	$4220 \pm 1084$	$29 \pm 7$ %
$\tau = 25$ ms	$14471 \pm 711$	$5407 \pm 1117$	$37 \pm 7$ %
$\tau = 30$ ms	$14163 \pm 732$	$6171 \pm 1034$	$44 \pm 7$ %

Table 8.1: The signal attenuation factor  $F(\tau)$  (Equation 8.18) was thresholded to remove voxels which were attenuated by more then 10% due to macroscopic field distortions. Values presented are the mean  $\pm$  standard deviation across the group ( $n = 8$ ). For each  $\tau$  the total number of voxels in GM before thresholding, after thresholding and the percentage of voxels removed is given.

#### 8.4.2 Characterisation of $M_{R'_2}$ with $\tau$

$R'_2$  was calculated in each subject using the signal attenuation corrected, ASE images acquired at each of the three asymmetric  $\tau$ 's as well as an estimate of  $R'_2$  determined by fitting the data to all four signals. This was done using Equation 8.16. Using Equation 8.14 the calculated  $R'_2$  was multiplied by the TE of the second echo used for BOLD acquisition in the dcfMRI protocol ( $TE = 29$  ms). This provided four estimates of  $M_{R'_2}$ . These were  $M_{\tau=20ms}$ ,  $M_{\tau=25ms}$ ,  $M_{\tau=30ms}$  and  $M_{\tau fit}$  and results are shown in Figure 8.2. A consistent trend of increasing  $M$  with  $\tau$  is demonstrated.

#### 8.4.3 Comparison of Haemodynamic Variables Measured using Calibrated BOLD, dcfMRI and $ASE_{R'_2}$

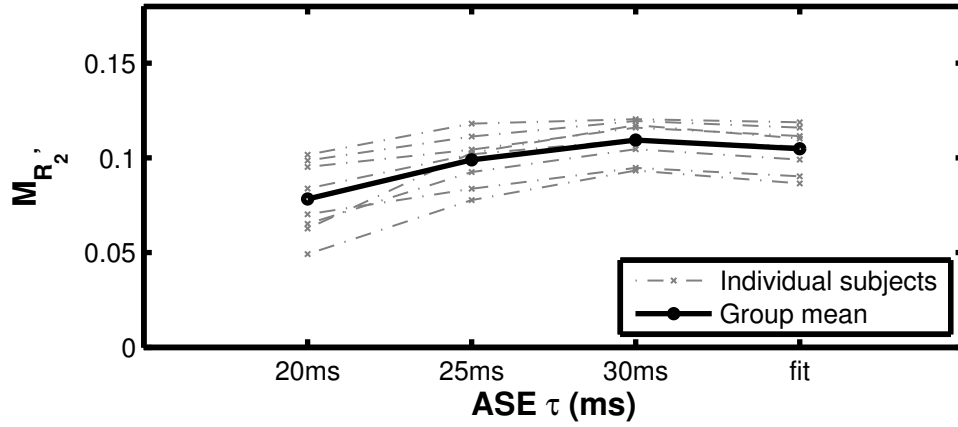


Figure 8.2: Subject specific (grey) and group mean (black)  $M_{R'_2}$  values calculated using four different  $\tau$  weightings are shown above.  $M_{R'_2}$  is calculated for a  $TE = 29$  ms which corresponds to the dual echo acquisition used in the dcfMRI protocol.

### Maximum BOLD Signal Change, M

M was measured using three different categories of technique. As described in the previous section, M was estimated by measuring the reversible transverse relaxation properties of the brain using ASE. This category,  $M_{R'_2}$ , provided four estimates of M as detailed above. M was also estimated using single point, calibrated BOLD methodologies. This provided estimates of M calculated from hypercapnia and hyperoxia referred to as  $M_{hc}$  and  $M_{ho}$  respectively. Finally M was estimated from the dcfMRI protocol giving  $M_{dcfMRI}$ . Group mean  $\pm$  standard deviation for M calculated in GM are presented in Table 8.2.  $M_{dcfMRI}$  offers the lowest estimate of maximum BOLD signal change with  $M_{R'_2}$  varying with  $\tau$  as would be expected from Figure 8.2. Figure 8.3 shows scatterplots of the M estimates made using  $ASE_{R'_2}$  techniques compared to the calibrated BOLD techniques in all 8 subjects. Intraclass correlation (ICC) was used to test the reproducibility of the



$ASE_{R'_2}$  measures, when compared to the other techniques, the results of which can be found in Table 8.3.

M in Grey Matter	
<u>dcfMRI</u>	
$M_{dcfMRI}$	$0.046 \pm 0.014$
<u>calibrated BOLD</u>	
$M_{hc}$	$0.096 \pm 0.031$
$M_{ho}$	$0.099 \pm 0.073$
<u><math>ASE_{R'_2}</math></u>	
$M_{\tau=fit}$	$0.105 \pm 0.012$
$M_{\tau=30ms}$	$0.109 \pm 0.011$
$M_{\tau=25ms}$	$0.099 \pm 0.014$
$M_{\tau=20ms}$	$0.078 \pm 0.019$

Table 8.2: Group mean  $\pm$  std, maximum BOLD signal change measured in GM for dcfMRI, calibrated BOLD and  $R'_2$  measured using ASE.

	$M_{\tau=20}$	$M_{\tau=25}$	$M_{\tau=30}$	$M_{\tau=fit}$
$M_{HC}$	-0.22	-0.07	0.02	-0.02
$M_{HO}$	0.20	0.18	0.18	0.18
$M_{dcfMRI}$	-0.13	-0.13	-0.05	-0.08

Table 8.3: ICC coefficient calculated for the relations shown in Fig. 8.3 ( $n = 8$ ).

### Comparison of $S_vO_2$ and $CMRO_2$ Measured using dcfMRI and $ASE_{R'_2}$ with hyperoxic calibrated BOLD

Group mean estimates of  $S_vO_2$  and  $CMRO_2$  in GM made using dcfMRI (interleaved hypercapnic-hyperoxic design) are shown on the first line of Table 8.4(i).

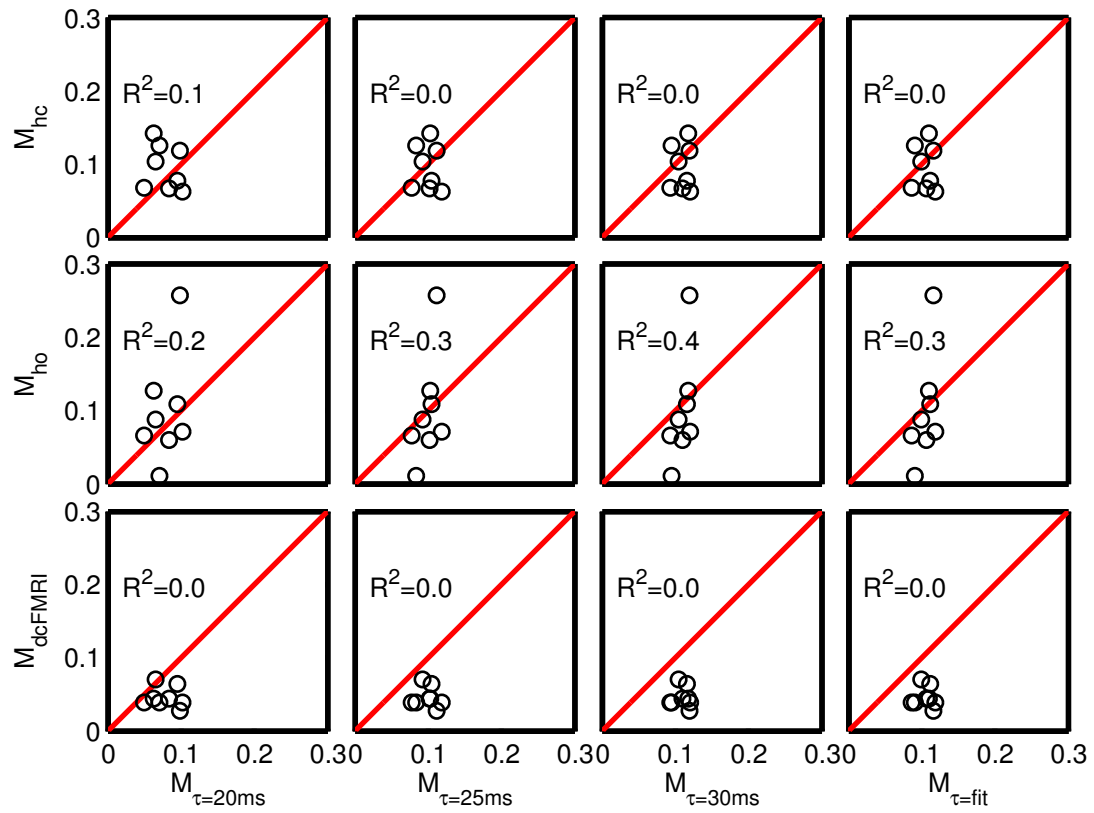


Figure 8.3: Scatter plots comparing GM measures of  $M$  made using  $ASE_{R'_2}$  to calibrated BOLD and dcFMRI techniques ( $n = 8$ ).

Group mean  $\text{CBF}_{baseline}$  in GM was the same with both techniques presented as the ASL data used for each calculation is a subset of the dcfMRI acquisition. Group mean  $\text{S}_v\text{O}_2$  and  $\text{CMRO}_2$  values in GM calculated from the combination of  $\text{M}_{R'_2}$  and the hyperoxic calibrated BOLD data subset are presented in Table 8.4(ii). It can be seen that  $\text{S}_v\text{O}_2$  varies with  $\tau$ , as would be expected from Table 8.2 where  $\text{M}_{R'_2}$  is shown to vary with  $\tau$ .

	$\text{S}_v\text{O}_2$	$\text{CMRO}_2$ ( $\mu\text{mol}/100\text{g}/\text{min}$ )
(i) <u>dcfMRI</u>		
Hypercapnia-Hyperoxia	$0.54 \pm 0.10$	$182.7 \pm 75.5$
(ii) <u><math>\text{ASE}_{R'_2} + \text{Hyperoxic calibrated BOLD}</math></u>		
Hyperoxia - $\text{M}_{\tau fit}$	$0.50 \pm 0.14$	$188.8 \pm 36.6$
Hyperoxia - $\text{M}_{\tau=30ms}$	$0.48 \pm 0.14$	$197.2 \pm 37.4$
Hyperoxia - $\text{M}_{\tau=25ms}$	$0.53 \pm 0.14$	$178.4 \pm 37.6$
Hyperoxia - $\text{M}_{\tau=20ms}$	$0.63 \pm 0.14$	$139.8 \pm 35.4$
$\text{CBF}_{base} = 49.5 \pm 10.1. \text{ ml}/100\text{g}/\text{min}$		

Table 8.4: Group mean  $\text{S}_v\text{O}_2$  and  $\text{CMRO}_2$  values in GM for dcfMRI (i) and  $\text{M}_{R'_2} + \text{hyperoxic calibrated BOLD}$  (ii). The M values calculated for the multiple  $\tau$  weighted ASE images are presented.  $\text{CBF}_{baseline}$  is the same for both techniques

Figure 8.4 shows scatterplots of the  $\text{S}_v\text{O}_2$  (top line) and  $\text{CMRO}_2$  (bottom line) estimates comparing dcfMRI and  $\text{ASE}_{R'_2} + \text{Hyperoxic calibrated BOLD}$  in all 8

subjects. ICC was used to test the reproducibility of the measures between both techniques the results of which can be found in Table 8.5.

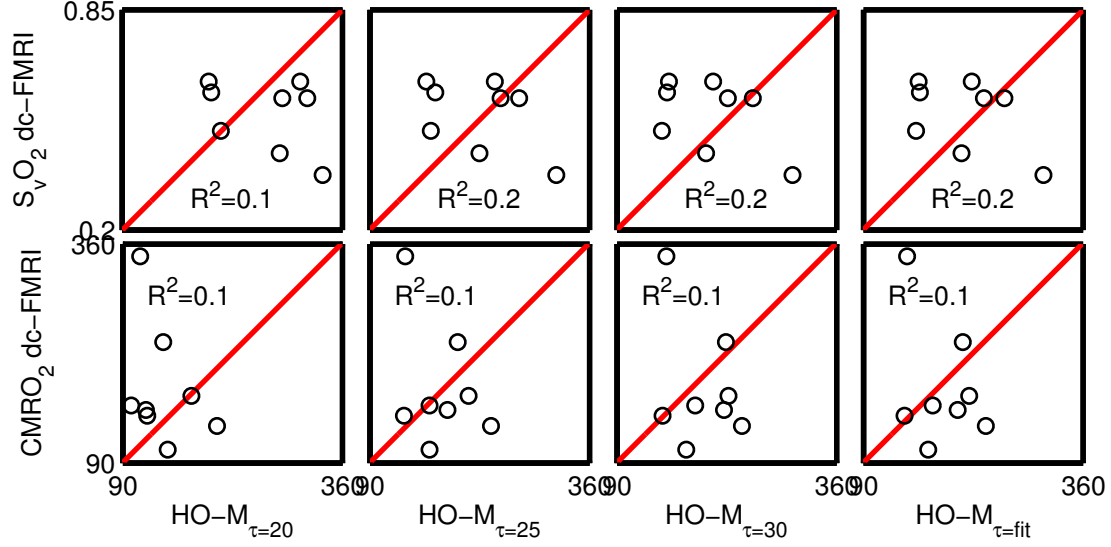


Figure 8.4: Scatter plots comparing GM measures of  $S_vO_2$  and  $CMRO_2$  between dcFMRI and  $ASE_{R'_2} + \text{Hyperoxic calibrated BOLD (HO - } M_{R'_2})$  for various measures of  $R'_2$  using different  $\tau$  weighted ASE's ( $n = 8$ ).

		$HO-M_{\tau=20}$	$HO-M_{\tau=25}$	$HO-M_{\tau=30}$	$HO-M_{\tau=fit}$
$S_vO_2$	$dcFMRI_{INT}$	-0.36	-0.43	-0.45	-0.44
$CMRO_2$	$dcFMRI_{INT}$	-0.26	-0.26	-0.22	-0.24

Table 8.5: ICC coefficient calculated for the relations shown in Fig. 8.4 ( $n = 8$ ).

## 8.5 Discussion

In this study we investigate the use of ASE to measure  $R'_2$  and in turn  $M$  as suggested by *Blockley et al.* [69, 121]. These measures of maximum BOLD signal change are then compared to respiratory manipulated FMRI calibration approaches. Finally we propose a substitution of  $R'_2$  derived  $M$  into the hyperoxic

calibrated BOLD approach, in an extension of dcfMRI, for the estimation of  $S_vO_2$  and absolute  $CMRO_2$ . By combining the two techniques we allow hypercapnia to be replaced in the dcfMRI protocol and circumvent problems experienced in qBOLD style modelling associated with the interdependence of  $S_vO_2$  and CBV.

### 8.5.1 ASE Signal Attenuation Correction, $F(\tau)$

The attenuation factor used to correct the ASE signal for macroscopic field inhomogeneities was thresholded cautiously in order to ensure voxels were excluded where through slice macroscopic gradients were large. From Table 8.1 the number of voxels removed due to thresholding increase with  $\tau$ . This is an expected behaviour and can be explained by considering the effects of increasing  $\tau$ . As  $\tau$  increases, the  $180^\circ$  refocusing pulse is moved closer to the preparation pulse effectively refocusing the echo further away from the optimal imaging time at TE. This allows more time for signal attenuations due to  $B_0$  inhomogeneities to enhance signal dephasing and manifest as signal attenuation at the time of image acquisition. This could be a potential source of bias as different sets of voxels are used in the calculation of M from different  $\tau$ 's due to the thresholding. Considering the worst case the different sets of voxels would have different OEF's for each  $\tau$ . However this is unlikely as PET studies have shown that OEF is reasonably uniform across the brain.

### 8.5.2 Characterisation of $M_{R'_2}$ with $\tau$

It can be seen from Fig 8.2 that the measurement of  $M$  depends on  $\tau$ . This effect was also noticed in a study using a gradient echo sampling of spin echo sequence (GESSE), similar in principle to ASE, to measure  $R'_2$  in the brain [127]. They noticed that the measurement of  $R'_2$  was dependent on SE time (what is referred to in this study as  $\tau$ ). This effect was attributed to the multicomponent structure of brain tissue. If each component has a different  $R_2$  relaxation time the fractional weighting contributed to the signal from that component is different at different  $\tau$ 's. These findings have previously led to the introduction of a multicompart-ment model used in the qBOLD approach [115] where main tissue, cerebrospinal fluid/interstitial fluid and intravascular compartments have been incorporated into the signal model to account for their separate contributions to  $R'_2$  relaxation.

### 8.5.3 Comparison of Haemodynamic Variables Measured using Calibrated BOLD, dcfMRI and ASE $_{R'_2}$

#### Maximum BOLD Signal Change, $M$

From Table 8.2 group average estimates of  $M$  made in GM using the dcfMRI technique are considerably lower than those made using calibrated BOLD or ASE. For the ASE derived measurements of  $M$ , estimates calculated at a  $\tau$  of 25 ms agree best with both hypercapnic and hyperoxic calibrated BOLD approaches. It can be seen in all ASE measures of  $M$  that standard deviation across subjects in

all  $\tau$  iterations is considerably lower than that measured using calibrated BOLD and equivalent to that using dcfMRI.

Scatterplots presented in Figure 8.3 compare M values derived from ASE to those measured using calibrated BOLD and dcfMRI techniques for each subject. Again it can be seen that values of M determined by dcfMRI are lower than ASE derived M's. From visual inspection of the scatterplots it would appear the measures of M made using hypercapnia and hyperoxia are the noisier measurements when compared to  $M_{ASE}$  as they have a larger spread and obvious outliers in the case of  $M_{HO}$ .

The ICC coefficients calculated in Table 8.3 test the reproducibility between techniques. Low ICC values ( $\leq 0$ ) indicate that M measures vary greatly between the two techniques with high ICC values (0.5 - 1) indicating the values measured using the two techniques are more agreeable. All techniques are shown to be in poor agreement with relation to subject reproducibility across techniques but ASE measures agree best with M's calculated using hyperoxic calibrated BOLD. A lack of true underlying biological variability as well as uncertainty in the measurement could contribute heavily towards the poor ICC's which show no appreciable correspondence.

### **Comparison of $S_vO_2$ and $CMRO_2$ Measured using dcfMRI and $ASE_{R'_2}$ with Hyperoxic Calibrated BOLD**

Estimates of  $S_vO_2$  and  $CMRO_2$  made using dcfMRI and  $ASE_{R'_2}$  with hyperoxia calibrated BOLD are compared in Table 8.4. Best agreement with ASE for  $S_vO_2$

and  $\text{CMRO}_2$  occur at  $\tau = 25$  ms. Scatterplots (Figure 8.4) and ICC coefficients (Table 8.5) show poor correlation between both methods for both measurements. This is not surprising considering the poor correlations between M values presented in Figure 8.3 and Table 8.5. When considering these comparisons it is important to note that the estimates of  $\text{S}_v\text{O}_2$  and  $\text{CMRO}_2$  are low and high respectively when made using dcfMRI and compared to literature as discussed by *Wise et al.* [3] and in **Chapter 4**.

The potential influence of varying compartmental  $R'_2$  relaxation on M measured at different  $\tau$ 's can also be seen in Table 8.4. As  $\tau$  increases so does the estimate of M. This has the effect of decreasing  $\text{S}_v\text{O}_2$  and therefore increasing  $\text{CMRO}_2$  as all other components of Equations 8.8 and 8.9 remain constant.

It must be noted that group average values of  $\text{S}_v\text{O}_2$  and  $\text{CMRO}_2$  are reasonable if not a bit high in all cases except  $\tau = 20$  ms when compared to expected values in GM. An analogous approach was attempted using  $\text{ASE}_{R'_2}$  with hypercapnic calibrated BOLD. Instead of using Equation 8.7, a BOLD signal model presented by *Wise et al.* [3] was used which introduces an  $\text{S}_v\text{O}_2$  term into this relation. However estimates of  $\text{S}_v\text{O}_2$  were unrealistic ( $0 > \text{S}_v\text{O}_2 > 1$ ). This was probably as a result of the dual calibrated model [3] reducing to Equation 8.7 and their not being enough information from the isometabolic CBF change induced by hypercapnia to delineate a unique value for  $\text{S}_v\text{O}_2$ . In light of this  $\text{ASE}_{R'_2}$  with hyperoxia calibrated BOLD is viewed as promising. Another important benefit is that the technique requires CBF to be measured only at normocapnia. This removes any limiting factors associated with measuring CBF changes with respiratory manipulations which are present in the dcfMRI hypercapnic-hyperoxic approach.



## Limitations and Further Work

The method and results in this study should be viewed as an intermediary step to developing a quick and effective measure of cerebral metabolism. However to make this technique a realistic option for providing quantitative, parametric maps of absolute CMRO<sub>2</sub> further investigation into a number of areas is required.

In this study the limiting factor to producing whole brain, parametric maps is the ASE measure of  $R'_2$ . The calculations of  $R'_2$  are cautiously thresholded to ensure that the measured  $R'_2$  can be attributed to mesoscopic magnetic field inhomogeneities. By introducing a multiple spiral acquisition [124–126] more confidence could be put in the estimates of  $R'_2$  by reducing macroscopic magnetic field inhomogeneities. Previous studies have demonstrated the application of ASE to measuring  $R'_2$  on a voxel by voxel basis [128].

Further work would be required to prove the sensitivity of  $R'_2$  to global and regional changes in physiology such as continuous visual and motor tasks (**Chapter 4**) or hypocapnia (**Chapter 7**) as has been done with the dcfMRI protocol. However previous studies measuring changes in  $R'_2$  with hypercapnia are promising [128].

Localisation of  $R'_2$  for measurement in the appropriate compartments for use in the hyperoxic calibrated BOLD model requires further consideration. This could be done by investigating diffusion weighting to suppress signal from intravascular flow [128] or by using more complex, compartmental style modelling analogous to the qBOLD approach [115] where main tissue, cerebrospinal fluid/interstitial fluid

and intravascular compartments have been incorporated into the signal model to account for their separate contributions to  $R'_2$  relaxation.

## 8.6 Conclusion

In this study we investigate the relationship between single-shot ASE, calibrated BOLD and dcFMRI techniques for the measurement of maximum BOLD signal change,  $M$ . From this a framework for calculating  $S_vO_2$  and in turn absolute  $CMRO_2$  using qBOLD style relaxometry and calibrated BOLD is presented. Measurements of  $R'_2$  are made using ASE allowing  $M$  to be known in a hyperoxic calibrated BOLD experiment. This then leaves  $S_vO_2$  to be estimated from the calibrated BOLD model. The technique can be viewed as an extension of the dcFMRI methodology where the hypercapnic respiratory manipulation is replaced by a relaxometry measure.

$ASE_{R'_2}$  with hyperoxic calibrated BOLD is a promising technique which allows problems associated with qBOLD modelling and measurement of  $S_vO_2$  from calibrated BOLD to be solved in a multi parametric approach. Group average measures of  $S_vO_2$  and  $CMRO_2$  in GM compare well with dcFMRI results. The concept and techniques used have the potential for a fast and effective method of producing whole brain, absolute  $CMRO_2$  maps in a short scan time without hypercapnia. However further investigation of  $R'_2$  measurement techniques is required to determine it's global and regional sensitivity to changes in baseline haemodynamic state and localisation of the signal to relevant compartments for integration into the calibrated BOLD model.

## Chapter 9

### Discussion and Conclusions

Brain function and health are intrinsically linked to oxygen metabolism. As a result, MR methods such as dcfMRI which provide detailed parametric maps of CMRO<sub>2</sub> consumption are desirable in both a research and clinical setting. dcfMRI is capable of producing a non-invasive, radioisotope free, easily implementable routine for measuring absolute CMRO<sub>2</sub> and as such offers a competitive alternative to the current gold standard PET techniques. It offers an absolute, quantitative measurement of oxygen metabolism which can be monitored longitudinally.

As such, dcfMRI has many prospective applications in basic neuroscience research and the research and clinical investigation of disease. The relationship between brain function and oxygen utilisation is important for the understanding of normal human brain function [129] and a measurement of CMRO<sub>2</sub> has the potential to provide a measure more tightly coupled with neural activity than the BOLD signal. Measurements of oxygen metabolism are of interest when investigating pathophysiology of stroke [130], particularly in the delineation of the ischemic penumbra [16]. Oxygen metabolism measurements are also of importance for the evaluation of hypoxia within tumours of the brain and other organs where hypoxia is related to tumour resistance to therapies [131–133]. Neurodegenerative disorders such as Alzheimer’s disease [134–136], Huntingtons disease [137], Parkinsons disease [138]

and other neurological disorders [13, 139, 140] also demonstrate marked changes of cerebral oxygenation. In a similar manner, dcfMRI could provide a non-invasive biomarker of efficacy and inform stop signals in the process of drug discovery and development for the treatment of such diseases [141].

This thesis aims to further develop the dcfMRI approach in terms of feasibility and application, aiding the transition of dcfMRI into research and clinical applications.

In **Chapter 3**, a dual-echo PASL and single-echo PCASL acquisition were compared to determine the optimal technique available in our imaging centre for implementation in the dcfMRI protocol. The detection of simultaneous task related changes in CBF and BOLD was chosen as the assessment criterion. The dual-echo PASL sequence was chosen as the optimal ASL acquisition available for implementation in all dcfMRI protocols throughout this thesis. When compared to a single-echo PCASL acquisition, the dual-echo PASL technique offered improved CBF sensitivity, higher temporal resolution and a greater correspondence between CBF and BOLD signal changes. It was also largely insensitive to errors in CBF calculation caused by velocity dependent tagging efficiency errors.

Although such a technique is not currently available in our centre, a dual-echo PCASL technique has the potential to offer improved perfusion signal SNR with optimised echo times. However, PCASL tagging efficiency has been shown to decrease with the administration of a hypercapnic challenge and further work is required to accurately reduce velocity dependent tagging efficiency errors. This could be achieved by relating phase contrast measures and PCASL tagging sim-

ulations, similar to the work presented by *Aslan et al.* [73] and *O’Gorman et al.* [142].

A more relevant improvement, currently available in our centre, is multi-TI ASL. This may better characterise CBF and overcome any AAT issues that may arise. However the implementation of this technique reduces the temporal resolution of the acquisition leading to lower SNR.

In **Chapter 4**, a dcfMRI framework was introduced and used to investigate regional changes in absolute CMRO<sub>2</sub>. dcfMRI provides measures of oxygen metabolism related parameters by measuring CBF and BOLD signal changes in the brain using an ASL acquisition and modelling these changes using a simple BOLD signal model. Regional elevations in absolute CMRO<sub>2</sub> were produced using continuous visual and motor stimulation. Two different respiratory manipulations were assessed: an interleaved hypercapnic-hyperoxic challenge allowing the estimation of  $[M$  and  $S_vO_2]$  and a simultaneous hypercapnic-hyperoxic challenge allowing the estimation of  $[M, S_vO_2, \alpha$  and  $\beta]$ .

When compared to an interleaved design, the simultaneous hypercapnic-hyperoxic respiratory manipulation was capable of detecting significant increases in absolute CMRO<sub>2</sub>, induced by continuous visual and motor stimulation as well as agreeable estimates of absolute CMRO<sub>2</sub> in grey matter. This demonstrates the sensitivity of dcfMRI to detect focal alterations in oxygen metabolism.

In **Chapter 5**, the repeatability of oxygen metabolism related parameters, made at rest using dcfMRI, were assessed using both interleaved and simultaneous hypercapnic-hyperoxic respiratory manipulations in a dcfMRI protocol. This was

achieved by using the data acquired in **Chapter 4** alongside an additional interleaved and simultaneous hypercapnic-hyperoxic dcfMRI protocol performed at rest on a separate day.

Physiological parameters measured at rest using interleaved and simultaneous designs were compared for intrasession and intersession repeatability using ICC's. The interleaved design results in more reproducible measures of CMRO<sub>2</sub>. However, questions remain over the sensitivity of the interleaved technique to detect changes in oxygen metabolism and associated parameters.

Further investigation into the repeatability of oxygen metabolism parameters made using dcfMRI is required. A larger, more structured repeatability study resembling that used by *Liu et al.* [91] to investigate the repeatability of TRUST may better characterise the repeatability of the dcfMRI measures. In **Chapter 5**, a rest and task measure was made within session and a single rest measure was repeated in a separate session. Repeatability may be better characterised by performing multiple within session measures and repeating this routine in several separate sessions on separate days. Repeatability of regional and global changes detected in oxygen metabolism could also be investigated by taking the same approach to performing multiple rest and task measures within session and in separate sessions. However, as the current acquisition time is relatively long (18 mins), these studies become quite time intensive and tedious. Acquisition time savings offered in **Chapter 6** may improve this. It may also be worth investigating if further improvements in repeatability can be gained through optimisation of the BOLD signal model similar to the approach taken by *Griffeth et al.* [85].

In **Chapter 6**, a retrospective analysis was performed on the interleaved and simultaneous hypercapnic-hyperoxic dcfMRI acquisitions to investigate the feasibility of acquiring shorter datasets for absolute CMRO<sub>2</sub> quantification. This was performed on the resting datasets acquired as part of **Chapter 4**.

The retrospective analysis demonstrated, in theory, that an interleaved respiratory manipulation used for quantification of absolute CMRO<sub>2</sub> in a dcfMRI protocol could be shortened by acquiring less data during each respiratory block. When using a simultaneous design, it was shown that acquisition was better shortened by using less respiratory blocks as opposed to shortening each block individually. This leads to reliable dcfMRI oxygen metabolism measures in  $\sim 9$  to 13 minutes. Further acquisition-time improvements could be made by reducing the amount of disregarded data during the transition times. Appropriate modelling of the CBF and BOLD signal during transitions would aid this.

In **Chapter 7**, dcfMRI was used to measure CBF related changes in OEF during voluntary hyperventilation. Resting measures were acquired using the previously established method of interleaved dcfMRI presented in **Chapter 4**. Subjects then used voluntary hyperventilation and an end-tidal CO<sub>2</sub> feedback task to achieve a new low flow baseline allowing changes in OEF to be measured.

dcfMRI detected significant changes in CBF and S<sub>v</sub>O<sub>2</sub> measured in global grey matter due to hypocapnia. This demonstrates the sensitivity of the dual calibrated fMRI protocol to detect changes in OEF and suggests that the technique is appropriate for clinical application in areas such as stroke or vascular dysfunction in which flow is impaired. However, it is important to note that reliable estimates of

$S_vO_2$  were not achieved in one of the six subjects scanned. Further improvement of this study could be achieved by increasing the number of subjects and by performing varying levels of hypocapnia to investigate if there is a linear effect on the oxygen metabolism and related parameters.

In **Chapter 8**, hypercapnic respiratory manipulations were replaced in the dcfMRI framework by relating a measure of  $R'_2$ , made using ASE, to maximum BOLD signal change,  $M$ . This allowed hypercapnia free measures of absolute  $CMRO_2$ .

Using ASE to measure  $R'_2$  and to infer  $M$  alongside a hyperoxic calibrated BOLD technique has the potential to provide regional measures of  $S_vO_2$  and absolute  $CMRO_2$ . This is an extension of the dcfMRI protocol which circumvents issues associated with hypercapnia and may have the potential to provide whole brain maps in a short scan time. More work is required to optimise the measure of  $M$  from  $R'_2$  which may include investigating other acquisition techniques or more sophisticated signal modelling. As this technique is closely related to the qBOLD class of techniques, a lot can be gained from the advancements made in this field. An in-depth review of this field has recently been published, *Yablonskiy et al.* [143], and provides a good basis for further optimisation.

In conclusion, dcfMRI is a promising technique which has demonstrated regional and global sensitivity to changes in oxygen metabolism related parameters. Further work will improve the repeatability of the technique with proposed time saving improvements resulting from reduced scan duration and the introduction of ASE measures of  $R'_2$ . This will help drive the adoption of this technique in clinical settings, offering a radioisotope free alternative to established PET methods.



## Appendix A

The following derivation applies to Section 2.4 and was taken from *Wise et al.* [3].

Starting from the *Davis/Hoge* model (Equation 2.14), which describes fractional BOLD signal changes  $\frac{\Delta S}{S_0}$  in terms of changes in CBF (related to CBV through the Grubb coefficient,  $\alpha$ ) and deoxyhaemoglobin concentration  $[dHb]$  from baseline (subscript 0):

$$\frac{\Delta S}{S_0} = M \left( 1 - \left( \frac{CBF}{CBF_0} \right)^\alpha \left( \frac{[dHb]}{[dHb]_0} \right)^\beta \right) \quad (A.1)$$

$M$  is the maximum possible BOLD signal change and is given by:

$$M = TE \cdot \kappa \cdot CBV_0 \cdot [dHb]_0^\beta \quad (A.2)$$

$A$  and  $\beta$  are constants that depend on vessel size and geometry as well as magnetic field strength. The is to find an expression for  $\left( \frac{[dHb]}{[dHb]_0} \right)$ . According to Fick's principle the cerebral rate of oxygen consumption is give by:

$$CMRO_2 = (C_aO_2 - C_vO_2) \cdot CBF \quad (A.3)$$

where  $C_aO_2$  and  $C_vO_2$  are the arterial and venous oxygen contents respectively and CBF represents blood flow to the tissue bed in which oxygen is extracted.

It is assumed that  $CMRO_2$  is unaltered during hypercapnia and hyeproxia challenges compared to the baseline condition, therefore:

$$(C_aO_{2|0} - C_vO_{2|0}) \cdot CBF = (C_aO_2 - C_vO_2) \cdot CBF \quad (A.4)$$

The venous oxygen content can be calculated from that bound to haemoglobin and that dissolved in the plasma:

$$C_vO_2 = \phi \cdot [Hb] \cdot S_vO_2 + P_vO_2 \cdot \epsilon \quad (A.5)$$

where  $S_vO_2$  is the venous blood oxygen saturation,  $\epsilon$  is the coefficient of solubility of oxygen in blood (0.0031 ml  $O_2$ /(dl<sub>blood</sub> mmHg)) and  $\phi$  is the  $O_2$  carrying capacity of haemoglobin (1.34 ml  $O_2$ /gHb). In practice, the dissolved oxygen ( $P_vO_2 \cdot \epsilon$ ) is negligible in venous plasma. The concentration of haemoglobin is assumed to be  $[Hb] = 15 \text{ g Hb dl}_{blood}^{-1}$ .

Substituting Equation A.5 into Equation A.4:

$$\frac{CBF_0}{CBF} = \frac{C_aO_2 - (\phi \cdot [Hb] \cdot S_vO_2)}{C_aO_{2|0} - (\phi \cdot [Hb] \cdot S_vO_{2|0})} \quad (A.6)$$

and the venous deoxyhaemoglobin concentration is given by:

$$[dHb] = [Hb](1 - S_v O_2) \quad (\text{A.7})$$

Substituting Equation A.7 into Equation A.6:

$$\frac{CBF_0}{CBF} = \frac{C_a O_2 - \phi([Hb] - [dHb])}{C_a O_{2|0} - \phi([Hb] - [dHb]_0)} \quad (\text{A.8})$$

Rearranging Equation A.8 gives an expression for venous deoxyhaemoglobin concentration with respect to baseline (normoxia and normocapnia) when arterial oxygen content is increased and/or CBF is altered:

$$\frac{[dHb]}{[dHb]_0} = \frac{CBF_0}{CBF} - \frac{1}{[dHb]_0} \left( \frac{1}{\phi} \left( C_a O_2 - \left( \frac{CBF_0}{CBF} \right) C_a O_{2|0} \right) + [Hb] \left( \frac{CBF_0}{CBF} - 1 \right) \right) \quad (\text{A.9})$$

for which the arterial oxygen content,

$$C_a O_2 = \phi \cdot [Hb] \cdot S_a O_2 + P_a O_2 \cdot \epsilon \quad (\text{A.10})$$

can be calculated using the relationship between oxygen partial pressure ( $P_a O_2$ ) and arterial oxygen saturation ( $S_a O_2$ ), (the Severinghaus equation):

$$S_a O_2 = \left( \frac{1}{\frac{23400}{(P_a O_2)^3 + 150(P_a O_2)} + 1} \right) \quad (\text{A.11})$$

Equation A.9 is then substituted into Equation A.1 and fit for  $M$  and  $S_vO_{2|0}$  where  $[dHb]_0 = [Hb](1 - S_vO_{2|0})$ . Baseline rate of cerebral oxygen consumption is given (in  $\text{ml}_{O_2}/100\text{g}/\text{min}$ ) by:

$$CMRO_{2|0} = (C_aO_{2|0} - C_vO_{2|0}) \cdot CBF_0 = C_aO_{2|0} \cdot OEF_0 \cdot CBF_0 \quad (\text{A.12})$$

allowing  $OEF_0$  also to be calculated once  $S_vO_{2|0}$  is estimated. Together Equation A.9 and Equation A.1 characterise the BOLD signal and incorporate the parameters  $\alpha$  and  $\beta$ . Experimental data acquired with simultaneous modulation of CBF and arterial oxygen content allowed  $\alpha$  and  $\beta$  to be estimated from the full signal model (Equations A.9 and A.1) in addition to  $M$  and  $S_vO_{2|0}$  and therefore  $OEF_0$  and  $CMRO_{2|0}$ . In the specific case of increased arterial oxygen content on top of increased CBF induced by hypercapnia a relationship can be formulated, based on the ratio of oxygen related BOLD signal changes at different levels of CBF, which can be used to constrain estimates of  $\alpha$  and  $\beta$  in combination with data acquired from interleaved hypercapnia and hyperoxia.

We begin with Equation A.1 expressed for the  $i$ th level of hypercapnia,

$$\frac{\Delta S_i}{S_i} = TE \cdot A \cdot CBV_i \cdot [dHb_i]_0^\beta \left( 1 - \left( \frac{CBF_i}{CBF_{i|0}} \right)^\alpha \left( \frac{[dHb_i]}{[dHb_i]_0} \right)^\beta \right) \quad (\text{A.13})$$

considering  $i = 1$  for one level of hypercapnia e.g. normocapnia and  $i = 2$  for a different level of hypercapnia. The ratio of oxygen-related signal changes where there is no CBF change with hyperoxia is given by:

$$\frac{\Delta S_1 \cdot S_2}{\Delta S_2 \cdot S_1} = \frac{CBV_1}{CBV_2} \cdot \frac{[dHb_1]_0^\beta}{[dHb_2]_0^\beta} \left( \frac{1 - \left( \frac{[dHb_1]}{[dHb_1]_0} \right)^\beta}{1 - \left( \frac{[dHb_2]}{[dHb_2]_0} \right)^\beta} \right) \quad (\text{A.14})$$

where  $[dHb_i]_0$  and  $[dHb_i]$  represent deoxyhaemoglobin concentrations for the  $i$ th level of hypercapnia at baseline and elevated  $P_aO_2$ .

The ratio of deoxyhaemoglobin concentrations can be expanded using a binomial series assuming that the arterial hyperoxia related change in  $[dHb]$  is small, namely

$$\left( \frac{[dHb] - [dHb]_0}{[dHb]_0} \right) \ll 1$$

$$\left( \frac{[dHb_i]}{[dHb_i]_0} \right)^\beta = \left( 1 + \frac{[dHb_i] - [dHb_i]_0}{[dHb_i]_0} \right)^\beta = 1 + \beta \left( \frac{[dHb_i] - [dHb_i]_0}{[dHb_i]_0} \right) + \dots$$

Substituting the first two terms into Equation A.14

$$\frac{\Delta S_1 \cdot S_2}{\Delta S_2 \cdot S_1} = \frac{CBV_1}{CBV_2} \cdot \frac{[dHb_1]_0^{\beta-1}}{[dHb_2]_0^{\beta-1}} \left( \frac{[dHb_1] - [dHb_1]_0}{[dHb_2] - [dHb_2]_0} \right) \quad (\text{A.15})$$

Then assuming that the hyperoxia related changes in BOLD signal are small, namely  $S_1 \cong S_2$  and for a pure change in CBF,  $\frac{[dHb_1]_0}{[dHb_2]_0} \cong \frac{CBF_2}{CBF_1}$ , then

$$\frac{\Delta S_1}{\Delta S_2} = \left( \frac{CBF_1}{CBF_2} \right)^\alpha \cdot \frac{(CBF_2)^{\beta-1}}{(CBF_1)^{\beta-1}} \left( \frac{[dHb_1] - [dHb_1]_0}{[dHb_2] - [dHb_2]_0} \right) \quad (\text{A.16})$$

During experimentation,  $[dHb_i] - [dHb_i]_0$  is not directly measured. However, for an increase in arterial oxygen content during hyperoxia, under the assumption that oxygen metabolism is unchanged, the extra-arterial oxygen appears as a change in venous deoxyhaemoglobin concentration. Namely,  $[dHb_i] - [dHb_i]_0$  is proportional to  $\Delta C_a O_{2|i} = C_a O_{2|i,hyperoxia} - C_a O_{2|i,normoxia}$ , the difference in arterial oxygen content induced by hyperoxia at the  $i$ th level of CBF. Therefore,

$$\frac{\Delta S_{1,O_2}}{\Delta S_{2,O_2}} = \left( \frac{CBF_1}{CBF_2} \right)^{1+\alpha-\beta} \quad (A.17)$$

where  $\Delta S_{i,O_2} = \frac{\Delta S_i}{\Delta C_a O_{2|i}}$  is the hyperoxia-induced BOLD signal change normalised to the hyperoxia-induced change in total arterial oxygen content, administered at the  $i$ th hypercapnic (CBF) level. This gives us a relationship which can be used with the experimental data from combined hypercapnia and hyperoxia estimate  $(1+\alpha - \beta)$

# Bibliography

- [1] D.P. Bulte, M. Kelly, M. Germuska, J. Xie, M.A. Chappell, T.W. Okell, M.G. Bright, and P. Jezzard. Quantitative measurement of cerebral physiology using respiratory-calibrated MRI. *NEUROIMAGE*, 60(1):582–591, MAR 2012.
- [2] C.J. Gauthier and R.D. Hoge. Magnetic resonance imaging of resting OEF and CMRO<sub>2</sub> using a generalized calibration model for hypercapnia and hyperoxia. *NEUROIMAGE*, 60(2):1212–1225, APR 2 2012.
- [3] R.G. Wise, A.D. Harris, A.J. Stone, and K. Murphy. Measurement of oef and absolute cmro: Mri-based methods using interleaved and combined hypercapnia and hyperoxia. *Neuroimage*, 83C:135–147, Jun 2013.
- [4] D Attwell and SB Laughlin. An energy budget for signaling in the grey matter of the brain. *JOURNAL OF CEREBRAL BLOOD FLOW AND METABOLISM*, 21(10):1133–1145, OCT 2001.
- [5] A Ames. CNS energy metabolism as related to function. *BRAIN RESEARCH REVIEWS*, 34(1-2):42–68, NOV 2000.
- [6] PA Robbins, J Conway, DA Cunningham, S Khamnei, and DJ Paterson. A comparison of indirect methods for continuous estimation of arterial PCO<sub>2</sub> in men. *JOURNAL OF APPLIED PHYSIOLOGY*, 68(4):1727–1731, APR 1990.
- [7] WL Young, I Prohovnik, E Ornstein, N Ostapkovich, and RS Matteo. Cerebral blood-flow reactivity to changes in carbon-dioxide calculated using

- end-tidal versus arterial tensions. *JOURNAL OF CEREBRAL BLOOD FLOW AND METABOLISM*, 11(6):1031–1035, NOV 1991.
- [8] P. van Gelderen, J. A. de Zwart, and J. H. Duyn. Pitfalls of MRI measurement of white matter perfusion based on arterial spin labeling. *MAGNETIC RESONANCE IN MEDICINE*, 59(4):788–795, APR 2008.
- [9] H. Yamauchi, H. Fukuyama, Y. Nagahama, H. Nabatame, K. Nakamura, Y. Yamamoto, Y. Yonekura, J. Konishi, and J. Kimura. Evidence of misery perfusion and risk for recurrent stroke in major cerebral arterial occlusive diseases from PET. *JOURNAL OF NEUROLOGY NEUROSURGERY AND PSYCHIATRY*, 61(1):18–25, JUL 1996.
- [10] ME Raichle and DA Gusnard. Appraising the brain’s energy budget. *PROCEEDINGS OF THE NATIONAL ACADEMY OF SCIENCES OF THE UNITED STATES OF AMERICA*, 99(16):10237–10239, AUG 6 2002.
- [11] DA Gusnard and ME Raichle. Searching for a baseline: Functional imaging and the resting human brain. *NATURE REVIEWS NEUROSCIENCE*, 2(10):685–694, OCT 2001.
- [12] J Murdoch and R Hall. Brain protection - Physiological and pharmacological considerations .1. The physiology of brain injury. *CANADIAN JOURNAL OF ANAESTHESIA-JOURNAL CANADIEN D ANESTHESIE*, 37(6):663–671, SEP 1990.
- [13] K. Ishii, H. Kitagaki, M. Kono, and E. Mori. Decreased medial temporal oxygen metabolism in Alzheimer’s disease shown by PET. *JOURNAL OF NUCLEAR MEDICINE*, 37(7):1159–1165, JUL 1996.
- [14] P. Borghammer, P. Cumming, K. Ostergaard, A. Gjedde, A. Rodell, C.J. Bailey, and M.S. Vafaee. Cerebral oxygen metabolism in patients with



- early Parkinson's disease. *JOURNAL OF THE NEUROLOGICAL SCIENCES*, 313(1-2):123–128, FEB 15 2012.
- [15] DJ Brooks, KL Leenders, G Head, J Marshall, NJ Legg, and T Jones. Studies on regional cerebral oxygen utilization and cognitive function in multiple-sclerosis. *JOURNAL OF NEUROLOGY NEUROSURGERY AND PSYCHIATRY*, 47(11):1182–1191, 1984.
- [16] J Sobesky, O Zaro-Weber, FG Lehnhardt, V Hesselmann, M Neveling, A Jacobs, and WD Heiss. Does the mismatch match the penumbra? Magnetic resonance imaging and positron emission tomography in early ischemic stroke. *STROKE*, 36(5):980–985, MAY 2005.
- [17] K.L. Leenders. PET - Blood-flow and oxygen-consumption in brain-tumors. *JOURNAL OF NEURO-ONCOLOGY*, 22(3):269–273, 1994.
- [18] S.S. Kety and C.F. Schmidt. The effects of altered arterial tensions of carbon dioxide and oxygen on cerebral blood flow and cerebral oxygen consumption of normal young men. *JOURNAL OF CLINICAL INVESTIGATION*, 27(4):484–492, 1948.
- [19] H Ito, M Ibaraki, I Kanno, H Fukuda, and S Miura. Changes in cerebral blood flow and cerebral oxygen metabolism during neural activation measured by positron emission tomography: comparison with blood oxygenation level-dependent contrast measured by functional magnetic resonance imaging. *JOURNAL OF CEREBRAL BLOOD FLOW AND METABOLISM*, 25(3):371–377, MAR 2005.
- [20] M M Ter-Pogossian, J O Eichling, D O Davis, and M J Welch. The measure in vivo of regional cerebral oxygen utilization by means of oxyhemoglobin

- labeled with radioactive oxygen-15. *J Clin Invest*, 49(2):381–391, Feb 1970.
- [21] MA Mintun, ME Raichle, WRW Martin, and P Herscovitch. Brain oxygen utilization measured with O-15 radiotracers and positron emission tomography. *JOURNAL OF NUCLEAR MEDICINE*, 25(2):177–187, 1984.
- [22] GL Lenzi, RSJ Frackowiak, T Jones, JD Heather, AA Lammertsma, CG Rhodes, and C Pozzilli. CMRO<sub>2</sub> and CBF by the O-15 inhalation technique - results in normal volunteers and cerebrovascular patients. *EUROPEAN NEUROLOGY*, 20(3):285–290, 1981.
- [23] DA Boas, G Strangman, JP Culver, RD Hoge, G Jasdzewski, RA Poldrack, BR Rosen, and JB Mandeville. Can the cerebral metabolic rate of oxygen be estimated with near-infrared spectroscopy? *PHYSICS IN MEDICINE AND BIOLOGY*, 48(15):2405–2418, AUG 7 2003.
- [24] P Mansfield. Multi-planar Image-formation using NMR Spin Echoes. *JOURNAL OF PHYSICS C-SOLID STATE PHYSICS*, 10(3):L55–L58, 1977.
- [25] CB Ahn, JH Kim, and ZH Cho. High-speed spiral-scan echo planar NMR imaging .1. *IEEE TRANSACTIONS ON MEDICAL IMAGING*, 5(1):2–7, MAR 1986.
- [26] GH Glover and S Lai. Self-navigated spiral fMRI: Interleaved versus single-shot. *MAGNETIC RESONANCE IN MEDICINE*, 39(3):361–368, MAR 1998.
- [27] YH Yang, GH Glover, P van Gelderen, AC Patel, VS Mattay, JA Frank, and JH Duyn. A comparison of fast MR scan techniques for cerebral activation studies at 1.5 Tesla. *MAGNETIC RESONANCE IN MEDICINE*, 39(1):61–67, JAN 1998.

- [28] Gary H. Glover. Spiral imaging in fMRI. *NEUROIMAGE*, 62(2, SI):706–712, AUG 15 2012.
- [29] J.L. Boxerman, L.M. Hamberg, B.R. Rosen, and R.M. Weisskoff. MR contrast due to intravascular magnetic-susceptibility perturbations. *MAGNETIC RESONANCE IN MEDICINE*, 34(4):555–566, OCT 1995.
- [30] S Ogawa, TM Lee, AS Nayak, and P Glynn. Oxygenation-sensitive contrast in magnetic-resonance image of rodent brain at high magnetic-fields. *MAGNETIC RESONANCE IN MEDICINE*, 14(1):68–78, APR 1990.
- [31] S. Clare, S. Francis, P.G. Morris, and R. Bowtell. Single-shot  $T^*(2)$  measurement to establish optimum echo time for fMRI: Studies of the visual, motor, and auditory cortices at 3.0 T. *MAGNETIC RESONANCE IN MEDICINE*, 45(5):930–933, MAY 2001.
- [32] R.B. Buxton, K. Uludag, D.J. Dubowitz, and T.T. Liu. Modeling the hemodynamic response to brain activation. *NEUROIMAGE*, 23(1):S220–S233, 2004. Conference on Mathematics in Brain Imaging, Univ Calif Los Angeles, Inst Pure & Appl Math, Los Angeles, CA, JUL 12-23, 2004.
- [33] R.B. Buxton, L.R. Frank, E.C. Wong, B. Siewert, S. Warach, and R.R. Edelman. A general kinetic model for quantitative perfusion imaging with arterial spin labeling. *MAGNETIC RESONANCE IN MEDICINE*, 40(3):383–396, SEP 1998.
- [34] RR Edelman, B Siewert, DG Darby, V Thangaraj, AC Nobre, MM Mesulam, and S Warach. Qualitative mapping of cerebral blood-flow and functional localization with echo-planar MR-imaging and signal targeting with alternating radio-frequency. *RADIOLOGY*, 192(2):513–520, AUG 1994.

- [35] SG Kim. Quantification of relative cerebral blood-flow change by flow-sensitive alternating inversion-recovery (FAIR) technique - application to functional mapping. *MAGNETIC RESONANCE IN MEDICINE*, 34(3):293–301, SEP 1995.
- [36] EC Wong, RB Buxton, and LR Frank. Implementation of quantitative perfusion imaging techniques for functional brain mapping using pulsed arterial spin labeling. *NMR IN BIOMEDICINE*, 10(4-5):237–249, JUN-AUG 1997.
- [37] E.C. Wong, R.B. Buxton, and L.R. Frank. Quantitative imaging of perfusion using a single subtraction (QUIPSS and QUIPSS II). *MAGNETIC RESONANCE IN MEDICINE*, 39(5):702–708, MAY 1998.
- [38] E.C. Wong, R.B. Buxton, and L.R. Frank. A theoretical and experimental comparison of continuous and pulsed arterial spin labeling techniques for quantitative perfusion imaging. *MAGNETIC RESONANCE IN MEDICINE*, 40(3):348–355, SEP 1998.
- [39] J.J. Wang, Y. Zhang, R.L. Wolf, A.C. Roc, D.C. Alsop, and J.A. Detre. Amplitude-modulated continuous arterial spin-labeling 3.0 T perfusion MR imaging with a single coil: Feasibility study. *RADIOLOGY*, 235(1):218–228, APR 2005.
- [40] W. Dai, D. Garcia, C. de Bazelaire, and D.C. Alsop. Continuous Flow-Driven Inversion for Arterial Spin Labeling Using Pulsed Radio Frequency and Gradient Fields. *MAGNETIC RESONANCE IN MEDICINE*, 60(6):1488–1497, DEC 2008.
- [41] Mustafa Cavusoglu, Josef Pfeuffer, Kamil Ugurbil, and Kamil Uludag. Comparison of pulsed arterial spin labeling encoding schemes and abso-

- lute perfusion quantification. *MAGNETIC RESONANCE IMAGING*, 27(8):1039–1045, OCT 2009. International School on Magnetic Resonance and Brain Function, Erice, ITALY, MAY 18-25, 2008.
- [42] Wen-Chau Wu, Shu-Fen Jiang, Shun-Chung Yang, and Shu-Hua Lien. Pseudocontinuous arterial spin labeling perfusion magnetic resonance imaging-A normative study of reproducibility in the human brain. *NEUROIMAGE*, 56(3):1244–1250, JUN 1 2011.
- [43] T.T. Liu and E.C. Wong. A signal processing model for arterial spin labeling functional MRI. *NEUROIMAGE*, 24(1):207–215, JAN 1 2005.
- [44] TT Liu, EC Wong, LR Frank, and RB Buxton. Analysis and design of perfusion-based event-related fMRI experiments. *NEUROIMAGE*, 16(1):269–282, MAY 2002.
- [45] T.L. Davis, K.K. Kwong, R.M. Weisskoff, and B.R. Rosen. Calibrated functional MRI: Mapping the dynamics of oxidative metabolism. *PROCEEDINGS OF THE NATIONAL ACADEMY OF SCIENCES OF THE UNITED STATES OF AMERICA*, 95(4):1834–1839, FEB 17 1998.
- [46] P.A. Chiarelli, D.P. Bulte, R.G. Wise, D. Gallichan, and P. Jezzard. A calibration method for quantitative BOLD fMRI based on hyperoxia. *NEUROIMAGE*, 37(3):808–820, SEP 1 2007.
- [47] I Horvath, NT Sandor, Z Ruttner, and AC McLaughlin. Role of nitric oxide in regulating cerebrocortical oxygen-consumption and blood-flow during hypercapnia. *JOURNAL OF CEREBRAL BLOOD FLOW AND METABOLISM*, 14(3):503–509, MAY 1994.

- [48] SP Yang and JA Krasney. Cerebral blood-flow and metabolic responses to sustained hypercapnia in awake sheep. *JOURNAL OF CEREBRAL BLOOD FLOW AND METABOLISM*, 15(1):115–123, JAN 1995.
- [49] R.D. Hoge, J. Atkinson, B. Gill, G.R. Crelier, S. Marrett, and G.B. Pike. Investigation of BOLD signal dependence on cerebral blood flow and oxygen consumption: The deoxyhemoglobin dilution model. *MAGNETIC RESONANCE IN MEDICINE*, 42(5):849–863, NOV 1999.
- [50] R.L. Grubb, M.E. Raichle, J.O. Eichling, and M.M. Terpogos. Effects of changes in  $P_A\text{CO}_2$  on cerebral blood volume, blood flow, and vascular mean transit time. *STROKE*, 5(5):630–639, 1974.
- [51] D.P. Bulte, P.A. Chiarelli, R.G. Wise, and P. Jezzard. Cerebral perfusion response to hyperoxia. *JOURNAL OF CEREBRAL BLOOD FLOW AND METABOLISM*, 27(1):69–75, JAN 2007.
- [52] Sarah B. Rockswold, Gaylan L. Rockswold, David A. Zaun, Xuewei Zhang, Carla E. Cerra, Thomas A. Bergman, and Jiannong Liu. A prospective, randomized clinical trial to compare the effect of hyperbaric to normobaric hyperoxia on cerebral metabolism, intracranial pressure, and oxygen toxicity in severe traumatic brain injury Clinical article. *JOURNAL OF NEUROSURGERY*, 112(5):1080–1094, MAY 2010.
- [53] Feng Xu, Peiying Liu, Juan M. Pascual, Guanghua Xiao, and Hanzhang Lu. Effect of hypoxia and hyperoxia on cerebral blood flow, blood oxygenation, and oxidative metabolism. *JOURNAL OF CEREBRAL BLOOD FLOW AND METABOLISM*, 32(10):1909–1918, OCT 2012.
- [54] Erica M. Richards, Gary Fiskum, Robert E. Rosenthal, Irene Hopkins, and Mary C. McKenna. Hyperoxic reperfusion after global ischemia

- decreases hippocampal energy metabolism. *STROKE*, 38(5):1578–1584, MAY 2007.
- [55] Michael N. Diring, Venkatesh Aiyagari, Allyson R. Zazulia, Tom O. Videen, and William J. Powers. Effect of hyperoxia on cerebral metabolic rate for oxygen measured using positron emission tomography in patients with acute severe head injury. *JOURNAL OF NEUROSURGERY*, 106(4):526–529, APR 2007.
- [56] M Jones, J Berwick, N Hewson-Stoate, C Gias, and J Mayhew. The effect of hypercapnia on the neural and hemodynamic responses to somatosensory stimulation. *NEUROIMAGE*, 27(3):609–623, SEP 2005.
- [57] Feng Xu, Jinsoo Uh, Matthew R. Brier, John Hart, Jr., Uma S. Yezhuvath, Hong Gu, Yihong Yang, and Hanzhang Lu. The influence of carbon dioxide on brain activity and metabolism in conscious humans. *JOURNAL OF CEREBRAL BLOOD FLOW AND METABOLISM*, 31(1):58–67, JAN 2011.
- [58] K Kogure, R Busto, P Scheinberg, and O Reinmuth. Dynamics of cerebral metabolism during moderate hypercapnia. *JOURNAL OF NEUROCHEMISTRY*, 24(3):471–478, 1975.
- [59] KM Sicard and TQ Duong. Effects of hypoxia, hyperoxia, and hypercapnia on baseline and stimulus-evoked BOLD, CBF, and CMRO2 in spontaneously breathing animals. *NEUROIMAGE*, 25(3):850–858, APR 15 2005.
- [60] AB Kliefloth, RL Grubb, and ME Raichle. Depression of cerebral oxygen utilization by hypercapnia in the rhesus-monkey. *JOURNAL OF NEUROCHEMISTRY*, 32(2):661–663, 1979.

- [61] P Novack, HA Shenkin, L Bortin, B Goluboff, AM Soffe, P Batson, and D Golden. The effects of carbon dioxide inhalation upon the cerebral blood flow and cerebral oxygen consumption in vascular disease. *JOURNAL OF CLINICAL INVESTIGATION*, 32(8):696–702, 1953.
- [62] Z Barzilay, AG Britten, RC Koehler, JM Dean, and RJ Traystman. Interaction of CO<sub>2</sub> and ammonia on cerebral blood-flow and O<sub>2</sub> consumption in dogs. *AMERICAN JOURNAL OF PHYSIOLOGY*, 248(4):H500–H507, 1985.
- [63] R.G. Wise, K.T.S. Pattinson, D.P. Bulte, P.A. Chiarelli, S.D. Mayhew, G.M. Balanos, D.F. O’Connor, T.R. Pragnell, P.A. Robbins, I. Tracey, and P Jezard. Dynamic forcing of end-tidal carbon dioxide and oxygen applied to functional magnetic resonance imaging. *JOURNAL OF CEREBRAL BLOOD FLOW AND METABOLISM*, 27(8):1521–1532, AUG 2007.
- [64] A.P. Fan, T. Benner, D.S. Bolar, B.R. Rosen, and E. Adalsteinsson. Phase-based regional oxygen metabolism (PROM) using MRI. *MAGNETIC RESONANCE IN MEDICINE*, 67(3):669–678, MAR 2012.
- [65] DA Yablonskiy. Quantitation of intrinsic magnetic susceptibility-related effects in a tissue matrix. Phantom study. *MAGNETIC RESONANCE IN MEDICINE*, 39(3):417–428, MAR 1998. 5th Annual Meeting of ISMRM, VANCOUVER, CANADA, APR, 1997.
- [66] HY An and WL Lin. Quantitative measurements of cerebral blood oxygen saturation using magnetic resonance imaging. *JOURNAL OF CEREBRAL BLOOD FLOW AND METABOLISM*, 20(8):1225–1236, AUG 2000.



- [67] X. He and D.A. Yablonskiy. Quantitative BOLD: Mapping of human cerebral deoxygenated blood volume and oxygen extraction fraction: Default state. *MAGNETIC RESONANCE IN MEDICINE*, 57(1):115–126, JAN 2007.
- [68] T. Christen, B. Lemasson, N. Pannetier, R. Farion, C. Segebarth, C. Remy, and E.L. Barbier. Evaluation of a quantitative blood oxygenation level-dependent (qBOLD) approach to map local blood oxygen saturation. *NMR IN BIOMEDICINE*, 24(4):393–403, MAY 2011.
- [69] N.P. Blockley, V.E.M. Griffeth, and R.B. Buxton. A general analysis of calibrated BOLD methodology for measuring CMRO<sub>2</sub> responses: Comparison of a new approach with existing methods. *NEUROIMAGE*, 60(1):279–289, MAR 2012.
- [70] D. S. Bolar, B. R. Rosen, A. G. Sorensen, and E. Adalsteinsson. QUantitative Imaging of eXtraction of Oxygen and TIssue Consumption (QUIXOTIC) Using Venular-Targeted Velocity-Selective Spin Labeling. *MAGNETIC RESONANCE IN MEDICINE*, 66(6):1550–1562, DEC 2011.
- [71] Jia Guo and Eric C. Wong. Venous oxygenation mapping using velocity-selective excitation and arterial nulling. *MAGNETIC RESONANCE IN MEDICINE*, 68(5):1458–1471, NOV 2012.
- [72] T.T. Liu and G.G. Brown. Measurement of cerebral perfusion with arterial spin labeling: Part 1. Methods. *JOURNAL OF THE INTERNATIONAL NEUROPSYCHOLOGICAL SOCIETY*, 13(3):517–525, MAY 2007.
- [73] S. Aslan, F. Xu, P.L. Wang, J. Uh, U.S. Yezhuvath, M. van Osch, and H. Lu. Estimation of Labeling Efficiency in Pseudocontinuous Arterial

- Spin Labeling. *MAGNETIC RESONANCE IN MEDICINE*, 63(3):765–771, MAR 2010.
- [74] R.W. Cox. AFNI: Software for analysis and visualization of functional magnetic resonance neuroimages. *COMPUTERS AND BIOMEDICAL RESEARCH*, 29(3):162–173, JUN 1996.
- [75] Mark Jenkinson, Christian F. Beckmann, Timothy Ej. Behrens, Mark W. Woolrich, and Stephen M. Smith. FSL. *NEUROIMAGE*, 62(2, SI):782–790, AUG 15 2012.
- [76] J. Mazziotta, A. Toga, A. Evans, P. Fox, J. Lancaster, K. Zilles, R. Woods, T. Paus, G. Simpson, B. Pike, C. Holmes, L. Collins, P. Thompson, D. MacDonald, M. Iacoboni, T. Schormann, K. Amunts, N. Palomero-Gallagher, S. Geyer, L. Parsons, K. Narr, N. Kabani, G. Le Goualher, D. Boomsma, T. Cannon, R. Kawashima, and B. Mazoyer. A probabilistic atlas and reference system for the human brain: International Consortium for Brain Mapping (ICBM). *PHILOSOPHICAL TRANSACTIONS OF THE ROYAL SOCIETY B-BIOLOGICAL SCIENCES*, 356(1412):1293–1322, AUG 29 2001.
- [77] M. Jenkinson and S. Smith. A global optimisation method for robust affine registration of brain images. *MEDICAL IMAGE ANALYSIS*, 5(2):143–156, JUN 2001.
- [78] W.C. Wu, M. Fernandez-Seara, J.A. Detre, F.W. Wehrli, and J.J Wang. A theoretical and experimental investigation of the tagging efficiency of pseudocontinuous arterial spin labeling. *MAGNETIC RESONANCE IN MEDICINE*, 58(5):1020–1027, NOV 2007.

- [79] H. Lu and Y. Ge. Quantitative evaluation of oxygenation in venous vessels using T2-Relaxation-Under-Spin-Tagging MRI. *MAGNETIC RESONANCE IN MEDICINE*, 60(2):357–363, AUG 2008.
- [80] G.H. Glover, T.Q. Li, and D. Ress. Image-based method for retrospective correction of physiological motion effects in fMRI: RETROICOR. *MAGNETIC RESONANCE IN MEDICINE*, 44(1):162–167, JUL 2000.
- [81] A.K. Harvey, K.T.S. Pattinson, J.C.W. Brooks, S.D. Mayhew, M. Jenkinson, and R.G. Wise. Brainstem Functional Magnetic Resonance Imaging: Disentangling Signal From Physiological Noise. *JOURNAL OF MAGNETIC RESONANCE IMAGING*, 28(6):1337–1344, DEC 2008.
- [82] J.H. Wang, M.L. Qiu, and R.T. Constable. In vivo method for correcting transmit/receive nonuniformities with phased array coils. *MAGNETIC RESONANCE IN MEDICINE*, 53(3):666–674, MAR 2005.
- [83] Y.Y. Zhang, M. Brady, and S. Smith. Segmentation of brain MR images through a hidden Markov random field model and the expectation-maximization algorithm. *IEEE TRANSACTIONS ON MEDICAL IMAGING*, 20(1):45–57, JAN 2001.
- [84] O. Leontiev and R.B. Buxton. Reproducibility of BOLD, perfusion, and CMRO<sub>2</sub> measurements with calibrated-BOLD fMRI. *NEUROIMAGE*, 35(1):175–184, MAR 2007.
- [85] V.E.M. Griffeth and R.B. Buxton. A theoretical framework for estimating cerebral oxygen metabolism changes using the calibrated-BOLD method: Modeling the effects of blood volume distribution, hematocrit, oxygen extraction fraction, and tissue signal properties on the BOLD signal. *NEUROIMAGE*, 58(1):198–212, SEP 1 2011.

- [86] G. Marchal, P. Rioux, M.C. Petittaboue, G. Sette, J.M. Traverre, C. Lepoec, P. Courtheoux, J.M. Derlon, and J.C. Baron. Regional cerebral oxygen-consumption, blood-flow, and blood-volume in healthy-human aging. *ARCHIVES OF NEUROLOGY*, 49(10):1013–1020, OCT 1992.
- [87] J.S. Perlmuter, W.J. Powers, P. Herscovitch, P.T. Fox, and M.E. Raichle. Regional asymmetries of cerebral blood-flow, blood-volume, and oxygen utilization and extraction in normal subjects. *JOURNAL OF CEREBRAL BLOOD FLOW AND METABOLISM*, 7(1):64–67, FEB 1987.
- [88] A. Kastrup, G. Kruger, T. Neumann-Haefelin, G.H. Glover, and M.E. Moseley. Changes of cerebral blood flow, oxygenation, and oxidative metabolism during graded motor activation. *NEUROIMAGE*, 15(1):74–82, JAN 2002.
- [89] J.P. Coles, T.D. Fryer, P.G. Bradley, J. Nortje, P. Smielewski, K. Rice, J.C. Clark, J.D. Pickard, and D.K. Menon. Intersubject variability and reproducibility of O-15 PET studies. *JOURNAL OF CEREBRAL BLOOD FLOW AND METABOLISM*, 26(1):48–57, JAN 2006.
- [90] J.P. Bremmer, B.N.M. van Berckel, S. Persoon, L.J. Kappelle, A.A. Lammertsma, R. Kloet, G. Luurtsema, A. Rijbroek, C.J.M. Klijn, and R. Boellaard. Day-to-Day Test-Retest Variability of CBF, CMRO<sub>2</sub>, and OEF Measurements Using Dynamic O-15 PET Studies. *MOLECULAR IMAGING AND BIOLOGY*, 13(4):759–768, AUG 2011.
- [91] P. Liu, F. Xu, and H. Lu. Testretest reproducibility of a rapid method to measure brain oxygen metabolism. *MAGNETIC RESONANCE IN MEDICINE*, 69(3):675–681, MAR 2013.

- [92] PE Shrout and JL Fleiss. Intraclass correlations - uses in assessing rater reliability. *PSYCHOLOGICAL BULLETIN*, 86(2):420–428, 1979.
- [93] D.V. Cicchetti. The precision of reliability and validity estimates re-visited: Distinguishing between clinical and statistical significance of sample size requirements. *JOURNAL OF CLINICAL AND EXPERIMENTAL NEUROPSYCHOLOGY*, 23(5):695–700, OCT 2001.
- [94] K.P. Eaton, J.P. Szaflarski, M. Altaye, A.L. Ball, B.M. Kissela, C. Banks, and S.K. Holland. Reliability of fMRI for studies of language in post-stroke aphasia subjects. *NEUROIMAGE*, 41(2):311–322, JUN 2008. 13th Annual Meeting of the Organization for Human Brain Mapping, Chicago, IL, JUN 10-14, 2007.
- [95] B.G. van den Bulk, P.C.M.P. Koolschijn, P.H.F. Meens, N.D.J. van Lang, N.J.A. van der Wee, S.A.R.B. Rombouts, R.R.J.M. Vermeiren, and E.A. Crone. How stable is activation in the amygdala and prefrontal cortex in adolescence? A study of emotional face processing across three measurements. *DEVELOPMENTAL COGNITIVE NEUROSCIENCE*, 4(SI):65–76, APR 2013.
- [96] M.G. Bright and K. Murphy. Reliable quantification of bold fmri cerebrovascular reactivity despite poor breath-hold performance. *NEUROIMAGE*, 83C:559–568, Jul 2013.
- [97] S.S. Kety and C.F. Schmidt. The effects of active and passive hyperventilation on cerebral blood flow, cerebral oxygen consumption, cardiac output, and blood pressure of normal young men. *JOURNAL OF CLINICAL INVESTIGATION*, 25(1):107–119, 1946.

- [98] I. Kanno, K. Uemura, S. Higano, M. Murakami, H. Iida, S. Miura, F. Shishido, A. Inugami, and I. Sayama. Oxygen extraction fraction at maximally vasodilated tissue in the ischemic brain estimated from the regional CO<sub>2</sub> responsiveness measured by positron emission tomography. *JOURNAL OF CEREBRAL BLOOD FLOW AND METABOLISM*, 8(2):227–235, APR 1988.
- [99] H. Ito, I. Kanno, M. Ibaraki, J. Hatazawa, and S. Miura. Changes in human cerebral blood flow and cerebral blood volume during hypercapnia and hypocapnia measured by positron emission tomography. *JOURNAL OF CEREBRAL BLOOD FLOW AND METABOLISM*, 23(6):665–670, JUN 2003.
- [100] H. Ito, I. Kanno, M. Ibaraki, T. Suhara, and S. Miura. Relationship between baseline cerebral blood flow and vascular responses to changes in PaCO<sub>2</sub> measured by positron emission tomography in humans: implication of inter-individual variations of cerebral vascular tone. *ACTA PHYSIOLOGICA*, 193(4):325–330, AUG 2008.
- [101] I. Yokoyama, Y. Inoue, T. Kinoshita, H. Itoh, I. Kanno, and H. Iida. Heart and brain circulation and CO(2) in healthy men. *ACTA PHYSIOLOGICA*, 193(3):303–308, JUL 2008.
- [102] J.J. Chen and G.B. Pike. Global cerebral oxidative metabolism during hypercapnia and hypocapnia in humans: implications for BOLD fMRI. *JOURNAL OF CEREBRAL BLOOD FLOW AND METABOLISM*, 30(6):1094–1099, JUN 2010.
- [103] A. Gjedde, P. Johannsen, G.E. Cold, and L. Ostergaard. Cerebral metabolic response to low blood flow: possible role of cytochrome oxidase inhibition.

- JOURNAL OF CEREBRAL BLOOD FLOW AND METABOLISM*, 25(9):1183–1196, SEP 2005.
- [104] R.W. McPherson, S.A. Derrer, and R.J. Traystman. Changes in cerebral CO<sub>2</sub> responsivity over time during isoflurane anesthesia in the dog. *JOURNAL OF NEUROSURGICAL ANESTHESIOLOGY*, 3(1):12–19, MAR 1991.
  - [105] J. Grote, K. Zimmer, and R. Schubert. Effects of severe arterial hypocapnia on regional blood-flow regulation, tissue PO<sub>2</sub> and metabolism in the brain cortex of cats. *PFLUGERS ARCHIV-EUROPEAN JOURNAL OF PHYSIOLOGY*, 391(3):195–199, 1981.
  - [106] M.G. Bright, M.J. Donahue, J.H. Duyn, P. Jezzard, and D.P. Bulte. The effect of basal vasodilation on hypercapnic and hypocapnic reactivity measured using magnetic resonance imaging. *JOURNAL OF CEREBRAL BLOOD FLOW AND METABOLISM*, 31(2):426–438, FEB 2011.
  - [107] M. Weckesser, S. Posse, U. Olthoff, L. Kemna, S. Dager, and H.W. Muller-Gartner. Functional imaging of the visual cortex with bold-contrast MRI: Hyperventilation decreases signal response. *MAGNETIC RESONANCE IN MEDICINE*, 41(1):213–216, JAN 1999.
  - [108] K.T.S. Pattinson, R. Rogers, S.D. Mayhew, I. Tracey, and R.G. Wise. Pharmacological fMRI: measuring opioid effects on the BOLD response to hypercapnia. *JOURNAL OF CEREBRAL BLOOD FLOW AND METABOLISM*, 27(2):414–423, FEB 2007.
  - [109] A. Kastrup, G. Kruger, T. Neumann-Haefelin, and M.E. Moseley. Assessment of cerebrovascular reactivity with functional magnetic resonance imaging: comparison of CO<sub>2</sub> and breath holding. *MAGNETIC RESONANCE IMAGING*, 19(1):13–20, JAN 2001.

- [110] H. Caspers, E.J. Speckmann, and A. Lehmenkuhler. DC potentials of the cerebral-cortex - seizure activity and changes in gas-pressures. *REVIEWS OF PHYSIOLOGY BIOCHEMISTRY AND PHARMACOLOGY*, 106:127–178, 1987.
- [111] M. Carbon, G. Wubbeler, L. Trahms, and G. Curio. Hyperventilation-induced human cerebral magnetic fields non-invasively monitored by multichannel ‘direct current’ magnetoencephalography. *NEUROSCIENCE LETTERS*, 287(3):227–230, JUN 30 2000.
- [112] R.S. Mohtasib, G. Lumley, J.A. Goodwin, H.C.A. Emsley, V. Sluming, and L.M. Parkes. Calibrated fMRI during a cognitive Stroop task reveals reduced metabolic response with increasing age. *NEUROIMAGE*, 59(2):1143–1151, JAN 16 2012.
- [113] S.S. Kannurpatti and B.B. Biswal. Detection and scaling of task-induced fMRI-BOLD response using resting state fluctuations. *NEUROIMAGE*, 40(4):1567–1574, MAY 1 2008.
- [114] DA YABLONSKIY and EM HAACKE. Theory of NMR signal behavior in magnetically inhomogenous tissues - The static dephasing regime. *MAGNETIC RESONANCE IN MEDICINE*, 32(6):749–763, DEC 1994.
- [115] Xiang He and Dmitriy A. Yablonskiy. Quantitative BOLD: Mapping of human cerebral deoxygenated blood volume and oxygen extraction fraction: Default state. *MAGNETIC RESONANCE IN MEDICINE*, 57(1):115–126, JAN 2007.
- [116] M.C. Sohlin and L.R. Schad. Susceptibility-Related MR Signal Dephasing Under Nonstatic Conditions: Experimental Verification and Conse-



- quences for qBOLD Measurements. *JOURNAL OF MAGNETIC RESONANCE IMAGING*, 33(2):417–425, FEB 2011.
- [117] J. Sedlacik and J.R. Reichenbach. Validation of Quantitative Estimation of Tissue Oxygen Extraction Fraction and Deoxygenated Blood Volume Fraction in Phantom and In Vivo Experiments by Using MRI. *MAGNETIC RESONANCE IN MEDICINE*, 63(4):910–921, APR 2010.
- [118] Thomas Christen, Benjamin Lemasson, Nicolas Pannetier, Regine Farion, Christoph Segebarth, Chantal Remy, and Emmanuel L. Barbier. Evaluation of a quantitative blood oxygenation level-dependent (qBOLD) approach to map local blood oxygen saturation. *NMR IN BIOMEDICINE*, 24(4):393–403, MAY 2011.
- [119] T. Christen, H. Schmiedeskamp, M. Straka, R. Bammer, and G. Zaharchuk. Measuring brain oxygenation in humans using a multiparametric quantitative blood oxygenation level dependent MRI approach. *MAGNETIC RESONANCE IN MEDICINE*, 68(3):905–911, SEP 2012.
- [120] T Christen, N. Pannetier, W. Ni, D. Qiu, N. Schuff, M. Moseley, and G. Zaharchuk. A fingerprinting approach to compute blood volume, vessel diameter and blood oxygenation maps in the human brain. *Proceedings of the 21st Annual Meeting ISMRM, Salt Lake City, Utah, USA*, 2013.
- [121] N.P. Blockley, V.E.M. Griffeth, A.B. Simon, and R.B. Buxton. A review of calibrated blood oxygenation level-dependent (BOLD) methods for the measurement of task-induced changes in brain oxygen metabolism. *NMR IN BIOMEDICINE*, 26(8, SI):987–1003, AUG 2013.
- [122] S. Ogawa, R.S. Menon, D.W. Tank, S.G. Kim, H. Merkle, J.M. Ellermann, and K. Ugurbil. Functional brain mapping by blood oxygenation level-

- dependent contrast magnetic-resonance-imaging - A comparison of signal characteristics with a biophysical model. *BIOPHYSICAL JOURNAL*, 64(3):803–812, MAR 1993.
- [123] F. Franconi, P. Mowat, L. Lemaire, P. Richomme, and J-J Le Jeune. Single-scan quantitative  $T_2^*$  methods with susceptibility artifact reduction. *NMR IN BIOMEDICINE*, 19(5):527–534, AUG 2006.
- [124] G.H. Glover and C.S. Law. Spiral-in/out BOLD fMRI for increased SNR and reduced susceptibility artifacts. *MAGNETIC RESONANCE IN MEDICINE*, 46(3):515–522, SEP 2001.
- [125] T.Q. Li, A. Takahashi, Y. Wang, V. Mathews, and G.H. Glover. Dual-echo spiral in/in acquisition method for reducing magnetic susceptibility artifacts in blood-oxygen-level-dependent functional magnetic resonance imaging. *MAGNETIC RESONANCE IN MEDICINE*, 55(2):325–334, FEB 2006. 11th Annual Meeting of the International-Society-for-Magnetic-Resonance-in-Medicine, TORONTO, CANADA, JUL 10-16, 2003.
- [126] K.D. Brewer, J.A. Rioux, R.C. N. D’Arcy, C.V. Bowen, and S.D. Beyea. Asymmetric spin-echo (ASE) spiral improves BOLD fMRI in inhomogeneous regions. *NMR IN BIOMEDICINE*, 22(6):654–662, JUL 2009.
- [127] N. Fujita, M. Shinohara, H. Tanaka, K. Yutani, H. Nakamura, and K. Murase. Quantitative mapping of cerebral deoxyhemoglobin content using MR imaging. *NEUROIMAGE*, 20(4):2071–2083, DEC 2003.
- [128] H. An and W.L. Lin. Impact of intravascular signal on quantitative measures of cerebral oxygen extraction and blood volume under normo- and hyper-

- capnic conditions using an asymmetric spin echo approach. *MAGNETIC RESONANCE IN MEDICINE*, 50(4):708–716, OCT 2003.
- [129] Marcus E. Raichle and Mark A. Mintun. Brain work and brain imaging. *ANNUAL REVIEW OF NEUROSCIENCE*, 29:449–476, 2006.
- [130] CP Derdeyn, TO Videen, KD Yundt, SM Fritsch, DA Carpenter, RL Grubb, and WJ Powers. Variability of cerebral blood volume and oxygen extraction: stages of cerebral haemodynamic impairment revisited. *BRAIN*, 125(3):595–607, MAR 2002.
- [131] JM Brown and WR William. Exploiting tumour hypoxia in cancer treatment. *NATURE REVIEWS CANCER*, 4(6):437–447, JUN 2004.
- [132] James L. Tatum, Gary J. Kelloff, Robert J. Gillies, Jeffrey M. Arbeit, J. Martin Brown, K. S. Clifford Chao, J. Donald Chapman, William C. Eckelman, Anthony W. Fyles, Amato J. Giaccia, Richard P. Hill, Cameron J. Koch, Murali Cherukuri Krishna, Kenneth A. Krohn, Jason S. Lewis, Ralph P. Mason, Giovanni Melillo, Anwar R. Padhani, Garth Powis, Joseph G. Rajendran, Richard Reba, Simon P. Robinson, Gregg L. Semenza, Harold M. Swartz, Peter Vaupel, David Yang, Barbara Croft, John Hoffman, Guoying Liu, Helen Stone, and Daniel Sullivan. Hypoxia: Importance in tumor biology, noninvasive measurement by imaging, and value of its measurement in the management of cancer therapy. *INTERNATIONAL JOURNAL OF RADIATION BIOLOGY*, 82(10):699–757, OCT 2006.
- [133] Sonal Davda and Tedros Bezabeh. Advances in methods for assessing tumor hypoxia in vivo: Implications for treatment planning. *CANCER AND METASTASIS REVIEWS*, 25(3):469–480, SEP 2006.

- [134] C Iadecola. Neurovascular regulation in the normal brain and in Alzheimer's disease. *NATURE REVIEWS NEUROSCIENCE*, 5(5):347–360, MAY 2004.
- [135] C Iadecola. Rescuing troubled vessels in Alzheimer disease. *NATURE MEDICINE*, 11(9):923–924, SEP 2005.
- [136] Andrei G. Vlassenko, S. Neil Vaishnavi, Lars Couture, Dana Sacco, Benjamin J. Shannon, Robert H. Mach, John C. Morris, Marcus E. Raichle, and Mark A. Mintun. Spatial correlation between brain aerobic glycolysis and amyloid-beta (A beta) deposition. *PROCEEDINGS OF THE NATIONAL ACADEMY OF SCIENCES OF THE UNITED STATES OF AMERICA*, 107(41):17763–17767, OCT 12 2010.
- [137] William J. Powers, Tom O. Videen, Joanne Markham, Lori McGee-Minnich, JoAnn V. Antenor-Dorsey, Tamara Hershey, and Joel S. Perlmutter. Selective defect of in vivo glycolysis in early Huntington's disease striatum. *PROCEEDINGS OF THE NATIONAL ACADEMY OF SCIENCES OF THE UNITED STATES OF AMERICA*, 104(8):2945–2949, FEB 20 2007.
- [138] MF Beal. Mitochondrial dysfunction in neurodegenerative diseases. *BIOCHIMICA ET BIOPHYSICA ACTA-BIOENERGETICS*, 1366(1-2):211–223, AUG 10 1998.
- [139] P Santens, J DeReuck, L Crevits, D Decoo, I Lemahieu, K Strijckmans, and P Goethals. Cerebral oxygen metabolism in patients with progressive supranuclear palsy: A positron emission tomography study. *EUROPEAN NEUROLOGY*, 37(1):18–22, 1997.

- [140] F Shishido, K Uemura, A Inugami, N Tomura, S Higano, H Fujita, H Sasaki, I Kanno, M Murakami, Y Watahiki, and K Nagata. Cerebral oxygen and glucose metabolism and blood flow in mitochondrial encephalomyopathy: A PET study. *NEURORADIOLOGY*, 38(2):102–107, FEB 1996.
- [141] Richard G. Wise and Cliff Preston. What is the value of human FMRI in CNS drug development? *DRUG DISCOVERY TODAY*, 15(21-22):973–980, NOV 2010.
- [142] Ruth L. O’Gorman, Paul E. Summers, Fernando O. Zelaya, Steven C. R. Williams, David C. Alsop, and David J. Lythgoe. In vivo estimation of the flow-driven adiabatic inversion efficiency for continuous arterial spin labeling: A method using phase contrast magnetic resonance angiography. *MAGNETIC RESONANCE IN MEDICINE*, 55(6):1291–1297, JUN 2006.
- [143] Dmitriy A. Yablonskiy, Alexander L. Sukstanskii, and Xiang He. Blood oxygenation level-dependent (BOLD)-based techniques for the quantification of brain hemodynamic and metabolic properties - theoretical models and experimental approaches. *NMR IN BIOMEDICINE*, 26(8, SI):963–986, AUG 2013.